

Orbital temporal and spectral properties of X-ray binaries

Nafisa Aftab

Department of Astronomy and Astrophysics
Raman Research Institute
Bengaluru

This dissertation is submitted for the degree of

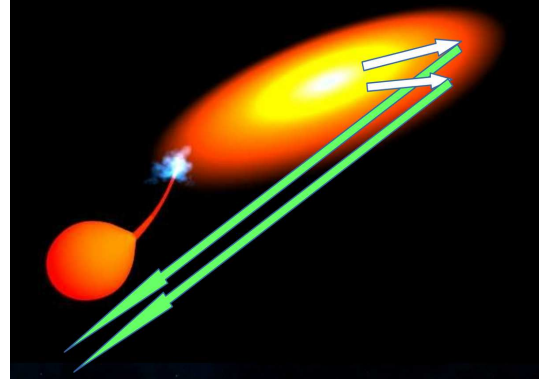
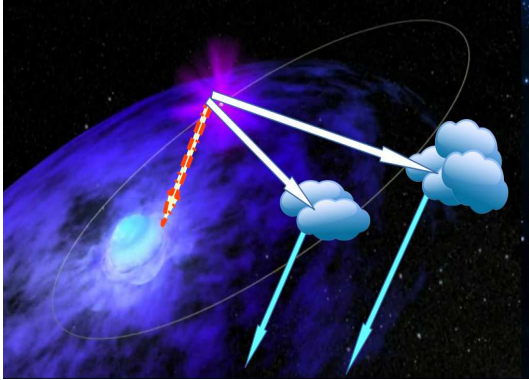
Doctor of Philosophy

Jawaharlal Nehru University

New Delhi

April 2018

*To my loving parents
for showing me the joy of an unbiased mind*



Primary photons can be traced from the history of reprocessed photons.

Looking at this, some queries pop up in my mind –

What for are we here on Earth? Is death pure annihilation with respect to the departed person? If the nature is so ordered, then would not the deprived get justice?

These questions remain unanswered, because we do not fully understand the concept of time.



Global peace can only be achieved, if we apply the same rationality everywhere, which we apply in sciences.

Certificate

This is to certify that the dissertation entitled 'Orbital Temporal and Spectral Properties of X-ray Binaries' submitted by Nafisa Aftab for the award of the degree of Doctor of Philosophy to Jawaharlal Nehru University, New Delhi is her original work. This has not been submitted or published for any other degree or qualification to any other university.

Prof. Ravi Subrahmanyam
Director

Prof. Biswajit Paul
Thesis Supervisor

Raman Research Institute,
Bengaluru 560 080
INDIA

Declaration

I, Nafisa Aftab, declare that the work reported in this dissertation titled 'Orbital temporal and spectral properties of X-ray binaries', is entirely original. This thesis is composed independently by me at the Raman Research Institute under the supervision of Prof. Biswajit Paul. I further declare that the subject matter presented in this thesis has not previously formed the basis for the award of any degree, diploma, membership, associateship, fellowship or any other similar title of any university or institution. I also declare that I have run it through TURNITIN plagiarism software.

Prof. Biswajit Paul

Nafisa Aftab

Department of Astronomy and Astrophysics
Raman Research Institute,
Bangalore 560080
INDIA.

Acknowledgements

‘Most difficult job of my thesis writing is, acknowledging my father in just one para’

I thank you dear reader, for your patience. I do not have scientific proofs for my words here or any reference to give you, but these are from the bottom of my heart.

I first express my sincere gratitude to the creator and cherisher of the wonderful Cosmos. I stand amazed to see your design ‘Oh, the Omnipotent’!, whether it is the behaviour of water within $(0-4)^{\circ}$ C on Earth or the sweeping of a pulsar beam in the sky. Nature has submitted its will to your sovereignty. You showered your endless mercy to me to get an opportunity to work at the joyful environment of Raman Research Institute (RRI). You made my PhD journey very peaceful. You saved me whenever I fell because of my mistakes. You helped me from sources beyond my imagination. Above all, you bestow your mercy towards everyone. My words are not enough to thank you. I sincerely beg to you to make me equally gratified to you in my good, tough and busy days.

Dear Dad! I can feel, how much you would be happy seeing the thesis. You realized my queries regarding the Universe and encouraged me to explore. You have given me enough freedom in accepting or rejecting a faith or developing a thought by rational analysis. You taught me without instruction. You introduced me with common people’s right before you introduced me animals in the zoo, all without words. You were with people at their tough times in whichever way you could, with your wise thoughts, kind words, time, business, lands..... everything. I remember your same smiling attitude at 2 am or 10 am, whenever people approached you. I respect you so much because your love for people was irrespective

of relation, cast, creed, colour or gender. You gave priority to the intensity of need. You would ease problems with your nice words and excellent sense of humour. Your dealings with people has taught me to analyze every situation in day-to-day life, that always prevents me from misunderstanding people, which has always been a great source of peace. I wish I could be 1% of you. Without you my life is empty; but I thank Almighty; the sustainer of the Universe for giving me such a precious gift; 'You', as my father.

My heartfelt gratitude to my thesis supervisor Prof. Biswajit Paul for giving me enough freedom to express my thoughts related to accretion physics, He has listened to me with patience, even when I was wrong. He let me find my mistakes by asking some simple questions. His deep insights has helped me to extract physics of extreme environment from the data. I also remain indebted for his wise suggestions at various stages during my PhD. Thank you Biswajit da, you made my Europe visits successful, which has helped me to discover the natural beauties and generous people over there.

I am grateful to the members of my thesis advisory committee, Ranjini (Prof. Ranjini Bandyopadhyay) and Shiv (Prof. Shiv Sethi) for their valuable suggestions during my PhD years. Thank you Ranjini and Shiv, you both made my PhD. journey smooth at RRI. I express my sincere thanks to the faculties from RRI and IISC for teaching us various courses during course work in the 1st year of PhD. I am also thankful to all the faculties at our department at RRI, I have learnt many things from them.

My sincere thanks to the director Prof. Ravi Subrahmanyam, administrative officers Krishna (former) and Murthy (present) for solving our problems in shortest time; I am thankful to our account officer and everybody at their office. I was in urgent need of money in my credit card at Stockholm during one of my scientific visit to Europe, thank you so much Murthy and Suresh (account officer) for sending me money at quickest possible time.

Many thanks to Radha, Marisa, Shailaja for ensuring smooth administration. Thank you Radha, I even did not know you then, you helped me to attend the interview by preponing

it to the first day of the interview session, my interview was scheduled for the last day. I came to Bangalore to visit my brother coincidentally and suddenly came to know about the interview; my departure was scheduled before the assigned date of my interview. Thank you Almighty; thanks to administration of RRI; thank you everybody at the interview panel; Desh, Ranjini, Sanjib, Sadiq, Yashodhan, Abhishek. You people did not give importance to preparation, rather emphasized on discussion.

RRI library has always been like my second home since my very first day at RRI. Many thanks to Meera, Manjunath (M.), Nagraj, Manju (K.), Vani, Vrinda, Geetha, Lingegowda, Chowdappa, Elumalai, Raju, Shridhara, Mahesh. You all have made the environment of the library very peaceful and provided smooth facilities. I have found you people very kind, whenever I approached to you with queries or for books, printouts, xeroxes, scanning, binding etc. Thanks so much for your belief and letting us access the library even after office hours and during holidays.

Thank you Jacob, Krishnamurthy, Sridhar and your team at the computer section, whenever I had any issue with my desktop, laptop or external hard discs, you all were always there with smart solutions.

Many thanks to the canteen staffs for providing us foods in proper time everyday, many times I took the plates and bowls to my office room and returned at the end of the day, thanks so much for your trust.

Vidya! You have been too kind to all of us. You had solutions to all our problems, even outside academics. You endured with love, even though I was too much forgetful. Later you moved to the administrative section of RRI, even from there you have been taking care of us. Thank you Vidya for everything. Thank you Harini for your kind help whenever I needed and ensuring smooth functioning of everything required for our stay at RRI. Thank you Padmashree for the certificates. Thank you Hanumantha and Lakshamma for ensuring our healthy stay at RRI.

I thank the doctors at RRI, for treating my friends (and colleagues) during their thesis work. During the years I have not visited them, as my mother treated me with Indian gooseberry, turmeric and other herbs.

Many thanks to the scenic beauties of RRI. I can say, I enjoyed Kodaikanal; Ooty; Mysore inside RRI. The green giant trees, the fragrances, colorful flowers, singing birds, swirling butterflies, cute infant monkeys, playful clowder, naughty owls have relaxed my mind every single day. Thanks to all the people at the horticulture section and many more people who maintain this picturesque view inside RRI by keeping it clean and healthy. I am thankful to the security department for their sincere effort to maintain peace inside the campus. I am grateful to them for their faith in me, as often I roam in the campus with naqab.

I thank all my teachers and senior students from school to university, who showed me the joy of doing Physics. My sincere thanks to Tarun sir, Timir sir, Sorbani di, Madhurima di. I am thankful to Somak da, Rajaram sir, Subir sir, Subroto sir, Kausik sir, Rajesh sir, Sushan mam, Gulab sir for their trust.

I am thankful to the High Energy Astrophysics Science Archive (HEASARC) online service provided by NASA/GSFC and *Swift*-BAT site, the data we have used for the thesis work have been obtained from these web sites.

I express my sincere thanks in advance to the referees for giving their valuable time to read the thesis.

I thank Prof. Oskinova; Prof. Ryde; Prof. Gogus; Prof. Santangelo; Prof. Torrejon; Prof. Roca; Prof. Pastor; Dr. Kretschmar, Dr. Furst for giving me opportunity to present my thesis work at their esteemed institutions and for their valuable suggestions. You people have taken care of all my needs, when I was away from my country. Thanks to Prof. Sidoli and Dr. Ponti (G.) for their interest in our work.

Thank you Ji Long, Chris, Daniel et al. for various helps I have got from you. As a whole I am grateful to the people of Europe for their wonderful hospitalities and kind helps at streets, railway stations, airports, everywhere. Thank you people of EU, you made me feel secure at the streets while traveling alone, even at midnight and dawn. Whenever any gentleman saw me carrying a luggage through the stairs, they had rushed to me and had borne my load. Most memorable is amazing help from brother Den Salauddin of Sweden (originally from Malaysia), who was completely unknown to me. He found me very sick in a bus from Arlanda airport, while getting down from the bus he came forward for help. He carried my heavy luggages to my destination through railway platform, streets and metro station. At that time, I could not have traveled so much distance with the heavy bags, without his kind help. While leaving, he asked me to inform him if I need any help while coming back to the airport on the next day. From the bottom of my heart the prayer came: 'Oh Lord! Make this brother, the richest man on Earth and be with him and his family at there tough times and ease their situations, as he has made my journey easy.' I prayed these for him, because if kindest people become richest, then I feel peace on Earth would be optimum. My mother, siblings, Vidya, my supervisor, our administrative officer, my friends at RRI were worried hearing about my sudden illness. This brother has eased my situation with Almighty's mercy. While carrying my luggage for such a long distance, this brother was doing his Ramzan fast in more than 20 hours long daytime in Stockholm, in June 2017. Thanks a lot brother Den.

I thank all the Guru-sisters and brothers (students and colleagues of my supervisor); Gayathri, Pragati, Nazma, Sanhita, Aru, Chandryee, Nandini, Jincy, Varun, GK, Rishin; I have learnt many things from the discussions with you all. Gayathri, you were always by my side at all the stages of my PhD years, whether it is some issues with plotting or analysis or anything. You helped me fixing various latex issues in Ubuntu during the preparation of the thesis. We together explored the fun side of physics and enjoyed funny issues in the QDP plots. We together observed and enjoyed the funny activities of birds, cats and monkeys at RRI. Thank you Gayathri for all these happy moments. Thank you Pragati, you cleared all my doubts related to *XMM-Newton* data analysis even from 14000 km away. During your

visit at RRI with your very hectic schedule, you sat with me and cleared my queries. You manifested wonderful gratitude towards your thesis supervisor, by helping his student at the moment of urgent need. I will try my best to follow your footsteps. Thank you Nazma, I have learnt a lot while working with you with the source IGR J18027–2016; you taught me to improve writing in a manuscript. Even after that, when we met in Jaipur you showed me some clever ideas to fit an emission line. Thank you Nandini for the *ASTROSAT* data and for helping me with Pragati to find the cause of that weird spectrum.

I have been very fortunate to have friends like Karamveer, Meera and Priyanka who have always been with me in my good and odd times since the very first day at RRI. Thank you gang at the Astro-floor; Abir, Arpita, Sourabh (Paul), Saurabh (Singh), Ravi, Chaitanya, Raju, Kartick, Siddhartha, Lijo, Viral, Naveen, Mayuri, Akash, Janakee, Aditi, Kshitija, Avik, Tanuman; Gang at other departments; Sreeja, Sushil, Deepak, Nomaan; We shared pleasant moments at RRI and many of us together discovered natural beauties of different corners of India. Thank you Abir and Arpita; I got help from you even without asking. Many thanks to Rakhee and Nirmal for hosting me in Stockholm, taking care of me, feeding me, carrying my heavy luggages when I was very sick. Thank you Rakhee, you showed me the tilted moon in the sky from Stockholm. Thank you Nirmal, you arranged my scientific visit to your Institute (KTH-RIT, Stockholm), even though you were new there at that time.

Thank you Sanhita for the ‘gediting’ idea of the image files, thank you Raju for the idea of on-line conversion of ps to eps files, that helped me to fix the last moment witty but serious latex issue, which was even not recognized by Google. Thank you Lijo for immediately sending your thesis template, when you heard from Gayathri that we could not find solution in ‘Google’ to tackle that issue. Thank you Saurabh (Singh), for your effort to convert my ps files to pdf in your MacBook, to get rid of the latex issue. Thank you Bhargavi and Prabhu, for your interest in our work and for increasing my strength, with your presence in my thesis colloquium.

Many thanks to the on-line converter site <https://image.online-convert.com/>; when I converted the ps files to eps format through this site; I got back the inverses and dashes in the plots in the thesis pdf.

Thank you all the sisters@Ushangini; thank you my dear friends; Rajoshree, Debosree, Ranjita, Sandhya, Priya, Saikat, Pritimoy, Sharmistha, Kaninika, Lopa, Raghu You have always been with me during various stages of my life. Thank you Tapasi (Pal) di for your wise suggestions when I was applying for Ph.D. Thank you Bani di; Suparna di; Lily (LDS) di; Soma di; Rinka, you all wanted to see me happy with astrophysics. Thank you Arpita (Kakinara) for the Physics we discussed together and for your effort in making me feel quantum mechanics. I thank Naveel et al. for escorting us from Srinagar airport and for their wonderful hospitalities during 2016 meeting of Astronomical Society of India in Kashmir University.

Thank you Shamim Uncle for your kind support to continue my studies, when the great call came to my father. Thank you Munna Dadi for your kind words and great understanding. Thank you Grandmom Roshena, you gifted me my dear father. I was not fortunate to see you, as you had to depart from earth when Dad was ~ 1 year old. Thank you Nana (my mother's father) for the love and affection during first few fortunate years of my life. Thank you Mina masi, for giving support to my mother, during our visit to native.

I thank my greatest enemy (\equiv sibling) without whom I can not live, my sister! who has always been with me in my moments of ups and downs. Together we start and end our day exploring funny things in the Universe. She has helped me a lot, in preparation of the thesis. Mainly, I bombarded her with horrible typos. I thank my brother with whom I never won any debate, even if I was right. He helped me to automate many of my analysis. Many times he debugged errors whole night in my scripts from several thousands of miles away, when I was peacefully sleeping. Thank you brother for the i7. It quickly runs long codes and has been immense helpful for producing the thesis work. I would have missed the interview at RRI for the PhD entrance, you informed me about the shortlist when I was enjoying Bangalore during holidays. Despite our horrible fights over Skype, I respect you because

you ignored the giant offers to implement your skills to find the cause of Cancer. I do not want you to know that I respect you, so please do not read my acknowledgement (because knowing this you would create new debate issues, would try to force me to sit for IQ tests when I will be very tired and would enjoy my low score) !!!! Thank you sister Shibrat for all your support to finish the proposals and paper works in time during my Munich visit. I thank my new sister Natalie (I met her in a metro station in Munich) for the discussion on the majesty of the 'Creator' and his (?) creation during my stay in Munich. I thank my hunky-bunky-munky cousins for making me laugh during my visit to the native.

I do not have enough words to thank my mother, who sacrificed many things to see me happy doing astrophysics. All my morning alarms fail, she with her non-stop effort wakes me up everyday. 'Maa', I apologize for making your mornings troublesome. I will try to improve. Thank you 'Maa' for treating my illness with your kitchen herbs. Sacrifice is a direct consequence of love, your whole life speaks that. Not only for the family, you extended your love beyond. You sacrificed your valuables, your properties to keep people happy, like Dad. Words can not describe those.....

Both of your lives have taught me the difference between love and attachment, which solves my worldly problems very fast with the mercy of Almighty. Seeing you both I realized that, my character is how I treat those who can do nothing for me. This helps me in self-correction and gives me immense peace. Being with truth gives great joy, because no two truths contradict, you both have showed me that without words. Credit for my PhD degree goes to you both, 'Maa' (Mom) and 'Bapi' (Dad).

Synopsis

A significant fraction of the observed X-ray Universe is comprised of X-ray binaries. In a binary star system two stars orbit the center of mass of the system. The X-ray binaries consist of a compact object (neutron star, black hole or white dwarf) and a companion star which can be of different nature. In High Mass X-ray Binaries (HMXB) the companion is massive ($M \geq 10M_{\odot}$), while Low Mass X-ray Binaries (LMXB) have a smaller mass stellar companion ($M \leq 1M_{\odot}$). X-rays are produced in binary stellar systems through an energetic phenomenon called 'accretion', in which the compact object due to its intense gravity whisks away matter from its companion and swallows it. Depending upon the characteristics of the two stars, the accretion can occur in different ways.

Magnetic field of a neutron star plays very crucial role in regulating the accretion of matter onto itself. In high magnetic field neutron star X-ray binaries, magnetic field of the neutron star channels the accreted matter onto its magnetic pole that gives rise to pulsed emission. This class of X-ray binaries are known as binary X-ray pulsar. Different sources shows different pulsation characteristics. Variety in the features of the compact object and the companion bring about several interesting flavours in their timing and spectral properties. One such feature is X-ray reprocessing, in which primary X-rays emitted by the compact object interact with the surrounding medium and get reprocessed into either same or different energy X-rays. This field is not much explored till date and many key issues to be solved. Variability is another interesting feature of these systems. The time scale of variability depends significantly upon the type of the two component stars. The variability includes flares (where X-ray intensity suddenly rises several times above average), off-states (in which case the X-ray intensity drops abruptly by several factors), eclipses (where the di-

rect X-ray emission from the compact star is blocked by its companion), dips (The X-ray intensity falls significantly below the average).

For more than 5 decades, with the help of balloon borne detectors to different generations of X-ray space missions many fascinating features of the X-ray Universe is being explored. Analysis of data from different sources have been revealing underlying physical causes and at the same time raising many open problems, hence opening the doors for further research. This thesis is made of two sections. The 1st part deals with comprehensive study of X-ray reprocessing in a number of HMXB and LMXB systems, where as the 2nd part explores the variability and other timing and spectral properties of two HMXB systems. The thesis mainly revolves around the data from the *XMM NEWTON*, *Swift* and *Suzaku* missions.

- Chapter 1 briefly discusses the scientific context of the thesis work. It introduces different types of X-ray binaries, various accretion mechanisms, accretion regimes, emission processes, variabilities, physics of X-ray reprocessing etc.
- A brief introduction to the X-ray detectors on board X-ray space missions followed by X-ray data analysis techniques are given in Chapter 2.
- Chapter 3 deals with X-ray reprocessing through eclipses in eclipsing HMXB systems including supergiant fast transients (SFXTs) with *XMM NEWTON* EPIC-pn. Eclipse and out-of-eclipse spectra of the sources have been interpreted to understand the X-ray reprocessing behaviour of the matter around compact object in these systems.
- Chapter 4 presents the X-ray reprocessing study in eclipsing LMXB systems with *XMM NEWTON* EPIC-pn. This study indicates some contrasting outcome with respect to X-ray reprocessing in HMXBs.
- In Chapter 5, variability study of a supergiant HMXB source IGR J18027–2016 is presented making use of *Swift* data. 15 pulse profiles of high and low states have been studied in search for its connection with luminosity. Spectra of the variable states were also interpreted for the better understanding of off-states like features.

- Chapter 6 focuses on the timing and spectral studies of HMXB system IGR J00370+6122 with *XMM NEWTON* and *Suzaku* with the aim to search for the nature of the compact object.
- Chapter 7 briefly summarizes the work carried out in the thesis and discusses some future prospects related to this.

List of publications

- Variability study of the high mass X-ray binary IGR J18027–2016 with Swift–XRT
Aftab, N., Islam, N., Paul, B. 2016, MNRAS 463, 2032-2038
- X-ray reprocessing: Through eclipse spectra of high mass X-ray binaries
Aftab, N., Paul, B., submitted to MNRAS
- X-ray reprocessing in low mass X-ray binaries
Aftab, N., Paul, B., in preparation

Other publication:

- Energy dependence of the eclipse profiles of high mass X-ray binaries
Jain, C., Aftab, N., Paul, B. and others, in preparation

Table of contents

	i
	v
	vii
List of figures	xxxii
List of tables	xxxv
Prologue	xxxvii
1 Introduction	1
1.1 Different flavours of X-ray binary systems	2
1.1.1 High mass X-ray binary (HMXB)	3
1.1.2 Low mass X-ray binary	7
1.2 Accretion in X-ray binary systems	11
1.2.1 Accretion efficiency	11
1.2.2 Eddington luminosity	12
1.2.3 Modes of accretion process	13
1.2.4 Accretion from Be star's disc	18
1.2.5 Roche lobe overflow	18
1.2.6 Accretion disc	20
1.3 Accretion and accretor's magnetic field connection	26
1.4 Different regimes of accretion	29
1.4.1 Magnetic inhibition of accretion	30
1.4.2 Propeller regime	32
1.4.3 Accretion powered pulsar	36
1.5 Emission processes in X-ray binaries:	42

1.5.1	Thermal emission:	42
1.5.2	Nonthermal emission:	43
1.5.3	Cyclotron Resonant Scattering Feature (CRSF)	50
1.6	Vaiabilities in X-ray binaries	51
1.6.1	Periodic variability	51
1.6.2	Nonperiodic variabilities:	56
1.7	X-ray reprocessing in X-ray binaries	60
1.7.1	X-ray reprocessing and binary eclipse connection	63
1.7.2	Reprocessed spectra during eclipse and spectral line	63
1.8	Motivation and outline of the thesis	66
2	The X-ray detectors and the analysis techniques	69
2.1	X-ray telescopes	70
2.2	Astronomical X-ray detectors	70
2.2.1	Gas proportional counters	73
2.2.2	Semiconductor X-ray detectors	76
2.2.3	Scintillation detectors	76
2.2.4	Charged couple devices (CCDs)	79
2.3	Quantum efficiency of X-ray detectors	80
2.4	Some features of the detectors on-board	81
2.4.1	All sky camera	81
2.4.2	Narrow field instruments	81
2.4.3	Background rejection	82
2.5	X-ray missions and the instruments used in the thesis work	82
2.5.1	<i>Swift</i>	83
2.5.2	<i>XMM Newton</i>	87
2.5.3	<i>Suzaku</i>	89
2.6	X-ray data analysis	90
2.6.1	Timing analysis	92
2.6.2	Spectral analysis	95
3	X-ray reprocessing: Through the eclipse spectra of high mass X-ray binaries with <i>XMM-NEWTON</i>	101
3.1	Introduction	101
3.2	Observation and data analysis	103
3.2.1	EVENT SELECTION FROM THE LIGHTCURVES	105
3.2.2	SPECTRAL ANALYSIS	105

3.3	Discussion	117
3.3.1	Cen X-3:	119
3.3.2	LMC X-4:	120
3.3.3	4U 1700-377:	121
3.3.4	Other sources	122
3.3.5	Comparison of SFXTs and SgHMXBs:	124
3.3.6	Various elements in the environment of supergiant HMXBs	124
3.4	Conclusion	124
4	X-ray reprocessing: Through the eclipse spectra of low mass X-ray binaries with <i>XMM-NEWTON</i>	137
4.1	Introduction	137
4.2	Observation and data analysis	139
4.2.1	EVENT SELECTION FROM THE LIGHTCURVES	140
4.2.2	SPECTRAL ANALYSIS	140
4.3	Discussion	171
4.4	Conclusion	178
5	Variability study of the High Mass X-ray Binary IGR J18027-2016 with <i>Swift</i>- XRT	179
5.1	Introduction	179
5.2	Data and Analysis	181
5.2.1	Pulsation Analysis	182
5.2.2	Orbital period analysis	185
5.2.3	Spectral Analysis	187
5.3	Discussion	189
6	Exploring the timing and spectral behaviour of IGR J00370+6122 with <i>Suzaku</i> and <i>XMM-Newton</i>	195
6.1	Introduction	195
6.2	Observation and data analysis	196
6.2.1	Timing analysis	198
6.3	Spectral analysis	199
6.4	Discussion	205
7	Summary and future prospects	209
	References	213

List of figures

1.1	Orbit of neutron star around a Be star	4
1.2	Corbet diagram	5
1.3	X-RAY colour-colour diagrams of Z and atoll sources	10
1.4	Bondi-Hoyle-Littleton accretion	15
1.5	Lightcurve of an SFXT system	17
1.6	Equipotential surfaces in a binary system	19
1.7	Roche-lobe overflow	19
1.8	Accretion disc around a compact object	21
1.9	Accretion disc spectrum	24
1.10	Distribution of angular speed around neutron star	25
1.11	Alfven radius	28
1.12	Interaction between neutron star's magnetosphere and inflowing plasma	33
1.13	Accretion powered pulsar	37
1.14	Warping in accretion disc	38
1.15	Accretion column geometry	40
1.16	Fan and pencil beam geometry	40
1.17	Accretion disc corona	41
1.18	Trajectory of an electron passing a positive ion	44
1.19	The bremsstrahlung spectrum of an electron beam	45
1.20	Spectrum for inverse Compton scattering	47
1.21	Synchrotron spectrum of electrons	50
1.22	Cyclotron Resonant Scattering Features	51
1.23	Pulse profile of GX 1+4	52
1.24	Power spectrum of 2S 0114+650	54
1.25	Lightcurve of LMC X-4	55

1.26	Three off-states have been detected in the 0.4-12 keV <i>Suzaku</i> XIS lightcurve of Vela X-1 (Doroshenko et al., 2011). Top panel shows zoomed view of the off-states. Image courtesy: Doroshenko et al. (2011)	58
1.27	Lightcurve of EXO 0748-676	59
1.28	Type-I X-ray burst in a lightcurve of MXB 1730-335	60
1.29	Type I and type II X-ray bursts in a lightcurve of A0535+262	61
1.30	Equivalent width corresponding to an emission line	64
1.31	Spectrum of 4U1538-522	65
2.1	Earth's atmosphere and some observatories	71
2.2	Three Wolter type mirror arrangements	72
2.3	Nested Wolter I mirror system	73
2.4	Basic geometry of a cylindrical proportional counter	74
2.5	Different regions of operation of gas filled detectors	75
2.6	schematic of a semiconductor detector	77
2.7	photon-matter interaction in a scintillation detector	78
2.8	Schematic of a scintillation detector	78
2.9	Schematic of a X-ray CCD	80
2.10	Schematic of the <i>Swift</i> satellite	83
2.11	Top Panel: A coded mask casts shadow on the detector plane. Image courtesy: Busboom et al. 1997. Bottom Panel: D shaped coded mask over CZT detector plane of Burst Alert Telescope (BAT). Image courtesy: (Barthelmy et al., 2005).	84
2.12	Schematic of the <i>XMM-Newton</i> satellite	86
2.13	EPIC pn CCDs	88
2.14	EPIC-pn CCD images of LMC X-4	89
2.15	Schematic of the <i>Suzaku</i> satellite	90
2.16	Schematic of <i>Suzaku</i> HXD instrument	91
2.17	LMC X-4 lightcurve	93
2.18	Orbital profile of Cen X-3	95
2.19	Pulse profile of IGR J18027-2016	96
2.20	IGRJ 16479-4514 spectrum	98
3.1	Schematic of X-ray reprocessing in an eclipsing HMXB system	102
3.2	Cen X-3 orbital profile, eclipse and out-of-eclipse spectra	125
3.3	Same as Figure 3.2 for LMC X-4 (OB ID: 0142800101)	126
3.4	Same as Figure 3.2 for LMC X-4 (OB ID: 0203500201)	126

3.5	Same as Figure 3.2 for SMC X-1 (OB ID: 0011450101)	126
3.6	Same as Figure 3.2 for 4U 1700–377 (OB ID: 0083280401)	127
3.7	4U 1700–377 (OB ID: 0600950101) orbital profile and eclipse spectrum . .	127
3.8	Same as Figure 3.2 for 4U 1538–522 (OB ID: 0152780201)	127
3.9	Same as Figure 3.2 for IGR J18027–2016 (OB ID: 0745060401)	128
3.10	Same as Figure 3.7 for IGR J16479–4514 (OB ID: 0512180101)	128
3.11	Same as Figure 3.7 for IGR J16418–4532 (OB ID: 0679810101)	128
3.12	Same as Figure 3.7 for IGR J17252–3616 (OB ID: 0405640201)	129
3.13	Same as Figure 3.7 for IGR J17252–3616 (OB ID: 0405640601)	130
3.14	Same as Figure 3.7 for IGR J17252–3616 (OB ID: 0405641001)	130
4.1	Schematic of X-ray reprocessing in an eclipsing LMXB system	138
4.2	Eclipse and out-of-eclipse events of AXJ 1745.6–2901 (OB ID: 0402430401)	153
4.3	Eclipse and out-of-eclipse events of EXO 0748–676 (OB ID: 0160760401)	154
4.4	Eclipse and out-of-eclipse events of MXB 1659–298 (OB ID: 0008620701)	155
4.5	Eclipse and out-of-eclipse events of XTE J1710–281 (OB ID: 0206990401)	156
4.6	Eclipse and out-of-eclipse spectra of AX J1745.6–2901 (OB ID: 0402430301)	157
4.7	Eclipse and out-of-eclipse spectra of AX J1745.6–2901 (OB ID: 0402430401)	158
4.8	Eclipse and out-of-eclipse spectra of AX J1745.6–2901 (OB ID: 0724210201)	159
4.9	Eclipse and out-of-eclipse spectra of AX J1745.6–2901 (OB ID: 0723410301)	160
4.10	Eclipse and out-of-eclipse spectra of AX J1745.6–2901 (OB ID: 0723410401)	161
4.11	Eclipse and out-of-eclipse spectra of AX J1745.6–2901 (OB ID: 0723410501)	162
4.12	Eclipse and out-of-eclipse spectra of AX J1745.6–2901 (OB ID: 0762250301)	163
4.13	Eclipse and out-of-eclipse spectra of EXO 0748–676 (OB ID: 0160760101)	164
4.14	Eclipse and out-of-eclipse spectra of EXO 0748–676 (OB ID: 0160760201)	165
4.15	Same as in Figure 4.14, for OB ID: 0160760301	166
4.16	Same as in Figure 4.14, for OB ID: 0160760401	167
4.17	Same as in Figure 4.14, for OB ID: 0160760601	168
4.18	Same as in Figure 4.14, for OB ID: 0160760801	169
4.19	Same as in Figure 4.14, for OB ID: 0160761301	170
4.20	Composite eclipse and out-of-eclipse spectra of EXO 0748–676	172
4.21	Eclipse and out-of-eclipse spectra of MXB 1659–298 (OB ID: 0008620601)	173
4.22	Eclipse and out-of-eclipse spectra of MXB 1659–298 (OB ID: 0008620701)	174
4.23	Eclipse and out-of-eclipse spectra of XTE J1710–281 (OB ID: 0206990401)	175
5.1	Pulse profiles of IGR J18027–2016 with <i>Swift</i> -XRT	183
5.2	Pulse fraction as a function flux	184

5.3	Orbital intensity profile with <i>Swift</i> BAT and XRT	185
5.4	Two sets of lightcurves and spectra showing variability	186
5.5	Spectra showing Fe K_{α} emission line	188
5.6	Two spectra showing variability	189
5.7	Spectral parameters as functions of flux	190
6.1	Position of IGR J00370+6122 in the Corbet diagram	197
6.2	<i>XMM-Newton</i> and <i>Suzaku</i> lightcurves	200
6.3	Orbital intensity profiles	201
6.4	Spin period search result	202
6.5	<i>XMM-Newton</i> and <i>Suzaku</i> spectra	204

List of tables

1.1	Properties of HMXB and LMXB systems	8
2.1	EPIC pn mode of operations	87
2.2	Features of <i>Suzaku</i> XIS and HXD instruments	91
3.1	Basic parameters of the eclipsing HMXBs	131
3.2	The <i>XMM-Newton</i> EPIC pn log of observations of the HMXBs	132
3.3	Best fit spectral parameters of the eclipsing HMXBs for <i>XMM-Newton</i> observations	133
3.4	Fe emission line parameters	134
3.5	Other emission line parameters	135
4.1	The <i>XMM-Newton</i> EPIC pn observation log of four LMXB systems	145
4.2	Best fit spectral parameters of AX J1745.6–2901	146
4.3	Emission and absorption line parameters of AX J1745.6–2901	147
4.4	The best fit models of EXO 0748–676	148
4.5	Best fit spectral parameters of EXO 0748–676	149
4.6	Ionized absorption model parameters of EXO 0748–676 during out-of-eclipse phase	150
4.7	The emission and absorption line parameters of EXO 0748–676	151
4.8	Best fit spectral parameters of MXB 1659–298 and XTE J1710–281	152
4.9	The emission and absorption line parameters of MXB 1659–298 for <i>XMM-Newton</i> observations	152
5.1	Log of <i>Swift</i> –XRT observations of IGR J18027–2016	193
5.2	Best fit spectral parameters of IGR J18027–2016	194
6.1	Best fit spectral parameters of IGR J00370+6122 for <i>XMM-Newton</i> observations	199
6.2	Best fit spectral parameters of IGR J00370+6122 for <i>Suzaku</i> observations	199

Prologue

"Astronomy has revealed the great truth that the whole universe is bound together by one all-pervading influence." - William Leitch

How the thesis has seen the light of day? I am indebted to the very first human being to my supervisor for their quest for the seen and unseen truth of the night sky. Some of them had to face very tough time, some sacrificed lap of luxuries just to show us the truth.

Dear reader! Kindly allow me to share these with you in brief.

Ancient humankind was very curious about every single object around them. That curiosity led them to discover from an handaxe to agriculture. Their inquisitive eye discovered the stars and planets; predicted their positions in the sky, even before the invention of telescopes. They used pole star as a pointer in the dark nights to get right direction for their destination, before they invented magnetic compass. Love for the glittering night sky made them to dive into its boundless mysteries.

Hipparchus (died after 127 BC), a Greek astronomer and mathematician discovered the precession of the equinoxes, annual changes of celestial longitudes, measured lengths of tropical and sidereal years. He made a catalog of 850 stars with apparent brightness. In 2nd century, Greek astronomer and mathematician Ptolemy in his famous work 'Almagesti' published a catalogue of more than 1020 stars. In this book he gave his prediction: 'Earth as the center of the Universe'. This geocentric theory was believed for many centuries.

In 8th century, first observatory was built in Baghdad (Iraq). Some more observatories were also built around Iraq and Iran around the same time. The astronomers designed sextants to measure the angle of an astronomical object with the horizon, they used mea-

surements to trace motions of the celestial bodies. Persian astronomer Abd al-Rahhman as-Shufi in 10th century wrote ‘Suwar al-Kawakib al-Thamaniyah wa-al-Arbaeen’ (short name: ‘The Book of the Fixed Stars’), which was one of the most comprehensive texts on constellations in the sky. He observed the Andromeda galaxy and the Large Magellanic Cloud with the naked eye and noted that as clouds. Ibn-Yunus of Egypt (~950-1009) in his major work ‘Al-Zij al-Hakimi al-kabir’, gave a detailed discussion on spherical astronomy; sundial theory; many tables and methods to describe different astrophysical phenomena. He corrected the precession of Earth given by Ptolemy. (Correct measure of the precession of equinoxes was found to be 1° in 70 years).

Egyptian astronomer Ibn al-Hasan ibn al-Haytham (965-1039) known as the ‘father of optics’, who in his famous book ‘The Book of Optics’, illustrated the experimental results on various optical phenomena. He speculated about the rectilinear propagation of light. His studies on binocular vision and as a whole on optics was very helpful for the development of binoculars and telescopes. He first gave the idea of testing a theory by repeated experiments, He noted “The duty of the man who investigates the writings of scientists, if learning the truth is his goal, is to make himself an enemy of all that he reads, and ... attack it from every side. He should also suspect himself as he performs his critical examination of it, so that he may avoid falling into either prejudice or leniency.”

Chinese astronomers in 11th century (1054) observed a supernova and mentioned it as a ‘guest star’ in their record. It was bright for a year. This supernova was also observed by ancient Indian astronomers of south-west America. This supernova was originated in the system which today we know as Crab nebula. 14th century’s Syrian Astronomer Ibn as-Shatir in his book ‘Kitab nihayat as-sul fi tashih al-usul’ (‘A Final Inquiry Concerning the Rectification of Planetary Theory’), gave details of planetary motions which is the first details correction of the geocentric theory.

Nicolaus Copernicus (1473-1543) of Poland followed Ibn as-Shatir’s calculations and brought the idea of heliocentric theory to the world of the Renaissance in 16th century. In this theory he put Sun at the centre, with Earth and other planets revolving around it. In 16th century Danish astronomer Tycho Brahe and his assistants referred Copernicus’s

calculation and gave predictions to the precise motion of the celestial objects in his famous work 'Astronomiae Instauratae Mechanica' (1598).

There is a controversy about the first designer of a Telescope, It is either Dutch eyeglass maker Hans Lippershey (or Lipperhey) or Zacharias Jansen or both independently at the same time or someone else. In early 17th century, Galileo Galilei of Italy quickly improved the simple telescope to a powerful one which magnified objects by 20 times. In his book 'Sidereus Nuncius' ('The Sidereal Messenger') he described what he had found with his Telescope: many more stars than what was visible with bare eye, moon's rough surface, revolving moons of Jupiter etc. The motion of the Jupiter's moon indicated more than one center of motion in the Universe. Supporting Copernican theory he published his results, which went against the traditional teachings of the Roman Catholic Church. He was arrested and tortured. Later he was allowed to his villa near Florence (Italy), where he spent rest of his life under house-arrest. That is one of the most painful incidence in the life of a Scientist whos main aim is to discover the truth. The original verses revealed to Prophet Jesus (may peace be upon him) was not in contradiction with the observed facts. Pope John Paul II acknowledged publicly that Galileo was correct, but it was nearly 350 years after his death.

Analyzing Tycho Brahe's observations, Johannes Kepler a German astronomer established that planets move in elliptical orbits around the Sun, not in circular paths; which was a common belief at that time. In early 17th century he discovered 3 famous laws of motion for planets and satellites.

In 17th Century, Sir Isaac Newton of England gave the world 'Fundamentals of Modern Science' through his book 'Philosophiae Naturalis Principia Mathematica'. He stated the law of Universal gravitation from the observation of heavenly bodies. In late 17th and early 18th century William Herschel and his sister Caroline mapped the whole sky systematically. Their map cleared many misconceptions, like the size and shape of our Milky Way Galaxy; position of the Sun etc.

Researches in Astronomy and Astrophysics was continued and even accelareted. Many observatories were constructed, like Pulkovo Observatory in St Petersburg (Russia), Royal Observatory at the Cape of Good Hope (South Africa) in 19th century. Optical instruments

was developed very fast with equatorial supports and mechanical drives. Many double stars or binaries could be resolved. Discovery of spectroscopy and photography put a spark in the understanding of physical processes inside different astronomical objects. Pierre Janssen (1824-1907) and Norman Lockyer (1836-1920) discovered Helium (He) in the Sun. Fraunhofer lines, observed by Joseph Fraunhofer (1787-1826) in the Solar spectrum was understood. Slowly other chemical elements in the Sun and other stars were revealed. Catalogues of different stellar spectra were prepared and preserved for further understanding of different species of elements inside stars.

In late 19th Century Universe was understood to be composed of a large number of galaxies, where each galaxy is a gravitationally bound system with a collection of large number of stars. In mid 20th Century (1933) Karl Jansky accidentally discovered radio waves from all directions of the sky, which gave birth to the Radio Astronomy. Today this radiation is known as Cosmic Microwave Background Radiation (CMBR). Grote Reber built a 9.6 m dish radio Telescope in 1937. He discovered many radio sources. Since then many radio telescopes are being built. In 1967, Jocelyn Bell Burnell first spotted pulsation in a radio source and later she and her colleagues confirmed that to be a rapidly spinning neutron star and named as radio pulsar.

In early 20th century a large telescope with 2.5 m reflector was built in Mount Wilson Observatory, in California (U.S.A.). Many more observatories and telescopes were built throughout the world. The Infrared Astronomical Satellite (IRAS) launched in space in 1983 was the first telescope to scan the sky in infrared. IRAS was a joint project of United States NASA, the Netherlands NIVR, and the United Kingdom SERC. The Hubble Space Telescope (HST), one of the largest space Telescope launched in space in 1990 to get deep view of space in near ultraviolet; visible; and near infrared. It was built in NASA in collaboration with European Space Agency (ESA). HST has gifted the world many outstanding discoveries, like determination of the rate of expansion of the Universe. HST is still active with good health.

In late 19th century (1895), German physicist Wilhelm Röntgen detected an energetic electromagnetic (EM) wave which ranges in $\sim 0.1-100$ keV, known as X-rays. In early 20th

Century, extensive study of the ionosphere drew attention of the Astrophysicists to search for UV and X-rays from upper atmosphere. Robert Goddard, an American engineer and physicist already invented liquid-propellant rocket (1926) by that time. Solar X-rays were discovered in 1949 by an Aerobbe rocket. Ricardo Giacconi and his team of Goddard Space Flight Center (U.S.A.) detected a cosmic X-ray source in 1962, with the help of a sounding rocket designed by Frank Paolini. In this observation, the rocket was scanning the sky and was not pointed at the source. So, a few years later the nature of the source was understood with the help of some rocket and balloon borne detectors. It was a neutron star X-ray binary, Scorpius X-1 (Sco X-1).

Immediately after that, NASA with the supervision of Giacconi launched (1970) first X-ray satellite 'Uhuru' ('Small Astronomy Satellite-1') in space. It used to scan nearly the entire sky with 12 min spin period. In this comprehensive survey *Uhuru* discovered many X-ray sources and produced first catalogue for cosmic X-ray sources, presently known as 4U Catalog. For example, 4U 1700-377 is an interesting X-ray source discovered with *Uhuru*. First X-ray pulsar, Centaurus X-3 was discovered with *Uhuru* in 1971. In 1970s after *Uhuru*, few more satellites like *Skylab*, *Ariel-5*, *Einstein* etc. were sent to space to explore more about the X-ray Universe. Nature of the X-ray sources and their physical origin started to be revealed with the help of these satellites.

Since then the study of X-ray astronomy was continued with the help of more advanced X-ray detectors on board space missions, for example *EXOSAT*, *Ginga* in 1980s; *ROSAT*, *RXTE* in 1990s; *Suzaku* in 2000s. *Chandra* (launched in July, 1999), *XMM-Newton* (launched in December, 1999), *INTEGRAL* (launched in October 2002), *Swift* (launched in November, 2004) are successfully operating for more than 10 years. These missions gave the World most outstanding discoveries of the outer space. Most massive galaxy cluster, 1000 times massive than our Galaxy (Milky way) was discovered with *XMM-Newton* in 2008; In 2012, *Chandra* discovered an unusual supernova which ripped the star's gut inside out. Recently *INTEGRAL* observed flash of gamma rays linked to the gravitational waves which is expected to be released by the collision of two neutron stars.

Nustar (launched in June, 2012) and *ASTROSAT* (launched in September, 2015) are two latest space missions observing deep into the X-ray Universe with advanced focusing telescopes and excellent timing resolution respectively. *LOFT* and *ATHENA* two of the approved future space missions by European Space Agency (ESA) are expected to be launched within 10 years. Large collecting area of *LOFT* with wide energy band; *ATHENA*, 100 times more sensitive than *XMM-Newton* and *Chandra* are expected to contribute breakthrough researches in high energy astrophysics.

POLIX, an Indian X-ray polarimeter is being developed at Raman Research Institute under the supervision of Prof. Biswajit Paul. It is a future payload of ISRO's (Indian Space Research Organisation) small satellite mission *XPoSat*. POLIX is expected to answer many key questions about the origin of X-rays in the extreme gravitational field with the help of polarization measurements in different X-ray sources.

This thesis focuses on physical origin of X-rays coming from the compact objects in high and low mass binary systems. We have used data from *XMM-Newton*, *Swift* and *Suzaku* space missions.

Chapter 1

Introduction

"The more I study nature, the more I stand amazed at the work of the Creator."

- Louis Pasteur

Stars ‘*the sparkling tiny dots in the sky*’ are fuelled by nuclear fusion. After loosing the nuclear fuel, either the star leaves behind a dense core or the core collapses under its own gravity. These highly dense objects are known as compact objects in the astrophysics. Depending upon the mass of the progenitor star the compact object can be of 3 different types. i) white dwarf ii) neutron star iii) black hole. If mass of the progenitor star $M \leq 8M_{\odot}$ (M_{\odot} is the mass of the Sun), then the star ends its life as white dwarf of mass $M_{WD} \leq 1.44M_{\odot}$ (Chandrasekhar, 1931). If the initial mass is $8M_{\odot} \leq M \leq 20M_{\odot}$, then the progenitor leaves behind a neutron star of mass $1.44M_{\odot} < M_{NS} \leq (2 - 3)M_{\odot}$. The highest mass of the neutron star is still uncertain. For a star of initial mass $M \geq (20 - 25)M_{\odot}$, the end product is a black hole of mass $M_{BH} > 3M_{\odot}$. The radius of the white dwarf is similar to the radius of earth (few thousands of kilometer) while neutron stars have radius equal to the size of a city (few tens of kilometer). Gravity is very intense near the surface of these compact objects and it increases from white dwarf to black hole. The density of matter in white dwarf is of the order of 10^6 gm cm^{-3} , while the density in neutron star is $\sim 10^{14} \text{ gm cm}^{-3}$ which is 10^{13} times of average density of earth. Size and density of the black hole could not be estimated,

as because of its intense gravity it swallows light from a far away distance known as its Schwarzschild radius.

A binary system is a gravitationally bound two star system, in which both the stars rotate around their common center of mass. X-ray binaries are those binary systems which are bright mostly in X-rays, though they may emit radio to γ rays. In these systems one star is a compact object, either neutron star; black hole or white dwarf, another star is either early type supergiant known as optical counterpart or late type red giant. The ultra-compact binaries have neutron stars with white dwarf companion. Capture of mass by the compact object from the companion i.e. ‘accretion’ (to be discussed in detail in section 1.2) is the sole cause of this radiation. Intense gravity of the compact objects makes the process of accretion very dynamic which gives rise to several interesting properties of X-ray binaries.

First X-rays from space was observed in solar corona in 1949 by sounding rocket experiments. Scientists were very curious to search for X-rays from outside solar system. Ricardo Giacconi’s team developed a sensitive detector to search for X-rays from distant stars. Finally in 1962 while sweeping the sky by an Aerobee rocket this detector detected intense X-rays from a direction of constellation Scorpius. But only after many years binary nature of this X-ray source has been revealed with multiple observations. This first X-ray source was named SCO X-1. Since then many balloon borne detectors to present generation X-ray satellites discovered many interesting features of X-ray binaries in Milky-way and in nearby galaxies like Large Magellanic Cloud (LMC), M31 etc. Still there are many key issues which are less explored.

Since this thesis deals with several temporal and spectral properties of X-ray binaries, So in the following sections we discuss current understanding of physical properties of X-ray binary systems.

1.1 Different flavours of X-ray binary systems

The behaviour of X-ray binary systems expected to depend upon parameters like i) mass of the two component stars ii) nature of the compact object like neutron star, black hole

or white dwarf iii) spectral type of the companion iv) separation between the two stars and orbital period of the system v) inclination of the orbit with respect to the line of sight vi) eccentricity of the orbit vii) size and structure of the accretion disc and its orientation with respect to the line of sight viii) distance from the binary system ix) spin of the compact object x) mass flow rate to the compact object from the companion xi) magnetic field of neutron star, if the compact object is neutron star or white dwarf xii) presence and nature of jets etc.

With increasing discoveries of X-ray binary systems with different features, classification of these systems became an important issue for better understanding of the physics of extreme environment. Many attempts have been made. But the categorization on the basis of mass of the companion has been found to be the most commonly used classification. High Mass X-ray Binary (HMXB) and Low Mass X-ray Binary (LMXB) systems are the two main subclasses with respect to the mass of the companion. Both the HMXB and LMXB systems can have neutron star or black hole as the compact object. The X-ray binary (XRB) systems in which the compact object is an accreting white dwarf is called cataclysmic variable (CV). This thesis deals with a number of HMXB and LMXB systems, so the following section discusses these two systems briefly.

1.1.1 High mass X-ray binary (HMXB)

In HMXBs the donor or the companion is an early spectral type of stars (O/B) with mass $M \geq 10M_{\odot}$. HMXB systems are formed from the evolution of a binary system made of two massive stars. The more massive star evolves faster and in ~ 2 million years of time scale exhausts its fuel. Then it explodes in supernovae and leaves behind neutron star or black hole which results into an HMXB system. Before the supernova explosion, there could be mass transfer from the exploding star to its companion. If the exploding star is lighter than its companion at the time of supernovae explosion then the binary system remains bound even after the explosion. HMXB systems are relatively young systems and mainly belong to the Galactic disc (Grimm et al., 2003). Depending upon the type of the companion star,

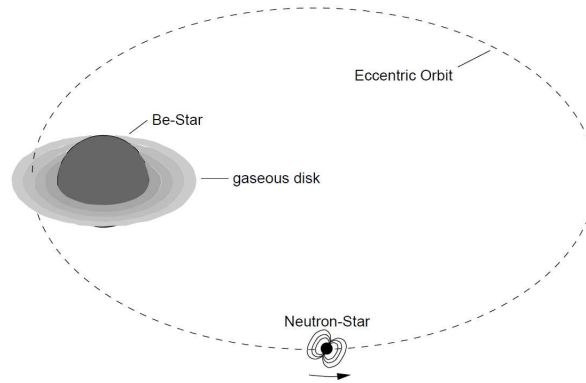


Fig. 1.1 Orbit of neutron star around a Be star. The neutron star accretes matter from Be star's disc once in every orbit which causes periodic type I X-ray burst. Image courtesy: Kretschmar (1996)

HMXB systems are divided into two classes, (1) Be High Mass X-ray Binary (BeHMXB) (2) Supergiant High Mass X-ray Binary (sgHMXB).

Be High X-ray Binary (BeXRB)

A BeXRB system consists of mainly a neutron star as compact object and a Be star as the companion. Be star is a B type (Be III/IV/V) fast rotating star which shows many emission lines in the optical/IR spectrum. Because of its fast rotation the low-velocity and high-density stellar wind (mass ejection rate $\sim 10^{-7} M_{\odot} \text{yr}^{-1}$) is accumulated in its spin equatorial plane and forms a disc. Till date except one system all the BeXRBs have neutron star as compact object. MWC 656 is the BeXRB system with a black hole as compact object (Casares et al., 2014). The neutron star in BeXRB a system accretes (to be discussed in details in section 1.2) matter from Be star's equatorial disc while passing through it. The orbit of these systems are highly eccentric. Therefore in every periastron passage of the neutron star in each orbit, an X-ray burst may occur with luminosity 10^{36} - $10^{37} \text{ erg s}^{-1}$ known as Type I X-ray burst. A schematic representation of the orbit of a Be XRB system is given in Figure 1.1.

BeXRBs are transient systems, most of the time it is in low state with luminosity $10^{34} \text{ erg s}^{-1}$, except some irregular giant Type II X-ray burst. Type II X-ray burst occurs due to sudden increase of mass ejection rate of the Be star, in which X-ray luminosity reaches $>$

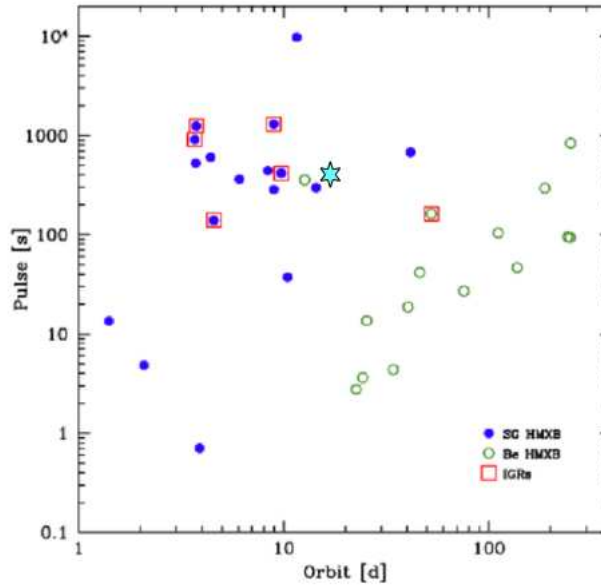


Fig. 1.2 Corbet diagram shows variation of spin period (Pulse [s]) with orbital period (Orbit [d]) in different classes of HMXB systems. Open and filled circles represent BeXRB and SgHMXB systems respectively. Red boxes denote sources discovered with mission *INTEGRAL*. Image courtesy: Corbet (1986)

10^{37} - $10^{38} \text{ erg s}^{-1}$. Figure 1.29 shows Type I and Type II X-ray burst in BeXRB system A0535+262.

The compact object rotates in a wide eccentric orbit with orbital period 10-400 days (Reig 2011, Paul and Naik 2011a). Most of the neutron stars in Be XRBs have spin period >10 sec. However there are few exceptions, like Be X-ray pulsar 4U 0115+634 and V 0331+530, which have spin period of 3.6 sec and 4.4 sec respectively. Be star's disc exhibits some cycle of activities like formation and dispersion. Because of which the system shows a superorbital period of $\sim(400-4000)$ days, seems to be correlated with their orbital period (Rajoelimanana et al., 2011). The spin and orbital period of the systems show clear correlation as seen in the Corbet diagram (Figure 1.2). In our Galaxy 28 Be XRBs have been confirmed (Sources in the Liu et al. 2007 and Liu et al. 2006 catalogs; updated with the 4th IBIS/ISGRI soft gamma-ray survey catalog, Bird et al. 2010).

Supergiant High X-ray binary (sgHMXB)

In sgHMXBs the compact object has an early spectral type of supergiant O/B type of optical companion (luminosity class I/II). The compact object in most cases is a neutron star (black hole in few cases). These systems have orbital period in the range 1-1000 days and the spin period is ≥ 100 s. The companion loses mass via radiatively driven highly supersonic ($\geq 1000 \text{ km s}^{-1}$) wind (10^{-8} - $10^{-6} M_{\odot} \text{ yr}^{-1}$). The compact object in most of the sgHMXB systems gains matter directly from companion's stellar wind and are persistent sources (Liu et al., 2006) with luminosity 10^{34} - $10^{35} \text{ erg s}^{-1}$. Due to inhomogeneities in wind parameters (velocity and density), these systems show flares (where luminosity rises by several factors) and low intensity states at arbitrary orbital phases. Indication of an accretion disc (to be discussed in section 1.2.6) has been found in some sgHMXB systems, for example in Cen X-3, GX 301-2 (in our Galaxy), LMC X-4 (in galaxy Large Magellanic Cloud) and SMC X-1 (in galaxy Small Magellanic Cloud). This can happen if the wind is highly dense or if the orbit is close. The distance between the two stars is so close that they can have mass transfer by Roche lobe overflow (to be discussed in section 1.2.5) in which matter from the surface of the supergiant is pulled by the compact object. In both the cases high angular momentum of the spilled matter forms disc around the compact object (accretion disc, discussed in section 1.2.6).

The compact object's mass capture rate is much less than the mass loss rate of the companion through the wind (details in section 1.2.3), most of the companion's wind carrying angular momentum is lost from the system. Two stars come closer because of gradual loss of angular momentum from the system and the binary orbit tends to be circular over long time. For example LMC X-4 has nearly circular orbit ($e \sim 0.0006$, Levine et al. 2000). The neutron stars in disc-fed sgHMXBs are fast pulsars with short pulse period (0.7 to 14.0 seconds) compared to the wind fed systems which have pulse period of a few hundred to a few thousand seconds (Mason et al. 2009, Jenke et al. 2012). The $P_{spin} - P_{orb}$ (spin vs orbital period) of these systems show anti correlation as seen in the Corbet diagram in Figure 1.2. These systems are short lived as nuclear burning time scale in supergiant phase (the time scale of primary fuel burning) is short.

The X-rays from the compact object propagate through the supergiant's wind and suffer scattering, absorption and reprocessing (Paul and Naik, 2011a). So the X-ray spectra of sgHMXBs show many reprocessed X-ray emission and absorption lines amongst which Fe K_{α} emission line is very common. X-rays from highly obscured supergiant systems may suffer very strong absorption with column density (along the line of sight) $\geq 10^{23} \text{ cm}^{-2}$. The column density can be highly variable with binary phase.

Supergiant Fast X-ray transient (SFXT)

SFXTs are a latest class of sgHMXB systems discovered with *INTEGRAL* satellite (Sguera et al., 2005a). These systems are transient systems, which shows very bright recurrent X-ray flares reaching luminosity $L_X \sim 10^{36}-10^{37} \text{ erg s}^{-1}$, which is $\sim 10^4$ times the average X-ray flux (Romano et al., 2007). In quiescent these systems have luminosity of the order of $10^{32}-10^{33} \text{ erg s}^{-1}$ (Sidoli et al. 2010, Bozzo et al. 2010a), which is lower than other two classes of HMXB systems. These systems consist of a compact object (mainly neutron star) and a O/B supergiant. What triggers these intense flares or what causes their average luminosity to be low are not well understood. Several theories have been proposed, like accretion from very high density clumps (Walter and Zurita Heras 2007, Ducci et al. 2009) or transition from inhibition of accretion to direct accretion regime due to changes in wind parameters. But how these changes occur in short time scale is not yet clear.

1.1.2 Low mass X-ray binary

Low mass X-ray binary (LMXB) systems host a late type (spectral type A or later i.e K, L, M type) faint optical counterpart of mass $M \leq 1M_{\odot}$ (or a white dwarf in few cases) as donor star and either black hole or neutron star as compact object. The nuclear time scale i.e the time scale of primary fuel burning is longer in low mass stars than in high mass stars. So most of the LMXBs are old systems (few billion years) and are found in the Galactic bulge population. Some LMXBs are also seen in Galactic halo and in globular clusters. In case of NS (neutron star) LMXB systems neutron stars have lower magnetic field ($\leq 10^8 \text{ Gauss}$) compared to the neutron stars in NS HMXB systems. The compact object sips matter from

Table 1.1 A comparison of properties of HMXB and LMXB systems.

Properties	HMXBs	LMXBs
Donor star	O-B ($M > 5 M_{\odot}$)	K-M or WD ($M < 1 M_{\odot}$)
Population	I (10^7 yr)	II ($5-15 \times 10^9$ yr)
$\frac{L_x}{L_{opt}}$	0.001-10	100-1000
Optical spectrum	stellar like	reprocessing
Accretion disc	in some systems	yes
X-ray spectrum	hard ($kT \geq 15$ keV)	soft ($kT \leq 10$ keV)
Orbital period	1-100 d	10 min-10 d
X-ray eclipses	common	rare
Magnetic field	strong ($\sim 10^{12}$ Gauss)	weak (10^7-10^8 Gauss)
X-ray pulsation	common (0.1-1000 s)	rare (0.1-100 s)
type I X-ray Bursts	absent	common
X-ray quasiperiodic oscillation (QPO)	rare (0.001-1 Hz)	common (1-1000 Hz)

the evolved companion as its outer layer enters into the zone where gravity of the compact object surpasses its own gravity (Roche lobe overflow, discussed in section 1.2.5). Types of variabilities are more in these systems compared to HMXB systems, such as bursts (rise of intensity by a factor of ~ 10 in short time scale), flares (moderate but abrupt rise in intensity), dips (fall in intensity by several factors) and Quasi Periodic Oscillation (QPO, semi-periodic modulation in intensity). Orbital periods of LMXBs are short in the range of 0.19-398 hr. QPO frequency may vary from milli Hz to kHz.

Pulsation is rarely seen in NS LMXBs, as magnetic field (responsible for pulsation) of the neutron stars in LMXBs decayed to low value due to their old age. Because of low magnetic field, the incoming matter touches the surface of the neutron stars. Gradual accumulation of matter increases pressure and hence temperature at its surface igniting the whole piled up matter. This nuclear burning is called thermonuclear burst in which the X-ray luminosity increases by a factor of 10 to 10^3 , but in most cases on the order of 100 (Lewin et al., 1993). These bursts are not seen or are not present in pulsating LMXBs. The magnetic channeling of matter to the polar caps of pulsating neutron stars piles up matter above poles and causes steady local thermonuclear burning. LMXB systems have less clear origin. Most

accepted mechanism is the capture mechanism, in which an isolated compact object which is a remnant of a massive star, captures a low mass optical star in close encounter. Eclipses are less common in LMXBs than HMXBs. One reason is companion's smaller size. But for edge on systems (inclination between line of sight and normal to the plane of the orbit $\sim 90^\circ$) photo-ionized corona (discussed in section 1.4.3) above and below the accretion disc scatters X-rays which obtrude eclipse.

According to the luminosity variation LMXB systems are classified into two classes i) Transient LMXB ii) Persistent LMXB. With Ariel V and Copernicus data Mason et al. (1976) found correlation between the intensity of LMXB sources and their hardness ratio (Ratio between hard X-ray photon counts to that of soft X-ray photon's, the energy range is not specific). Hasinger and van der Klis (1989) have studied powerspectra of 16 LMXBs as functions of their behaviour in X-ray colour-colour diagram (CCD). CCD is a plot of hard colour versus soft colour, where hard colour (soft colour) is the ratio of photon counts in two higher (lower) energy bands in a particular interval of time. The energy range is not specific, but in both the cases (hard and soft colour), the photon counts in the numerator should correspond to higher energy band between the two concerned energy bands. Based on some correlation between X-ray timing and spectral properties Hasinger and van der Klis (1989) have classified low magnetic field neutron star LMXBs into two categories, i) Z ii) atoll type of LMXBs.

Transient LMXB

Most of the BH (black hole) LMXBs and some of the NS (neutron star) LMXBs have been observed to be transient (Shakura and Sunyaev 1973, Motta et al. 2017). The X-ray luminosity has been observed to be in the range of 10^{30} - $10^{34} \text{ erg s}^{-1}$ in dormant state with occasional outbursts (thermonuclear bursts), which lasts for weeks to months.

Persistent LMXB

Majority of the LMXBs with neutron star as compact objects are seen to be persistent showing X-ray luminosity $\geq 10^{36} \text{ erg s}^{-1}$ (Shakura and Sunyaev 1973, Motta et al. 2017).

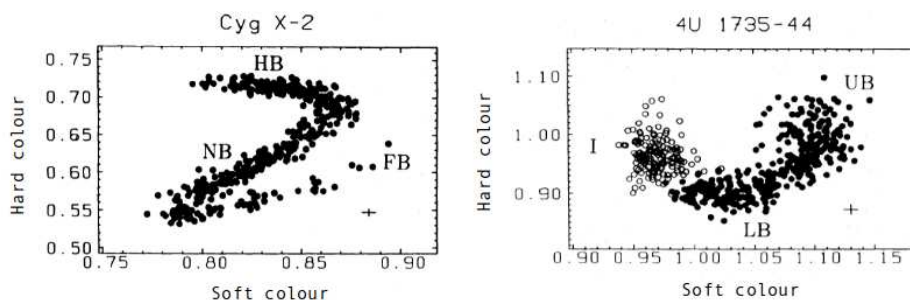


Fig. 1.3 X-RAY colour-colour diagrams of Z (Cygnus–X2, left figure) and atoll (4U 1735–44, right figure) sources. Each point corresponds to 200s of EXOSAT data. Soft (hard) band for Cygnus–X2: 0.9–3.2–4.7 (4.7–6.4–19.1) *keV*. Soft (hard) band for 4U 1735–44: 0.9–2.9–4.5 (4.5–6.1–20.5) *keV*. X and Y axes show soft and hard colour respectively. Image courtesy: Hasinger and van der Klis (1989).

Z source

The sources which produce Z kind of shape in X-ray CCD are named as Z sources. They produce three different branches in the CCD, i) Horizontal branch (HB) ii) Normal Branch (NB) iii) Flaring Branch (FB). In HB, mass accretion rate and X-ray count rate show positive correlation, in NB negative correlation and in FB both type of correlation have been observed. These sources are persistently luminous (except J1701–462). Their luminosities are in the range $L_{EDD} < L < 3L_{EDD}$. Z sources do not show bursts but show strong flares during the flaring branch, which lasts for several thousands of seconds (Barnard et al. 2003; Church et al. 2006). In NB increase of mass accretion rate has been observed which increases temperature and radiation pressure in the inner accretion disc and launches relativistic radio jets (Church et al., 2014). 6 Z sources are known so far. Sco X–1, Cyg X–2 are examples of Z type LMXBs. All the Z sources have been detected in Radio bands.

Atoll source

The sources which show C kind of pattern in the X-ray CCD are classified as atoll sources. The magnetic field and the mass accretion rate of the atoll sources are less compared to Z sources. Atoll sources show two distinct states (hard and soft) in the CCD. The hardest X-ray state is called ‘island’ and the softest state is called ‘banana’ state. In ‘banana’ state hardness is nearly constant over a wide range of luminosities, but in ‘island’ state, the hardness shows

anti-correlation with luminosity (Hasinger and van der Klis, 1989). Orbital period of these sources are less than the Z sources. Number of atoll sources are much more than Z sources. Some of these sources are persistent and some are transient. Their luminosities are low ($L < L_{EDD}$). 4U 1636–536, 4U 1728–34 are examples of atoll sources.

Sources have been observed to switch between Z and atoll type (Homan et al., 2007), for example 4U 1820–30. Wang and Chang (2013) suggested that Z and atoll sources are actually two evolutionary phases of NS LMXBs, rather two distinct sources. Z or atoll like behaviour of a LMXB source is determined by whether the magnetospheric boundary in the accretion disc is radiation or gas pressure dominated, or whether the Keplerian velocity just outside the boundary is sub or supersonic (Hasinger and van der Klis, 1989). X-ray CCD of Z source Cygnus–X2 and atoll source 4U 1735–44 are given in Figure 1.3.

1.2 Accretion in X-ray binary systems

In X-ray binary systems, the compact object because of its intense gravity gains matter in different ways from its companion. The gradual accumulation of matter on the compact object is known as accretion.

1.2.1 Accretion efficiency

As the matter approaches the compact object, its gravitational potential energy decreases. For the simplest assumption, if we assume that the loss of gravitational potential energy is converted to radiation then the accretion luminosity can be written as

$$L_{acc} = \frac{GM_*\dot{M}}{R_*} \quad (1.1)$$

(Frank et al., 2002). M_* and R_* are the mass and radius of the compact object respectively. \dot{M} is the rate of accretion of mass of the compact object. The ratio $\frac{M_*}{R_*}$ denotes that, the efficiency of energy release is directly proportional to the compactness of the compact object. For neutron star the ratio $\frac{M_*}{R_*}$ is more than 100 times greater than that of the white dwarf of

similar mass. So for same \dot{M} the accretion luminosity of a NS XRB would be greater than that of a white dwarf XRB. In case of BH XRBs most of the accreted matter sinks into the hole and is not converted to radiation. The uncertainty can be parametrized by a dimensionless parameter η called accretion efficiency where

$$L_{acc} = \eta \dot{M} c^2 \quad (1.2)$$

(Frank et al., 2002). η is the fraction of the rest mass energy of the accreted mass which is converted to radiation. For BH XRBs η is estimated to be ~ 0.1 . For $1 M_{\odot}$ accreting neutron star it is ~ 0.15 . Accreting black hole or accreting neutron star are nearly similar source of energy conversion in an X-ray binary system. In case of nuclear energy being the source of radiation, the accretion efficiency is ~ 0.007 , which is much smaller compared to the efficiency of energy conversion in accretion process.

1.2.2 Eddington luminosity

Arthur Eddington obtained an upper limit of luminosity of a spherically symmetric radiating object mainly with hydrogen plasma. The luminosity beyond which the radiation pressure overcomes gravity is known as Eddington luminosity or Eddington limit (Rybicki and Lightman, 1979). Radiation exerts force mainly on the electrons of the plasma through Thomson scattering. The electrons drag protons with them due to Coulomb attraction. In the limiting condition the inward gravitational force on electron proton pairs equals the outward force due to radiation pressure at any arbitrary distance r from the center of the radiating object. This can be expressed as

$$\frac{GM_*(m_p + m_e)}{r^2} = \frac{(L_E/4\pi r^2)}{c} \sigma_T \quad (1.3)$$

Where m_p and m_e are the masses of the proton and electron respectively, M_* is the mass of the radiating star, r is the distance from the central object to the electron-proton pairs, c is the speed of light, σ_T is the cross-section for Thomson scattering and L_E is the Eddington

luminosity. $L_E/4\pi r^2$ is the intensity of radiation at a distance r from the source, intensity divided by speed of light (c) is the radiation pressure and this pressure multiplied by σ_T gives the force on an electron-proton pair at a distance r from the source. Ignoring mass of the electron we can write

$$L_E = \frac{4\pi GM_* m_p c}{\sigma_T} \quad (1.4)$$

$$\simeq 1.3 \times 10^{38} \left(\frac{M_*}{M_\odot} \right) \quad (1.5)$$

In units of erg s^{-1} , L_E depends upon the mass of the radiating object. If the accretion occurs over a fractional area x of the compact object then maximum luminosity becomes xL_E . When luminosity of the accreting object exceeds xL_E , the accretion can temporarily be suspended. For a nuclear burning source the outer layer will be blown off if its luminosity exceeds L_E .

If we assume potential energy loss of the accreted matter to be fully converted to radiation, then Eddington luminosity implies a maximum limit of the mass accretion rate. In that case equating equation 1.1 and 1.4 we get

$$\dot{M}_{EDD} = \frac{4\pi m_p c R_*}{\sigma_T} = 1 \times 10^{-3} M_\odot \text{ yr}^{-1} \left(\frac{R_*}{R_\odot} \right) \quad (1.6)$$

But in reality, potential energy to radiation conversion is not 100% efficient, neither of the accretion and the radiation is perfectly spherically symmetric. So the accretion rate is usually less than \dot{M}_{EDD} .

1.2.3 Modes of accretion process

Investigating physical properties of the X-ray binary systems, three different ways of accretion have been proposed, namely i) direct accretion from wind ii) accretion from Be star's disc iii) Roche lobe overflow, which are discussed briefly in the following section.

Direct accretion from wind

In HMXB systems, massive OB stars produce intense winds of the order of 10^{-6} - $10^{-5} \dot{M} \text{ yr}^{-1}$ due to line scattering of the continuum radiation (Kudritzki and Puls, 2000). The wind is accelerated from the companion's surface and gains a terminal velocity (v_α). The instantaneous velocity $v_\omega(r)$ of a wind particle at a distance r from the companion can be written as

$$v_\omega(r) = v_\alpha \left(1 - \frac{R_C}{r}\right)^\beta \quad (1.7)$$

Where R_C is the radius of the companion and $\beta \sim 0.8$ - 1.2 . The supergiant's wind is highly supersonic ($v_\omega(r) \geq 1000 \text{ km s}^{-1}$), which is much higher than the orbital velocity of the neutron star. Bondi (Hermann Bondi 1952) suggested spherically symmetric accretion, where the compact object is embedded in the supergiant's wind. In this approximation mass accretion rate from non-self-gravitating gas can be given by

$$\dot{M} = 4\pi R_B^2 v_\omega(r) \rho_\omega(r) = 4\pi (GM_{NS})^2 \frac{v_\omega(r) \rho_\omega(r)}{v_{rel}^4} \quad (1.8)$$

where $R_B = \frac{GM_{NS}}{v_{rel}^2}$ (obtained from balancing gravitational and centripetal force at a distance r from the compact object) is called Bondi radius after the name of Hermann Bondi, which is the gravitational capture radius of the compact object. $\rho_\omega(r)$ is the wind density at a distance r from the compact object and v_{rel} is the relative velocity of the accreted wind with respect to the neutron star i.e. $v_{rel} = \sqrt{v_\omega^2(r) + v_{orb}^2(r)}$. Since $v_{orb} \ll v_\omega$, so $v_{rel} \sim v_\omega$ and

$$\dot{M} \propto \rho_\omega(r) v_\omega^{-3} \quad (1.9)$$

\dot{M} is known as Bondi-Hoyle-Littleton mass accretion rate. The X-ray luminosity of the system can be given by

$$L_X \propto \dot{M} \propto \rho_\omega(r) v_\omega^{-3} \quad (1.10)$$

The interaction of the infalling plasma with the neutron star's magnetosphere does not allow the accretion to be perfectly spherically symmetric. Shakura et al. (2012) suggested quasi-spherical accretion onto the magnetized neutron star. The inflowing plasma forms

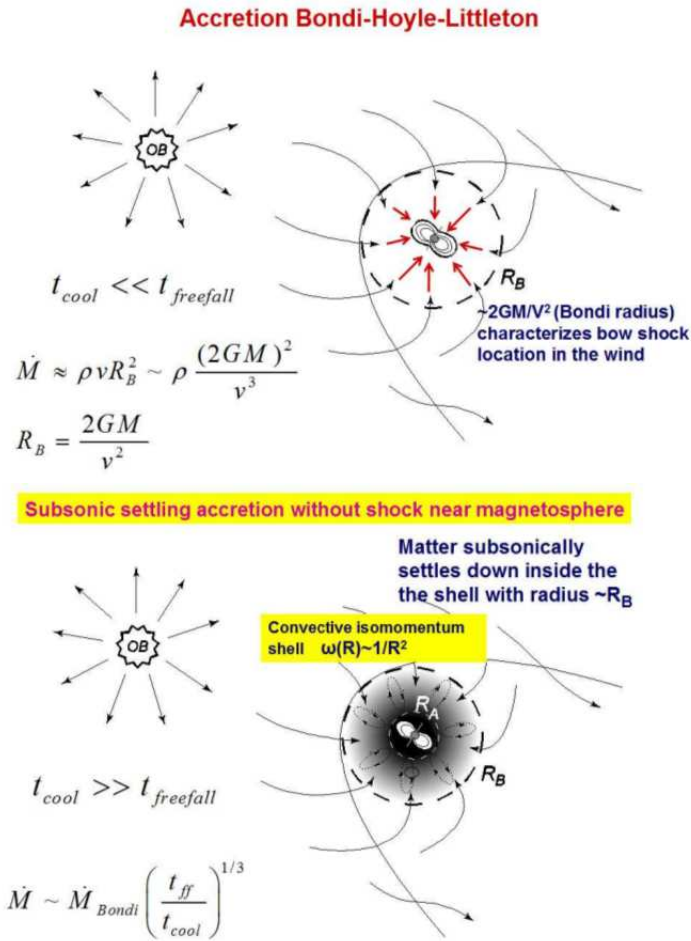


Fig. 1.4 **Top figure:** Bondi-Hoyle-Littleton accretion for cooling plasma. Plasma cooling time is much less than its free fall time ($t_{cool} \ll t_{freefall}$). **Bottom figure:** Settling accretion of hot plasma. In this regime $t_{cool} \gg t_{freefall}$. Image taken from Shakura and Postnov (2017).

shock at some distance from the magnetosphere. Depending upon the efficiency of cooling of the shocked matter, two different cases of quasi-spherical accretion can occur. i) supersonic or Bondi-Hoyle-Littleton accretion ii) subsonic or settling accretion.

In supersonic accretion the shocked plasma rapidly cools down via Compton scattering and the matter enters the magnetosphere at Alfvén radius via Rayleigh-Taylor instability and gets accreted by the neutron star. The mass accretion rate is same as given by Bondi and Hoyle (Bondi and Hoyle, 1944), so this regime is also called Bondi-Hoyle-Littleton

accretion. This kind of accretion occurs in bright X-ray pulsars with X-ray luminosity $L_X > 4 \times 10^{36} \text{ erg s}^{-1}$ (Burnard et al. 1983, Shakura et al. 2012).

When the plasma cooling time is much longer than its free fall time, the shocked plasma remains hot at R_B for long time. A quasi-static shell is formed around the magnetosphere and the matter subsonically settles down inside the shell. The accretion in this condition is known as subsonic accretion. The hot, turbulent plasma penetrates the magnetosphere (at Alfvén radius) by viscous stresses with velocity much smaller than the free fall velocity. Mass accretion rate in this regime is much smaller than Bondi mass accretion rate. This type of accretion occurs in faint pulsars with $L_X < 4 \times 10^{36} \text{ erg s}^{-1}$ (Shakura et al., 2012). For circular orbit L_X depends only upon wind properties like mass loss rate of the companion; velocity and density distribution of the wind material, while for eccentric orbit it varies with orbital phase even if the wind properties remain same. If the accreted matter is highly dense or have high angular momentum then the accreted matter can also form accretion disc and the focused wind forms accretion stream from the inner Lagrangian point to the magnetospheric boundary (to be discussed in section 1.3) of the compact object. The mass accretion rate of the compact object is much less than the mass loss rate of the companion star, as most of the wind matter is lost in the interstellar medium (ISM).

L_X is in the range of 10^{35} - $10^{37} \text{ erg s}^{-1}$ for wind accreting systems. HMXBs like 4U 1700–377 have been found to be purely wind accreting systems while accretion disc has been observed in few HMXBs like GX 301–2 and SMC X–1. Observations of some wind accreting SgHMXBs indicate the possibility of wind accretion in large clumps (Feldmeier 1995, Oskinova et al. 2006) which is an active part of research in high energy astrophysics.

Wind accretion in SFXT systems

Several hours long intense outbursts in SFXTs indicate clumpy and dense (10^4 - 10^5 times denser than homogeneous stellar wind) wind accretion by the compact object (Walter and Zurita Heras, 2007). Numerical simulations of wind flow from the supergiant star indicates formation of dense clumps due to instabilities in the wind (Oskinova et al., 2007).

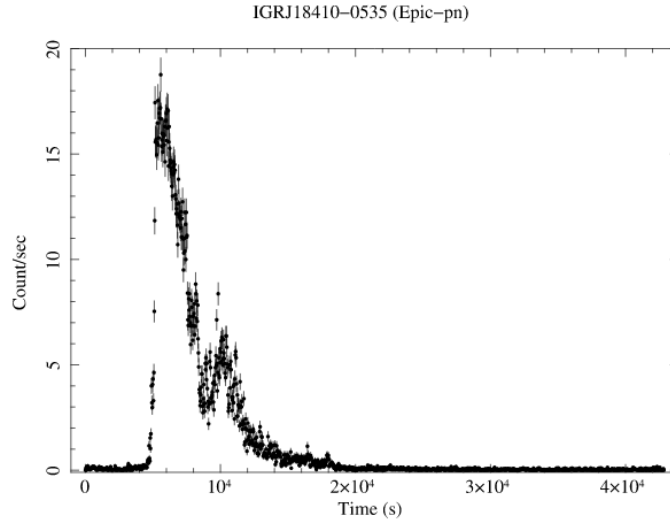


Fig. 1.5 XMM-Newton Epic-pn lightcurve (0.3–12 keV) of SFXT IGR J18410–0535 shows an outburst. Image courtesy: Bozzo et al. (2011)

Detection of pulsations and the X-ray spectra in outburst and quiescence suggest that most of the SFXTs host NS accretors. Bozzo et al. (2008) suggest centrifugal and/or magnetic ‘gating’ mechanisms for the sudden outburst and long quiescence (to be discussed in detail in section 1.4). Figure 1.5 shows an outburst in the lightcurve of SFXT IGR J18410–0535 (Bozzo et al., 2011).

Wind accretion in symbiotic XRB systems

Evidence of wind accretion has also been found in some LMXB systems. These systems are called symbiotic XRBs (SyXRBs). In these systems the compact object accretes slow and dense winds from its red giant companion (Masetti et al. 2006; Nespoli et al. 2010; Hynes et al. 2014; Bahramian et al. 2014). These sources show highly variable X-ray intensity with bright flares (Masetti et al., 2007). The mass loss rate of the companion is less than $10^{-10} M_{\odot} \text{ yr}^{-1}$.

The average X-ray fluxes are in the range of 10^{-11} – $10^{-10} \text{ erg s}^{-1} \text{ keV}^{-1}$. The orbital period of these systems are large (months to years) and the X-ray pulsation also has been found to be very slow (hundreds to ~ 18400 s, Corbet et al. 2008). GX 1+4 is a symbiotic XRB system accretes from M-type companion (Corbet et al., 2008). It has orbital period of

(1161 ± 12) days (Hinkle et al., 2006) and a spin period of 2 minutes (Jablonski et al., 1997).

1.2.4 Accretion from Be star's disc

In BeXRB systems when the neutron star passes through the disc of its Be companion, it accretes wind from Be star's equatorial disc (has been discussed in section 1.1.1). Sharp increase of mass accretion rate results into powerful type I outbursts with luminosity 10^{36} - $10^{37} \text{ erg s}^{-1}$. During this closest approach or periastron passage of the neutron star, often accretion disc is formed and the neutron star spins up (Bildsten et al., 1997). When the neutron star comes out of periastron, its luminosity slowly decreases. This type I outburst is seen once in every orbit. In wide eccentric orbit of BeXRB systems, neutron star is usually dim. So most of the BeXRB systems are transient with some irregular type II X-ray bursts (discussed in section 1.1.1).

1.2.5 Roche lobe overflow

The gravitational potential at a distance r from the center of momentum of the binary system can be written by

$$\phi_R = -\frac{GM_1}{r_1} - \frac{GM_2}{r_2} - \frac{\omega^2 r^2}{2} \quad (1.11)$$

ϕ_R is known as Roche potential after the name of French astronomer Édouard Roche. r_1 and r_2 are the distances from the center of the star of mass M_1 and M_2 respectively to the point at position r . ω is the orbital period of the binary system about the center of mass.

Interference of gravity of both the stars leads to the formation of equipotential surfaces around both the star. In each of these surfaces gravitational potential is constant. These surfaces are referred to as Roche lobe of each star. The effective Roche lobe radius is given by

$$R_{L_i}(i = 1, 2) = \frac{0.49q_i^{-2/3}}{0.6q_i^{-1/3} + \ln(1 + q_i^{-1/3})} \quad (1.12)$$

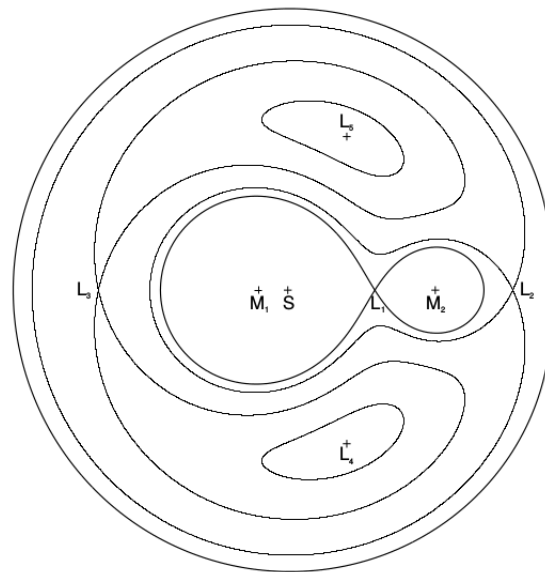


Fig. 1.6 Equipotential surfaces of the Roche potential in a binary system of two stars (mass M_1 and M_2). S represents the center of mass of the system. L_1 is the inner Lagrangian point. Other turning points L_2 , L_3 , L_4 , L_5 are also labeled. Image courtesy: Kretschmar (1996)

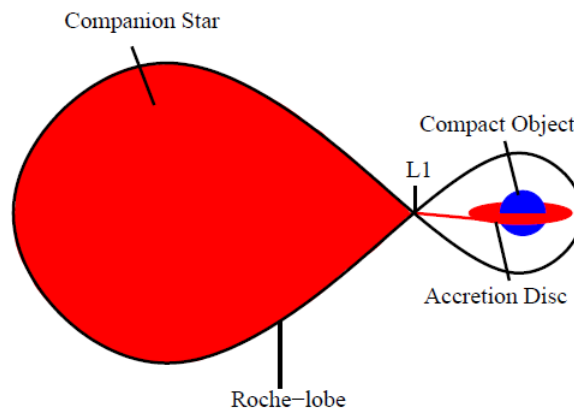


Fig. 1.7 Roche-lobe overflow from the companion to the compact object through inner Lagrangian (L_1) point. The transferred matter forms accretion disc around the compact object due to its angular momentum. Image courtesy: Mück (2014)

Where $q_1 = \frac{M_1}{M_2}$ and $q_2 = q_1^{-1}$, a is the orbital separation (Frank et al., 2002). The Roche lobe of the two stars intersect at a point between the two stars, called inner Lagrangian point L_1 . Any material inside a Roche lobe is gravitationally bound to the central star. If one of the star fills its Roche lobe in the evolutionary process, then the matter that happen to cross L_1 (by processes like thermal velocity) is pulled by the other star and matter flows from the former to the later star. This process is known as the Roche lobe overflow in accretion. This kind of mass transfer have been observed in LMXB systems and in few HMXB systems with supergiant companion. A cartoon picture of the Roche lobe overflow is given in Figure 1.7.

1.2.6 Accretion disc

The material that crosses the inner Lagrangian point carries sufficient angular momentum which does not allow the material to fall on the compact object directly. This material then spirally approaches the compact object. The circulation radius of the material with angular momentum J is given by

$$R_{circ} = \frac{J^2}{GM_*} \quad (1.13)$$

As the material moves inward its angular momentum decreases. To conserve the angular momentum some of the material move outward. As a result a disc is formed around the compact object, which is known as accretion disc (Frank et al., 2002).

Accretion disc structure

For steady accretion i.e. time independent accretion, viscous torques between any two layers of the disc causes the transport of energy and momentum inward and outward. Weak magnetic field of plasma in the disc also adds turbulence in the motion of this plasma. Viscous or radial drift time scale (t_{vis}) gives an estimation of time in which a disc annulus moves a radial distance R where

$$t_{vis} = \frac{R}{v_R} \quad (1.14)$$

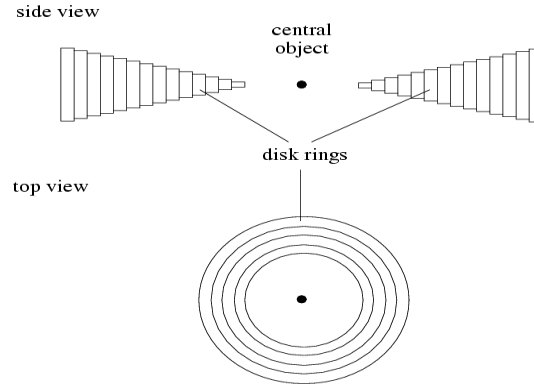


Fig. 1.8 Accretion disc around a compact object. Image courtesy: <https://www.aanda.org/articles/aa/full/2004/46/aa1522/aa1522.right.html>

v_R is the radial velocity of the disc annulus (Frank et al., 2002). In the assumption of steady thin disc, viscous dissipation does not depend upon the nature of viscosity. Viscous dissipation per unit disc face area can be written as (Frank et al., 2002)

$$D_r = \frac{3GM_*\dot{M}}{8\pi r^3} \left[1 - \left(\frac{R_*}{r} \right)^{1/2} \right] \quad (1.15)$$

The disc luminosity can be written as

$$L_{Disc} = \frac{GM_*\dot{M}}{2R_*} = \frac{1}{2}L_{acc} \quad (1.16)$$

So only half of the total luminosity is radiated from the disc due to gradual distribution of matter on the disc. The scale height h (the height of the disc above disc plane) at a distance r from the accretor can be given by

$$h \approx c_s \left(\frac{r}{GM_*} \right)^{1/2} r \quad (1.17)$$

where c_s is the sound speed. For thin disc

$$c_s \ll \sqrt{\frac{GM_*}{r}} \quad (1.18)$$

(Frank et al., 2002). So, Keplerian speed $\left(\sqrt{\frac{GM_*}{r}}\right)$ of matter in the disc is highly supersonic. The radial drift velocity v_r of matter on the disc is quite smaller than the circular speed of a disc annulus. Where v_r can be written by

$$v_r \propto \frac{c^2(s)}{v_\phi} \quad (1.19)$$

v_ϕ is the azimuthal velocity of matter drifting radially.

Shakura and Sunyaev (1973) gave a model of the accretion disc by introducing a parameter ($\alpha \leq 1$) related to the disc viscosity, where

$$\nu = \alpha c_s h \quad (1.20)$$

ν is a viscosity parameter given by $\nu = \lambda \bar{v}$, where λ is the mean free path of the particles in the disc and \bar{v} is their average thermal speed. A simple model of the Shakura-Sunyaev disc is given in Figure 1.8.

Accretion disc temperature

In equilibrium all the energy generated due to viscous dissipation in a disc annulus is radiated away. If the disc is assumed to be optically thick (The dimension of the disc is much greater than the mean free path of the radiated photon) then the radiation would be black-body radiation with an effective temperature of the annulus $T_{eff}(r)$. So the temperature of optically thick, geometrically thin steady-state accretion disc at a distance r from the accretor can be expressed as (Frank et al., 2002)

$$T_{eff}(r) = \left[\frac{3GM_*\dot{M}}{8\pi\sigma r^3} \left(1 - \sqrt{\frac{R_*}{r}}\right) \right]^{1/4} \quad (1.21)$$

Asuming $R_* \ll r$

$$T_{eff}(r) = \left(\frac{3GM_*\dot{M}}{8\pi\sigma r^3} \right)^{1/4} \quad (1.22)$$

The profile peaks at

$$T_{peak} = 0.5 \left(\frac{3GM_*\dot{M}}{8\pi\sigma R_*^3} \right)^{1/4} \quad (1.23)$$

The equation 1.23 indicates that the effective temperature will be higher towards the inner part of the disc. T_{peak} can have values of the order of 10^4 ; 10^7 ; 10^5 K for a white dwarf; neutron star and a $10^6 M_\odot$ black hole as accretors respectively.

Accretion disc spectrum

Equation 1.22 shows that the temperature varies with the radius of the disc annuli. The accretion disc can be thought of a collection of rings, all radiating locally as a blackbody with their own effective temperature which increases inward. The total power emitted by the accretion disc per unit area per unit frequency per unit solid angle can be obtained by summing the contribution from each annulus and can be written by (Kolb, 2010)

$$F_\nu \propto \frac{1}{d^2} \int_{r_{in}}^{r_{out}} \frac{2h\nu^3}{c^2} \frac{1}{\exp\left(\frac{h\nu}{kT_{eff}(r)}\right) - 1} 2\pi r dr \quad (1.24)$$

Where r_{in} and r_{out} are the inner and outer radius of the accretion disc, d is the distance from the emitter to the observer. Since T_{eff} is higher ($T_{eff} \propto r^{-3/4}$) towards the inner part of the disc, so most of the power comes from the inner accretion disc.

For low energy photons $h\nu \ll kT_{out}$ (As the temperature T_{out} is the minimum temperature in the disc). So

$$F_\nu \propto \nu^2 \int T_{eff}(r) r dr \quad (1.25)$$

or

$$F_\nu \propto \nu^2 \quad (1.26)$$

As the integral is independent of ν . Hence the disc spectrum resembles the Rayleigh-Jeans tail for low energy photons.

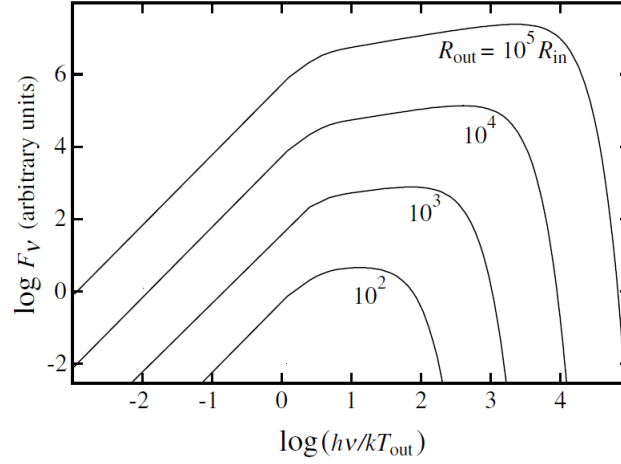


Fig. 1.9 Spectrum of an optically thick accretion disc radiating locally as a blackbody. Accretion disc can be thought of collection of rings made of plasma, the temperature being highest nearest to the source. The spectrum is often called multicolour blackbody spectrum. Different spectrum corresponds to different ratio of the inner and outer radii of the accretion disc, as indicated in the figure. Image courtesy: (Kolb, 2010)

For high energy photons $h\nu \gg kT_{in}$ (As T_{in} is the maximum temperature in the disc).

$$F_{\nu} \propto \nu^3 \int \exp\left(-\frac{h\nu}{kT_{eff}(r)}\right) r dr \quad (1.27)$$

Neglecting contribution from $\exp\left(-\frac{h\nu}{kT_{out}}\right)$ as $T_{out} \ll T_{in}$

$$F_{\nu} \propto \nu^3 \exp\left(-\frac{h\nu}{kT_{in}}\right) \quad (1.28)$$

So the disc spectrum takes the form of Wein tail for high energy photons.

For intermediate energy photons $kT_{out} \ll h\nu \ll kT_{in}$ and

$$F_{\nu} \propto \nu^{1/3} \quad (1.29)$$

Which is the characteristic of the accretion disc spectrum for the intermediate energy of photons. These range depends upon the difference between the inner and outer disc temperature.

Fig 1.9 shows the spectrum of an accretion disc.

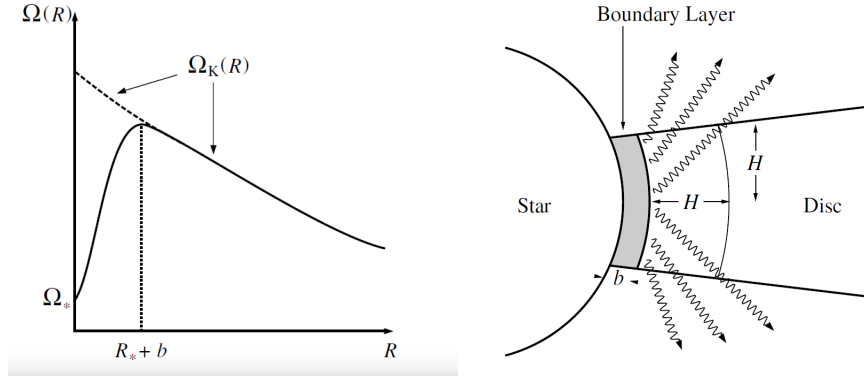


Fig. 1.10 **Left panel:** The distribution of angular speed with distance from the neutron star. R_* is the neutron star's radius and Ω_* is the angular speed at its surface. b is the width of the boundary layer. In the boundary layer the angular speed deviates from its Keplerian value. Image courtesy: Frank et al. (2002) **Right panel:** Optically thick boundary layer around the neutron star in an azimuthal plane. Image courtesy: Frank et al. (2002)

The boundary layer

The angular speed of the accreted plasma deviate from the orbital Keplerian speed in the region between the inner accretion disk and the surface of the neutron star or white dwarf accretor. This region is named as boundary layer. The physical characteristics of the boundary layer is not well established. In this region the orbital speed of plasma smoothly decreases from Keplerian speed to the angular speed of the accretor. The distribution of angular speed in the boundary layer is shown in the left panel of Figure 1.10.

The radial width of the boundary layer can be expressed as (Frank et al., 2002)

$$b \sim \frac{R_*^2}{GM_*} c_s^2 \sim \frac{H^2}{R_*} \quad (1.30)$$

Where H is the scale height just outside the boundary layer. The radial width of the boundary layer is much smaller than the scale height H . The schematic view of the boundary layer is shown in the right panel of Figure 1.10.

If the density of the plasma just outside the boundary layer i.e. in the innermost part of the accretion disc is high enough then this region will be optically thick and will radiate as blackbody. Considering the radial extent of this blackbody emitter equal to the scale height

It can be shown that the characteristic boundary layer temperature (Frank et al., 2002)

$$T_{BL} \sim \left(\frac{R_*}{H}\right)^{1/4} T_* \quad (1.31)$$

Where T_* is the characteristic disc blackbody temperature.

$$T_{BL} \sim 1 \times 10^5 \dot{M}_{16}^{7/32} m_*^{11/32} R_9^{-25/32} K \quad (1.32)$$

\dot{M}_{16} is the mass accretion rate in units of $10^{-16} M_\odot \text{ yr}^{-1}$, m_* is the mass of the compact object in units of M_\odot , R_9 is the radius of the compact object in units of 10^9 cm . It can be shown that (Frank et al., 2002)

$$T_{BL} \sim 3T_* \quad (1.33)$$

T_{BL} is significantly higher than the peak temperature in the disc. The luminosity of the boundary layer is

$$L_{BL} = \frac{GM_*\dot{M}}{2R_*} \left[1 - \left(\frac{\omega_c}{\omega_k}\right)^2\right] \quad (1.34)$$

ω_c and ω_k are respectively the angular speed of the accreting star and the Keplerian speed at the surface of the star. Since $\omega_c \ll \omega_k$, So L_{BL} can be written as

$$L_{BL} = \frac{GM_*\dot{M}}{2R_*} \quad (1.35)$$

Which is equal to half of the total accretion luminosity and equal to the disc luminosity.

1.3 Accretion and accretor's magnetic field connection

For low magnetic field neutron star or white dwarf, the accretion disc is extended to the surface of the compact object. But for higher values of the magnetic field ($\sim 10^7 \text{ Gauss}$ for white dwarf and $\geq 10^{12} \text{ Gauss}$ for neutron star) of the accretor the disc is disrupted at a large distance by its magnetic field. The field strength of the dipole like magnetic field of the neutron star or white dwarf at a distance r from the center of the compact object can be

written as

$$B \sim \frac{\mu}{r^3} \quad (1.36)$$

Where μ is a constant and is given by $\mu = B_* R_*^3$, B_* is the field strength at the surface of the accretor. So the magnetic pressure at a distance r can be written as

$$P_{mag} = \frac{4\pi B^2}{\mu_o 8\pi} \quad (1.37)$$

Or

$$P_{mag} = \frac{4\pi \mu^2}{\mu_o 8\pi r^6} \quad (1.38)$$

μ_o is the permeability of free space. As the matter approaches the magnetic accretor P_{mag} increases, finally at a certain distance from the accretor the magnetic pressure just exceeds the ram and gas pressure of the infalling matter. Thus radial infall of matter is halted at this distance. This distance is known as Alfvén radius (R_M) of the magnetic neutron star or white dwarf. For supersonic accretion ram pressure is significant and it can be expressed as

$$P_{ram} = \rho v_{eff}^2 \quad (1.39)$$

where ρ and v_{eff} are respectively the density and free fall velocity of the gas.

$$v_{eff} = \sqrt{\frac{2GM_*}{r}} \quad (1.40)$$

and

$$|\rho v| = \frac{\dot{M}}{4\pi r^2} \quad (1.41)$$

$$P_{mag}(R_M) = P_{ram}(R_M) \quad (1.42)$$

From equation 1.38, 1.39 and using equation 1.40, 1.41 and 1.42 (Frank et al., 2002)

$$\left(\frac{4\pi}{\mu_o}\right) \frac{\mu^2}{8\pi R_M^6} = \frac{\sqrt{2GM_*} \dot{M}}{4\pi R_M^{5/2}} \quad (1.43)$$

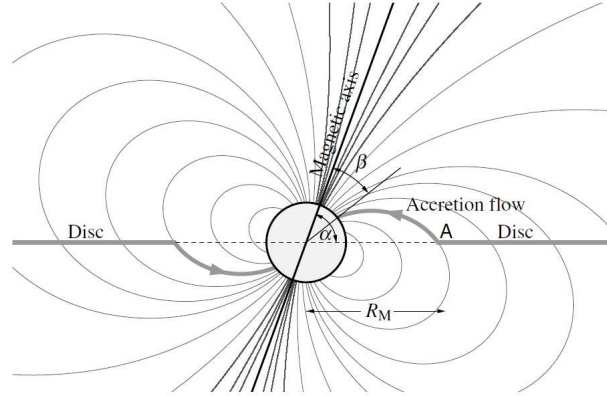


Fig. 1.11 The accretion disc is truncated at Alfvén radius (R_M) for a magnetic accretor (neutron star or white dwarf). The incoming matter is channeled from the Alfvén radius to the accretor's poles. Image courtesy: Frank et al. (2002)

Or

$$R_M = \left[\frac{\mu^2}{\sqrt{8GM_*\dot{M}}} \left(\frac{4\pi}{\mu_o} \right) \right]^{2/7} \quad (1.44)$$

Or

$$R_M = 5.1 \times 10^8 m_*^{-1/7} \dot{M}_{16}^{-2/7} \mu_{30}^{4/7} \text{ cm} \quad (1.45)$$

μ_{30} is the value of μ in units of 10^{30} Gauss cm^3 i.e. $\mu_{30} = \frac{\mu}{10^{30}}$, \dot{M}_{16} is the mass accretion rate in units of $10^{-16} \text{ gm s}^{-1}$. Substituting M_\odot with luminosity, R_M for neutron star accretor can be written as

$$R_M|_{NS} = 2.9 \times 10^8 m_*^{1/7} R_6^{-2/7} L_{37}^{-2/7} \mu_{30}^{4/7} \text{ cm} \quad (1.46)$$

and for white dwarf accretor,

$$R_M|_{WD} = 5.5 \times 10^8 m_*^{1/7} R_9^{-2/7} L_{33}^{-2/7} \mu_{30}^{4/7} \text{ cm} \quad (1.47)$$

R_6 and R_9 are the radius of the accretor in units of 10^6 and 10^9 cm, L_{37} and L_{33} are the source luminosities in units of $10^{37} \text{ erg s}^{-1}$ and $10^{33} \text{ erg s}^{-1}$. During radial infall the matter reaches Alfvén radius and then it is channeled to the magnetic poles through the magnetic field lines. A schematic view of the Alfvén radius and the channeling of matter to the poles of the magnetic accretor is given in Figure 1.11. Because of some instabilities (to be

discussed in the next section) some of the accreted plasma slips through the Alfvén radius. Inside Alfvén radius the motion of the plasma is regulated by the magnetic field lines. This region is called magnetosphere of the magnetic accretor. More intense is the magnetic field of the accretor bigger is the magnetosphere.

1.4 Different regimes of accretion

Large variability including off-states and flares have been observed in many X-ray binary systems, specially in wind-fed neutron star HMXB systems. This can occur due to sudden change in accretion rate. To understand sudden abrupt changes in accretion rate we first need to recall the accretion and co-rotation radius of the neutron star.

The gravitational capture radius or accretion radius is the distance from the neutron star where the strong gravity of neutron star starts focusing matter towards itself (Bondi, 1952). This can be given as

$$R_a = \frac{2GM_{NS}}{v_w^2} = 3.7 \times 10^{10} v_8^{-2} \text{ cm} \quad (1.48)$$

v_8 is the velocity of companion's wind in 10^3 km s^{-1} or 10^8 cm s^{-1} . The matter is captured from a cylindrical region of length R_a . So the mass capture rate (\dot{M}_{capt}) is much smaller than the mass loss rate (\dot{M}_w) of the companion and can be written as

$$\frac{\dot{M}_{capt}}{\dot{M}_w} \simeq \frac{R_a^2}{4a^2} = 2 \times 10^{-5} v_8^{-4} a_{10}^{-2} \quad (1.49)$$

Where a is the orbital size and a_{10} is the same in units of 10 days.

Corotation radius (R_{co}) of the neutron star is the distance from the neutron star where the Keplerian angular speed is same as the neutron star's angular speed. R_{co} can be expressed as

$$R_{co} = 1.7 \times 10^{10} P_{NS}^{2/3} \text{ cm} \quad (1.50)$$

P_{NS3} is the neutron star's spin period in units of 10^3 seconds. The Alfven radius expressed in equation 1.45 can also be written as

$$R_M = 3.3 \times 10^{10} \dot{M}_{-6}^{-1/6} v_8^{-1/6} a_{10}^{1/3} \mu_{33}^{1/3} \text{ cm} \quad (1.51)$$

\dot{M}_{-6} is \dot{M}_w in units of $10^{-6} M_\odot \text{ yr}^{-1}$. From equation 1.48 and 1.51 we can see that R_a and R_M depends upon wind parameters which can change in short time scales, where R_{co} depends only upon neutron star's spin which changes in evolutionary time scale. So relative positions of R_a and R_M with respect to R_{co} can vary over short time scales. This leads to the transitions between different accretion regime (Bozzo et al., 2008). Transition to different accretion regimes leads to bursts, flares, off-states etc. In the thesis we have found variabilities including off-states like features. Following Bozzo et al. (2008) different accretion regimes are briefly described below.

1.4.1 Magnetic inhibition of accretion

when $R_M > R_a$, the companion's wind interacts with the neutron star's magnetosphere without significant gravitational focusing. Very little matter penetrates the magnetosphere. This happens in case of high magnetic field neutron stars. The wind forms a bow shock at neutron star's magnetospheric boundary. Around the stagnation point of the shock the kinetic energy of the inflowing wind matter gets converted into thermal energy. The temperature of the shocked region is estimated as

$$T_{shock} = \frac{m_p v_w^2}{3k} \approx 4 \times 10^7 v_8^2 \text{ K} \quad (1.52)$$

For simplicity, considering mass of the gas particle equal to the mass of hydrogen ion or mass of proton (m_p), the power emitted from this region or the luminosity (L_{shock_I}) can be written as

$$L_{shock_I} = \frac{\pi}{2} R_M^2 \rho_w v_w^3 = 4.7 \times 10^{29} R_M^2 v_8^2 a_{10}^{-2} \dot{M}_{-6} \text{ erg s}^{-1} \quad (1.53)$$

This power is mainly emitted in X-ray band (Toropina et al., 2006). Depending upon the relative positions between R_M and R_{co} two regimes of accretion can take place, which are briefly discussed below.

Super Keplerian magnetic inhibition regime

If $R_M > R_{co}$, then matter at R_M along the field lines rotates with angular speed smaller than the angular speed of matter present between R_M and R_{co} and the angular speed of the neutron star. The matter just inside R_M propels some of the matter at R_M i.e. centrifugal gate is closed. So centrifugal barrier along with magnetic inhibition makes the accretion rate very low. Friction between the matter inside and outside the magnetosphere near R_M releases X-rays of luminosity L_{FR} which can be expressed as

$$L_{FR} = \pi R_M^2 \rho_w v_w (R_M \Omega)^2 \quad (1.54)$$

Ω is the angular speed of matter at R_M .

$$= 3.7 \times 10^{29} R_{M,10}^4 \dot{M}_{-6} a_{10}^{-2} P_{NS3}^{-2} \text{ erg s}^{-1} \quad (1.55)$$

This regime is called super Keplerian magnetic inhibition regime, because the magnetosphere exerts a rotational pull on the matter at R_M i.e. just outside the magnetosphere, to force the matter rotate with greater speed than their Keplerian angular speed at that position. In this regime the neutron star spins down. Total X-ray luminosity in this regime (L_{TSp}) comes from the shock luminosity (L_{shock_I}) and the luminosity originated from friction (L_{FR}). i.e.

$$L_{TSp} = L_{shock_I} + L_{FR} \quad (1.56)$$

Sub Keplerian magnetic inhibition regime

If $R_M < R_{co}$, i.e. ($R_a < R_M < R_{co}$), then the angular speed at R_M is greater than that at R_{co} . The matter at R_{co} exerts rotational drag on the matter at R_M and tries to lower its angular speed from its Keplerian value. So this regime is named as sub Keplerian mag-

netic inhibition regime. The matter at magnetospheric boundary i.e. at R_M is not pushed away, so centrifugal gate is open. While channeling towards the pole by magnetic field lines the matter penetrates inside the magnetosphere through Kelvin Helmholtz instabilities because of different densities of plasma inside and outside the magnetospheric boundary. This diffusion of matter inside the neutron star magnetosphere produces heat mostly in X-rays. Corresponding luminosity can be expressed as

$$L_{KH_I} = 3.5 \times 10^{34} \eta_{KH} R_{M,10}^2 a_{10}^{-2} \dot{M}_{-6} \left(\frac{\rho_i}{\rho_e} \right) \left(1 + \frac{\rho_i}{\rho_e} \right)^{-1} \text{ erg s}^{-1} \quad (1.57)$$

$\eta_{KH} \sim 0.1$, is an efficiency factor. ρ_i and ρ_e are the plasma density inside and outside the magnetospheric boundary at R_M .

The total luminosity in this regime is given by

$$L_{TSb} = L_{shock_I} + L_{KH_I} \quad (1.58)$$

But, since $L_{shock_I} \ll L_{KH_I}$, so $L_{TSb} \sim L_{KH_I}$. Comparing equation 1.53, 1.55 and 1.57 we can see that the luminosity in the sub Keplerian magnetic inhibition regime is more compared to that in super Keplerian magnetic inhibition regime ($L_{TSb} > L_{TSp}$).

1.4.2 Propeller regime

When $R_M < R_a$, the magnetic gate is open. Matter from the companion is shocked at R_a and accelerated towards the magnetosphere and halts at its boundary. The matter redistributes itself in the region between R_a and R_M . The shape and properties of this region depends upon the property of companion's wind and its interaction with the neutron star's magnetosphere. This regime of accretion is known as propeller regime as matter at magnetospheric boundary is pushed tangentially along its surface. Depending upon the relative positions between R_M and R_{co} , two different scenario arises which are discussed below.

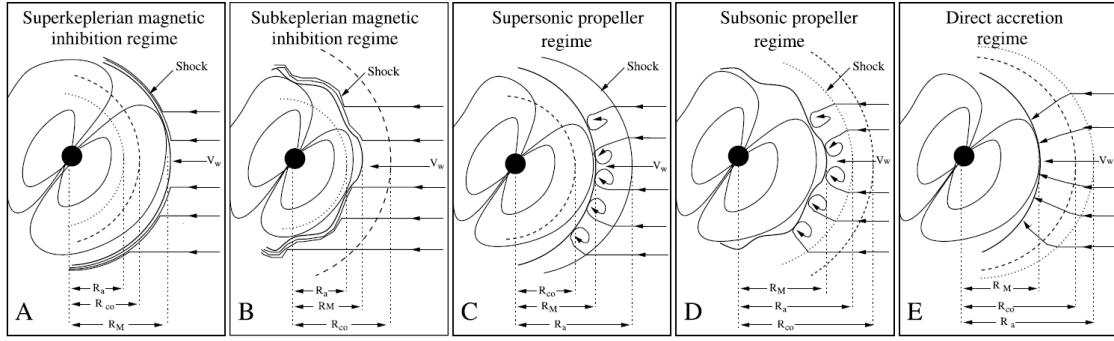


Fig. 1.12 A schematic view of the interaction of neutron star's magnetosphere and the inflowing plasma from its supergiant companion. Relative positions of magnetospheric or Alfvén radius (solid line), the co-rotation radius (dashed line), and the accretion radius (dotted line) causes different accretion regimes. The wavy solid line is used for Kelvin-Helmholtz unstable magnetospheric boundary at R_M . Convective motions in the propeller regimes are represented with small eddies at magnetospheric boundary. Image courtesy: Bozzo et al. (2008).

Supersonic propeller regime

When $R_M > R_{co}$, then the matter at R_M which is rotating with the magnetic field lines with speed less than the angular speed of matter at R_{co} is pushed away from the surface. The power generated because of shock at R_a is radiated away from the surface. The power radiated because of shock at R_a is given by (Davies and Pringle, 1981)

$$L_{shockII} = \frac{9}{32} \pi R_a^2 \rho_w v_w^3 \simeq 2.6 \times 10^{29} R_{a10}^2 v_8^2 a_{10}^{-2} \dot{M}_{-6} \text{ erg s}^{-1} \quad (1.59)$$

According to the treatment of Davies and Pringle (1981), when the rotational velocity of the neutron star's magnetosphere at R_M is supersonic then the friction between the layers inside the magnetosphere draws rotational energy from the neutron star. So the neutron star spins down. Turbulent motion of matter at R_M convects this energy outwards and radiates this energy through the outer boundary. In this regime the Alfvén radius can be expressed as

$$R_M \simeq 2.3 \times 10^{10} a_{10}^{4/9} \dot{M}_{-6}^{2/9} v_8^{4/9} \mu_{33}^{4/9} \text{ cm} \quad (1.60)$$

and luminosity in this regime is given by

$$L_{sdI} = 2\pi R_M^2 \rho(R_M) c_S^3(R_M) \quad (1.61)$$

$$\simeq 5.4 \times 10^{31} \dot{M}_{-6} a_{10}^{-2} v_8^{-1} R_{M10}^{1/2} \left[1 + \frac{16R_{a10}}{3R_{M10}} \right]^{1/2} \text{ erg s}^{-1} \quad (1.62)$$

$\rho(R_M)$ is the plasma density at R_M . c_S is the sound speed given by

$$c_S = v_{eff}(R_M) = \sqrt{\frac{2GM_{NS}}{R_M}} \quad (1.63)$$

The total luminosity in this regime can be expressed as

$$L_{Tpp} = L_{shockII} + L_{sdI} \quad (1.64)$$

As $L_{shockII} \ll L_{sdI}$, so $L_{Tpp} \sim L_{sdI}$.

Subsonic propeller regime

When $R_M < R_{co}$, magnetosphere's rotation becomes subsonic with respect to the surrounding medium. According to Davies and Pringle (1981), R_M for this region can be written as

$$R_M \simeq 2 \times 10^{10} a_{10}^{4/7} \dot{M}_{-6}^{2/7} v_8^{8/7} \mu_{33}^{4/7} \text{ cm} \quad (1.65)$$

Centrifugal gate is open as $R_M < R_{co}$. But the energy of the matter is high enough to penetrate the magnetosphere. This regime of accretion is called subsonic propeller regime. Some of the matter accumulated in the region between R_a and R_M pierce the magnetosphere through Kelvin-Helmholtz instabilities and Bohm diffusion, corresponding luminosities can be respectively written as

$$L_{KHII} = \frac{GM_{NS} \dot{M}_{KH}}{R_{NS}} \quad (1.66)$$

$$L_{KHII} = 1.8 \times 10^{35} \eta_{KH} P_{NS3}^{-1} R_{M10}^3 \dot{M}_{-6} a_{10}^{-2} v_8^{-1} \left[1 + \frac{16R_{a10}}{5R_{M10}} \right]^{3/2} \left(\frac{\rho_i}{\rho_e} \right)^{1/2} \left(1 + \frac{\rho_i}{\rho_e} \right)^{-1} \text{ erg s}^{-1} \quad (1.67)$$

and

$$L_{diff} \simeq \frac{GM_{NS} \dot{M}_{diff}}{R_{NS}} \quad (1.68)$$

$$L_{diff} \simeq 4.5 \times 10^{30} \dot{M}_{-6} a_{10}^{-2} R_{M10}^{9/4} \mu_{33}^{-1/2} \zeta_{1/2} v_8^{-1} \left[1 + \frac{16R_{a10}}{5R_{M10}} \right]^{3/2} \text{ erg s}^{-1} \quad (1.69)$$

$\zeta \sim 0.1$ is an efficiency factor.

Rotational energy dissipation of the neutron star leads to radiation with luminosity given by

$$L_{sdII} = 2\pi R_M^5 \rho(R_M) \Omega^3 \quad (1.70)$$

Or

$$L_{sdII} = 2.2 \times 10^{30} P_{NS3}^{-3} R_{M10}^5 \dot{M}_{-6} v_8^{-1} a_{10}^{-2} \left[1 + \frac{16R_{a10}}{5R_{M10}} \right]^{3/2} \text{ erg s}^{-1} \quad (1.71)$$

L_{sdII} also contributes to the total luminosity (L_{Tpb}), but contribution of L_{KHII} is significant in this regime. So

$$L_{Tpb} \simeq L_{KHII} \quad (1.72)$$

Direct accretion regime

Accretion to occur without any hindrance requires the following conditions to be satisfied

i) $R_M < R_a$

ii) $R_M < R_{co}$

iii) The density of matter just outside R_M should be high enough to cool the accumulated matter between R_a and R_M .

The critical density $\rho_{max_{12}}$ above which accretion occurs efficiently through the magnetosphere, is given by

$$\rho_{max_{12}} = 0.83 P_{NS3}^{-3} R_{M10}^{5/2} \left(1 + \frac{16 R_{a10}}{5 R_{M10}} \right)^{3/2} \quad (1.73)$$

This regime of accretion is called direct accretion. The accretion rate is comparable with the accretion rate in Bondi-Hoyle approximation. The X-ray intensity (L_{DX}) in this regime is the highest X-ray luminosity amongst all the regimes discussed above. The luminosity in this regime can be written as

$$L_{DX} = \frac{M_{NS} \dot{M}_{capt}}{R_{NS}} \quad (1.74)$$

Or

$$L_{DX} = 2 \times 10^{35} \dot{M}_{-6} a_{10}^{-2} v_8^{-4} \text{ erg.s}^{-1} \simeq 2 \times 10^{35} \dot{M}_{-15} \text{ erg s}^{-1} \quad (1.75)$$

$\dot{M}_{-15} = \frac{\dot{M}_{capt}}{10^{15}} \text{ gm s}^{-1}$. A schematic view of all the above regimes of accretion is given in Figure 1.12.

1.4.3 Accretion powered pulsar

As discussed in section 1.3, when the magnetic pressure equals the ram and gas pressure of the inflowing matter then the matter is forced to channel along the magnetic field line and fall into the poles of the neutron star. The accumulated matter heats up and forms hot spot. The radius of the hot spot ($\sim 0.1 R_{NS}$) is much smaller compared to the radius of the neutron star (R_{NS}). The area of the accreting spot is of the order of $\sim 1 \text{ km}^2$ (Davidson and Ostriker, 1973). If the magnetic axis and axis of rotation of the neutron star is not aligned, then the radiation from the hot spots sweep the sky in every rotation of the neutron star. As a result we see pulsation mostly in X-rays with a period equal to the spin period of the neutron star. These pulsating neutron stars are called accretion powered pulsar, because the energy they radiate is originated from the accretion of matter onto the neutron star. A cartoon picture of an accretion powered pulsar is given in Figure 1.13.

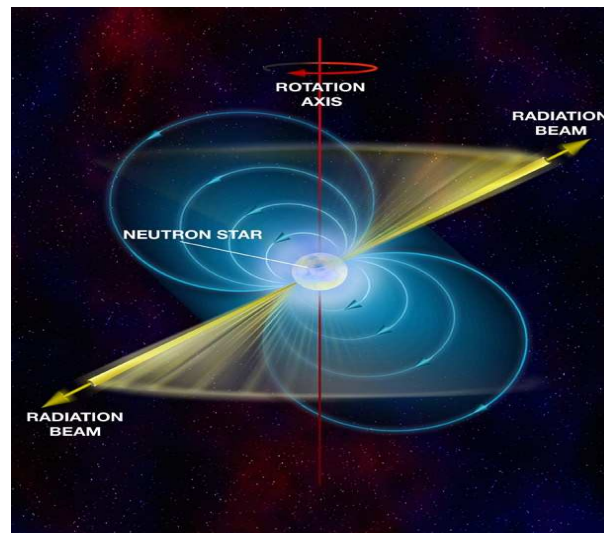


Fig. 1.13 Cartoon picture of an accretion powered pulsar. Misaligned rotation and magnetic axes of the neutron star give a lighthouse kind of effect on earth, whose magnetic axis sweep earth in every rotation of the neutron star. Image courtesy: <https://onwardtotheedge.wordpress.com/2013/01/14/neutron-stars/>

They are also called X-ray pulsars, as most of the energy they emit are in X-rays. The accreting neutron stars are strongly magnetized neutron stars, which are mainly found in young HMXBs. First observed X-ray pulsar is Centaurus X-3 (Cen X-3) discovered in 1967 with a rocket-based detector (Chodil et al., 1967) and later confirmed with Uhuru satellite (Schreier et al. 1972a, Giacconi et al. 1971). X-ray pulsations have been seen in ~ 120 HMXB systems (Coe et al., 2010) most of which are Be XRB pulsar (~ 70 , Reig 2011). Out of ~ 110 LMXB systems (Estrada-Carpenter et al., 2014) only few 10s show X-ray pulsation because of their low magnetic field. Most of the HMXB and LMXB pulsars spin period are found ≥ 100 s and ≤ 10 s respectively. However there are few fast rotating LMXB X-ray pulsars known as milliseconds X-ray pulsars whose spin period are in the range of (1-10) milliseconds.

Accretion disc warps

If the spin axis of the compact object and axis of the accretion disc orbiting the compact object are misaligned, then the accretion disc experiences a torque due to general relativistic effect named as Lense-Thirring effect (Lense and Thirring, 1918). As a result the plane of

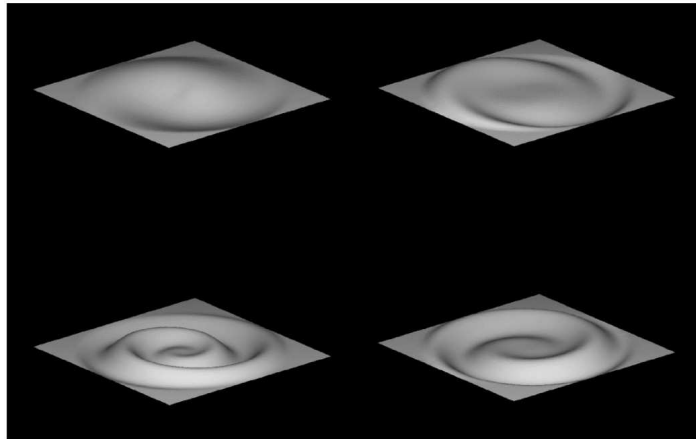


Fig. 1.14 Schematic representation of different types of warping in accretion disc. Image courtesy: Maloney and Begelman (1997).

the disc starts precessing about the spin axis of the compact object. The accretion disc made of plasma experiences differential precession at different radii. This causes to form warps in the accretion disc at different radii.

If the torque is very strong compared to viscous forces between the disc layers then it forces inner accretion disc axis to align with the spin axis of the central compact object. This effect is known as Bardeen-Petterson effect. The accretion disc gets a twisted shape. One possible origin of QPO observed mostly in LMXBs could be twisted disc (Stella et al., 1999). The warps decay due to viscous forces acting at their location. This decay time scale depends upon the strength of viscosity. So in a precessing disc, warps form and decay. Since the disc viscosity is poorly understood, so it is difficult to give proper estimation of warp decay time. However if precession period at the position of the warp is assumed to be of the same order of viscous time scale, then the warp damps in nearly one precession period time scale and if viscous time scale is long then the warp lasts for several precession periods. Simple models of warps in the accretion disc is given in Figure 1.14. Warps interact with direct X-rays emitted from the compact object and reprocess it. It causes appearance of dips in the lightcurve by absorbing direct X-rays of different energies. Variable warp structures can cause variabilities in the X-ray reprocessing properties of a binary system with accretion disc.

Accretion column

In moderate or high magnetic field neutron stars ($\geq 10^8$ Gauss) the accreted plasma is channelled to the neutron star's polar caps by magnetic field lines disrupting the accretion disc at Alfvén radius (Basko and Sunyaev, 1976). The plasma follows a free fall flow with speed $\geq 0.4c$ on the magnetic poles of the neutron star and forms a funnel like structure above the poles, which is called accretion column of the pulsar. The structure of this accretion column depends upon the interaction of plasma with neutron star's magnetic field which is not very well understood. However three types of shapes have been proposed. i) solid ii) hollow iii) spaghetti type. Solid and hollow type of accretion column have been shown in Figure 1.15.

Soft photons from the hot spots get converted to X-rays and γ rays by inverse Compton scattering with the highly energetic free falling plasma. The emission pattern of these high energy photons depends upon the mass accretion rate, hence on the luminosity of the pulsar. For large accretion rate, relativistic inflowing plasma develops a shock front at a distance above the neutron star surface, which makes the accretion column optically thick along the magnetic field lines. So the hard photons can only escape through the side walls of the accretion column perpendicular to the magnetic fields near poles. These beams of photons are named fan beams as they resemble rotating blades of a fan. The critical luminosity above which fan beams form is given by

$$L_{crit} = 2.72 \times 10^{37} \left(\frac{\sigma_T}{\sqrt{\sigma_{\parallel}\sigma_{\perp}}} \right) \left(\frac{r_0}{R} \right) \left(\frac{M}{M_{\odot}} \right) \text{ erg s}^{-1} \quad (1.76)$$

(Basko and Sunyaev, 1976). Where r_0 is the radius of the polar cap, σ_{\parallel} and σ_{\perp} are the energy averaged cross sections for photons scattered in the parallel and perpendicular directions to the magnetic field (Becker, 1998).

For low \dot{M} , $L < L_{crit}$ and the accretion column above the neutron star surface is optically thin. This enables the hard photons to escape the accretion column parallel to the magnetic field lines near poles forming pencil beams. However strong gravity of the neutron star can bend the fan beam, which might appear as pencil beam far away from the neutron star. A simple model of the fan and pencil beam geometry is given in Figure 1.16.

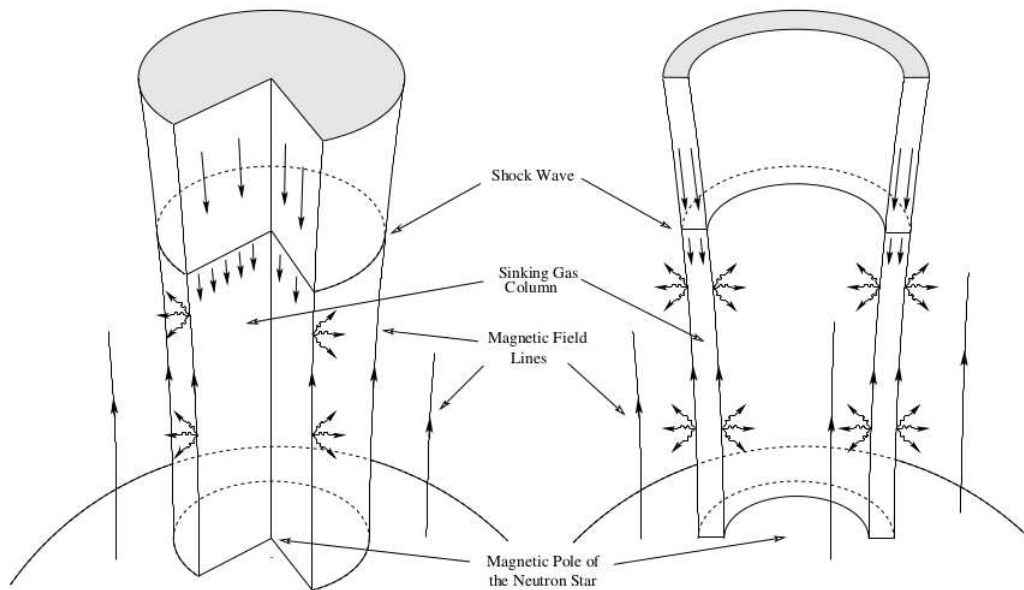


Fig. 1.15 Schematic representation of two geometries (left: solid, right: hollow) of accretion column (Basko and Sunyaev, 1976). Image courtesy: (Basko and Sunyaev, 1976). Image not to scale.

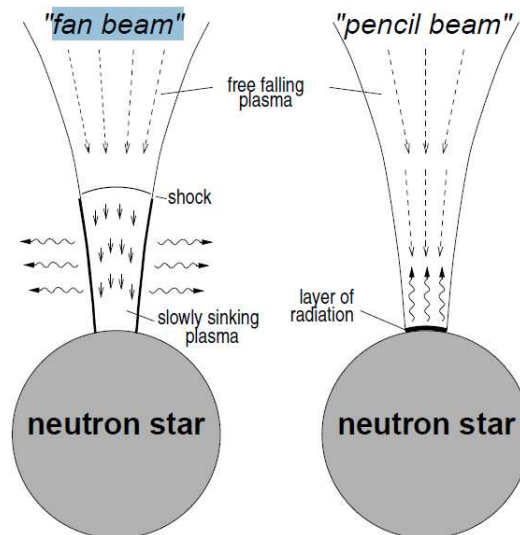


Fig. 1.16 **Left panel:** Fan beam geometry. For high mass accretion rate, photons emitted from the hot spot interacts with the infalling plasma and forms shock. Photons can not penetrate the shock front but escape perpendicular to the accretion column forming shape of a fan. **Right panel:** Pencil beam geometry. When mass accretion rate is low no shock is formed. The photons from the hot spot are emitted parallel to the accretion column, which resembles the shape of a pencil. Image courtesy: Kretschmar (1996)

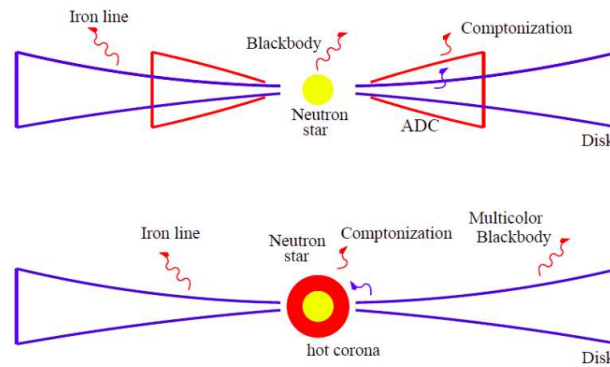


Fig. 1.17 **Top panel:** Accretion disc corona (ADC) above and below the accretion disc. The ADC Comptonize the soft blackbody photons emitted from the neutron star (Western model). **Bottom panel:** ADC surrounding the neutron star upscatters multicolour blackbody photons emitted from the accretion disc. (Eastern model). Image courtesy: (Church and Bałucińska-Church, 2004).

Accretion disc corona

Accretion disc corona (ADC) is diffused envelope of low density matter above and below the accretion disc (or surrounding the neutron star). The composition of ADC is still debated. ADC were first suggested to analyze shallow intensity profile in some LMXBs during eclipses (White and Holt, 1982). X-rays from the compact object irradiate the accretion disc and some of the heated matter of the disc leave the disc and distribute themselves on both the side of the disc as ADC. The corona reprocesses the emission from the compact object which gives rise to residual flux during eclipse (Begelman et al., 1983). There are different models to describe the origin and properties of ADC. Dove et al. (1997) proposes plane parallel or slab geometry on both sides of cold accretion disc. According to their model the maximum self consistent temperature is $\sim 140 \text{ keV}$ with optical depth ≥ 0.2 for a disc temperature $kT_{discBB} \leq 200 \text{ eV}$. Stella and Rosner (1984) suggested ‘magnetic boundary driven’ energy transport produced by the shear in the accretion disc. Magnetorotational instability (MRI) driven time dependent energy transfer from the core of the disc is also suggested to form the hot corona. According to their model the weak magnetic field of the core amplified by the MHD turbulence becomes buoyant and comes out of the disc. A schematic view of ADC according to Western and Eastern model is given in Figure 1.17.

1.5 Emission processes in X-ray binaries:

As matter approaches the compact object, viscous forces between different layers heats it up. The hot plasma radiates. Interacting with electrons of different energies the photons gain or loose energy. Motion of these hot plasma in their Coulomb field and in magnetic field of the accretor (NS or WD) yield electromagnetic radiation. Various emission processes in X-ray binary systems are briefly discussed below.

1.5.1 Thermal emission:

The radiation arises from purely thermal motions of the constituents of a matter is known as thermal emission. Thermal motion implies random movement of particles associated with thermal energy of the system. Thermal energy of a system is directly proportional to its temperature. Higher the temperature, higher is the energy of thermal radiation from a system. For example thermal radiation from hot inner accretion disc peaks in X-rays, while comparatively cooler outer accretion disc emit mostly in optical/UV band. Blackbody radiation is a thermal radiation from a system under some special conditions, which is briefly discussed below.

Blackbody radiation:

When the matter and radiation of a system is in thermodynamic equilibrium then the radiation from the system is known as blackbody radiation, which is described by Planck function (Rybicki and Lightman, 1979)

$$B_{\nu}(T) = \frac{2h\nu^3}{c^2} \frac{1}{e^{\frac{h\nu}{k_B T}} - 1} \quad (1.77)$$

The frequency at which the spectrum peaks depends upon the temperature, which is given by Wein displacement law given by

$$\lambda_{max} T = 5.1 \times 10^{-3} \text{ m K} \quad (1.78)$$

The blackbody emission can be characterized by a mean photon energy

$$E_{BB} = 2.7kT \quad (1.79)$$

1.5.2 Nonthermal emission:

The emission caused by some external effect other than thermal motion of particles is called nonthermal emission. The origin of nonthermal emission could be motion of charged particles in electric (Coulomb) or magnetic field or due to interaction between photons and electrons. All these nonthermal emission processes are briefly discussed below.

Thomson scattering:

In Thomson scattering a photon collides with a stationary or slow moving electron ($v \ll c$) and is scattered without any change of frequency (Rybicki and Lightman, 1979). This kind of elastic scattering occurs when the photon's energy is much less than the rest mass energy of the electron ($h\nu \ll m_e c^2$). This scattering is symmetric with respect to the scattering angle and the scattered radiation is polarized even if the incident beam is unpolarized. Total cross section for Thomson scattering is given by $\sigma_T = 6.653 \times 10^{-29} \text{ m}^2$.

Bremsstrahlung radiation

The radiation from an accelerating charge in the Coulomb field of another charge is known as bremsstrahlung (in German), which means braking radiation. The total power emitted per unit volume per unit frequency ($\frac{\partial P}{\partial \nu \partial V}$) by electrons of charge e^- moving with speed v in the Coulomb field of charge $+Ze$ is given by (Rybicki and Lightman, 1979)

$$\epsilon_v^{ff} = \frac{\partial P}{\partial \nu \partial V} = 2\pi \times \frac{16e^6}{3c^3 m^2 v} n_e n_i Z^2 \ln\left(\frac{b_{max}}{b_{min}}\right) \quad (1.80)$$

Where n_e and n_i are respectively electron and ion density. Depending upon the velocity of the electrons, the value of b_{min} (minimum value of b as shown in Figure 1.18) can have a wide range. To approach the accurate power, a correction factor known as Gaunt factor

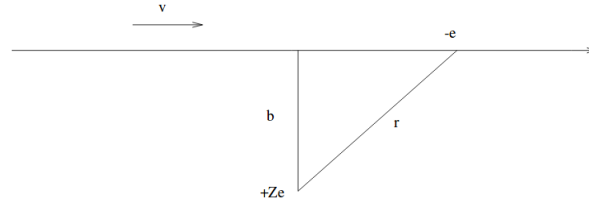


Fig. 1.18 A simple trajectory of an electron passing an ion of charge $+Ze$. b is the shortest distance from the trajectory to the ion. Image courtesy: Rybicki and Lightman (1979)

$(g_{ff}(\nu, w))$ is introduced. So,

$$\epsilon_{\nu}^{ff} = 2\pi \times \frac{16\pi e^6}{3\sqrt{3}c^3 m^2 \nu} n_e n_i Z^2 g_{ff}(\nu, w) \quad (1.81)$$

Where

$$g_{ff}(\nu, w) = \frac{\sqrt{3}}{\pi} \ln\left(\frac{b_{max}}{b_{min}}\right) \quad (1.82)$$

Thermal bremsstrahlung

If the electrons have a thermal distribution of speeds, then the radiation is called thermal bremsstrahlung and the power is given by (Rybicki and Lightman, 1979)

$$\epsilon_{\nu}^{ff} = \frac{2^5 \pi e^6}{3mc^3} \left(\frac{2\pi}{3km}\right) T^{-1/2} Z^2 n_e n_i e^{-h\nu/kT} \bar{g}_{ff} \quad (\text{erg s}^{-1} \text{ cm}^{-3} \text{ Hz}^{-1}) \quad (1.83)$$

$\bar{g}_{ff} = \bar{g}_{ff}(T, \nu)$ is an velocity averaged Gaunt factor.

The total power per unit volume (ϵ_{ν}^{ff}) emitted in thermal bremsstrahlung process is given by

$$\epsilon_{\nu}^{ff} = \frac{dP}{dV} = \sqrt{\frac{2\pi kT}{3m}} \frac{2^5 \pi e^6}{3mhc^3} Z^2 n_e n_i \bar{g}_B \quad (1.84)$$

$\bar{g}_B = \bar{g}_B(T)$ is the frequency average of the velocity averaged Gaunt factor.

$$\epsilon_{\nu}^{ff} = 1.4 \times 10^{-27} T^{1/2} n_e n_i Z^2 \bar{g}_B \quad (\text{erg s}^{-1} \text{ cm}^{-3}) \quad (1.85)$$

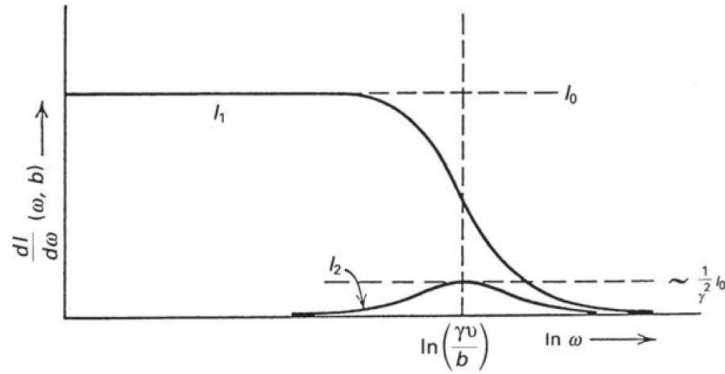


Fig. 1.19 The bremsstrahlung spectrum of an electron beam. Top graph: acceleration of the electrons are parallel to its initial velocity. Bottom graph: acceleration of the electrons are perpendicular to its initial velocity. Image courtesy: Jackson (1975).

Figure 1.19 gives bremsstrahlung spectrum for a beam of electrons accelerating parallel and perpendicular to its initial velocity. Bremsstrahlung radiation is observed in Radio emission from HII regions, from ionized winds and jets, X-ray emission from clusters of galaxies.

Compton scattering:

Compton scattering is an inelastic scattering of a photon by an electron where the electron gains energy from the photon (Rybicki and Lightman, 1979). This occurs when the incident photon's energy is greater than the electron's rest mass energy ($h\nu > m_e c^2$). The increase of wavelength of the photon upon losing its energy can be written as

$$\lambda' - \lambda = \lambda_c (1 - \cos\theta) \quad (1.86)$$

where λ and λ' are the wavelength of the incident and the scattered photon respectively. The Compton length $\lambda_c = \frac{h}{m_e c} \sim 2.43 \times 10^{-10}$ cm. If $\lambda \ll \lambda_c$ then the photon's energy loss is negligible and the regime turns to Thomson scattering.

Inverse Compton scattering:

In inverse Compton scattering, a relativistic electron collides with a low energy photon, which is scattered with higher energy than before. In this process the electron loses its kinetic energy to photon. Average energy of the photon per scattering upon colliding with an electron is given by (Rybicki and Lightman, 1979)

$$\left\langle \frac{\Delta E_\gamma}{E_\gamma} \right\rangle = \frac{4k_B T_e - h\nu}{m_e c^2} \quad (1.87)$$

Where T_e is the electron's temperature given by $T_e = \frac{m \langle v^2 \rangle}{3k_B}$ (Obtained from equating mean energy per particle in 3 degrees of freedom to the electron's kinetic energy).

If $h\nu > 4k_B T_e$, then the photons loses energy to the electron (Compton effect)

For $h\nu = 4k_B T_e$, photons energy does not change (Thomson scattering)

When $h\nu < 4k_B T_e$, the photon gets upscattered gaining energy from the electron (Comptonization)

In inverse Compton scattering, the photon upon colliding with an ultrarelativistic electron, is scattered with frequency

$$\nu_{out} \propto \gamma^2 \nu_0 \quad (1.88)$$

where $\gamma = (1 - \beta^2)^{-1/2}$ and $\beta = \frac{v}{c}$. v is velocity of the electron.

The maximum frequency of the upscattered photon is

$$\nu_{max} \approx 4\gamma^2 \nu_0 \quad (1.89)$$

and the average frequency of the upscattered photons is

$$\langle \nu \rangle = \frac{4}{3} \gamma^2 \nu_0 \quad (1.90)$$

This upscattering of lower energy photons can convert a radio photon to UV (ultraviolet), a far IR (Infrared) photon to X-ray and an optical photon to γ ray photon in astrophysical sources like X-ray binaries and active galactic nuclei (AGN).

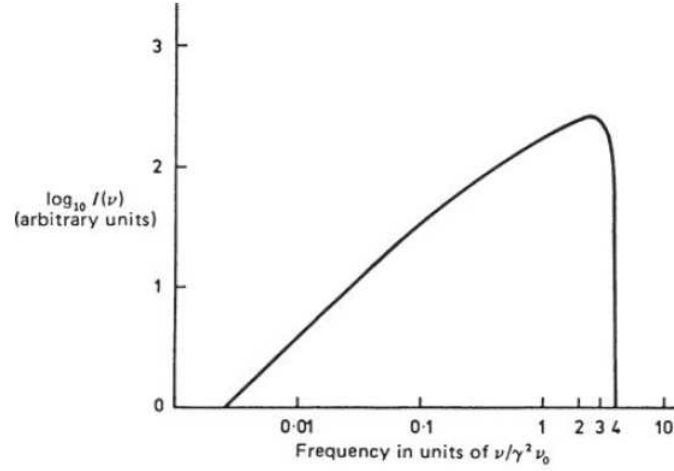


Fig. 1.20 The emission spectrum for inverse Compton scattering. ν_0 is the frequency of the photons before collision with the high energy electrons. Image courtesy: Blumenthal and Gould (1970)

The average power emitted from an isotropic distribution of electrons in single scattering with an isotropic distribution of photons is given by

$$P_{comp} = \frac{4}{3} \sigma_T c \gamma^2 \beta^2 U_{ph} \left[1 - \frac{63}{10} \frac{\gamma \langle \epsilon^2 \rangle}{mc^2 \langle \epsilon \rangle} \right] \quad (1.91)$$

U_{ph} is the photon energy density. The total power from such medium is

$$P_{Tot} = \left(\frac{4k_B T_e}{m_e c^2} \right) c \sigma_T n_e U_{ph} \quad (\text{erg s}^{-1} \text{ cm}^3) \quad (1.92)$$

This process is very effective in cooling plasma. The time scale of Compton cooling of relativistic electrons is given by

$$t_{cc} = \frac{\gamma m_e c^2}{P_{comp}} \quad (1.93)$$

P_{comp} is radiated power per unit volume. For nonrelativistic electrons

$$t_{cc} = \frac{k_B T_e}{P_{comp}} \quad (1.94)$$

The Comptonization goes on, till the photon's energy increases to $4k_B T_e$. One astrophysical example of inverse Compton scattering is Sunyaev-Zeldovich (SZ) effect, in which cosmic

microwave background (CMB) photons are upscattered by hot ($T_e \sim 10^8 K$) electrons in the intracluster gas.

Compton y parameter gives the significance of energy change of photons in a finite thermal medium, which is defined by

$y = (\text{average fractional energy change per scattering}) \times (\text{Mean number of scattering})$

It can be expressed by (Rybicki and Lightman, 1979)

$$y = \frac{k_B T_e N_s}{m_e c^2} \quad (1.95)$$

Where N_s is the number of scattering. For significant change of energy of photons, $y = \frac{1}{4}$. Due to repeated scattering, photon spectrum evolves. It is expressed by Kompaneet's equation.

$$\frac{\partial n}{\partial t_c} = \left(\frac{k_B T_e}{m c^2} \right) \frac{1}{x^2} \frac{\partial}{\partial x} [x^4 (n' + n + n^2)] \quad (1.96)$$

where t_c (mean time between scattering) = $(n_e \sigma_T c) t$, n is photon density and $x = \frac{h\omega}{k_B T}$. An emission spectrum for inverse Compton scattering is given in Figure 1.20.

Synchrotron Radiation

When a relativistic charged particle moves in a magnetic field at an angle with the field, then the particle moves in a helical path and radiates. This radiation is known as synchrotron radiation and in non relativistic regime this is called cyclotron radiation. The power emitted by an electron moving with velocity βc in a medium with magnetic energy density U_B (Rybicki and Lightman, 1979) is given by

$$P = \frac{4}{3} c \sigma_T \beta^2 \gamma^2 U_B \quad (1.97)$$

The total power, per unit volume per unit frequency emitted by a number of electrons having a distribution of velocities can be given by the relation

$$P_T(\omega) \propto \omega^{(p-1)/2} \quad (1.98)$$

Where $\omega = 2\pi\nu$ and ν is the frequency of radiation, p is the particle distribution index associated with particles density distribution, $(p-1)/2$ is the spectral index of radiation.

Neutron star's high magnetic field ($\geq 10^{12}$ Gauss) generates synchrotron emission from radio to γ rays. A synchrotron photon can be absorbed by another electron or any other charge in the system. This absorption process is known as synchrotron self absorption. The source function (S_ν , ratio of the emission to the absorption coefficient) for a power law distribution of particles is given by

$$S_\nu \propto \nu^{5/2} \quad (1.99)$$

The observed intensity of synchrotron emission from a optically thin medium has been found to be proportional to the emission function ($\propto \nu^{(p-1)/2}$) and for optically thick medium it is proportional to the source function ($\propto \nu^{5/2}$). The synchrotron spectrum from a power law distribution of electrons are given in Figure 1.21. More self absorption occurs in an optically thick medium. Hot electrons in the plasma upscatter the synchrotron photons, this process is known as synchrotron self-Compton. If in a source, synchrotron self-Compton dominates, then the source appears to be X-ray bright.

The synchrotron radiation is elliptically polarized. But this radiation from a distribution of particles which varies smoothly with pitch angle (the angle between the direction of magnetic fields and the particle's initial velocity into the magnetic field) are partially linearly polarized. For particles with power law distribution of energies ($N(E)dE = CE^{-p}dE$, $E_1 < E < E_2$), the degree of polarization is given by (Rybicki and Lightman, 1979)

$$\Pi = \frac{p+1}{p+\frac{7}{3}} \quad (1.100)$$

C and p are positive constants specific to the distribution.

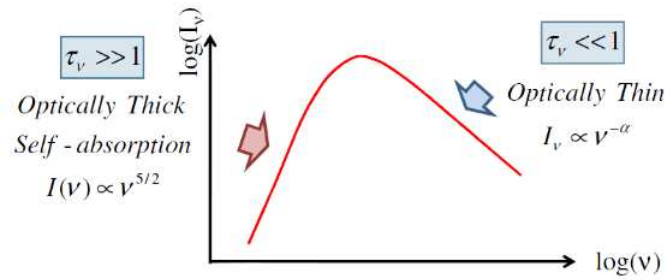


Fig. 1.21 Synchrotron spectrum of electrons with a power law distribution ($\alpha = -\frac{p-1}{2}$). Image courtesy: Lecture Slides (astro.caltech.edu)

1.5.3 Cyclotron Resonant Scattering Feature (CRSF)

In neutron star's magnetic field, the electrons in the accreted plasma gyrate with specific energies. These energy levels are called Landau levels. If an incident photon's energy is equal to the difference between two Landau levels, then the photon is absorbed by the electron at lower Landau level and the electron attains the energy of the next Landau level. This absorption is reflected in the X-ray spectra of many accretion powered pulsars. The feature is called Cyclotron Resonant Scattering Feature (CRSF) (Harding and Daugherty 1991 and references there in). This Resonant Scattering occurs near the magnetic pole of the neutron star. These features are very powerful tool to estimate the magnetic field near the pole of accretion powered pulsars. Cyclotron line centroid energy can be expressed as

$$E_{CRSF} = 11.6 \times \frac{B_{12}n}{(z+1)} \text{ keV} \quad (1.101)$$

B_{12} is the magnetic field strength in units of 10^{12} Gauss, n is the number of Landau level, z is the gravitational redshift at the origin of this line. $n = 1$ denotes fundamental cyclotron line, while $n > 1$ refers to its harmonics. For example, fundamental cyclotron line from a region ($z = 0$) with magnetic field strength $\sim 10^{12}$ Gauss will be ~ 11.2 keV, while its second and third harmonic would be ~ 22.4 keV and ~ 33.6 keV respectively. Figure 1.22 shows CRSF in the spectrum of HMXB pulsar Her X-1.

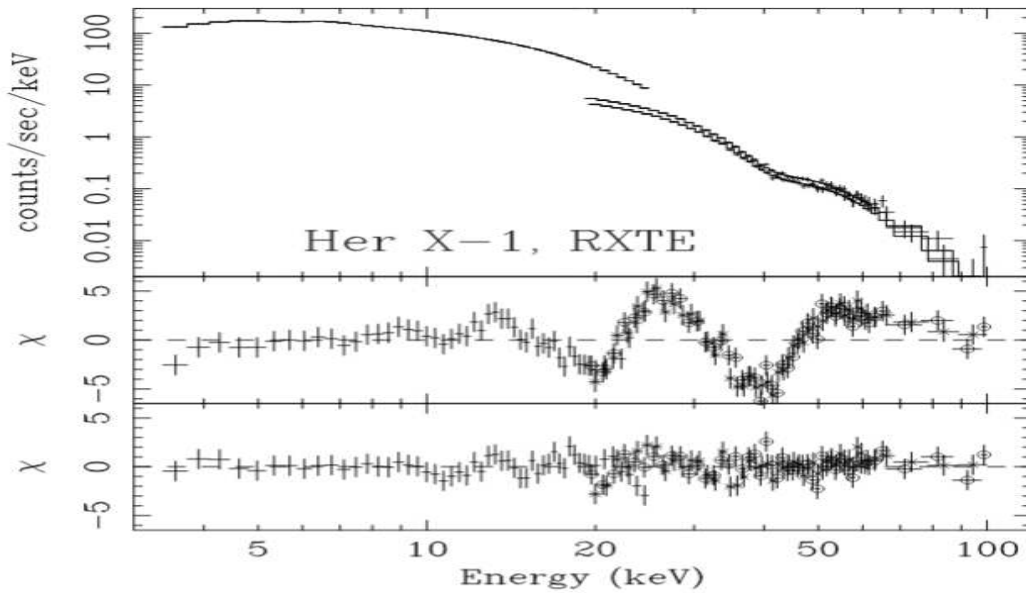


Fig. 1.22 Cyclotron Resonant Scattering Features (CRSF) in RXTE spectrum of Her X-1

1.6 Variabilities in X-ray binaries

Both the HMXB and LMXB systems are observed to be variable in time scales of seconds to decades. Some variabilities are periodic and some are not periodic. Some of the non-periodic variabilities can be predicted with a margin of time scale and some can not be predicted at all. In this thesis we have found variabilities in some of the systems. So a brief discussion of periodic and non-periodic variabilities is given below.

1.6.1 Periodic variability

Periodic variabilities have been observed in X-ray binaries from millisecond (ms) to month time scales.

Pulsation

In a high magnetic field neutron star, the accreting matter is channelled to its magnetic poles and forms accretion column with electron energy of 10s of keV , which emit mainly in X-rays. The cross section of the X-ray bright accretion column is known as hot spots. For the neutron stars with magnetic axis tilted from its rotation axis, the hot spot appears to

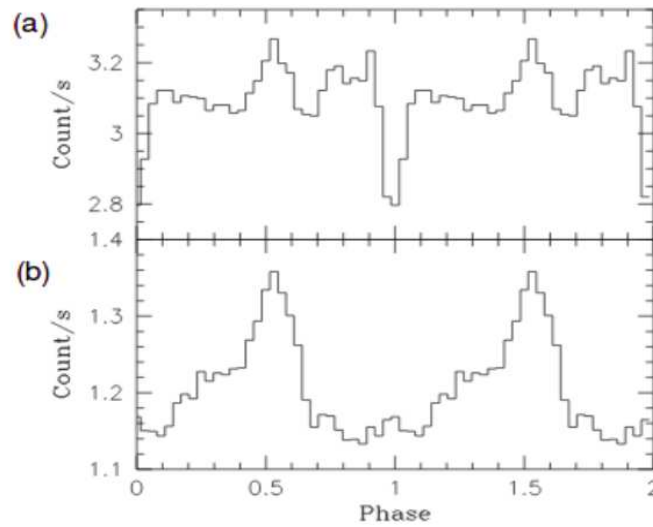


Fig. 1.23 Energy dependent pulse profile of HMXB pulsar GX 1+4. Top: Pulse profile in (1.5-3) keV energy band. Bottom: Pulse profile in (30-40) keV energy band. Image courtesy: Doty et al. (1981)

move in and out with a period equal to the neutron star's spin. This variation is known as pulsation and the period is known as the pulse period, because the intensity variation of the emission with respect to time appears like a pulse. This pulsation can only be seen from earth if the magnetic axis of a pulsar sweeps the earth. Pulse period is shorter in LMXBs compared to HMXBs. It can be as low as milliseconds. For example LMXB IGR J17062–6143 has a pulse period of 6 ms (Strohmayer and Keek, 2017). HMXBs 2S 0114+650 and 4U 2206+54 have pulse period of 9600 s and 5560 s respectively (Wang and Chang, 2013). The luminosity variation during a pulse period is understood with the help of pulse profiles, which is an average lightcurve of a source folded with its pulse period (to be discussed in details in the next chapter). In most of the systems the pulse profiles are observed to depend upon the emission energy and the source luminosity. Figure 1.23 shows variations in the pulse profile of HMXB pulsar GX 1+4 with emitted energy (Doty et al. 1981, Greenhill et al. 1998).

The pulse profiles are very helpful tool to understand the geometry of the accretion column and beaming pattern. Change of pulse periods has been observed in many neutron star X-ray binaries. The rate of change of pulse period (\dot{P}) is related to the X-ray luminosity (L) and other intrinsic properties of the neutron star (Ghosh and Lamb, 1979). \dot{P} can be

expressed as

$$\dot{P} = -5.0 \times 10^{-5} \mu_{30}^{\frac{2}{7}} n(\omega_s) S_1(M) P^2 L_{37}^{\frac{6}{7}} \text{ s yr}^{-1} \quad (1.102)$$

Where μ_{30} is magnetic dipole moment in units of $10^{30} \text{ Gauss cm}^3$; L_{37} is the source luminosity in units of $10^{37} \text{ erg cm}^{-2}$; ω_s is the fastness parameter, defined as the ratio of the angular frequency of the pulsar to that of the accreting matter. $n(\omega_s)$ is a function of ω_s and $S_1(M)$ is a function of mass and radius of the neutron star.

Orbital intensity modulation

The compact object and its companion rotate about their common center of mass. The observed X-ray intensity appears to have a modulation with a period equal to the orbital period of the system. This modulation comes from the scattering and absorption of X-rays from the accretion disc, accretion stream and/or companion's wind with orbital phase dependent morphology. The orbital period of a binary system is given by (Frank et al., 2002)

$$P = \sqrt{\frac{4\pi^2 a^3}{GM}} \quad (1.103)$$

Where $M = M_{CS} + M_{NS}$, M_{CS} and M_{NS} are respectively mass of the companion and the neutron star, 'a' being the binary separation. Due to compact orbit LMXBs have short orbital period, ranging from minutes to days. For example LMXB 4U 1543-624 has orbital period of 18.2 minutes (Wang and Chakrabarty, 2004) and GRO J1744-28 has orbital period of 11.8 days (Finger et al., 1996). HMXBs have wider orbit and hence longer orbital period, from few days to months. For example LMC X-4 and Be 4U 1145-619 have orbital period of 1.41 days (Chevalier and Ilovaisky, 1977) and 187 days (Warwick et al., 1985) respectively. However there are few exceptions, like HMXB Cygnus X-3 has short orbital period of 4.7 hours (Ghosh et al., 1981). Long orbital period X-ray binaries usually have eccentric orbit. Due to tidal interaction between the compact object and its companion, the eccentricity decreases and the orbit tends to be circular (Sepinsky et al., 2007).

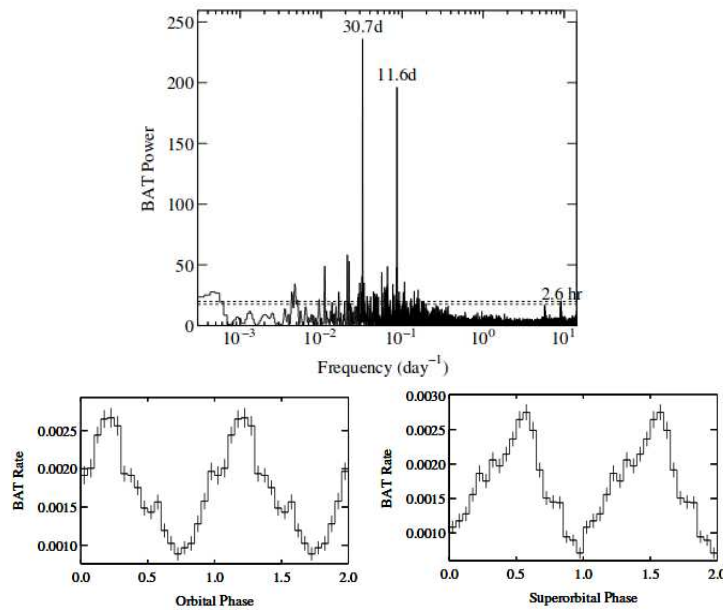


Fig. 1.24 **Top Panel:** Power spectrum of *Swift*–BAT lightcurve of 2S 0114+650. Stronger peak corresponds to superorbital period of 30.7 days. Orbital period of the source is 11.6 days. **Bottom left panel:** *Swift*–BAT lightcurve of 2S 0114+650 folded with its orbital period **Bottom right panel:** Lightcurve folded with superorbital period. Image courtesy: Corbet and Krimm (2013)

Superorbital intensity modulation

A periodicity larger than the orbital period has been observed in some X-ray binaries. This period is known as superorbital period of these systems. More than 35 systems have been found with superorbital periods. The modulation is stable in Her X–1, LMC X–4, Cygnus X–1, SS 433 (Wen et al., 2006). SMC–1 switches between two stable superorbital periods of ~ 40 days and ~ 65 days respectively (Trowbridge et al. 2007, Hu et al. 2011). LMXB GRS 1758–258 has a superorbital period of 600 days, whose orbital period is 18 days (Smith et al., 2002). There are few systems with very short orbital period but long superorbital period. For example 4U1820–303 and 4U 1916–053 have orbital, superorbital period of (0.008 days, 176 days) and (0.035 days, 199 days) respectively (Ogilvie and Dubus, 2001). Power spectrum of *Swift*–BAT lightcurve of 2S 0114+650, an unusual HMXB system shows (Top panel of Figure 1.24) peaks corresponding to superorbital period (30.7 d) along with that of orbital period (11.6 d). Figures in the bottom panel of Figure 1.24 gives the *Swift*–

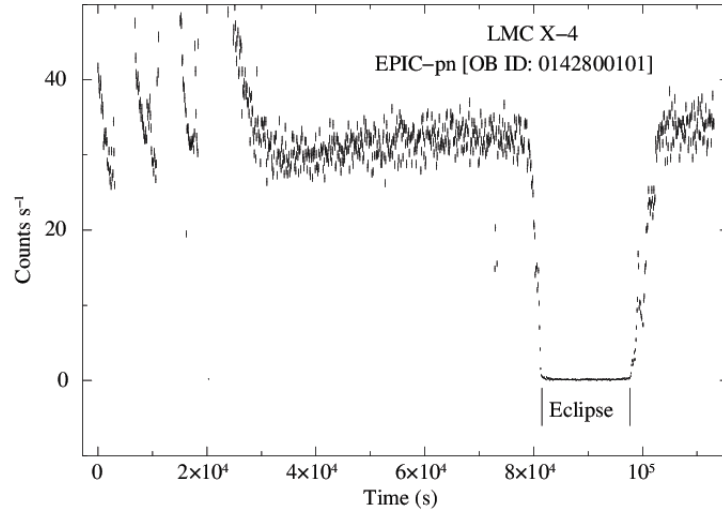


Fig. 1.25 0.3-10 keV *XMM Newton* EPIC-pn lightcurve of LMC X-4 with eclipse in the duration shown by two solid lines. Image courtesy: (Aftab and Paul, 2018)

BAT lightcurve of 2S 0114+650 folded with superorbital and orbital period respectively (Corbet and Krimm, 2013). The cause of superorbital intensity modulation could be due to 1) precession of accretion disc (Priedhorsky et al., 1983) or jets (Romero et al., 2002), 2) tidal forces exerted on the tilted disc by the companion star (Katz, 1973). 3) interaction with a third body (Sood et al., 2007)

Eclipse

Some of the X-ray binary systems show X-ray eclipses in which the direct emission from the compact object is blocked by the companion or absorbed by the outer accretion disc structure in every orbit. The X-ray intensity goes down during eclipse. The probability of occurrence of eclipse for a tilted binary inclination can be given by the ratio between solid angle made at compact object by the companion in its orbital cycle and 4π (4π = total solid angle around compact object).

$$P_{eclipse} = \frac{\pi R_c^2 / r}{4\pi} = \frac{R_c^2}{4r} \quad (1.104)$$

Where R_c is the radius of the companion and r is the distance between the compact object and its companion. Smaller the size of the orbit, greater is the probability. In terms of the

orbital period of the binary, the probability can be expressed as,

$$P = 0.19 \left(\frac{R_c}{R_\odot} \right) T^{-\frac{2}{3}} \left(\frac{M_c}{M_\odot} \right)^{\frac{1}{3}} \quad (1.105)$$

Where R_\odot and M_\odot are respectively the radius and mass of the Sun. T is the orbital period of the binary in days. Longer period binaries have less chance for the occurrence of the eclipse, compared to the binaries with similar mass and radius of the companion star but with shorter orbital periods. As mass and the radius of the companion increases, the chance becomes more. So more number of HMXBs show eclipses compared to LMXBs. The probability of occurrence of eclipses increases with the binary inclination. With inclination of $50 \leq i \leq 90$, most of the HMXBs show eclipses, LMXBs typically show eclipses above ~ 75 degrees of inclination. Till now X-ray eclipses have been seen in nearly 16 HMXBs and 8 LMXBs. Cen X-3, 4U153-522 are the examples of eclipsing HMXB systems and HerX-1, EXO 0748-676 are the LMXBs which show X-ray eclipses. Accurate orbital period can be measured with the help successive mid eclipse timings. Eclipsing binaries are excellent tools to investigate orbital parameters and X-ray reprocessing studies. Figure 1.25 shows eclipse in *XMM Newton* EPIC-pn lightcurve of LMC X-4 (Aftab and Paul, 2018).

Periodic outburst in Be X-ray Binaries

In Be XRB systems as discussed in section 1.1.1, the compact object accretes matter from the Be star's disc once in every orbit. The increased mass accretion rate causes a type I X-ray outburst, which gets reflected in the lightcurve of these systems. The recurrence period of these bursts is equal/nearly equal to the orbital period of the system. Figure 1.29 shows these periodic type I bursts in Be XRB A0535+262.

1.6.2 Nonperiodic variabilities:

Different types of nonperiodic variabilities have been observed in both the HMXBs and LMXBs in time scales of seconds to decades. These variabilities are discussed in details below.

Quasi Periodic Oscillation (QPO):

X-ray Power Density Spectrum (PDS, described in details in section 2.6.1 of the next chapter) of a neutron star or a black hole binaries show one or more additional peaks other than that for orbital period. The sharpness of these features are measured by a quality factor (Q), which is defined as the ratio between the central frequency of the feature and its Full Width at Half Maximum (FWHM).

$$Q = \frac{\nu_0}{FWHM} \quad (1.106)$$

The feature for which $Q > 2$, is known as Quasi Periodic Oscillation (QPO). Broader features are considered as noise. The strength of a QPO feature is the area under the QPO feature in the normalised PDS.

In case of neutron star XRBs the frequency of QPO can be greater or smaller than pulsar spin frequency. Low frequency QPOs (LFQPOs) have been observed between few mHz to $\sim 30 Hz$ in BH XRBs and upto $\sim 60 Hz$ in NS XRBs. High frequency QPOs (HFQPOs) are seen in (100-500) Hz range in BH XRBs and from few hundred Hz to more than 1 kHz in NS XRBs. The origin of QPOs is still not clear. Several models have been proposed. One possible reason of the occurrence of LFQPOs could be due to oscillation of incoming matter in transitional layer near the compact object (Titarchuk and Osherovich, 2000). HFQPOs could arise because of some relativistic effect on the orbital motion (Stella et al., 1999) or it could arise due to resonance between different frequencies in matters in the accretion stream (Abramowicz and Kluźniak 2001, Abramowicz et al. 2004, Kato 2005, Kato 2004). The frequency of QPOs has been found to be related with magnetic field, luminosity and spectral state of the source (Alpar and Shaham 1985; van der Klis 1989).

Off-states

Off-states are very low intensity states found in accreting systems, where the X-ray luminosity of the source drops by several factors, so that the source becomes totally/almost undetectable by an X-ray instrument. The exact origin of off-states is not yet very clear. It

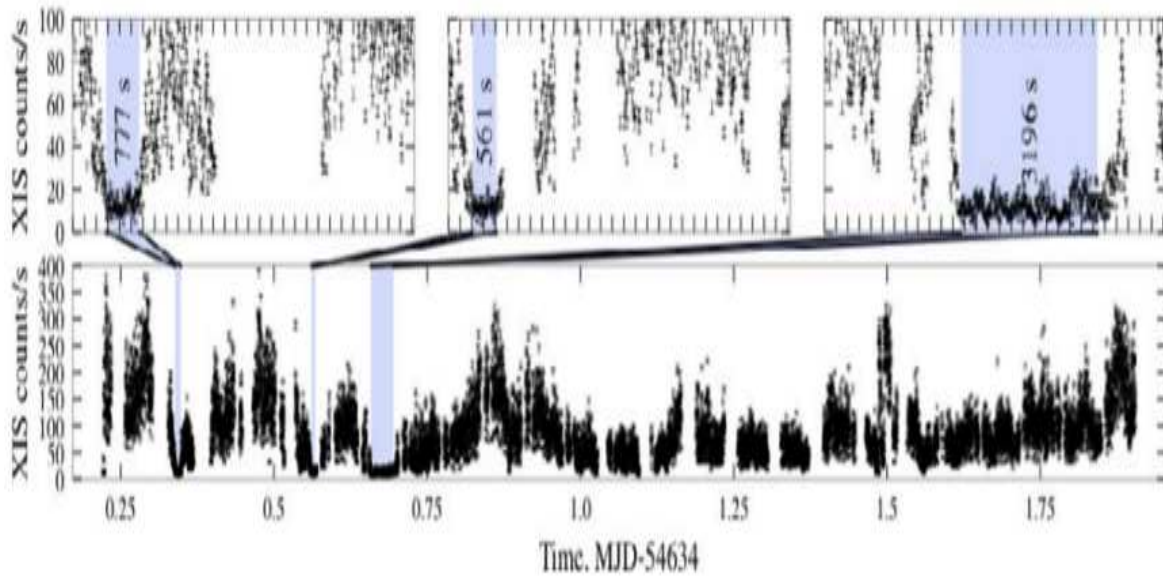


Fig. 1.26 Three off-states have been detected in the 0.4–12 keV *Suzaku* XIS lightcurve of Vela X–1 (Doroshenko et al., 2011). Top panel shows zoomed view of the off-states. Image courtesy: Doroshenko et al. (2011)

could be due to various reasons, such as transition from accretion regime to inhibition or propeller regime; accretion from low density wind blob/blobs; hydrodynamic instabilities near the neutron star magnetosphere etc. The nature of the off-states and hence its origin changes from source to source and can also be different for a particular source at different epochs. Figure 1.26 shows three off-states in the *Suzaku*-XIS lightcurve of Vela X–1 (Doroshenko et al., 2011).

Dips

Few LMXBs show a sudden decrease of the source intensity. This feature is known as dip. Absorption of direct emission from the compact object by the structures in the accretion disc is thought to be one of the cause of dipping features. The dips are observed to be both periodic and aperiodic in nature. Figure 1.27 shows dips in the *XMM-Newton* EPIC-pn lightcurve of EXO 0748–676. A total of ten dipping sources are known so far.

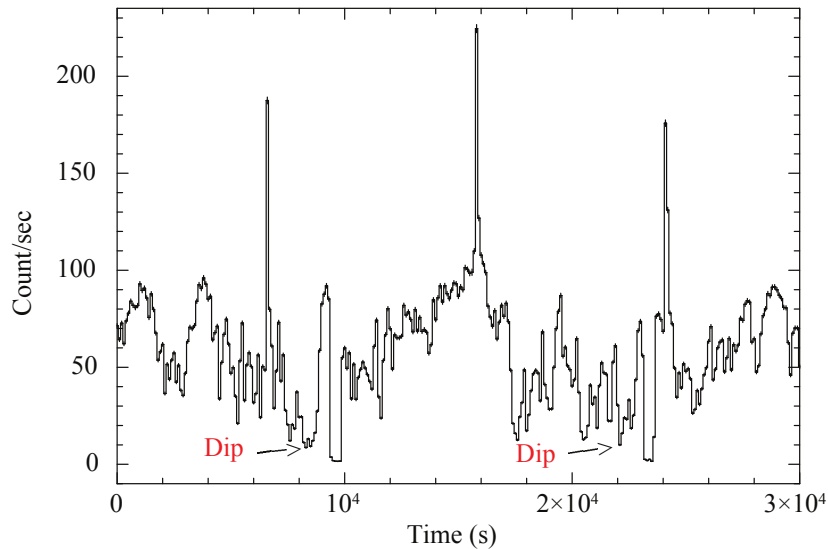


Fig. 1.27 0.3-10 keV *XMM Newton* EPIC-pn lightcurve of EXO 0748–676. The dip in the lightcurve is shown with the arrow. Image courtesy: (Aftab and Paul)

Burst

In low mass X-ray binaries, aperiodic X-ray bursts have been observed in which X-ray luminosity rises very fast but declines slowly. In low magnetic field neutron stars spiraling accretion disc deposits accreting material on its surface. The nature of the accreting material depends upon the evolutionary stage of the companion. As more matter piles up, the density, pressure and temperature increases at deeper layers and finally it triggers nuclear reactions of H/He or both. These reactions produce large amount of heat, the radiation from which peaks in the X-rays and hence type-I X-ray bursts occur, which was first explained by Grindlay et al. (1976) and Belian et al. (1976). It is more likely that, ignition takes place locally and the resulting flame propagates through the surface of the neutron star, which may spread all over the surface or spread on a significant fraction of it. The unstable burning propagates rapidly and releases energy very fast. Once the energy is released, the neutron star accumulates new fluids and similar process results into recurrent type-I X-ray bursts. The interval between any two type-I X-ray bursts mainly depends on the mass accretion rate and nature of the accreting matter (pure He/ mixture of H and He/ some other combination depending on the type of the companion star). Generally it has been observed to occur in intervals of few hours to few days. The burst profiles of type-I X-ray bursts show rapid rise

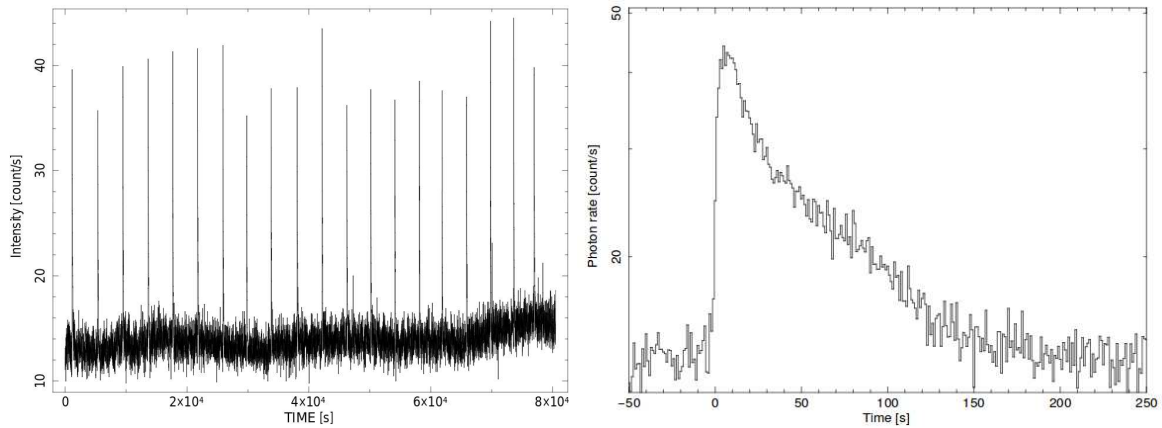


Fig. 1.28 **Left panel:** Chandra lightcurve shows 20 type-I X-ray bursts from MXB 1730–335 (known as a rapid burster). The recurrence times of the bursts are in the range of (0.9–1.2) hr (in ’t Zand et al., 2017). **Right Panel:** Average lightcurve of these 20 X-ray bursts. The flux scale is logarithmic. Image courtesy: in ’t Zand et al. (2017)

in fraction of a second to few seconds, which lasts for 1–10 seconds and decline in ~ 10 seconds to ~ 100 seconds. In two of the neutron star LMXBs (MXB 1730–335 and GRO 1744–28) type-II X-ray bursts have been observed, in which X-ray intensity rises and falls abruptly with no gradual decay pattern. These bursts are thought to cause due to sudden increase of mass accretion rate. Left panel of Figure 1.28 shows 20 type-I X-ray bursts in the Chandra lightcurve of MXB 1730–335 and the right panel of this Figure shows average lightcurve of those 20 X-ray bursts (in ’t Zand et al., 2017). Figure 1.29 shows both type-I and type-II X-ray bursts in Be XRB A0535+262 (Paul and Naik, 2011b).

1.7 X-ray reprocessing in X-ray binaries

In X-ray binaries, X-rays originate in the inner accretion disc (in case of disc accretion) or from the pole of the neutron star in case of pulsars or from the interface of magnetosphere and companion’s wind. These X-rays are called primary X-rays. Some part of these X-rays come out of the system directly. But a significant fraction interacts with the surrounding matter. After interaction these X-rays leave the system with same or lower energies than the original X-rays before interaction. This phenomenon is known as X-ray reprocessing in X-ray binary systems and the secondary X-rays are called reprocessed X-rays. The interaction

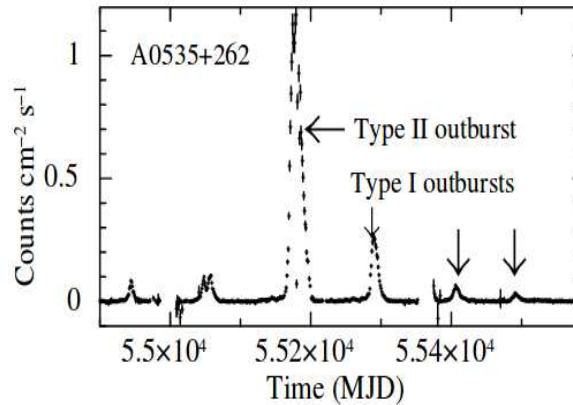


Fig. 1.29 15-50 keV *Swift*-BAT lightcurve shows both type I and type II X-ray bursts in Be XRB A0535+262. The bursts are shown with the arrow (Paul and Naik, 2011b). Image courtesy: Paul and Naik (2011b)

of primary X-rays with the surrounding matter can be of different types. For example low energy X-rays upon colliding with very low energy electrons come out with same energy as it had before the interaction. Higher energy X-rays interact with lower energy electrons, give off some of their energy to the electrons via Compton scattering and come out as lower energy X-rays. Moderate energy X-rays get upscattered by relativistic electrons and gain energy. Some X-rays interact with ionized or neutral atoms, excite electrons and give rise to different spectral lines. The X-ray reprocessing characteristics as seen from the earth depends upon several factors, some of which are discussed below.

i) Density and distribution of matter around the compact object.

If the compact object is embedded in the dense wind of the companion star, then the primary X-rays encounter more number of scattering which results into greater reprocessing. This is common in SgHMXB systems. Wind outflow from supergiant stars is not homogeneous. Often the wind contains clumps of different densities and sizes and intra-clump region is filled with rarefied wind materials. In this case X-ray reprocessing varies with the distribution of matter around the compact object. If the primary X-rays are reprocessed in the rarefied wind then less number of primary X-rays get chance to interact with matter

hence less reprocessing occurs. This can also happen in some LMXB system with red giant companion.

ii) Structures in the accretion disc.

Accretion disc is the main reprocessing agent in LMXBs. Accretion disc also exists in some HMXB systems (Cen X-3, LMC X-4, SMC X-1: Savonije 1978; van der Meer et al. 2007). Often some structures (warps, discussed in section 4.3.1) form and decay in the accretion disc. The structures can differ in density, temperature, shape etc. and faces different solid angle to the primary radiation. The structures evolve with time. These gives variation in the X-ray reprocessing.

iii) Orbital phase of the system.

In the time scale of one binary orbit our line of sight crosses different phase of the orbit (in case of inclined systems). A binary system with inhomogeneous wind or with twisted disc, the direct X-rays traverse medium of different characteristics (density, temperature, spatial extent etc.) and hence get reprocessed differently, which shows variation in the X-ray reprocessing characteristics of the system.

iv) The chemical composition and ionization levels of the matter around the compact object.

The matter surrounding the compact object, whether wind or accretion disc is gained from the companion star. So large fraction of the matter contains hydrogen and helium. But depending upon the evolutionary stage of the companion star, the matter can have materials like carbon; oxygen; silicon; iron etc. Their interaction with the primary X-rays depends upon their ionization state (which depends upon temperature), hence these materials reprocess the primary X-rays differently which often reflected in the X-ray spectra as specific

spectral lines.

- v) The viewing angle of the observer.

For face on systems the X-ray reprocessing is expected to show less variation. As for these systems we receive direct X-rays all the time except when these are heavily absorbed by dense wind clumps. For edge on systems the X-ray reprocessing is most dynamic.

1.7.1 X-ray reprocessing and binary eclipse connection

Primary X-rays come out of the system directly, when they do not face any obstacle. In this condition the detected X-rays are a mixture of primary and reprocessed X-rays. But during eclipse the primary X-rays are blocked by the companion and the X-rays we receive are the reprocessed X-rays only. Analysis of these reprocessed X-rays can help us to trace the process of interaction of their parent X-rays (i.e. the primary X-rays from which the secondary X-rays originated upon interaction) with the surrounding matter. Hence open the door to characterize the binary environment in much more efficient way compared to the out-of-eclipse phase. In this thesis we have studied X-ray reprocessing in a number eclipsing HMXB and LMXB systems, details of which are given in Chapter 3 and 4.

1.7.2 Reprocessed spectra during eclipse and spectral line

In normal condition, when the source is not eclipsed then the spectrum is a combination of direct and reprocessed spectrum. The X-ray spectrum obtained during eclipse is the pure reprocessed X-ray spectrum. The intensity of the reprocessed X-rays is expected to be smaller by a factor of a few, because of the absence of direct X-ray photons. This factor depends upon the source luminosity, inclination of the system with the line of sight of the detector and on other binary parameters. If metal atoms and/or ions are present in the binary atmosphere, then the primary X-rays interacting with them produce characteristic X-ray emission and/or absorption in the spectra. For example an X-ray photon with energy greater than 7.1

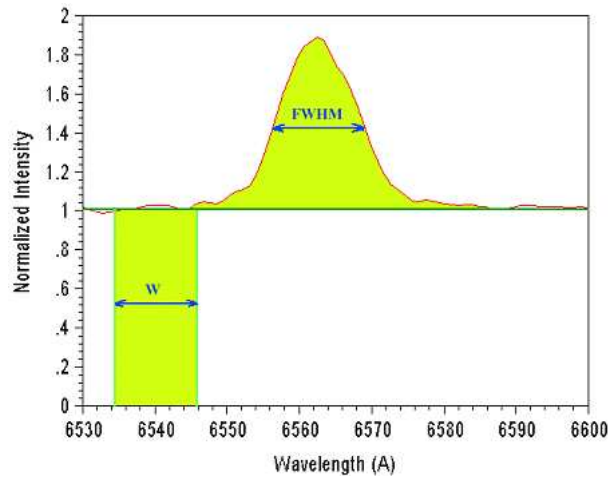


Fig. 1.30 Equivalent width (w) corresponding to the emission line shown with the Gaussian function. Image taken from <http://www.astrosurf.com/buil/us/spe2/hresol17.htm>

keV can knock out a K shell electron of Fe (iron) atom, the electron in the L or M shell fills the gap of the knocked out K shell electron. As a result a 6.4 Fe K_{α} photon or 7.1 keV K_{β} X-ray photon is produced which is equivalent to the energy gap between the L-K shell or M-K shell respectively. In similar processes other X-ray spectral lines, like Oxygen K_{α} at 0.52 keV ; Silicon L_{α} at 1.84 keV ; Calcium K_{β} at 4.01 keV emission/absorption lines can originate. The emission and absorption lines can be seen on continuum spectrum with increased and reduced intensity respectively. In this thesis we have found very intense Fe K_{α} emission line in most of the HMXBs during eclipses (details are given in Chapter 3). Other than that we have also found few spectral lines including Silicon and Calcium lines.

During eclipse, the continuum goes down by several factors, which increases the equivalent width of a spectral line. Thus the detection of a spectral line becomes more significant during eclipse with greater confidence. These spectral lines give useful informations about the chemical composition of matter around the compact object and thus temperature and other features of the binary system. The shape may differ from a narrow line if there are other factors like Doppler broadening. The strength of a spectral line is measured by its equivalent width, which is defined as ratio of the area of the emission (absorption) line above (below) the continuum and the height of the continuum. This can be described with

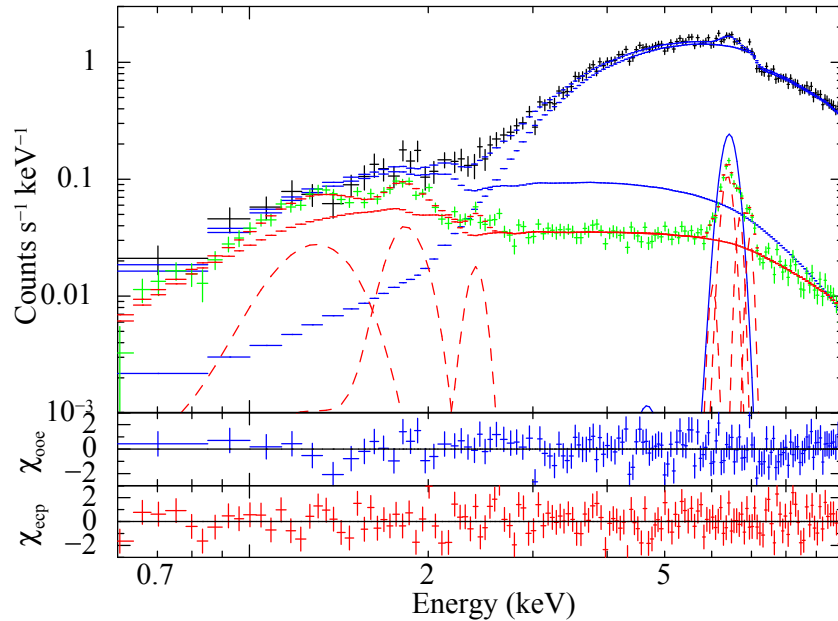


Fig. 1.31 *XMM-Newton* EPIC-pn spectrum of 4U1538–522 during eclipse (green) and out-of-eclipse (blue) phase. 6.4 keV K_{α} emission line is more prominent during eclipse. The equivalent width during eclipse is ≥ 792 eV, while that during out-of-eclipse phase is ~ 79 eV

the figure in the left panel of Figure 1.31, where a rectangle of area equal to the area of the spectral line above the continuum is obtained. This area (A) divided by the height of the continuum (I) gives the equivalent width ($w = A/I$).

When the compact object is not in eclipse, then the line intensity may be less significant compared to the continuum and therefore difficult to measure accurately, if the line intensity itself is not intense. This results into low equivalent width and the line detection becomes less significant. But during eclipse the lower continuum raises the equivalent width and the line detection becomes more significant. In the right panel of Figure 1.31 we can see that the 6.4 keV Fe K_{α} emission line is more significant during eclipse than out-of-eclipse phase. Equivalent width is very useful to compare the strengths of different spectral lines from a source, to compare the strengths of the same spectral line in the spectra from different sources and also to compare the strength of the same line in the same source but at different epoch. These can give useful insight about the distribution of different material in different binary systems and in a binary system at different epoch.

1.8 Motivation and outline of the thesis

X-ray binaries which are located at least few kilo parsecs away from earth, looks like point objects even with most sensitive X-ray imaging instruments (Chandra High Resolution Camera) on board X-ray space missions. So the configuration of an X-ray binary system, like wind accretion geometries from the high mass star to the compact object; structures and orientation of the accretion disc etc. can not be resolved. Moreover, extreme gravity of the compact objects make these systems very unique to study the distribution of density of matter, temperature, pressure etc. around this systems. To understand different aspects of X-ray binaries we need to analyze and interpret X-ray timing and spectral data with point like images of the systems.

The main subject matter of this thesis is to study X-ray reprocessing in HMXB and LMXB systems. The motivation is to explore the difference in the environment of these binary systems and also to investigate the changes in the X-ray reprocessing properties in a same source at different epochs. Study of reprocessing of higher energy X-rays into same/lower energy X-rays can help us to probe i) the chemical composition or the metallicities of the reprocessing medium and their distribution around the compact object ii) wind structure near the compact object iii) Evolution of high and low mass stars etc. Now major challenge in understanding X-ray reprocessing in X-ray binaries is the presence of brighter primary radiation with the reprocessed emission. This can be best studied when the primary emission from the compact object is blocked by the companion and that happens during eclipses. So, study of the eclipse spectra and its comparison with the out-of-eclipse spectra of a binary system gives most effective information about the reprocessing medium around the compact object. We carried out first comprehensive studies of X-ray reprocessing in HMXB and LMXB systems through eclipse spectra.

X-ray Variability studies of HMXB systems provide useful insights into the accretion mechanisms in these systems and its effect on various characteristics of the systems. Pulse profile studies of the neutron star in a variable source can give valuable informations about

the geometries of accreting material and phase dependent wind structures, if present in the system.

There are few HMXB systems in which X-ray pulsation has not been found even after more than a decade of their discoveries. Lack of pulsation creates ambiguity on the confident detection of the nature of the compact object. So for the confirmation about the nature of the compact object more and more X-ray timing and spectral studies are required in broadband.

The thesis is comprised of 6 more chapters which are organized as follows:

- Chapter 2 describes various X-ray timing and spectral analysis techniques which have been used in the thesis work. We also give brief introduction of various X-ray detectors and the space missions from which we have taken data for the purpose of analysis
- Chapter 3 deals with X-ray reprocessing through eclipse in 9 HMXB systems with *XMM NEWTON* EPIC-pn. We interpreted eclipse spectra of these systems, compared their eclipse and out-of-eclipse spectra (whenever available) and compared eclipse spectra of all the 9 HMXBs. These reveal many interesting X-ray reprocessing properties of matter around the compact object, mainly supergiant companion's wind in HMXB systems.
- Chapter 4 discusses X-ray reprocessing in 4 LMXB systems with *XMM NEWTON* EPIC-pn through eclipses. Comparison of the eclipse and the out-of-eclipse spectra of each source and comparison between eclipse spectra of all the sources yield many useful informations about the reprocessing matter in the LMXB systems, which is mainly the accretion disc of the compact object and any structure in it. These indicate some contrasting outcome with respect to X-ray reprocessing in HMXBs.
- In chapter 5, we report the variability study of a supergiant HMXB source IGR J18027–2016 with *Swift*-XRT. Here we study 15 pulse profiles of high and low states of the source in search for its connection with luminosity. Spectral studies of the variable states are also included in the thesis for the better understanding of the off-states like features in the source.

- We have searched for pulsation in an HMXB system IGR J00370+6122 with *Suzaku* and *XMM NEWTON*. We also carried out X-ray spectral studies of this source to get clues about the nature of the compact object. Chapter 6 provides details of the timing and spectral analysis of this source.
- Chapter 7 briefly summarizes the work carried out in the thesis and discusses some future prospects related to this.

Chapter 2

The X-ray detectors and the analysis techniques

"To acquire knowledge, one must study; but to acquire wisdom, one must observe."

- Marilyn vos Savant

The atmosphere above earth acts as nearly transparent windows for some electromagnetic radiation (visible, high frequency radio wave), while for some of the radiation it behaves like an opaque door (Top panel of Figure 2.1). Optical and radio telescopes can follow visible radiation and radio waves from ground (Bottom panel of Figure 2.1) respectively quite well. But the atmosphere absorbs the incoming X-rays and makes its detection impossible from the ground. So the X-ray detectors are required to be sent to space above the atmosphere (few hundreds of *km* away) on-board satellites. The satellites called X-ray space missions, carry X-ray detectors; maintains its working environment; provides operation command from ground station. The detectors can detect the arrival time of X-ray photons, their energy, counts of photons during a particular interval of time, direction of the source of the photons and can also detect their polarization state. Using these informations, science studies of the X-ray Universe is being performed. Since 1974 after the launch of 'UHURU' the first earth-orbiting X-ray space mission, many different generations of X-ray missions have flown and are flying to space providing excellent studies of X-rays from sin-

gle stars, X-ray binaries, galaxy clusters, active galactic nuclei (AGNs), supernova remnants, diffuse gas etc. and are revealing many mysteries.

2.1 X-ray telescopes

An optical telescope focuses visible light at the focal plane of an assembly of mirrors and forms optical image of an object in the sky. X-rays due to their high energy (low wavelength) penetrate any material and are absorbed (and/ or scattered) upon normal incidence. X-rays at grazing incidence are reflected from smooth surfaces made of high density metals. So the design of an X-ray telescope for focusing X-rays are completely different than an optical telescope. In 1952, Hans Wolter gave the idea of significant focusing of X-rays (at very low grazing angle, $< 2^\circ$) using paraboloid and hyperboloid dense metal surfaces. Out of his 3 ideas (shown in Figure 2.2) Walter type I mirror design gives the most effective focusing of X-rays with wide field of view. In this mirror system X-rays are made incident first upon paraboloid and then upon hyperboloid surfaces and finally focused at the focal plane of the hyperboloid. To collect more number of photons these mirror assembly can be nested co axially one inside other with a small gap (as shown in Figure 2.3).

X-ray detectors are placed at the focal plane of the X-ray telescopes. An imaging detector forms an X-ray image of the source along with detection of various other parameters like energy and timing of the X-ray photons.

2.2 Astronomical X-ray detectors

In order to detect an X-ray photon, it is made to be absorbed in the detector often by photoelectric process and an output signal is produced. The amplitude of the signal is proportional to the energy of the incoming X-ray photon. The signal strength is then translated to the energy of the incoming X-ray photon. Till date different types of X-ray detectors have been developed. In the following section we discuss some of the widely used detectors in X-ray space missions.

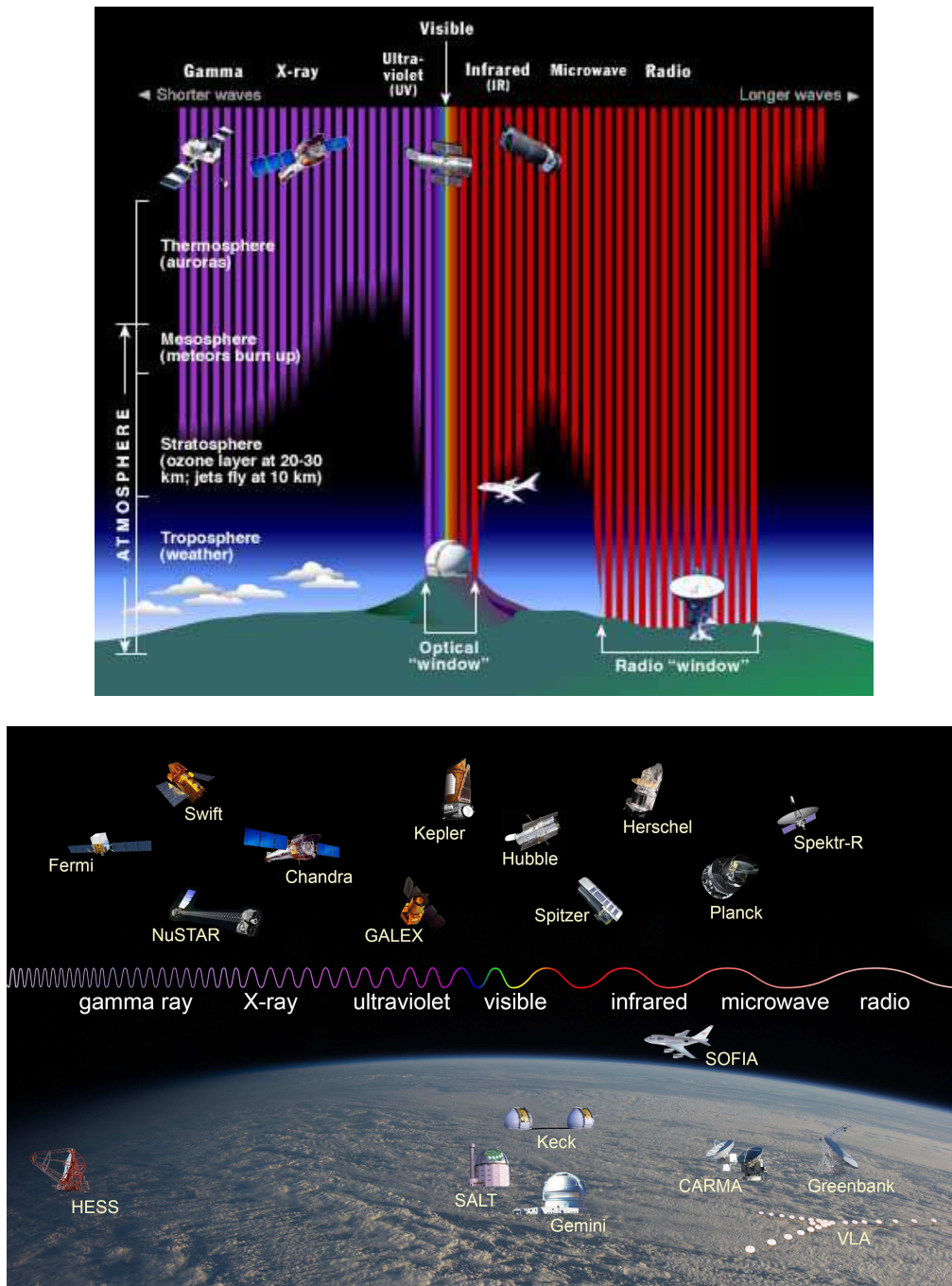


Fig. 2.1 **Top panel:** Earth's atmosphere absorbs some types (X-ray, γ ray etc) of electromagnetic radiation and allows some part (visible, radio). The vertical lines show how far the wave travels before being extensively absorbed. Image courtesy: STScI/JHU/NASA

Bottom panel: Some of the space and ground based observatories operating at different wavelength range across the electromagnetic spectrum. Image courtesy: Observatory images from NASA, ESA (Herschel and Planck), Lavochnik Association (Spektr-R), HESS Collaboration (HESS), Salt Foundation (SALT), Rick Peterson/WMKO (Keck), Gemini Observatory/AURA (Gemini), CARMA team (CARMA), and NRAO/AUI (Greenbank and VLA); background image from NASA

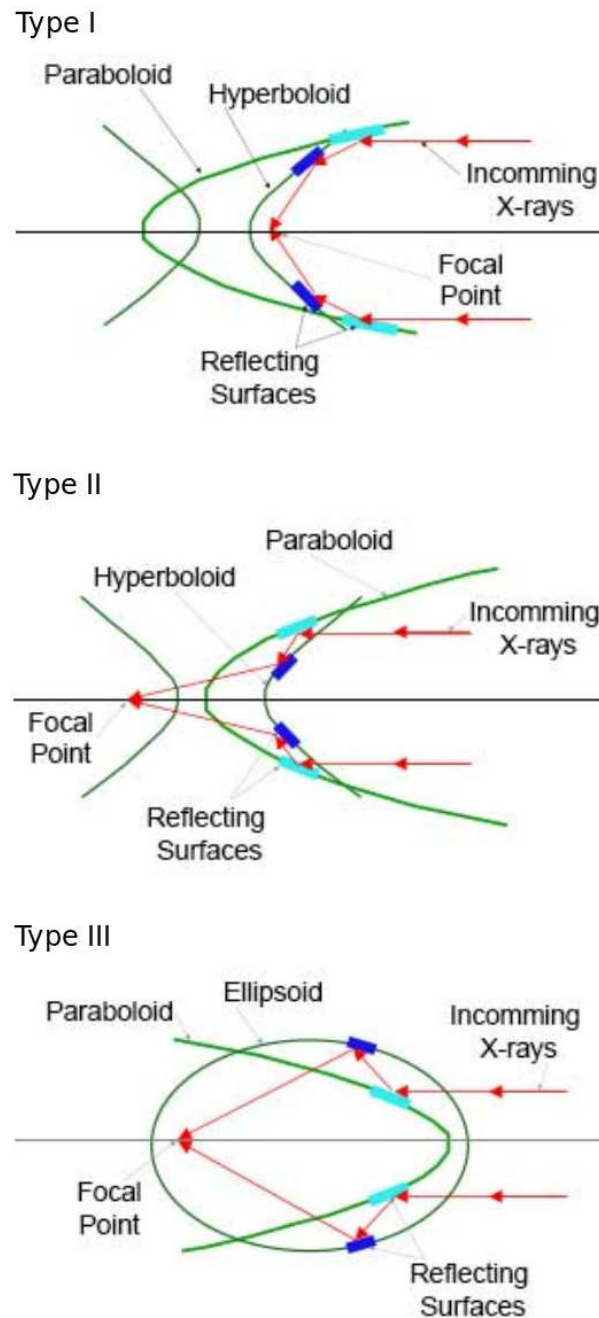


Fig. 2.2 Three types of mirror arrangements for significant X-ray reflection developed by Wolter. Wolter I system (top figure) is being widely used in space missions for most effective X-ray focusing. In this system X-rays are first made to incident upon paraboloid then upon hyperboloid surfaces and finally focused at the focal plane of the hyperboloid. Middle and bottom figures show arrangements in Wolter II and III systems respectively. Image courtesy: NASA's Imagine the Universe

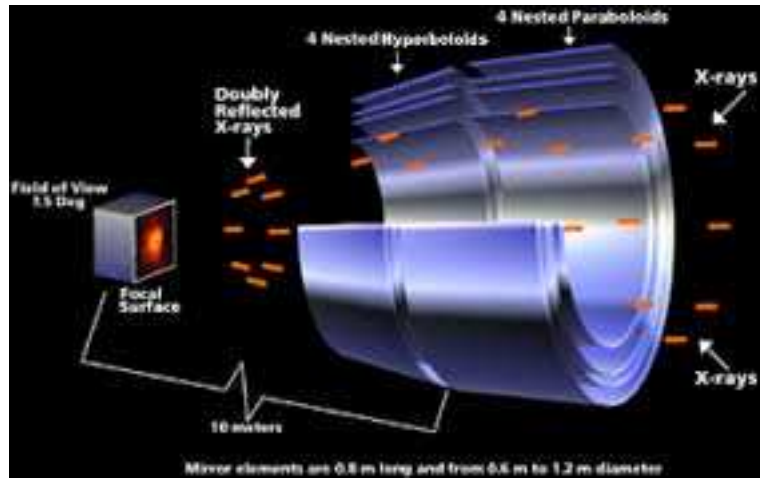


Fig. 2.3 Nested Wolter I mirror system. Nested mirrors increase number of collected photons. Image courtesy: NASA/CXC/D.Berry

2.2.1 Gas proportional counters

Proportional counter is based on the principle of controlled multiplication of free electrons in gas. In a gas filled detector an X-ray photon ionizes the gas with its photo-electron and create electron and positive ion pairs. The positive ion and electron accelerate towards cathode and anode of the gas tube respectively. During this migration the ion and electron collide with neutral gas atoms, ionize them and create further electron ion pairs. This process forms a cascade like feature from primary to secondary electron ion pairs known as Townsend avalanche. If E is the energy of the incident photon and w is the work function of the gas atom (The minimum energy required to free an electron from the atom) then total number of free electrons produced are $N \sim \frac{E}{2w}$, as the average energy used to create per electron ion pair is about a factor of 2 larger than the work function. The number of secondary electron ion pairs increase with the increase of voltage between the cathode and anode. All the electrons are collected at the cathode and ions at the anode, this produces electric signal in the circuit. Amplitude of the signal or pulse height gives the measurement of the incident X-ray photon's energy. Ionization chamber is the simplest of the gas filled detector, which is used when the incident photon's energy is high enough to produce large pulse height.

In proportional counter, the anode is kept at sufficiently high voltage (few tens of thousands *Volts/m* near the anode), so that the interaction between the photon and gas can pro-

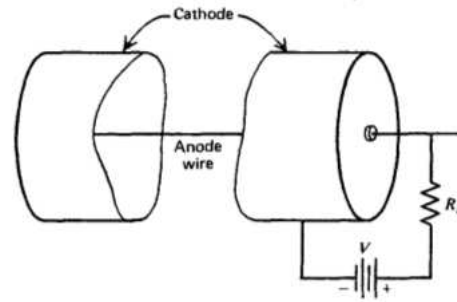


Fig. 2.4 Basic geometry of a cylindrical proportional counter. The output signal is developed across load resistance R_L . Image courtesy: Glenn F. Knoll, Radiation Detection and Measurement, 3rd edition (Knoll, 2000)

duce moderate pulse height, even if the incident photon's energy is low. Inert gas enables free transport of the electrons and ions. Argon is commonly used for economy purposes in gas proportional counters. Proportional counters can have different geometries, but most common is the cylindrical type, as shown in Figure 2.4. Further increase of the electric field between the cathode and anode increases gas multiplication, due to slow mobility of the positive ions (because of its heavier mass compared to electron) a cloud of positive ions are formed, which creates a voltage within the tube with polarity opposite to the polarity of the applied voltage. This introduces a random nonlinearity between the pulse strength and the energy of the incident photon. This high voltage region of operation is known as Geiger-Mueller region. Detector operating in this condition is called Geiger-Mueller detector. Figure 2.5 shows different region of operation of a gas filled detector. In limited proportional region, just after the proportional region space charge effect starts dominating and finally at the end of this region and at the onset of Geiger-Mueller region all the energy information of the incoming photon is lost. So a Geiger-Mueller counter can measure count rate of high energy X-ray photons but can not provide informations about their energy (Details can be found in Knoll 2000).

The value of the electric field at a distance r from the central anode wire is given by

$$E(r) = \frac{V}{r \ln(b/a)} \quad (2.1)$$

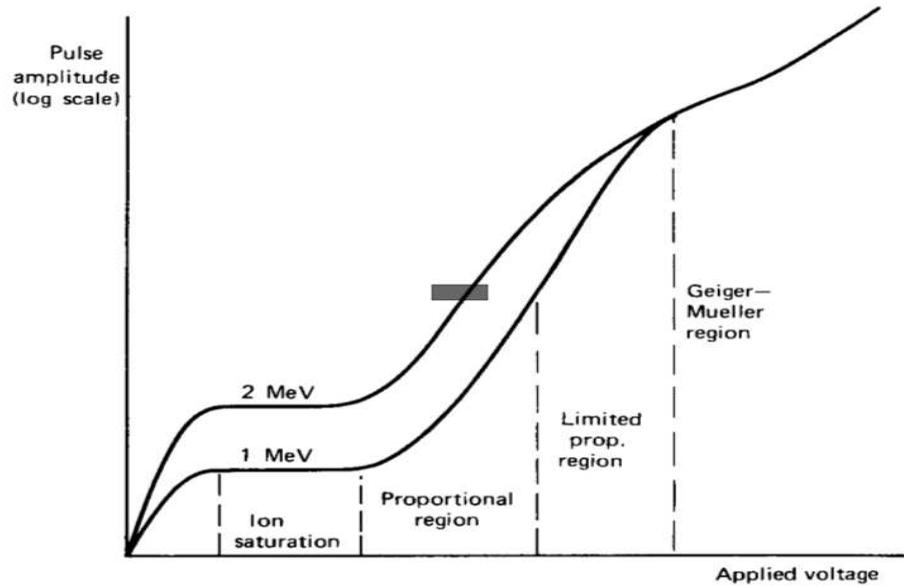


Fig. 2.5 Different regions of operation of gas filled detectors for two values of incident radiation. X axis indicates applied voltage between cathode and anode, where Y axis provides the pulse height of the detected pulse. Different regions measure the energies of the two radiations distinctly, but the Geiger-Mueller region can not distinguish between the energy of the two radiation. Image courtesy: Glenn F. Knoll, Radiation Detection and Measurement, 3rd edition (Knoll, 2000)

Where V is the voltage applied between anode and cathode. a is the radius of anode wire and b is the radius of the cathode tube. As from equation 2.1 we see $E(r) \propto \frac{1}{r}$, so $E(r)$ is high at the immediate vicinity of the anode. $E(r)$ decreases towards the inner surface of the cathode (Knoll, 2000). Efficiency of charge multiplication falls away from the anode. Non uniform charge multiplication leads to the variable energy to pulse height conversion. To prevent this, the diameter of the anode wire is kept uniform.

During charge multiplication, some neutral gas atoms get excited (but not ionized) and emits secondary photons (mainly UV). These photons can lead to spurious pulses and hence can affect the energy measurement of the original X-ray photons. To prevent this effect some additional gas known as quench gas is added, which absorbs these secondary photons. Methane, Carbon-di-oxide etc. can be used as quench gas. 90 % Argon + 10 % methane, known as $P-10$ gas is the most general purpose proportional counter gas. X-rays of different energies; low to high, come from space. So for Astronomy purposes proportional counter is widely used on-board X-ray missions. It is a non imaging X-ray detector.

ASTROSAT has 3 Xenon gas filled proportional counters (LAXPC) operating in the energy range of 3-80 keV. 5 Proportional Counter Array (PCA) on-board *RXTE* (Rossi X-ray Timing Explorer) mission was also Xenon gas proportional counter operated in the energy range of 2-60 keV.

2.2.2 Semiconductor X-ray detectors

Semiconductor X-ray detector is a solid-state device that is made of semiconductor materials. Their operation is like ionization chambers, in this case charge carriers are electrons and holes. When a semiconducting material is cooled sufficiently, the conduction band becomes completely empty. In this condition an X-ray photon incident upon the detector material produces a bunch of electron-hole pairs. The electrons jump to the conduction band, the electric field in the semiconductor drives the electrons (in the conduction band) to the output circuit and produces pulse. The pulse height is proportional to the energy of the incident photon. Silicon (Si), Germanium (Ge), Cadmium telluride (CdTe), Cadmium zinc telluride (CdZnTe or CZT) etc. are used in this type of detector as semiconducting material. A detector made of CdTe and CZT provides better efficiency for detection of hard X-rays over Si and Ge detectors. These materials can be used as monolithic detector or can be used as an array of pixels (tiny unit of a detector). Burst Alert Telescope (BAT) on-board *Swift* is made of 32,768 pieces of $4 \times 4 \times 2$ mm CdZnTe (CZT) pixels which covers $1.2 \text{ m} \times 0.6 \text{ m}$ sensitive detector area (Discussed in details later in this chapter).

2.2.3 Scintillation detectors

Scintillation detector acts on the principle of generating UV / visible light from interaction of high energy radiation with the detector material. These UV / visible photons produce a signal pulse, which is detected at the output. The materials either gas, liquids or solids which have scintillating property are used in the detector. Incoming high energy photons depending upon their energies, interact (through either of the three processes, photoelectric absorption; Compton scattering; pair production) with the scintillating material and remove

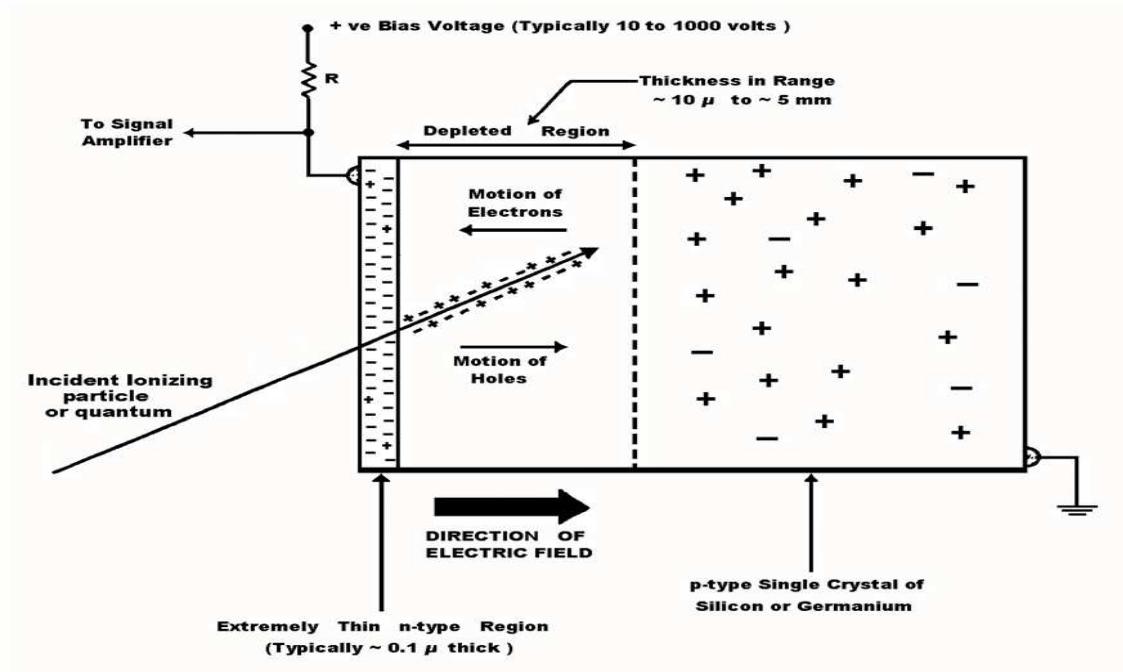


Fig. 2.6 An incoming X-ray photon creating electron hole-pairs in a p-n junction of a semiconductor detector. Image courtesy: Texas A&M University / Nuclear Safeguards Education

electrons from the atom. The energetic electrons collide with the atoms and/or molecules of the scintillating material and excite the bound electrons, which upon de-excitation emit electromagnetic radiation. This radiation mainly peaks in the visible range. These secondary photons generate photoelectrons upon incident on a photocathode in a photomultiplier tube. The tube send this electrons to the output amplifier circuit which gives the energy of the incident X-ray photons.

Argon (Ar), Krypton (Kr), Xenon (Xe) are used in gas scintillation proportional counter, where Sodium Iodide (NaI) and Cesium iodide (CsI) doped with Thallium (Tl), Bismuth germanate (BGO), Gadolinium silicate (GSO) are popular scintillator materials which are used in solid state scintillation detectors.

Suzaku Hard X-ray Detector (HXD), a 4×4 detector is surrounded by BGO scintillator for background shield and for the detection of high energy X-ray and γ rays from transients. Also each detector unit is kept in wells made of BGO crystal. At the bottom of each BGO well, GSO scintillators are glued for the detection of high energy X-rays (> 50 keV).

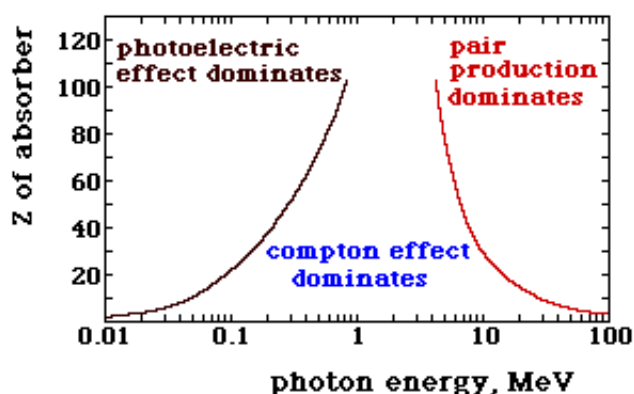


Fig. 2.7 Three types of photon-matter interaction in a scintillation detector. Lower and higher energy X-ray photons produce electrons via photoelectric effect and Compton scattering respectively. γ ray photons produce electron by pair production. Image courtesy: Adapted from <http://zuserver2.star.ucl.ac.uk>

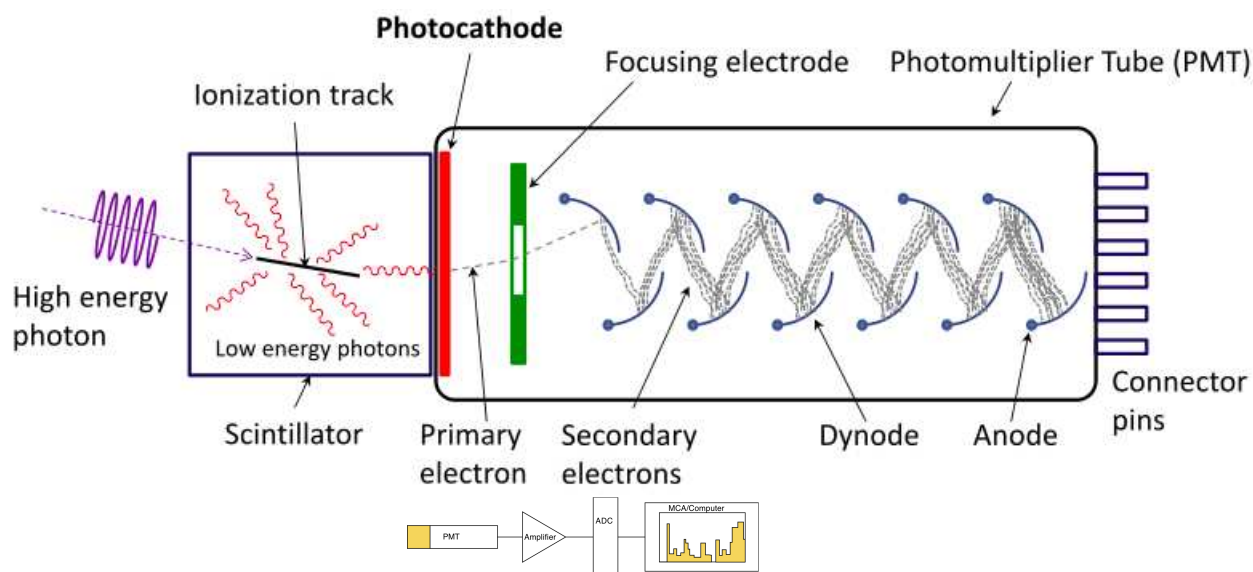


Fig. 2.8 **Top panel:** High energy photons upon incidence on a scintillating material release visible photons, which produce photoelectrons in the photomultiplier tube. Image courtesy: Qwerty123uiop (adapted from <https://commons.wikimedia.org/wiki/File:PhotoMultiplierTubeAndScintillator.svg>)

Bottom panel: Measurement of the signal strength at the output electronics. Image courtesy: Adapted from <http://wanda.fiu.edu>

2.2.4 Charged couple devices (CCDs)

Charge-coupled device (CCD) has been proved to be the most efficient X-ray detector for imaging purposes. CCD was invented by Willard S. Boyle and George E. Smith in 1969. One of the earliest application of CCD was at the University of Arizona (Smith, 1976) for ground based optical observations. CCD consists of an array of light sensitive elements called 'pixels' which produce potential wells when clock signal is applied. Pixel sizes for astronomical purposes are 9-30 μm . The pixels can store and transport charges. When photons fall on it, electron hole pairs are generated due to photoelectric effect (Figure 2.9). In case of optical photons one photon generates one electron, while one X-ray photon generates large number of electrons. Specific voltage sequence is applied to the pixels which shift charges (produced by the photo electrons) to the output amplifier. The amplifier converts charge to voltage and some external electronics convert sequence of voltages into two-dimensional digital image. The pixels can transfer charge in different ways, namely column/row; x/y; parallel/serial (Lesser, 2015). Depending upon the purpose of detection, CCDs can be operated in different ways. A full-frame CCD exposes all its pixels to the incident photons. In a frame store CCD, half of the pixels are covered with an opaque mask and half are exposed to photons, this makes the shift fast. CCDs are also used as front illuminated or back illuminated devices by making the incidence of photons from the front side or back side of the device respectively by fixing its orientation. Due to thermal electron generation in silicon, a dark signal is produced. To minimize its effect of contamination of the original charges, the CCDs are cooled with liquid nitrogen below $-100\text{ }^{\circ}\text{C}$. *XMM-Newton* EPIC pn, *Swift* XRT, *Suzaku* XIS are the CCD detectors which have been used in the thesis.

Often during bright state of the source more than one photon fall on the same pixel during the processing time of the first photon. The detector sees these photons as one photon of higher energy (as energy of these photons are deposited in the system). This effect is known as pile up, which distort the spectral shape of the source. Central pixels are heavily piled up as these are pointed to the center of the source. To avoid the effect of pile up data from central few pixels are rejected. In the thesis work we have found pile up effect in some sources in their out-of-eclipse state (discussed in chapter 3). We avoided this effect by

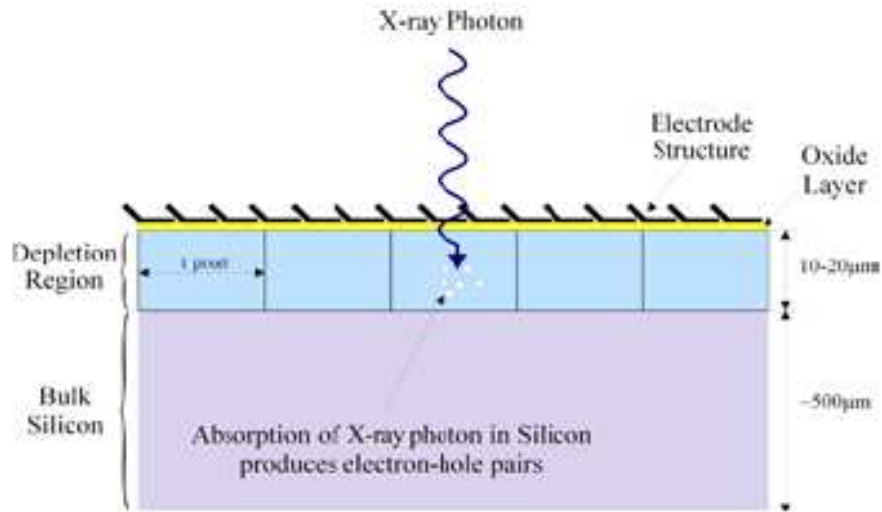


Fig. 2.9 An X-ray photon is absorbed in silicon layer of a CCD and produces electron-hole pairs. The adjacent pixels shift the charges to the output circuit which detects the X-ray photons and forms image of the source. Image courtesy: [http://www.andor.com/learning-academy/quantum-efficiency-\(qe\)-in-high-energy-ccd-detectors-understand-qe-in-a-high-energy-ccd](http://www.andor.com/learning-academy/quantum-efficiency-(qe)-in-high-energy-ccd-detectors-understand-qe-in-a-high-energy-ccd)

removing central 5'' from the image of the source and extracted the spectra from an annular region of inner radius of 5''.

2.3 Quantum efficiency of X-ray detectors

Quantum efficiency of an X-ray detector, which is a measure of efficiency with which a detector detects photons can be expressed as

$$QE_{\lambda} = \frac{N_a}{N_i} = (1 - R_{\lambda}) [e^{-\frac{\alpha_{\lambda}}{t}}] \quad (2.2)$$

Where N_i and N_a are the numbers of incident and absorbed photons, R_{λ} is the surface reflectance of the detector, α_{λ} is the absorption length dependent upon the wavelength of the incident photons, t is the thickness of the semiconductor pixels. Since most of the semiconductor detectors are made of silicon pixels, so the quantum efficiency can be increased by reducing surface reflectance (R_{λ}) with some coatings and increasing the thickness (t) of the absorbing material.

2.4 Some features of the detectors on-board

The detectors on-board X-ray missions have two main functions, to detect new X-ray source and to observe known sources at scheduled times. To fulfill these requirements X-ray detectors of two distinct features are developed in the satellite, namely all sky camera and narrow field instruments. Following section gives a brief overview of these features.

2.4.1 All sky camera

All sky camera (ASC) is an X-ray instrument on-board X-ray missions which scans nearly full sky by revisiting the same portion in frequent interval. The aim of its operation is to search for new transients and to record the flux variations from the known sources. A new transient source can appear at any time at any direction in the sky. Outbursts, X-ray novae etc. in known sources is also unpredicted most of the time. So ASC has large field of view to cover maximum possible portion of the sky at a time. For nearly full sky scanning, the camera rotates about satellite's spin axis through an assembly of motors. All sky monitor (ASM) is the first all sky camera on-board mission Ariel 5, launched into space in 1974 (Holt, 1976). All sky monitor (ASM) on-board Ginga (Tsunemi et al., 1989), ASM on-board RXTE, Burst alert telescope (BAT) on-board *Swift*, Monitor of all sky X-ray image (MAXI) on-board International Space Station (ISS) (Matsuoka et al., 2009) etc. are examples of all sky camera or scanners. Scanning sky monitor (SSM) is the X-ray monitor on-board India's latest X-ray mission *ASTROSAT*. In the thesis we have used all sky camera BAT on-board *Swift* mission to get long term light curve for 15 sources analysed in the thesis. BAT views 80% of the sky in every 90 minutes.

2.4.2 Narrow field instruments

Narrow field instruments or pointing instruments observe a particular source (or sources according to science purposes) for some particular duration with its center of field of view pointed towards the source. EPIC-pn (on board *XMM Newton*), XRT (on board *Swift*), LAXPC (on board *ASTROSAT*) etc. are the examples of pointing instruments. In this thesis

we have made use of *XMM Newton*-EPIC-pn, *Swift*-XRT and *Suzaku*-XIS, HXD as pointing instruments. The pointing instruments observe known sources with preplanned schedule according to the accepted proposals. If sudden outburst, X-ray novae or some new transient is found then these instruments may observe those events or sources as per target of opportunity scheme (ToO).

2.4.3 Background rejection

An X-ray detector on-board satellite is exposed to cosmic rays too. Their arrival is completely random. To differentiate X-ray and cosmic ray interaction in the detector several ways can be adapted, like i) choosing upper threshold of the X-rays to be detected below cosmic ray energy, for example in our analysis with *XMM Newton* EPIC pn which operates in the energy range of 0.3-15 keV we have generated the lightcurve and spectra upto 10 keV to avoid particle background. ii) making large depth of the detector shell, so that cosmic ray event can deposit more energy than most energetic X-ray photons iii) noticing rise time of the signal. A particle event leave a long ionization track, while an X-ray event leave a point like ionization cloud which makes shorter rise time of the signal. iv) surrounding the X-ray detector from 3 to 5 side with another detector called anti-coincidence detector. Coincident signal in both the detectors are likely to be due to cosmic ray event (because of its long interaction track) and hence are rejected. This is the most efficient background rejection method amongst all these mentioned above.

2.5 X-ray missions and the instruments used in the thesis work

In the thesis work we have used data from the following X-ray space missions and on-board instruments.

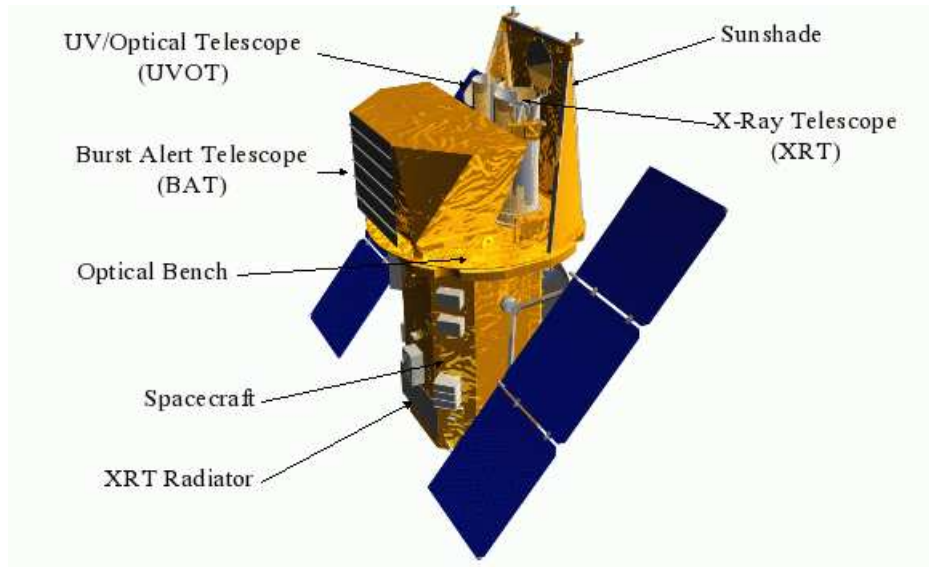


Fig. 2.10 Different instruments of *Swift* satellite, including BAT and XRT. Image courtesy: Gehrels et al. (2004).

2.5.1 *Swift*

Swift satellite was launched into orbit in November 2004, with the aim to understand the origin of powerful gamma-ray bursts (GRBs) and till date it is active with good health. It was built in a partnership between United States, United Kingdom, and Italy. As GRBs come from any direction of the sky, so to search for these an all sky monitor named Burst alert telescope (BAT) was boarded on the satellite. The satellite has other two instruments, X-ray Telescope (XRT) and Ultraviolet and Optical Telescope (UVOT). These are co-aligned and pointed to the center of field of view (FOV) of BAT. These three instruments together have been answering many key issues related to GRBs along with other scientific investigations in the optical to Gamma ray regime. Amongst its three instruments we have used data from BAT and XRT in the thesis.

BAT

BAT is a coded aperture instrument with CdZnTe (CZT) detector with an FOV $100^\circ \times 60^\circ$. It operates in the energy range of 15-150 keV (Barthelmy et al., 2005) with a detection sen-

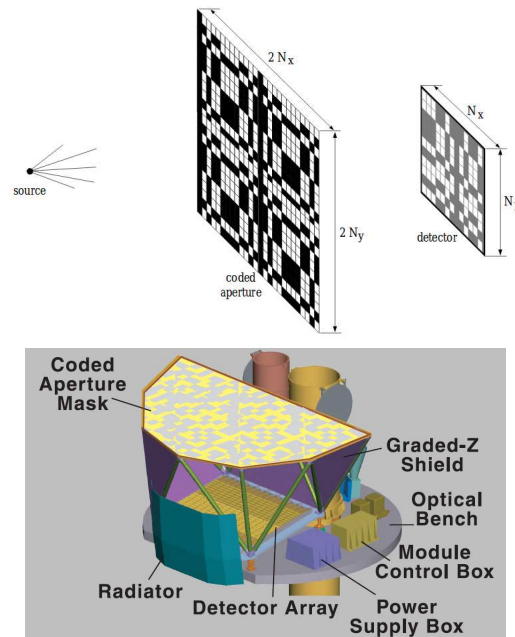


Fig. 2.11 **Top Panel:** A coded mask casts shadow on the detector plane. Image courtesy: Busboom et al. 1997. **Bottom Panel:** D shaped coded mask over CZT detector plane of Burst Alert Telescope (BAT). Image courtesy: (Barthelmy et al., 2005).

sitivity of 5.3 mCrab in one day of observation time (Krimm et al., 2013a). 32,768 pieces of $4 \times 4 \times 2 \text{ mm}$ CZT cover a $1.2 \text{ m} \times 0.6 \text{ m}$ area in a position sensitive detector plane. 128 detector elements are fabricated into 8×16 arrays. Each element is connected to specific channel for readout. Above this detector plane, a D-shaped coded mask made of $\sim 54,000$ lead tiles each of size $5 \text{ mm} \times 5 \text{ mm} \times 1 \text{ mm}$ is mounted on a 5 cm thick composite honeycomb panel (Gehrels et al., 2004). In coded mask aperture imaging technique, a sheet with some specific transparent and opaque pattern (called mask) for incoming photons are placed over a position sensitive detector. The size of the smallest unit of the mask is made of the order of detector's spatial resolution (in't Zand, 1992). The incoming photons from a source fall on the mask and cast shadow on the detector plane as shown in the top panel of Figure 2.11. Photon distribution is obtained from the cross-correlation of the shadow and the mask pattern (Busboom et al., 1998). bottom panel of Figure 2.11 shows D shaped coded mask in BAT. BAT operates in two modes, scan-survey mode and burst mode. Survey mode produces hard X-ray data of all sources in its field of view in 5 minute time bins for 18 energy intervals. Burst mode identifies burst positions. When BAT detects a burst it determines its

position within few seconds and within 20-70 s it aligns the two narrow field instruments XRT and UVOT to collect simultaneous data from the burst (Barthelmy et al., 2005). During survey mode if a burst occurs, it switches to photon counting mode with a buffer to save preburst information. The point spread function of the detected source image is $17'$ (Gehrels et al., 2004).

Hard X-ray light curves of all the X-ray sources since the start of operation of BAT can be obtained from <https://swift.gsfc.nasa.gov/results/transients/>. The website provides two lightcurve of binsizes 1 day and 1 *Swift* orbit around earth. We have used more than 10 years of lightcurves for high mass X-ray binaries to get the eclipse phases, details of which are given in Chapter 3. We have also used BAT data of high mass X-ray binary IGR J18027–2016 and IGR J00370+6122 to get long term orbital profile which are given in Chapter 5 and 6 respectively.

XRT

XRT is a narrow field instrument or pointed instrument of *Swift* mission with FOV $23.6' \times 23.6'$. It operates in the energy range of 0.2-10 keV. XRT is a focusing telescope which uses grazing incidence Wolter I X-ray mirrors of 3.5 m focal length which focuses X-rays onto a CCD detector plane. The CCD plane consists of an array of 600×600 pixels, each with $40 \mu\text{m} \times 40 \mu\text{m}$ size and $2.5'$ pixel⁻¹ resolution. The point spread function of the detected source image is $15''$ (Gehrels et al., 2004). XRT operates on three read-out modes: i) Imaging (IM) ii) Windowed timing (WT) iii) Photon counting (PC). In IM mode image of the source is obtained by CCD read-out and position recognition of the photons are not done. WT mode gives 1.7 ms time resolution and one dimensional imaging, for flux less than 600 *mCrab*. PC mode provides full imaging and spectroscopic resolution with 2.6 s time resolution. We have used 33 *Swift*-XRT observations over a period of 5.5 years to study the supergiant HMXB system IGR J18027–2016, details are given in Chapter 5.

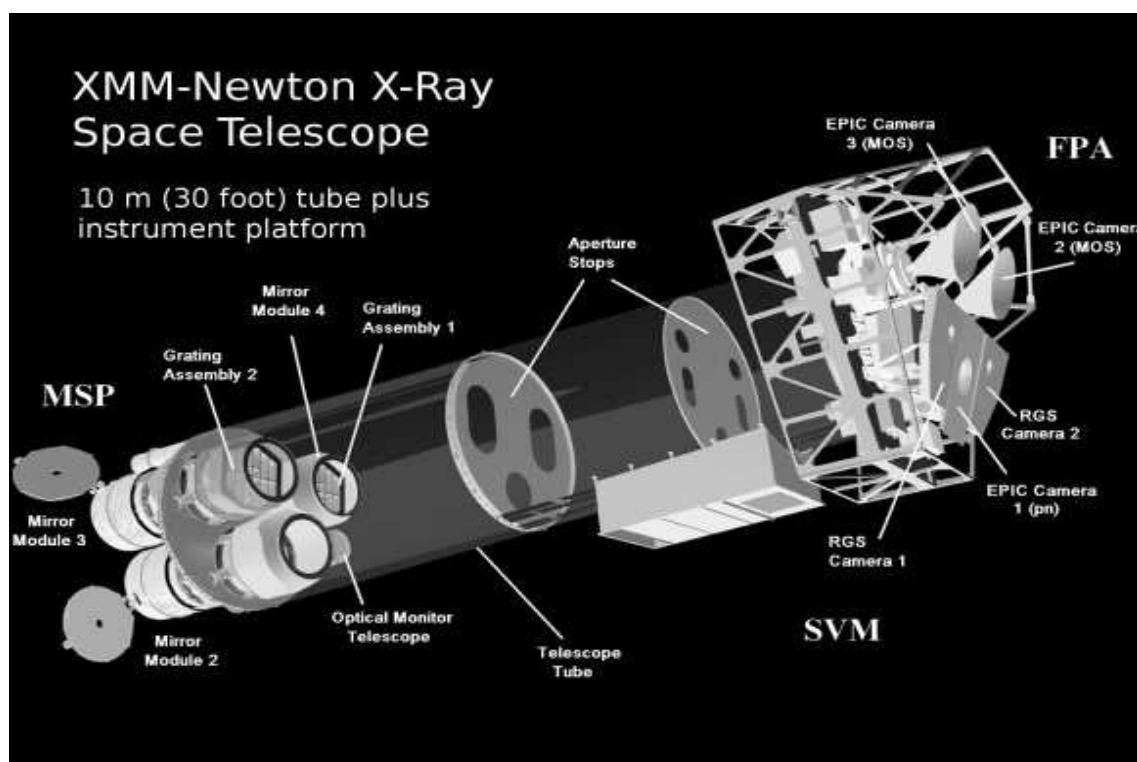
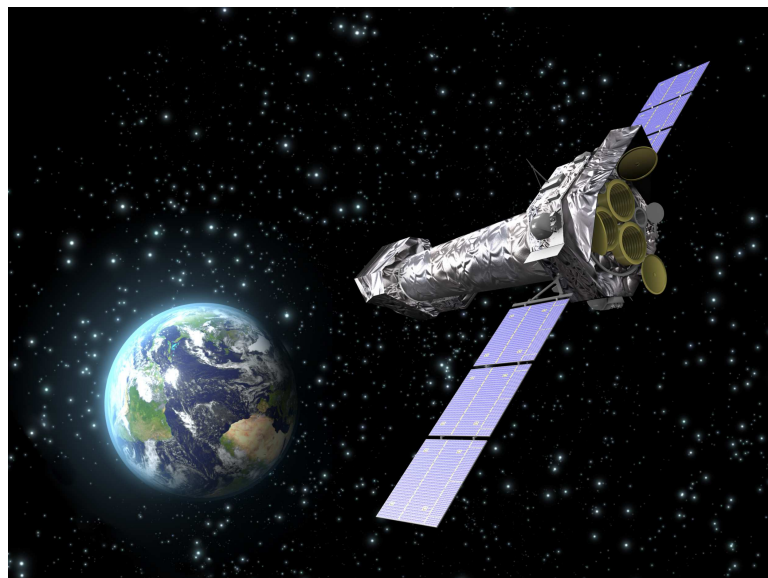


Fig. 2.12 **Top panel:** *XMM-Newton* satellite. Image courtesy: Adapted from <http://sci.esa.int/xmm-newton/42885-xmm-newton-spacecraft/> **Bottom panel:** Instruments of *XMM-Newton* including EPIC pn. Image courtesy: ESA/XMM-Newton

Table 2.1 A brief introduction of the modes of EPIC pn operations

Mode	pixel \times pixel	Timing resolution	Maximum count rate for point source counts s ⁻¹ (mCrab)
Full frame	376 \times 384	73.4 ms	2 (0.23)
Large window	198 \times 384	47.7 ms	3 (0.35)
Small window	63 \times 64	5.7 ms	25 (3.25)
Timing	64 \times 200	0.03 ms	800 (85)
Burst	64 \times 180	7 μ s	60000 (6300)

2.5.2 XMM Newton

X-ray Multi-Mirror Mission named after Sir Isac Newton as (*XMM-Newton*) is an X-ray space observatory launched in space by European Space Agency (ESA) on December 1999 and is still in operation. It was placed in highly eccentric orbit to avoid radiation belts surrounding the Earth. It was built to get answers of several cosmic mysteries related to black holes and the origin of the Universe. It is also called High Throughput X-ray Spectroscopy Mission, because of its excellence in spectroscopic measurement in soft X-ray band. The satellite consists of 3 sets of co-aligned X-ray telescopes each with an effective area of 1500 cm⁻² with three detectors at its focal plane, three European photon imaging camera (EPIC) and two Reflection grating spectrometers (RGS). Two of the cameras are made of Metal oxide semiconductor (MOS) CCD (Turner et al., 2001) arrays and one uses pn CCDs (Strüder et al., 2001). Another coaligned instrument Optical/UV Monitor (OM) telescope (Mason et al., 2001) provides simultaneous optical and UV coverage with the X-ray instruments. In the thesis work we have used EPIC pn instrument, which is discussed briefly in the following section. Figure 2.12 shows satellite *XMM-Newton* and its instruments including EPIC pn.

EPIC-pn

The pn camera is a 6 cm \times 6 cm single silicon wafer embedded with 12 pn CCDs each of 300 micron thickness. Each CCD is made of 64 \times 189 pixels. pn CCDs are illuminated from

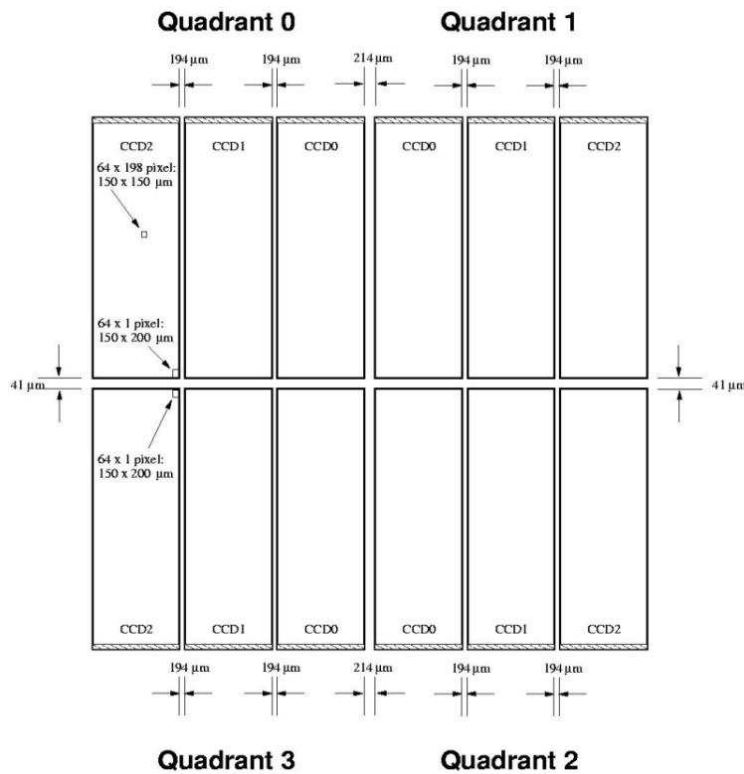


Fig. 2.13 Full frame of 6cm×6cm EPIC pn base with 12 CCDs. Image courtesy: Adapted from <https://www.cosmos.esa.int/web/xmm-newton/boundaries-pn>

rear side. The pn camera detects X-rays in the energy range (0.15-15) keV over a field of view (FOV) of $30'$. It provides moderate spectral ($E/\Delta E \sim 20-50$) and angular resolution ($6''$). 97% of the sensitive area of the CCDs are open to the FOV. To protect the camera from radiation damage it is shielded on all sides except the X-ray entrance window with 3 cm thick Aluminium sheet. The camera is kept at its nominal operating temperature -100° C. All the CCDs gather data at all times, but according to the science requirement different read out modes can be chosen. The pn camera operates in main 2 modes: 1) Imaging mode 2) Timing mode. Imaging mode provides several submodes and the timing mode offers one special mode with finest timing resolution. A brief introduction of the modes and sub modes are given in Table 2.1.

In the thesis work we have used EPIC pn instrument to study the eclipse and out-of-eclipse spectra of eclipsing X-ray binaries, details of which are given in Chapter 3 and 4.

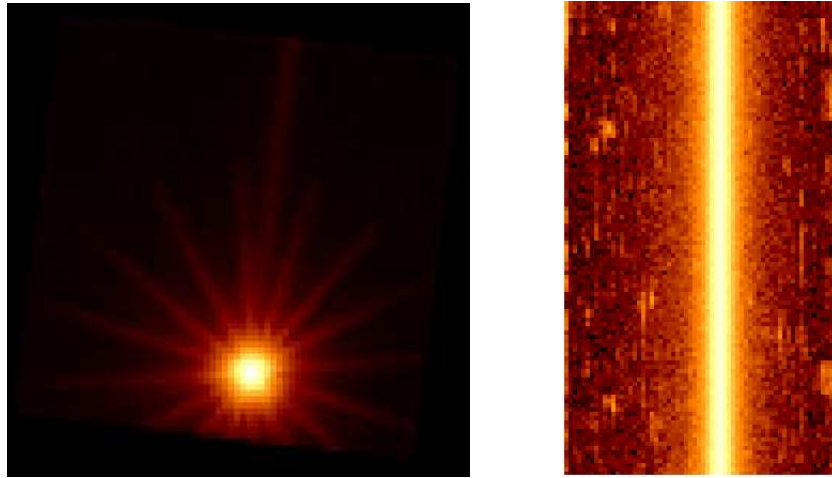


Fig. 2.14 EPIC-pn CCD image of LMC X-4 in imaging mode (left panel) and in timing mode (right panel) obtained with *XMM-Newton* SAS tool. Image courtesy: Aftab and Paul (2018)

2.5.3 *Suzaku*

Suzaku (ASTRO E II) Japan's fifth X-ray astronomy satellite, was developed in collaboration with US. It was launched in space in 2005 with the aim of studying hot plasmas with X and γ rays, structure and evolution of the universe, wide band spectroscopy of AGNs etc. The satellite was operational till 2015. It was placed in a nearly circular orbit with altitude 550 km, this orbit was inclined at an angle of 31° with earth's orbit around Sun. It carried 5 soft X-ray detectors namely, one X-ray spectrometer (XRS); 4 X-ray imaging spectrometer (XIS) and one hard X-ray detector (HXD). One week after the launch XRS shut down due to malfunction in cooling system.

In the thesis we have used data from XIS and HXD instruments. The following section gives a brief description of the two instruments. Figure 2.15 shows the different instruments on-board *Suzaku* mission.

XIS

4 XIS (XIS 0, XIS 1, XIS 2, XIS 3) detectors sensitive in the energy range (0.2-12) keV, made of CCDs provided X-ray imaging and were located at the focal plane of 4 X-ray telescopes (XRT) (Koyama et al., 2007). Out of 4 XIS instruments, XIS 0, XIS 1 and

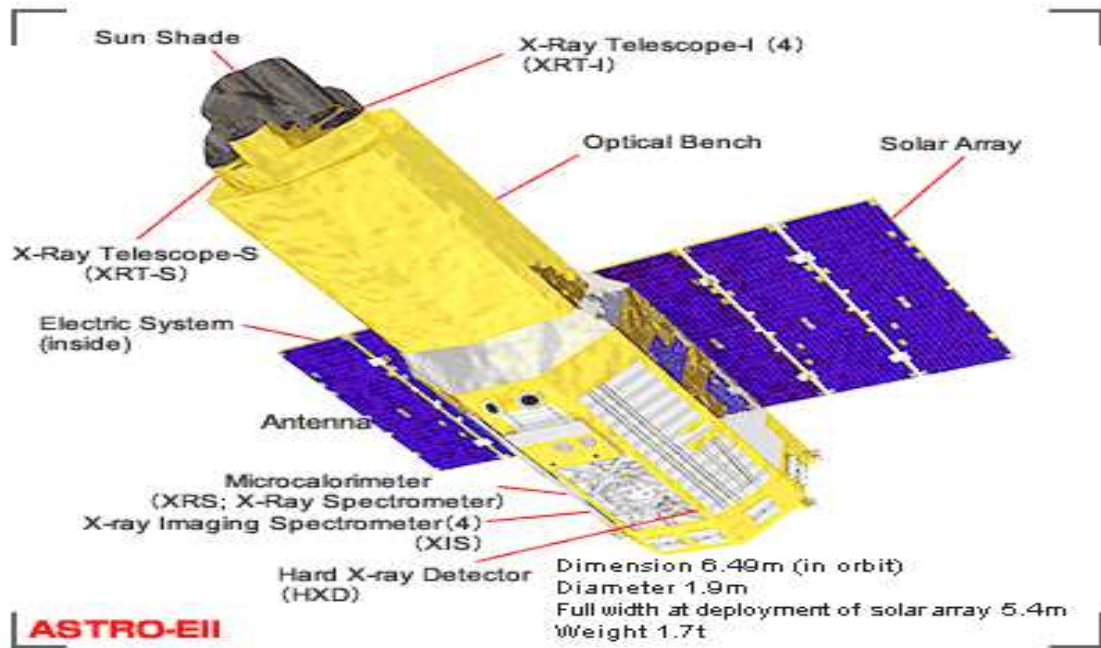


Fig. 2.15 Instruments of *Suzaku* mission showing XIS and HXD. Image courtesy: Adapted from <http://global.jaxa.jp/article/special/xray/>

XIS 3 were operational and in this thesis we have used this 3 XIS instruments to study the timing and spectral behaviour of an HMXB system IGR J00370+6122. The features of XIS instruments are given in Table 2.2.

HXD

The hard X-ray detector (HXD) operates in the energy range of (10-700 *keV*) comprised of two detectors, one made with GSO well type phoswich counter (>50 *keV*) another made of silicon PIN diodes (<50 *keV*). Table 2.2 gives a brief description of the instrument.

2.6 X-ray data analysis

For each observation, the space missions record timeseries (X-ray photon detection times with bin size equal to time resolution of specific instruments); photon counts in each time bin; energy of the detected photons. Some future (*XPoSat*, INDIA; *IXPE*, Sweden) X-ray missions can provide polarization states of the incoming X-ray photons. To extract science

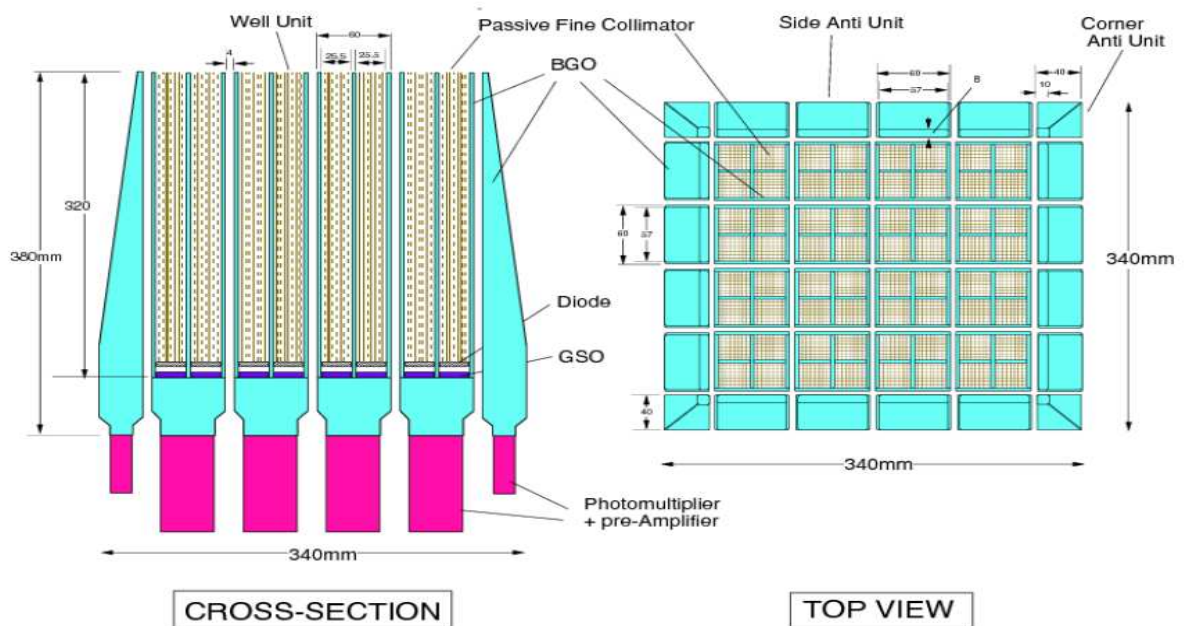


Fig. 2.16 Schematic of *Suzaku* HXD instrument which consists of two types of detector, i) GSO scintillator ii) Pin semiconductor. The whole instrument was shielded with scintillating crystal BGO. Each of the pair of detector units is covered with a well type structure made of BGO. Image courtesy: *Suzaku* ABC guide (<https://heasarc.gsfc.nasa.gov/docs/suzaku/analysis/abc/node10.html>)

Table 2.2 A brief introduction of the XIS and HXD instruments on-board *Suzaku*

	XIS	HXD
Type	Imaging	Non-imaging
Number of sensors	4 (one CCD chip/sensor)	1 (16 identical units)
Number of pixels	1024 x 1024	-
pixel size	24 <i>micron</i> x 24 <i>micron</i>	-
Field of View (FOV)	19'x19'	0.56° x 0.56° ($E < 100$ keV) 4.6° x 4.6° ($E < 1$ keV)
Effective area per sensor	400 cm^2 (at 1.5 keV) 250 cm^2 (at 6 keV)	160 cm^2 (at 15 keV) 300 cm^2 (at 120 keV)
Energy resolution (FWHM)	120 eV (at 6 keV) 50 eV (at 1 keV)	3 keV (10-30 keV) 9% (at 662 keV)
Spatial resolution	~1.8'	-

from these raw data it is required to first clean the data from various imperfections / contaminations configuration of the telescope, high background from charged particles etc. This is done with mission specific pipelines (CIFBUILD, ODFINGEST etc. for *XMM Newton*, XRT-PIPELINE for *Swift*) and software packages (XSELECT for *Swift* and *Suzaku*; EVSELECT for *XMM Newton*). For storing and processing astronomical images with time series and energy values of the X-ray photons the file format requires to be Flexible imaging transport system (FITS) type.

The cleaned event file obtained in the above process contains timing, imaging and spectral informations. For understanding the behaviour of a system, separately timing and spectral analysis needs to be carried out. In the thesis we have carried out most of our timing and spectral studies with the help of NASA's High Energetic Astrophysics Science Archive Research Center (HEASARC) provided software HEASoft. HEASoft provides XRONOS and XSPEC packages for the timing and spectral studies respectively.

2.6.1 Timing analysis

In timing analysis of the cleaned data, first step is to get X-ray intensity of the source with respect to time. The intensity vs timeseries plot is known as lightcurve. Lightcurve directly gives the informations about flares, outbursts, off-states, dips etc. To get some more useful insights of a system, lightcurves can be analyzed further with the help of some more FTOOLS within XRONOS. FTOOLS are some task specific routines in a software package. The FTOOLS for the timing analysis are briefly discussed below.

LCURVE

FTOOL 'LCURVE' produces lightcurve of desired bin size and plots it. Simultaneously it can produce and plot upto 4 lightcurves. Along X axis it plots timeseries and along y axis counts s^{-1} . It can also produce hardness ratio of upto 3 lightcurves (when plotted simultaneously). In this routine several filters can be specified, like time window; orbital and spin phase window etc. Lightcurve can also be plotted in multiple interval in multiple frames. X (time) and Y (counts s^{-1}) axis can be zoomed to get a closure view of the flux variation. Figure 6.2 shows EPIC pn lightcurve of LMC X-4 obtained with this FTOOL.

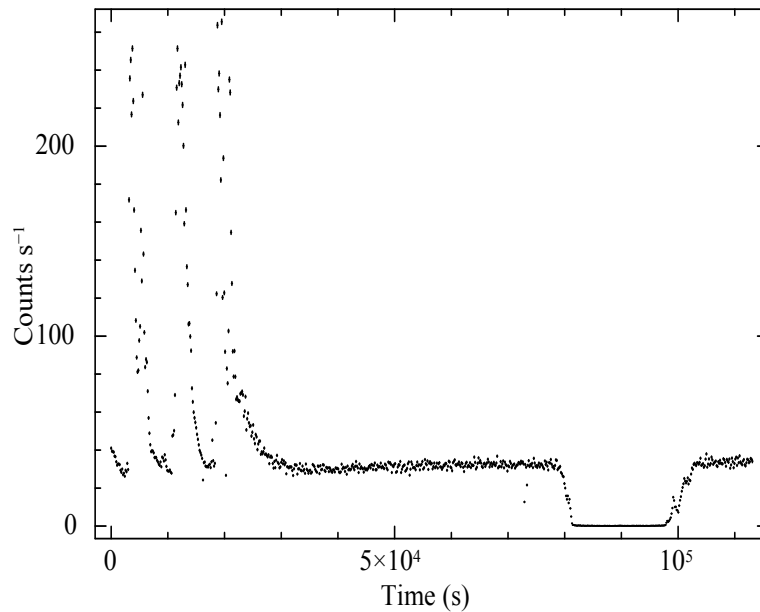


Fig. 2.17 An EPIC pn lightcurve of LMC X-4 obtained with FTOOL 'LCURVE', X axis gives timeseries in *second* and Y axis gives intensity in units of *Counts s⁻¹*. Image courtesy: Aftab and Paul (2018)

To add or subtract multiple lightcurves FTOOL 'LCMATH' is used. It requires lightcurve FITS files as inputs.

Period search

Looking at a lightcurve the orbital period of a binary system and spin period of a pulsar cannot be determined accurately. For that XRONOS uses the following FTOOLS.

POWSPEC

'POWSPEC' calculates power present in a signal with frequency ($\frac{1}{\text{Time}}$) using fast Fourier transform (FFT) or slow Fourier transform algorithm and plots the result. The routine takes lightcurve as input and generates output file containing power versus frequency in FITS format. Usually a signal from X-ray binaries is a superposition of multiple signals of different frequencies. If the power spectrum shows narrow peak at a particular frequency, then the time period corresponding to that frequency gives the orbital (or spin) period of the binary (neutron star or white dwarf) system. Figure 1.25 of Chapter 1 shows a 'POWSPEC' plot of an HMXB system 2S 0114+650. Sometime power spectra

shows more than one secondary peaks beside the main peak. These may correspond to the super-orbital period for HMXBs or quasi periodic oscillation of some structures in the accretion disc, mainly in case of LMXBs.

EFSEARCH

‘EFSEARCH’ enables finer period search around a trial period. The lightcurve; a trial period; a range of periodicity around the trial period with some specified time resolution are fed to the routine, which folds the lightcurve within the range of specified period. For each folded lightcurve it obtains a χ^2 by comparing the folded lightcurve with a constant and generates a plot of χ^2 vs period. If periodicity is present in the lightcurve within the specified range of period, then a sharp peak of χ^2 is noticed in the plot at that period. The routine generates an output FITS file with the values of search period vs χ^2 . In this thesis ‘EFSEARCH’ has been used in search for refined orbital period in a number of HMXB and LMXB systems and in search for pulse period in IGR J18027–2016 and IGR J00370+6122.

Periodic flux variation

In almost all timing studies of X-ray binaries carried out in this thesis, we needed to see the periodic flux variation over one orbital period and for pulsars in one spin period too. For that, the timeseries is sliced at the interval of orbital (or spin) period and the count rate of each time bin is averaged. This algorithm generates a folded intensity profile. When the profile is obtained by slicing the timeseries with orbital (spin) period then it is called orbital (pulse) profile. Following routine is used to generate orbital and pulse profiles.

EFOLD

The FTOOL ‘EFOLD’ obtain orbital and /or pulse profile of a source and produce a plot with orbital (spin) phase along X axis and average count rate per phase bin along Y axis. As inputs, the routine mainly requires lightcurve FITS file; folding period (orbital or spin period); number of phase bin in a given period; epoch of phase zero. Some filters, like preferred phase interval or time duration of the input light curve can also be given in the input. The routine can simultaneously produce

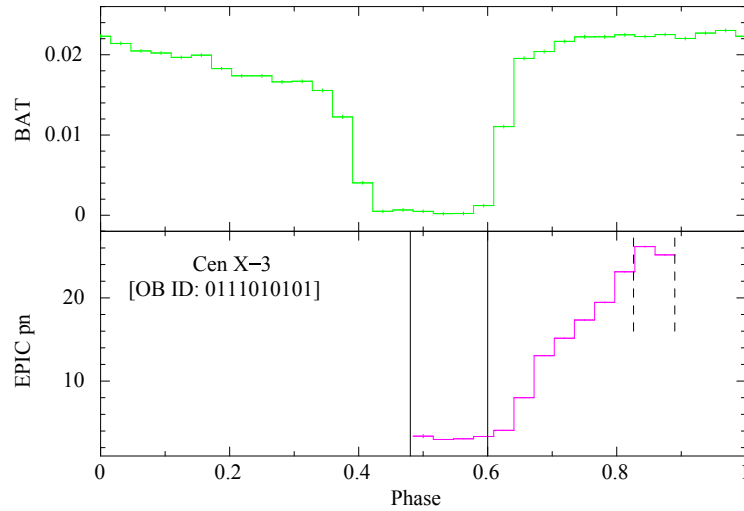


Fig. 2.18 Orbital profile of Cen X-3 obtained with *Swift*-BAT (Top panel) and *XMM-Newton* EPIC pn (Bottom panel) obtained with FTOOL ‘EFOLD’. Image courtesy: Aftab and Paul (2018)

and plot profiles for 4 lightcurves folded with the same period. In the thesis we have obtained average orbital and pulse profiles of a number of XRB systems with the FTOOL ‘EFOLD’. Figure 2.18 shows orbital profile of Cen X-3 with BAT and EPIC pn and Figure 2.19 shows pulse profile of IGR J18027-2016 with *Swift*-XRT obtained with this FTOOL. Where 0-1 phase corresponds to one complete period.

2.6.2 Spectral analysis

X-rays of different energies are emitted through different mechanisms from an X-ray binary system, as discussed in the previous Chapter (section 1.5). An X-ray spectrum is represented by the graph of intensity versus energy of the detected X-rays. A detector’s response in sensing the energy of the incident X-ray photons is not same throughout its area. Effective area of the X-ray telescope, quantum efficiency and energy resolution of the detector are all energy dependent and these informations are required to carry out X-ray spectroscopic measurements.

We have used XSPEC software package for the spectral analysis of 15 X-ray binaries studied in the thesis (to be discussed in detail in the following chapters).

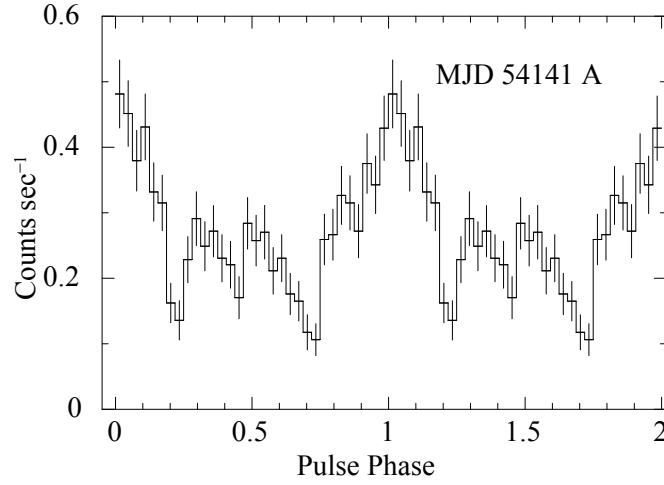


Fig. 2.19 Pulse profile of *Swift*-XRT lightcurve of IGR J18027–2016 obtained with FTOOL ‘EFOLD’. Image courtesy: Aftab et al. (2016)

Spectra fitting

The incident X-ray photons interact with the detector elements. The observed X-ray spectrum is significantly different from true X-ray spectrum of the source, because of various energy dependence of the instrument (effective area of the telescope, quantum efficiency and energy resolution of the detector etc.) To get the true shape of the spectrum, correct detector response to the X-ray photons of different energies is required. If $f(E)$ is the true spectrum, $C(J)$ is photon counts per channel at J th channel and $R(J, E)$ is the instrument response which is proportional to the probability of detection of the incident X-ray photon of energy E at J th channel, then

$$C(J) = \int_0^{\infty} f(E) R(J, E) dE \quad (2.3)$$

To determine $f(E)$ by inverting $R(J, E)$ is difficult and / or no unique solution may exist, so XSPEC choose a model for the true source spectrum ($f(E)$) predicting count rate at each channel ($C_p(J)$), match with the measured count rate at each channel ($C(J)$) applying χ^2 statistics, where

$$\chi^2 = \frac{\sum (C(J) - C_p(J))^2}{\sigma^2(J)} \quad (2.4)$$

and $\sigma(J) = (C(J) - C_p(J))$, the error associated with each count $C(J)$. The χ^2 is obtained for a particular number of channels for a certain number of degrees of freedom (DOF), where DOF is given by number of data-points (number of $C(J)$ s) minus number of model parameters. XSPEC

checks for the goodness of fit. Reduced χ^2 or χ_{red}^2 ($\frac{\chi^2}{DOF}$) gives a measure of goodness of fit. A model or set of models are accepted if $\chi_{red}^2 \sim 1$.

XSPEC models

There are numerous inbuilt models in XSPEC. These are additive, multiplicative, convolution etc. type of models. XSPEC also allows users to use their own models in spectral fitting. In the thesis we have used the following models.

POWERLAW:

‘POWERLAW’ is the simplest model, used primarily to fit spectra from X-ray binaries. This model can be expressed as

$$X_{po}(E) = KE^{-\Gamma} \quad (2.5)$$

Where Γ is photon index of ‘POWERLAW’ and is dimensionless quantity. K is normalization factor in units of *photons keV⁻¹ cm⁻² s⁻¹* at 1 keV. ‘POWERLAW’ is an additive model.

PHABS:

The next important model component to fit X-binary spectra is ‘PHABS’, which is based on photoelectric absorption. The photons reach the detector after traversing a long distance through different medium and are expected to suffer photoelectric absorption. The line of sight medium is assumed to be made of hydrogen with corresponding amount of other elements with solar abundance and the column density of hydrogen associated with it is called equivalent hydrogen column density. This is a multiplicative model.

Model ‘PHABS’ is given as

$$X_{phabs}(E) = e^{-N_H \sigma(E)} \quad (2.6)$$

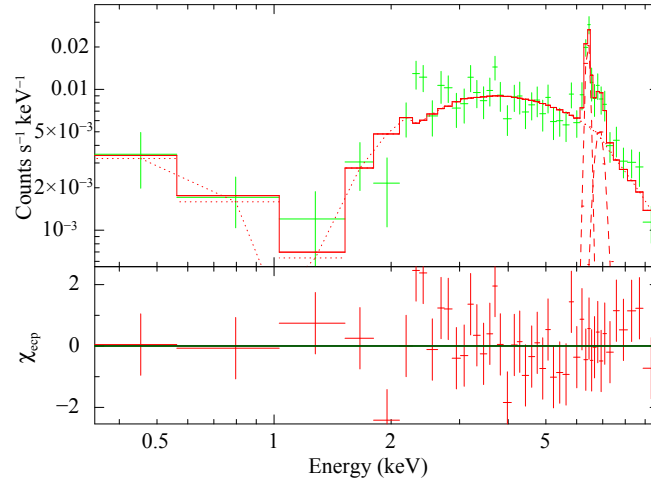


Fig. 2.20 Top panel shows An EPIC pn spectrum of IGRJ 16479–4514 obtained with XSPEC models. This spectrum is best fitted with a ‘POWERLAW’ modified by photoelectric absorption (‘PHABS’), two Gaussian functions(‘GAUSS’) and a blackbody emission (‘BBODYRAD’). Bottom panel shows χ corresponding to each energy bin as a deviation of the model from the actual data. X axis is Energy in KeV. Image courtesy: Aftab and Paul (2018)

Where $\sigma(E)$ is photoelectric absorption cross-section, and N_H is equivalent hydrogen column density in units of 10^{22} atoms cm^{-2} .

PCFABS:

Sometimes the X-ray absorber covers the source partially (i.e. covers some part of the source). Model ‘PCFABS’ accounts for that, which is given as,

$$X_{pcfabs}(E) = fe^{-N_{H1}\sigma(E)} + (1 - f) \quad (2.7)$$

N_{H1} is equivalent hydrogen column density in units of 10^{22} atoms cm^{-2} corresponding to partial covering and f is dimensionless covering fraction, given by $0 < f \leq 1$. $f = 1$ denotes full covering. ‘PCFABS’ is used as an additional absorbing column density in addition to ‘PHABS’

BBODYRAD:

Often below 2/3 keV, an excess over the power-law component is observed in the X-ray spectra of pulsars or other X-ray sources. The soft X-ray emission is known as soft excess. In some sources, blackbody could be the dominant model component and is modeled with XSPEC model 'BBODYRAD'. This model is expressed as

$$X_{bd}(E) = \frac{K \times 1.0344 \times 10^{-3} E^2 dE}{e^{E/KT} - 1} \quad (2.8)$$

Where kT is the temperature of the radiating region. $K = \frac{R_S^2}{d_{10}^2}$, where R_S is the source radius in km and d_{10} is the detector to source distance in units of $10 kpc$.

BREMSS:

In this thesis, in some cases soft excess required model 'BREMSS' for the best fit. 'BREMSS' models the X-ray photons originated in the bremsstrahlung process, which is given by

$$X_{brems}(E) = \frac{3.02 \times 10^{-15}}{4\pi d^2} \int n_e n_i dV \quad (2.9)$$

Where d is distance to source in cm and n_e and n_i are the electron and ion densities in cm^{-3} .

GAUSS:

Often a narrow excess is seen in the X-ray spectrum at some specific energies after the continuum of the spectra is well fitted. These are due to some emission lines at particular energies. XSPEC model 'GAUSS' is appropriate to fit the emission lines, which is given by

$$X_{Gauss}(E) = K \frac{1}{\sqrt{2\pi}\sigma} e^{-\frac{(E-E_c)^2}{2\sigma^2}} \quad (2.10)$$

Where E_c is the centroid of the emission line energy in keV , σ is the line width in keV , K is the total $photons cm^{-2} s^{-1}$ associated with the emission line.

GABS:

Model ‘GABS’ corresponds to absorption line and is given by

$$X_{abs}(E) = e^{\frac{-t}{\sqrt{2\pi}\sigma}} e^{-0.5\left(\frac{E-E_a}{\sigma}\right)^2} \quad (2.11)$$

Where E_a is the centroid energy of the absorption line in keV, σ is the line width in keV, t is the line depth in keV.

EDGE:

Model ‘EDGE’ is required to fit sharp absorption feature, which is given as

$$\begin{aligned} X_{edge}(E) &= 1 \quad (E \leq E_c) \\ &= e^{-D\left(\frac{E}{E_c}\right)^{-3}} \quad (E \geq E_c) \end{aligned} \quad (2.12)$$

Here E_c is the threshold energy and D is the absorption depth at the threshold.

HIGHECUT:

In some spectra above certain energies an exponential feature is seen in the spectrum, this feature is fitted with model ‘HIGHECUT’, which can be expressed as

$$\begin{aligned} X_{hc}(E) &= e^{\frac{(E_{cut}-E)}{E_f}} \quad (E \geq E_c) \\ &= 1.0 \quad (E \leq E_{cut}) \end{aligned} \quad (2.13)$$

Figure 2.20 shows an EPIC pn spectrum of IGR J16479–4514 fitted with XSPEC models. This spectrum is best fitted with a ‘POWERLAW’ modified by photoelectric absorption (‘PHABS’), two Gaussian functions(‘GAUSS’) and a blackbody emission (‘BBODYRAD’).

Chapter 3

X-ray reprocessing: Through the eclipse spectra of high mass X-ray binaries with *XMM-NEWTON*

"All my life through, the new sights of Nature made me rejoice like a child."

- Marie Curie

3.1 Introduction

In HMXB systems the companion star is a high mass star ($\geq 10M_{\odot}$), either a main-sequence star or a supergiant. A fraction of the amount of X-rays emitted due to accretion onto the compact object interact with the surrounding matter (accretion disc or companion's wind or companion's surface or all of these in some cases) and are re-emitted mainly as the same or lower energy X-rays. This phenomenon is known as X-ray reprocessing. Analyzing these reprocessed X-ray emissions we can infer the environment of the compact object in an X-ray binary system. But the difficult aspect of studying reprocessed X-rays in X-ray

The work presented in this chapter has been submitted to MNRAS and is under review

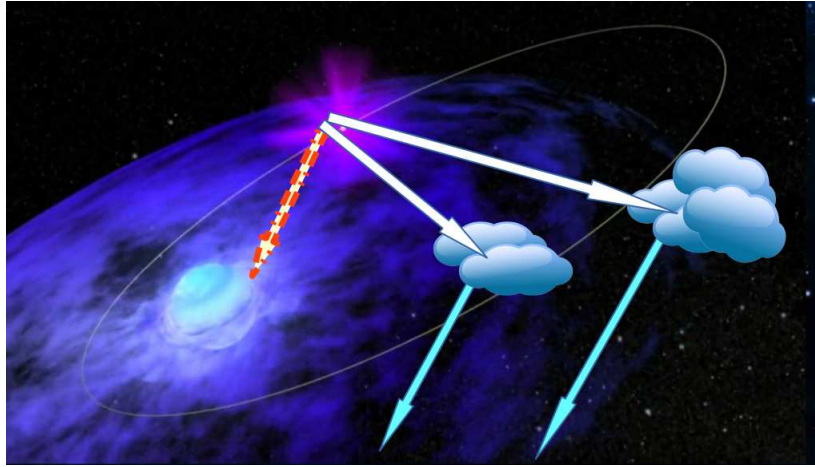


Fig. 3.1 Schematic of X-ray reprocessing in a HMXB system during eclipse. The primary X-ray photons emitted by the compact object are blocked by the companion. Only the reprocessed X-ray emissions scattered by the companion's wind reach the observer. The white arrows represent direct X-rays from the compact object, while the arrows with colour cyan represent the reprocessed X-rays. The white arrow with red dashed border represents the direct X-ray emission, which is being blocked by the companion. So the observer sees only the reprocessed X-ray emissions during eclipse. Image courtesy: Some parts of the image has been taken from <https://www.youtube.com/channel/UC8SgBnHvY8wzrX3c0VcHfFg> and <http://mzayat.com/single/3170388.html>

binary systems is that the reprocessed emission is detected along with the primary emission from the compact object, which is much brighter. During eclipse, the primary emission is blocked by the companion star and only the reprocessed emission is detected, allowing more clear study of the reprocessing agents. Figure 3.1 represents a cartoon picture of X-ray reprocessing in a HMXB system during eclipse.

In this work we have analyzed all available observations of the HMXBs with *XMM-Newton* EPIC pn that include eclipses, i.e in 7 Supergiant HMXBs or SgHMXBs (Cen X-3, 4U 1700-377, 4U 1538-52, SMC X-1, LMC X-4, IGR J18027-2016, IGR J17252-3616) and in 2 Supergiant Fast X-ray Transients (SFXTs) namely IGR J16479-4514 and IGR J16418-4532. A list of the important parameters of these sources are given in Table 3.1. We have

also analyzed the out of eclipse spectra, whenever available in the same observation along with the eclipse.

We try to infer the X-ray wind characteristics of these systems, which is the main re-processing agent in the high mass X-ray binaries. The eclipse spectrum of some of these sources have been studied before (Naik and Paul, 2012; van der Meer et al., 2005; Ebisawa et al., 1996), but here we report results from first comprehensive study of all available HMXB eclipse spectrum with *XMM-NEWTON* EPIC pn in a systematic manner.

3.2 Observation and data analysis

XMM-Newton was launched into space in December 1999 which consists of 3 sets of co-aligned X-ray telescope each with an effective area of 1500 cm^2 with the following focal plane instruments: three European Photon Imaging Camera (EPIC) and two Reflection Grating Spectrometers (RGS). Two of the cameras are made of Metal Oxide Semi-conductor (MOS) CCD (Turner et al., 2001) arrays and one uses pn CCDs (Strüder et al., 2001). The pn camera is placed at the focal plane of one telescope and the two MOS cameras along with the RGS are placed at the focal plane of other two telescopes. There is one co aligned Optical/UV Monitor (OM) telescope (Mason et al., 2001) which provides simultaneous optical and UV coverage with the X-ray instruments.

According to the observation requirements different read out modes can be selected (Lumb et al., 2012), namely full frame; large window; small window; timing mode. The MOS and pn cameras provide imaging over the $30'$ field of view in the energy range of 0.15–15 keV with a spectral resolution of 20–50 (E/ Δ E) and angular resolution of $6''$.

We referred to Liu et al. (2000) for eclipsing HMXBs and then looked for the available EPIC pn observations in HEASARC online service. We shortlisted all EPIC pn observations

covering eclipse/eclipses comparing with long term *Swift*-BAT orbital profiles (Left figures in Figure 3.2-3.14). We found eclipse observations of 9 HMXBs with a total of 13 observations, 11 of which were carried out in the imaging mode, rest of the two are with timing mode. The Details of the mode of operation are given in Table 3.2. We used the *XMM-Newton* Science Analysis Software (SAS) version 14.0.0 to reduce the data. We extracted the event files with the SAS tool EVSELECT. We checked for flaring particle background and did not find it in any of the observations. We extracted the events in the energy range of 0.3-12 keV. We first extracted the lightcurve for the whole duration of observation, then identified the eclipse and out-of-eclipse (whenever available) duration comparing it with the long term average BAT orbital profile and extracted the eclipse and out-of-eclipse events. From these events we extracted source along with background images for each observation. Seeing the image quality we decided the size of the source region to avoid contribution from excess background counts and edge of a CCD. In case of observations with imaging mode we extracted (18-30)'' circular source regions. For each observation we extracted circular background region of same size of the source region from a region which is free from any other X-ray sources. In case of timing mode we extracted box regions with $33 \leq \text{RAWX} \leq 42$ for the source and $3 \leq \text{RAWX} \leq 5$ for the background for one observation (ID 0203500201) of LMCX-4, and with $28 \leq \text{RAWX} \leq 42$ for the source and $4 \leq \text{RAWX} \leq 6$ for the background for one observation (ID 0083280401) of 4U1700-377. We checked for pileup with the SAS task EPATPLOT. For some of the observations in Imaging mode during out-of-eclipse phases we noticed pile-up (Cen X-3, OB ID: 0111010101; LMC X-4, OB ID: 0142800101; SMC X-1, OB ID: 0011450101) and in these phases we removed the hotpixels of central 5'' region to get rid of the effect of pileup in the science products. For these observations we extracted annular source regions with inner radius 5''.

3.2.1 EVENT SELECTION FROM THE LIGHTCURVES

We extracted source and background lightcurves from the source and background region files respectively from the single and double events (with $PATTERN \leq 4$) for the full exposure time for each observation with the SAS task EVSELECT. We subtracted the background lightcurve from the source lightcurve to obtain background subtracted source lightcurve using HEASARC FTOOL LCMATH. We confirmed the eclipse and the out-of-eclipse phases (whenever available) by plotting the EPIC pn lightcurve along with the average orbital profile of long term *Swift*-BAT lightcurve (Krimm et al., 2013a) for each observation, which are shown in left figures of Figure 3.2-3.14, where in the top panels we showed the long term *Swift*-BAT orbital profiles and in the bottom panels we showed the EPIC pn lightcurves. We showed the duration of eclipse events within two solid lines and that of the out-of-eclipse persistent phases within two dashed lines for the observations which cover both the eclipse and out-of-eclipse phases. Then we extracted separately 1) eclipse events 2) out-of-eclipse persistent events from the event files, for the observations which covers both the eclipse and the out-of-eclipse phases. The observations which was taken during eclipse phases only, we extracted eclipse spectra from the full event files of those observations. For that we first noticed the start and end time of each phases, then using the SAS task GTIBUILD we generated the good time intervals of the two phases. Then using the SAS task EVSELECT we extracted the eclipse and out-of-eclipse events (whenever available) for each observations.

3.2.2 SPECTRAL ANALYSIS

We extracted the spectra for both the eclipse and the out-of-eclipse phases (when available), from the single and double events (with $PATTERN \leq 4$) excluding the events which are at the edge of a CCD and at the edge to a bad pixel (with $FLAG=0$). For the extraction of the

spectra we used the SAS task EVSELECT. We generated response and ancillary files using the SAS task RMFGEN and ARFGEN respectively. We then extracted spectra from these eclipse events for each observation and from the events during out of eclipse persistent phases whenever available. We rebinned the spectra with the SAS routine SPECGROUP to have at least 20 counts per bin to be able to use χ^2 statistics. For observation ID 0405640201, 0405640601, 0405641001 of IGR J17252–3616 and 0679810101 of IGR J16418–4532 and 0600950101 of 4U 1700-377, each observation was taken only during eclipse. Observation ID 0512180101 of IGR J16479–4514 has observation during a small part of the ingress along with total eclipse phase, So for these 6 observations no out-of-eclipse spectra is available.

The out-of-eclipse spectra and the eclipse spectra are shown in the top panels of each figures at right in Figure (3.2-3.6) and in Figure (3.8 and 3.9) where the middle and the bottom panels show the contribution of each bin towards the χ^2 for the out of eclipse and eclipse spectra respectively. Top panels in the left figures of Figure 3.7 and Figure (3.10-3.14) show eclipse spectrum of these 6 observations where the bottom panels show the contribution of χ^2 for each bin for the eclipse spectra only.

ECLIPSE AND OUT-OF-ECLIPSE SPECTRA OF THE HMXBs

The eclipse spectra were primarily fitted with powerlaw modified by photoelectric absorption and a high energy cut-off for some sources. A few of the sources showed excess low energy emission and a blackbody component was added to the model for these sources. Excess narrow emission profiles were seen in some of the spectra at specific energies. The excess at specific energies were fitted with gaussian functions. Some sources show a significant soft excess below 1.5 keV while the power-law component is highly absorbed. The soft excess, therefore cannot originate at the same location as the power-law for these obser-

vations. We have fitted the soft excess as a blackbody with a different absorption column density in those observations, only for the purpose of characterizing its temperature and flux. If the soft excess originates in a much larger region elsewhere in the binary, its true nature may not be a blackbody and a bremsstrahlung may be a more appropriate description. The best fit parameters for the eclipse and the out-of-eclipse spectra for all eclipsing HMXBs and details of individual sources are discussed below.

Cen X-3:

The EPIC pn observation of Cen X-3 (OB ID: 0111010101) covers a large fraction of the total eclipse, eclipse egress and a small part of the out-of-eclipse persistent phase.

The eclipse spectrum of this observation was best fitted with a powerlaw modified by photoelectric absorption, a blackbody emission (bbodyrad), and 8 gaussian functions for emission lines at 0.98, 1.43, 1.98, 2.62, 3.34, 6.41, 6.66, 6.94 keV. The out-of-eclipse spectrum has been fitted with the same models used for the best fit of the eclipse spectrum but with different model parameters. The details are given in Table 3, 4 and 5. In the out-of-eclipse phase the power law photon index is slightly smaller, total flux in the energy range of (0.3-10) keV is larger by a factor of ~ 10 compared to the eclipse phase. We have detected 3 Fe emission lines (Fe K_{α} , Fe XXV and Fe XXVI) in both the eclipse and the out-of-eclipse phases. The flux for the three lines are 0.88, 2.12, 1.65 respectively in the eclipse phase and 15.01, 11.64, 9.58 respectively in the out-of-eclipse phase in units of 10^{-4} photons $\text{cm}^{-2} \text{sec}^{-1}$. Corresponding equivalent width are ~ 104 eV, ~ 246 eV, ~ 209 eV in the eclipse phase respectively and ~ 189 eV, ~ 131 eV, 139 eV in the out-of-eclipse phase respectively.

In the out-of-eclipse phase Fe K_{α} emission line flux and the equivalent width both increase, while the ionized Fe XXV and Fe XXVI emission line flux increase but the equivalent width decrease from their values in the eclipse phase. Fe K_{α} emission line flux increases more than 17 times and corresponding equivalent width increases by a factor of ~ 2 in the out-of-eclipse phase. The Fe XXV and Fe XXVI both emission line fluxes increase by a factor of more than 5 but their equivalent width falls by a factor of ~ 2 in the out-of-eclipse phase compared to their values in the eclipse phase. Same have been reported earlier from the same observation (Naik and Paul, 2012) and from an ASCA observation of Cen X-3 (Ebisawa et al., 1996)

LMC X-4:

We have analyzed two observations of LMC X-4, where first one was observed on 9th September 2003 and the second one was observed on 16th June 2004. The first EPIC pn observation of LMC X-4 (OB ID: 0142800101) covers three pre eclipse bursts, out-of-eclipse persistent emission, eclipse ingress, full length of the total eclipse and eclipse egress. Another observation of this source (OB ID: 0203500201) included out-of-eclipse persistent phase, eclipse ingress, full length of the total eclipse including a small burst and eclipse egress phases.

In the first observation (OB ID: 0142800101) of LMC X-4 there were three bursts at the beginning of the observation, we extracted out-of-eclipse spectrum for this observation excluding the period of the burst where the source intensity was steady, which is shown by the dotted lines in the left panel of Figure 3.3. The pulse profile evolution of LMC X-4 during and after the flares have been reported from this observation (Beri and Paul,

2017b). In the other observation (OB ID: 0203500201) of LMC X-4 a small burst has been found during eclipse, we extracted the eclipse spectrum for this observation excluding the events during the bursts. Eclipse spectrum of the first observation (OB ID: 0142800101) of LMC X-4 was fitted with a powerlaw modified by photoelectric absorption, along with a blackbody and a gaussian function for Fe K_{α} emission line. The fit was giving very low value of the line of sight equivalent hydrogen column density or N_{H} . We then referred to Beri and Paul (2017a) and Naik and Paul (2004) and also HEASARC TOOL in search for average N_{H} near the source and in HEASARC within 1° from the position of LMC X-4. Accordingly we have frozen N_{H} with a value of $0.1 \times 10^{22} \text{ cm}^{-2}$. The best fit value for the line energy was 6.36 keV with a flux of $0.08 \times 10^{-4} \text{ photons cm}^{-2} \text{ sec}^{-1}$. For the out-of-eclipse spectrum of this observation the best spectral fit was obtained with a model consisting of a power-law modified by photoelectric absorption, a blackbody emission, a bremsstrahlung radiation and two gaussian functions, one for Fe XXV emission line another for a low energy emission of 0.80 keV. N_{H} was frozen with the same value as for the eclipse spectrum. In the out-of-eclipse phase, the power law photon index increases by ~ 0.5 , total flux in the energy range of (0.3-10) keV is larger by factor of more than 278 compared to the eclipse phase. low ionized (or neutral) Fe K_{α} emission line has been detected during eclipse with high equivalent width ($\sim 663 \text{ eV}$) but it was absent in the out-of-eclipse phase, while highly ionized 6.56 keV Fe XXV emission line has been detected in the out-of-eclipse phase, with line flux of $3.54 \times 10^{-4} \text{ photons cm}^{-2} \text{ sec}^{-1}$ and equivalent width of $\sim 144 \text{ eV}$, but it was absent in the eclipse phase.

Second observation of LMC X-4 (OB ID: 0203500201) was carried out in timing mode. The best fit model for the eclipse spectrum of this observation was obtained with a powerlaw modified by photoelectric absorption and a blackbody emission. The line of sight

hydrogen column density was fixed at $0.1 \times 10^{22} \text{ cm}^{-2}$ for the eclipse spectrum similar to the eclipse and the out-of-eclipse spectrum of the previous observation of this source. The out-of-eclipse spectrum of this observation got the best fit with a powerlaw modified by photoelectric absorption with $N_{\text{H}} = 0.05 \times 10^{22} \text{ cm}^{-2}$, a bremsstrahlung radiation and 3 gaussian functions of emission energies 0.98, 6.38, 6.99 keV. The powerlaw photon index in the out-of-eclipse phase increases by ~ 0.8 , while total flux in the energy range of (0.3-10) keV was larger by a factor of ~ 86 compared to the eclipse phase. We have detected Fe K_{α} emission line in the out-of-eclipse phase with a flux of $1.55 \times 10^{-4} \text{ photons cm}^{-2} \text{ sec}^{-1}$ and the equivalent width of $\sim 116 \text{ eV}$. The ionized Fe XXVI emission line has been detected in the out-of-eclipse phase with an emission flux of $2.37 \times 10^{-4} \text{ photons cm}^{-2} \text{ sec}^{-1}$ and an equivalent width of $\sim 194 \text{ eV}$ respectively. In the eclipse spectrum we found some positive residuals in (6-7) keV energy range, but due to poor statistics we could not constrain the energy of the emission lines. However just to compare the line fluxes, we fitted the eclipse spectrum with the two Fe emission lines (Fe K_{α} and Fe XXVI), freezing the line energy and the width as obtained in the out-of-eclipse spectrum. Including these lines we have obtained very little improvement of χ^2 from a value of 103.83 for 94 degrees of freedom to 100.64 with 92 degrees of freedom. We have found a flux of $2.62 \times 10^{-6} \text{ photons cm}^{-2} \text{ sec}^{-1}$ for Fe K_{α} emission line and a flux of $2.87 \times 10^{-6} \text{ photons cm}^{-2} \text{ sec}^{-1}$ for Fe XXVI emission line respectively, which are less significant than 3σ . Nominal values of the emission fluxes for Fe K_{α} and Fe XXVI emission line, when included in the model are lower by a factor of ~ 59 and ~ 83 compared to the out-of-eclipse spectrum respectively.

SMC X-1:

SMC X-1 (Observation ID: 0011450101) covers a very small portion of the out-of-eclipse persistent phase, eclipse ingress and full length of the total eclipse during the EPIC pn observation.

The eclipse spectrum of SMC X-1 has been modeled with a powerlaw with high energy cut-off modified by photoelectric absorption, a blackbody emission and a gaussian function for Fe K_{α} emission line of 6.38 keV. The high energy cut-off was found to have a value of 2.46 keV with a folding energy of 3.6 keV. The best fit for the out-of-eclipse spectrum was found with the above models except the Fe K_{α} emission line. The high energy cut-off was found to have a value of 2.59 keV with a folding energy of 8.12 keV. The powerlaw photon index has a negative value ($\Gamma = -0.56$) in the eclipse phase and it increases to 0.2 in the out-of-eclipse phase. We also get good fit for the eclipse spectrum with the same models as mentioned above for this phase with the same powerlaw photon index (0.2) as obtained for the best fit of the out-of-eclipse spectrum, but with nearly double high energy cut-off and folding energy. χ^2 (194.10) for this fit is higher than χ^2 (181.73) of the previous fit. So we report the parameter values in Table 3.3 and 3.4 from the previous fit only. The total flux in the energy range of (0.3-10) keV in the out-of-eclipse phase is larger by a factor of ~ 77 compared to its value in the eclipse phase. During the eclipse phase we have detected Fe K_{α} emission line with flux and equivalent width of 0.07×10^{-4} photons $\text{cm}^{-2} \text{sec}^{-1}$ and ~ 126 eV respectively. We did not detect any Fe K_{α} emission line during the out-of-eclipse phase, but we can not rule out the line as the duration of the out-of-eclipse phase compared to the eclipse phase was very short (lower by a factor of ~ 44) and the continuum flux was higher by a large factor (~ 77 times) in the out-of-eclipse phase from the eclipse phase. We derived an upper limit of equivalent width of ~ 13 eV for an emission line at 6.4 keV which is one

order of magnitude lower than its value in eclipse phase.

4U 1700–377:

We have analyzed two observations of 4U 1700–377 (OB IDs: 0083280401, 0600950101) carried out on 20th February 2001 and 1st September 2009 respectively. The first one covers some part of the total eclipse, the eclipse egress and a small portion of the out-of-eclipse persistent phase and the second one covers nearly full length of the eclipse phase.

The first observation (OB ID: 0083280401) was carried out in timing mode. For the eclipse spectrum in this observation the best fit has been obtained with a powerlaw modified by photoelectric absorption and a gaussian function with energy 6.19 keV. This observation ID includes a shorter duration of the eclipse and the spectrum has limited statistics. Only one Fe emission line is detectable. The out-of-eclipse spectrum of this observation initially was fitted with the above models. The soft excess in the out-of-eclipse spectrum could not be fitted by a blackbody emission with the same photoelectric absorption as the power law. Addition of a less absorbed blackbody emission gives the best fit with the line of sight equivalent hydrogen column density $0.01 \times 10^{22} \text{ cm}^{-2}$ which is 4 orders of magnitude lower than that for the powerlaw. The powerlaw photon index has a negative value (-0.07) during eclipse, in the out-of-eclipse phase it increases by ~ 0.8 and has a positive value (0.74). The total flux in the energy range of (0.3-10) keV is large by ≥ 8 times compared to the eclipse phase. 6.19 keV and 6.21 keV emission lines in the eclipse and the out-of-eclipse phase respectively are slightly lower than 6.4 keV Fe K_{α} emission line. There are uncertainties about the energy response calibration of EPIC-PN in the timing mode, perhaps due to that Fe K_{α} emission line has been detected with little lower energies. During eclipse 6.19 keV

emission line flux has been found to be 8.79×10^{-4} photons $\text{cm}^{-2} \text{sec}^{-1}$ with a very high equivalent width of ~ 1429 eV. During out-of-eclipse phase the flux for 6.21 keV emission line is found to be 26.29×10^{-4} photons $\text{cm}^{-2} \text{sec}^{-1}$ which is ~ 3 times higher than its value during eclipse and the equivalent width decreases by a factor of 9 to ~ 160 eV

The eclipse spectrum from the second observation (OB ID: 0600950101) has been fitted with a powerlaw modified with high energy cut-off by photoelectric absorption, blackbody emission and 13 gaussian functions with energies 0.81, 1.28, 1.75, 1.97, 2.34, 2.57, 2.99, 3.70, 4.12, 6.39, 6.68, 7.05 and 7.49 keV. The powerlaw photon index is found to have a negative value of -1.34. Value of the high energy cut-off was determined to be 5.58 keV with a folding energy of 4.59 keV. The best fit was obtained with the addition of an edge at 7.06 keV. The Fe K_{α} emission line flux has been found to be 4.89×10^{-4} photons $\text{cm}^{-2} \text{sec}^{-1}$ with very high equivalent width of ~ 1061 eV. The Fe XXV emission line flux has been found to be low, 0.26×10^{-4} photons $\text{cm}^{-2} \text{sec}^{-1}$ with very small equivalent width of ~ 22 eV. 7.05 keV emission line flux and equivalent width has been found to be 0.88×10^{-4} photons $\text{cm}^{-2} \text{sec}^{-1}$ and ~ 219 eV respectively.

In the eclipse spectrum of the second observation we have detected many emission lines while in the eclipse spectrum of the first observation we have detected only one emission line. The eclipse duration covered in the first observation was significantly shorter than that in the second observation. We checked for the upper limits of the emission lines which were not detected in the eclipse spectrum of the first observation and we have found low upper limit of equivalent width of those lines. For example in the first observation during eclipse, we obtained an upper limit on equivalent width of ~ 174 eV for a second Fe emission lines from a fit with the line energy in the range of 6.8-7.25 keV. Equivalent width of 7.05 keV emission line was found to be ~ 219 eV in the eclipse spectrum of the second observation.

We can say that because of limited statistics we could not constrain other emission lines in the eclipse phase of the first observation.

4U 1538–522:

The EPIC pn observation of 4U 1538–522 (OB ID: 0152780201) covers a small part of the out-of-eclipse persistent phase, eclipse ingress and full length of the total eclipse.

The eclipse spectrum of this observation was best fitted with a powerlaw modified by photoelectric absorption, 7 gaussian functions with energies 1.26, 1.85, 2.40, 6.02, 6.38, 6.69 and 6.95 keV. The out-of-eclipse spectrum of this observation got the best fit with a powerlaw modified by photoelectric absorption along with a less absorbed blackbody emission. The line of sight equivalent hydrogen column density associated with the powerlaw emission is $17.17 \times 10^{22} \text{ cm}^{-2}$, while that for the blackbody emission is found to be $0.54 \times 10^{22} \text{ cm}^{-2}$. This value is less by a factor more than 30 than that for the powerlaw emission. The powerlaw photon index in the out-of-eclipse phase increases by ~ 0.5 and the total flux in the energy range of (0.3-10) keV is enhanced by a factor of ≥ 30 compared to its value in the eclipse phase. Both the eclipse and the out-of-eclipse spectrum show the signatures of Fe K_{α} emission line with fluxes of $0.57 \times 10^{-4} \text{ photons cm}^{-2} \text{ sec}^{-1}$ and $2.46 \times 10^{-4} \text{ photons cm}^{-2} \text{ sec}^{-1}$ with equivalent width of $\sim 792 \text{ eV}$ and $\sim 79 \text{ eV}$ respectively. The flux for the Fe K_{α} emission line increases by a factor of ≥ 4 while the equivalent width decreases by a factor of more than 10 in the out-of-eclipse phase from its value in the eclipse phase. Figure 3.8 shows that the soft X-ray emission in the eclipse and the out-of-eclipse spectra overlaps, corresponding flux in the energy range of 0.3-2.0 keV is obtained as 1.76×10^{-13}

ergs cm⁻² sec⁻¹ and 2.08×10^{-13} ergs cm⁻² sec⁻¹ respectively.

IGR J18027–2016:

The EPIC pn observation of IGR J18027–2016 (OB ID: 0745060401) covers a major part of the total eclipse, eclipse egress and some part of the out-of-eclipse phase.

The eclipse spectrum of this observation was best fitted with a powerlaw modified by photoelectric absorption and a gaussian function for the low ionized (or neutral) Fe K α emission line of energy 6.51 keV. The best fit for the out-of-eclipse spectrum has been obtained with a powerlaw modified by photoelectric absorption only. The powerlaw photon index in the eclipse phase has been found to be negative (-0.24), in the out-of-eclipse phase it increases by ~ 1 and becomes positive (0.71). The total flux in the energy range of (0.3-10) keV in the out-of-eclipse phase is increased by a factor of ≥ 43 . Fe K α emission line has been detected only in the eclipse spectrum with slightly higher energy of 6.51 keV with high equivalent width (~ 1608 eV). The flux for this emission line was found to be 0.14×10^{-4} photons cm⁻² sec⁻¹.

IGR J16479–4514:

The EPIC pn observation of IGR J16479–4514 (OB ID: 0512180101) covers the eclipse ingress and a major part of the total eclipse. We extracted only eclipse spectrum from the total eclipse event for this observation.

The eclipse spectrum of this observation was best fitted with a powerlaw modified by photoelectric absorption with two gaussian functions with energies 6.41 keV and 6.88 keV

and a less absorbed blackbody emission associated with the line of sight equivalent hydrogen column density of $0.58 \times 10^{22} \text{ cm}^{-2}$ which is a factor of ~ 8 lower than that associated with the powerlaw. The powerlaw photon index has been found to be 1.28 which is the highest amongst all the eclipse spectrum of all the sources described here. The Fe K_{α} emission line flux is low with a value of $0.09 \times 10^{-4} \text{ photons cm}^{-2} \text{ sec}^{-1}$ and equivalent width of $\sim 803 \text{ eV}$. The energy value for the 6.88 keV emission line is not well constrained like Fe XXVI emission line for other observations (Please see Table 3.4), the flux for this emission line is $0.05 \times 10^{-4} \text{ photons cm}^{-2} \text{ sec}^{-1}$ with an equivalent width of $\sim 567 \text{ eV}$.

IGR J16418–4532:

The EPIC pn observation of IGR J16418–4532 (OB ID: 0679810101) covers only a major part of the total eclipse.

So for this observation we extracted the eclipse spectrum only, which has been best fitted with a powerlaw modified by photoelectric absorption and a gaussian function of low ionized (or neutral) Fe K_{α} emission line of energy 6.46 keV. The powerlaw photon index has been found to be negative with a value of -0.28. The Fe K_{α} emission line flux has been found to be $0.07 \times 10^{-4} \text{ photons cm}^{-2} \text{ sec}^{-1}$ with a high equivalent width of 1903 eV.

IGR J17252–3616:

We have analyzed three observations of IGR J17252–3616, all during eclipse phases observed between 29th august-27th September, 2006 (OB IDs: 0405640201, 0405640601, 0405641001).

All three observations were initially fitted with powerlaw modified by photoelectric absorption. For the best fit, the first observation needed a less absorbed blackbody emission and two gaussian functions. One gaussian is for Fe K_{α} emission line of 6.4 keV and another with a value of 7.01 keV. The second observation got the best fit with the same models as the first observation, except the gaussian with a value of 7.01 keV. While the third observation got the best fit with addition of a gaussian function for Fe K_{α} emission line of energy 6.4 keV. The soft excess for this observation could not be fitted with blackbody emission. The power-law photon index was found to have a value of 0.24, 0.81 and -0.52 respectively in the three observations, while the Fe K_{α} emission line flux was 0.13, 0.18, and 0.04 in units of 10^{-4} photons cm^{-2} sec^{-1} respectively. The equivalent width was found to be significantly different for the three observations with values of ~ 2695 eV, ~ 1831 eV and ~ 921 eV respectively. The flux and equivalent width associated with 7.01 keV emission line is 0.05×10^{-4} photons cm^{-2} sec^{-1} and ~ 1227 eV respectively in the first observation. The line of sight equivalent hydrogen column density for the power law component for the three observations are 9.34, 18.17 and 13.48 respectively while that for the blackbody component are 0.90 and 2.67 for the first two observations respectively (all values in units of 10^{22} cm^{-2}) which are lower compared to the same for the power-law component by a factor of >10 and ~ 7 respectively.

3.3 Discussion

During the X-ray eclipses, direct emission from the compact object is blocked by the companion and the observed X-rays during eclipses are the reprocessed emission of the primary X-rays from the surrounding medium. For HMXBs, the main reprocessing agent is the stellar wind of the companion and any structures in the wind, if present. Among the mul-

multiple spectral components, the continuum is expected to be strongly suppressed during the eclipses and the emission lines which are often produced in a larger region in the stellar wind are expected to be suppressed to a lesser extent. The eclipse spectrum is therefore expected to show larger equivalent width and better detectability of the emission lines compared to the out-of-eclipse spectrum. However depending upon the distribution of the material around the compact object and the wind density, this effect can be different in different sources. To investigate the phenomena of X-ray reprocessing in stellar wind in a large number of HMXBs, and to find if there are significant system to system differences, we have analyzed 13 eclipse observations of 9 HMXBs with the out-of-eclipse observations, whenever available along with the eclipse phases in the same observation. We then compare the eclipse spectra of these sources, and also compare the eclipse and out-of-eclipse spectra of some sources. We have found some similarities and significant differences in the reprocessing properties of the HMXB systems we have analyzed. All these HMXBs are with supergiant companion stars with stellar mass in the range of $\sim 16M_{\odot}$ to $52M_{\odot}$, radius in the range of $8R_{\odot}$ to $26R_{\odot}$ and orbital period of binaries in the range of 1.41 days to 9.74 days. Accretion in three of these systems, LMC X-4, Cen X-3, and SMC X-1 are at least in parts due to Roche Lobe overflow (Savonije, 1978; van der Meer et al., 2007).

A summary of the comparison of various aspects of the X-ray reprocessing in these HMXBs is as follows: Equivalent width of the low ionized (or neutral) Fe K_{α} emission line during eclipse is found to have a wide range, from ~ 126 eV (in SMC X-1, OB ID: 0011450101) to ~ 2695 eV (in IGR J17252-3616, OB ID: 0405640201) i.e. a factor of >20 larger in the later source. Ratio of the equivalent width of these Fe K_{α} emission line during the eclipse and the out-of-eclipse phases also have a large range, from ~ 0.55 (in Cen X-3) to ~ 10 (in 4U 1538-522). Flux ratio of the eclipse to out-of-eclipse spectra shows a

wide range, from ~ 8 (in 4U 1700–377, OB ID: 0083280401) to ~ 278 (in LMC X–4, OB ID: 0142800101), which differs by a factor of ~ 35 . Even in the same source LMC X–4, the ratio of flux in the out-of-eclipse and the eclipse phase varies as much as by a factor of >3 (from ~ 278 to ~ 86) in different observations. Here we discuss the results of some individual sources.

3.3.1 Cen X–3:

In Cen X–3 (OB ID: 0111010101) three Fe emission lines i.e. 6.41 keV (Fe K_α) and 6.66 keV (Fe XXV) and 6.9 keV (Fe XXVI) have been detected. Equivalent width of Fe XXV and Fe XXVI emission lines have been observed to be higher in the eclipse phase as expected. The equivalent width of Fe K_α emission line has been found to be lower in the eclipse phase compared to the out-of-eclipse phase as observed by Naik and Paul (2012) and Ebisawa et al. (1996). Fe K_α emission line flux increases by a factor of more than 17 as the source comes out of the eclipse while FeXXV and FeXXVI emission line fluxes increase by a factor of ~ 5.5 and ~ 5.8 respectively. Similar result was obtained by Naik and Paul (2012). These observations confirm that most of the Fe K_α line emitting region were closer to the source and distributed in a region of size comparable or smaller than the radius of the companion star from the compact object. Ionization state of the Fe atoms are expected to be high near the compact object because of its intense X-ray emission. Two outcomes indicate low ionized Fe atoms to be closer to the compact object than highly ionized Fe atoms, i) equivalent width of Fe K_α emission line is lower during eclipse than its value in the out-of-eclipse phase ii) rate of increase of Fe K_α emission line flux is higher outside eclipse compared to the rate of increase of Fe XXV and Fe XXVI emission line flux. This is possible if the Fe atoms closer to the source are in very dense optically thick accretion disc

or in dense accretion stream. High density of the disc or the stream keeps the Fe atoms low ionized inspite of them being near to the source.

3.3.2 LMC X-4:

During eclipse in the first observation of LMC X-4 (OB ID: 0142800101) low ionized (or neutral) Fe K_{α} emission line has been detected with high equivalent width (~ 664 eV), but this line was absent in the out-of-eclipse phase. The large increase (>278 times) of the total flux in the out-of-eclipse phase perhaps strongly suppressed this emission line which makes it undetectable during the out-of-eclipse phase. Fe XXV emission line has been detected during the out-of-eclipse phase but it was absent in the eclipse phase, which indicates most of the highly ionized wind material which emits Fe XXV photons was distributed in a region less than the distance comparable to the radius of the companion from the compact object. During eclipse, the detection of low ionized (or neutral) Fe K_{α} emission line is marginal in the second observation of LMC X-4 (OB ID: 0203500201). However we can not rule out this line as the statistics of the eclipse spectrum of this observation is very poor. During out-of-eclipse phase in the second observation Fe K_{α} emission line is comparatively stronger. This indicates most of the low ionized Fe atoms were closer to the source during this observation. When the source came out of the eclipse, these Fe atoms showed their presence through the 6.38 keV emission line during the out-of-eclipse phase. This can happen only if these Fe atoms are in the dense accretion disc and/or accretion stream during this observation. Highly ionized 6.99 keV Fe XXVI emission line has also been detected during out-of-eclipse phase of the second observation, but it is insignificant in the eclipse phase, which possibly indicates that the origin of this emission line was very near to the compact object. However due to poor statistics of the eclipse spectrum we can not make any definitive comment about the scenario. During eclipse phase in the first observation of LMC X-4, the

total flux (0.3-10.0 keV) is lowered by a large factor (>278) from the out-of-eclipse phase while in the second observation this flux is decreased by a factor of ~ 86 which signifies a difference in the density and/or spatial distribution of the reprocessing material between these two observations. During eclipse in the first observation low ionized (or neutral) 6.36 keV Fe K_{α} emission line has been detected, while in the second observation during eclipse phase the detection of Fe K_{α} emission line is insignificant. In the first observation during the out-of-eclipse phase amongst Fe emission lines only highly ionized 6.56 keV Fe XXV emission line has been detected but in the second observation low ionized (or neutral) 6.38 keV Fe K_{α} emission line and highly ionized 6.99 keV XXVI emission line have been detected during out-of-eclipse phase. Presence of 6.99 keV Fe XXVI emission line during the out-of-eclipse phase in the second observation and its absence in the first observation in the same phase, again the absence of Fe XXV emission line in the out-of-eclipse phase in the second observation and its presence in the out-of-eclipse phase of first observation indicates hotter wind near the compact object during the second observation. But the presence of low ionized (or neutral) 6.38 keV Fe K_{α} emission line during the out-of-eclipse phase in the second observation raise a question. It can be justified if during the second observation low ionized Fe atoms are distributed closer to the source and in optically thick accretion disk or in the dense accretion stream. The high density of the stream makes them low ionized in spite of these Fe atoms being near to the source.

3.3.3 4U 1700–377:

Two observations of 4U 1700–377 were separated by a span of more than 8 years. In the first observation of 4U 1700–377 (OB ID: 0083280401) low ionized Fe K_{α} emission line has been detected in both the eclipse and out-of-eclipse phases with slightly lower value of emission line energy (6.19 keV and 6.21 keV respectively in the eclipse and out-

of-eclipse phases). The equivalent width of this low ionized (or neutral) Fe K_{α} emission line during eclipse was found to be higher as compared to the out-of-eclipse phase which is expected. The emission flux and the equivalent width of low ionized (or neutral) Fe K_{α} emission line was found to be higher in this observation during eclipse as compared to the other observation of this source during eclipse. This signifies greater reprocessing by low ionized Fe atoms during this observation compared to the later one or comparatively colder wind during this observation as Fe XXV and Fe XXVI emission lines have not been detected during this observation. Many low energy emission lines have been detected in the eclipse spectrum of the second observation but not detected in the eclipse phase of the first observation due to limited statistics.

The second observation of 4U 1700–377 (OB ID: 0600950101) covers only eclipse and in this phase low ionized (or neutral) Fe K_{α} and highly ionized Fe XXV emission lines have been detected along with other low energy emission lines and one emission line of energy 7.05 keV. 7.05 keV emission line can be Fe K_{β} line. The equivalent width of the low ionized (or neutral) Fe K_{α} emission line was very high (~ 1061 eV) and that of the Fe XXV emission line was quite low (~ 22 eV) in this observation. This indicates most of the Fe atoms lower ionized than Fe X were distributed far away from the source (at least at a distance comparable to the radius of the companion star from the compact object) during this observation.

3.3.4 Other sources

In SMC X–1 a weaker low ionized (or neutral) 6.38 keV Fe K_{α} emission line has been detected during eclipse but its detection is marginal in the out-of-eclipse phase with the lowest equivalent width amongst all sgHMXBs. Probably the bright continuum emission has suppressed this emission line in the out-of-eclipse phase.

In 4U 1538–522, the low ionized (or neutral) Fe K_{α} emission line has been observed in both the eclipse and the out-of-eclipse phase with greater equivalent width during eclipse phase as expected. The line of sight hydrogen column density for powerlaw and the soft excess differs by a large factor (>30) which indicates that soft X-ray emission are coming from a different region away from the source. Again nearly equal soft X-ray flux (0.3–2.0 keV) in the eclipse and the out-of-eclipse spectra indicates the origin of the soft X-rays far away (at least further away than the size of the companion) from the compact object and is not blocked during eclipse.

The low ionized (or neutral) Fe K_{α} emission line has been detected during eclipse with high equivalent width (~ 1608 eV) in IGR J18027–2016 but has not been detected in the out-of-eclipse phase, which is similar to the observation of SMC X–1 except that the equivalent width in case of SMC X–1 during eclipse phase was found low (~ 126 eV).

The observation of IGR J16479–4514, IGR J16418–4532 and the three observations of IGR J17252–3616 covered only eclipse. In these observations low ionized (or neutral) Fe K_{α} emission lines have been detected with large equivalent widths. In the first observation (OB ID: 0405640201) of IGR J17252–3616 the equivalent width was found to be largest (~ 2695 eV) amongst all the observations analyzed in this work. Different equivalent width (921–2695 eV) and flux (0.04–0.18 photons $\text{cm}^{-2} \text{sec}^{-1}$) of Fe K_{α} emission line in 3 observations of IGR J17252–3616 indicate a change of distribution and density of low ionized Fe atoms surrounding the compact object at least at a distance equal to the radius of the companion over a period of 1 month.

In the out-of-eclipse phase of the first observation of 4U 1700–377 and in 4U 1538–522, also in the eclipse phase of IGR J16479–4514 and in the first two observations of IGR J17252–3616, the line of sight equivalent hydrogen column density for the soft X-ray

emission are lower by several factor ($\sim 4-30$) than that for the power law. This signifies different origin for the hard and soft X-rays in these sources during observations mentioned above. Detection of a soft excess, even when the power-law component is absorbed by a very large column density of material ($\sim 10^{24} \text{ cm}^{-2}$) is known in some HMXBs (GX 301-2: Islam and Paul 2014a), and it has been attributed to a different origin of the soft component compared to the power-law component.

3.3.5 Comparison of SFXTs and SgHMXBs:

The SFXTs have much lower average X-ray luminosity compared to the SgHMXBs. The SFXTs also show low equivalent width of Fe emission line outside eclipse (Pradhan et al. 2017, submitted to A&A). However the equivalent width during eclipse in the two SFXTs (IGR J16479–4514, IGR J16418–4532) in our sample have equivalent width large and comparable to the SgHMXBs.

3.3.6 Various elements in the environment of supergiant HMXBs

We have found many emission lines other than Fe lines in 4 supergiant HMXB systems (Cen X–3, LMC X–4, 4U 1700–377, 4U 1538–522). In both the eclipse and out-of-eclipse phases in Cen X–3 and in either of the phases in other 3 sources we see the emission lines (Table 3.5), which indicates presence of various materials in the binary environment.

3.4 Conclusion

- We have found ample diversity in the X-ray reprocessing characteristics in high mass X-ray binaries. Even in the same source at different epochs the variation is quite large, which implies significantly dynamic wind structure surrounding the compact object in HMXBs.

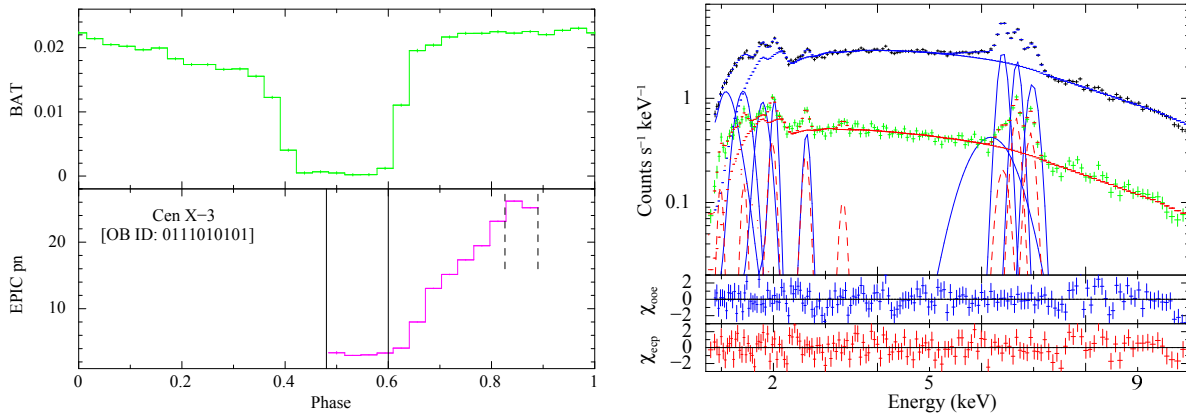


Fig. 3.2 **Left figure:** Top panel shows the long term average BAT orbital profile of Cen X–3 and the bottom panel shows EPIC pn light curve of Cen X–3 (OB ID: 0111010101) folded with its orbital period. The eclipse spectrum and the out-of-eclipse spectrum was extracted from the duration shown with the solid and the dotted lines respectively. **Right figure:** Top Panel gives the EPIC pn out-of-eclipse and the eclipse spectrum of Cen X–3, where datapoints for the out-of-eclipse spectrum are plotted with colour black and that of eclipse spectrum are plotted with colour green. Model components of the out-of-eclipse and the eclipse spectrum is shown with the colour blue and red respectively. The emission line for the out-of-eclipse spectrum is shown with blue solid line and those for the eclipse spectrum are shown with red dash lines. The middle and bottom panels show the residuals to the best fit spectral model for the out-of-eclipse spectrum and the eclipse spectrum respectively.

- Equivalent width of Fe emission lines in SFXTs are large during eclipse similar to that in SgHMXBs. Cen X–3 was one exception for which equivalent width was lower during eclipse for Fe k_{α} emission line.
- In few sources, in some particular phases we have found different origin for the hard and soft X-rays.
- There are signatures of various elements in the HMXB environment.

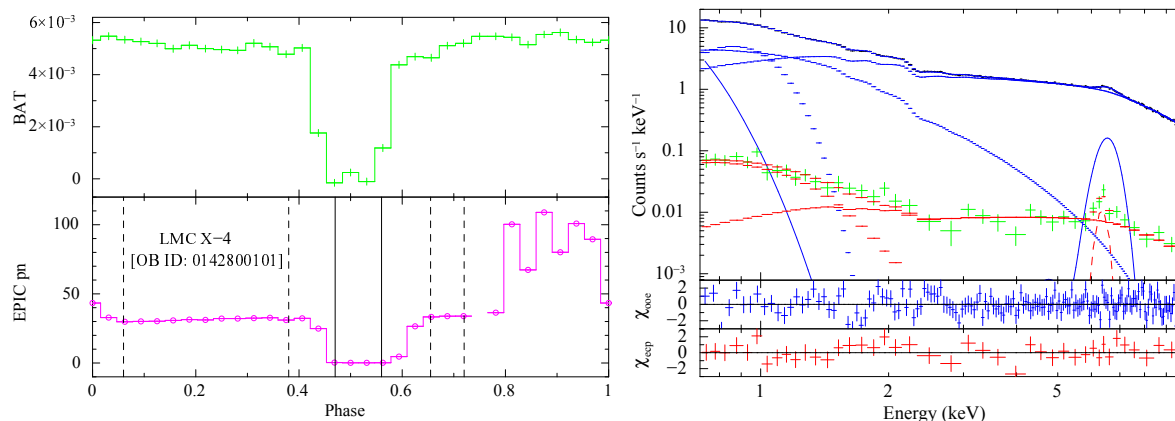


Fig. 3.3 Same as Figure 3.2 for LMC X-4 (OB ID: 0142800101)

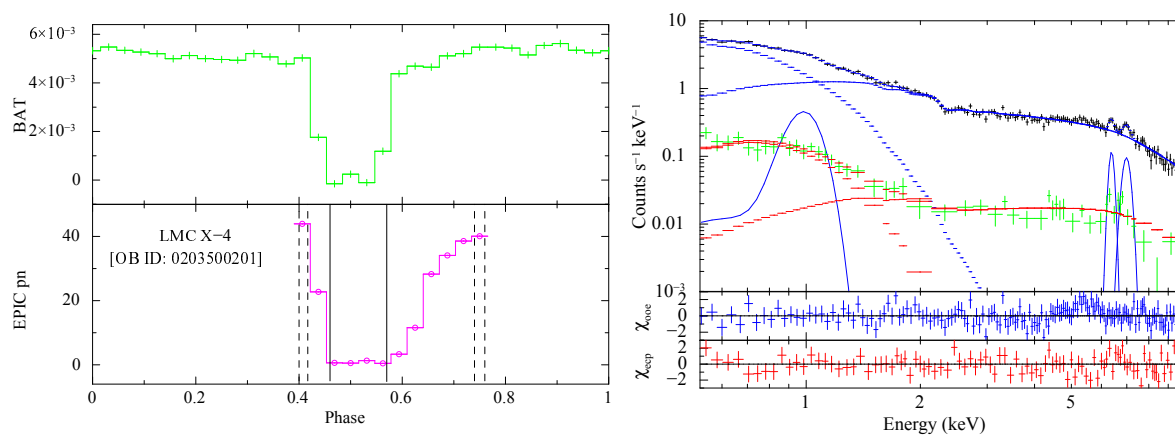


Fig. 3.4 Same as Figure 3.2 for LMC X-4 (OB ID: 0203500201)

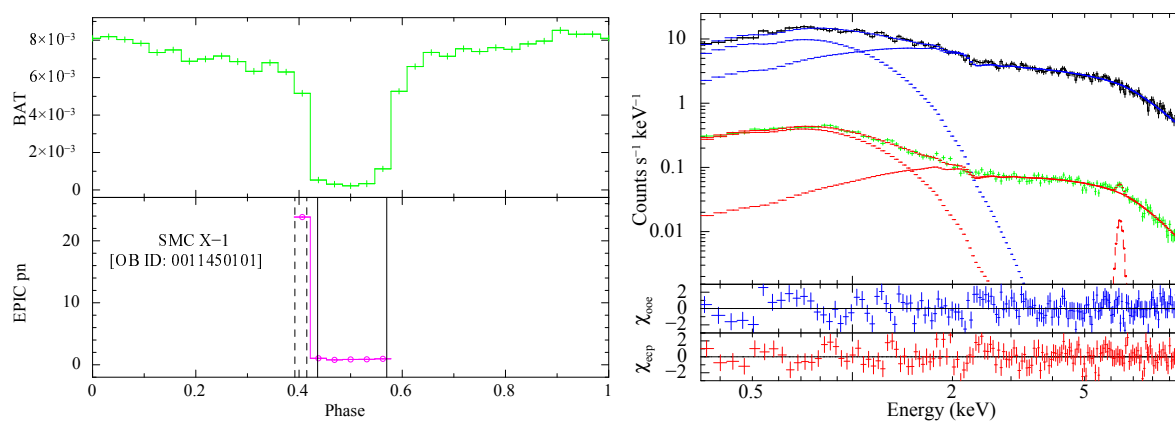


Fig. 3.5 Same as Figure 3.2 for SMC X-1 (OB ID: 0011450101)

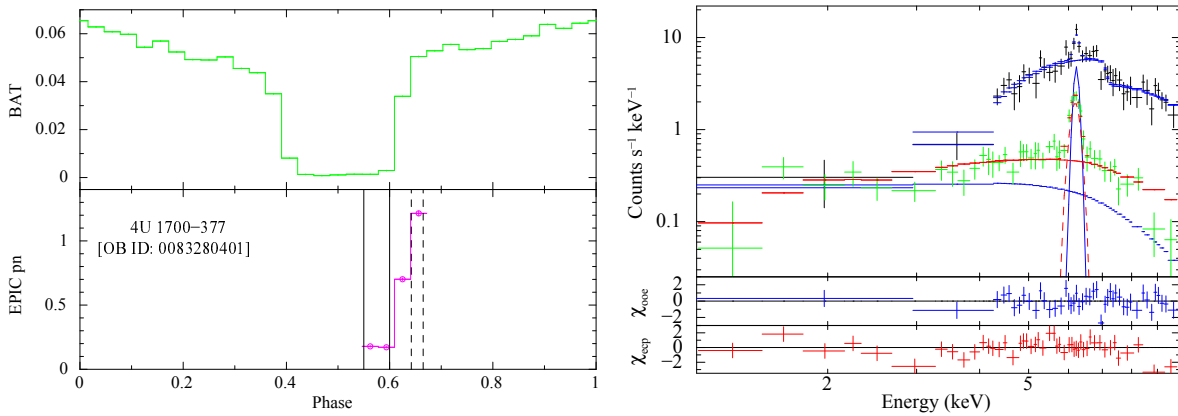


Fig. 3.6 Same as Figure 3.2 for 4U 1700-377 (OB ID: 0083280401)

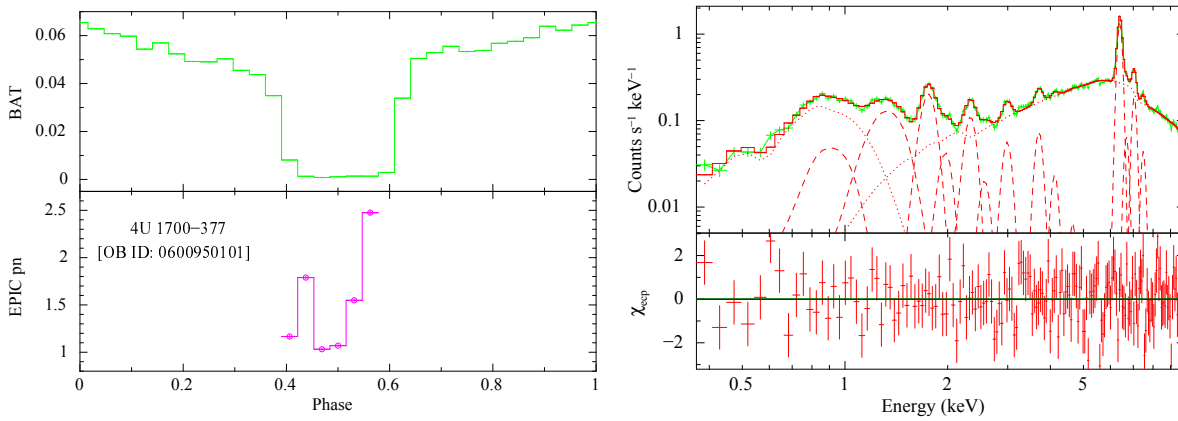


Fig. 3.7 **Left figure:** Top panel shows the long term average BAT orbital profile of 4U 1700-377 and the bottom panel shows EPIC pn light curve of 4U 1700-377 (OB ID: 0600950101) folded with its orbital period. **Right figure:** Top Panel gives the EPIC pn eclipse spectrum of 4U 1700-377. The bottom panels show the residuals to the best fit spectral model for the eclipse spectrum.

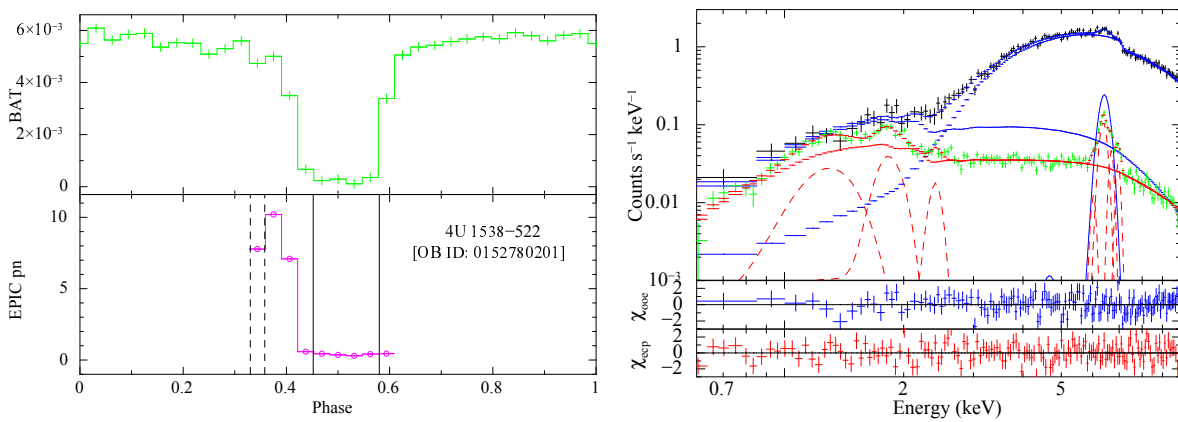


Fig. 3.8 Same as Figure 3.2 for 4U 1538-522 (OB ID: 0152780201)

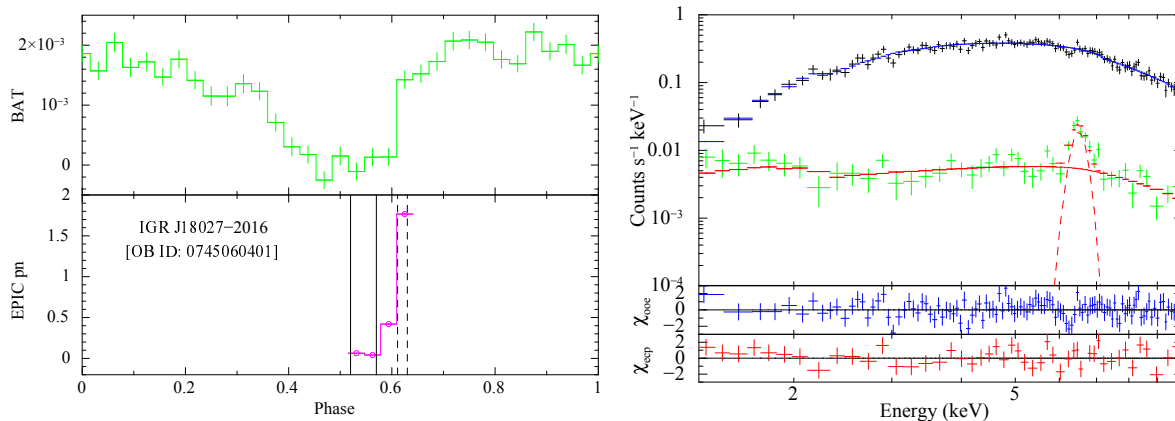


Fig. 3.9 Same as Figure 3.2 for IGR J18027-2016 (OB ID: 0745060401)

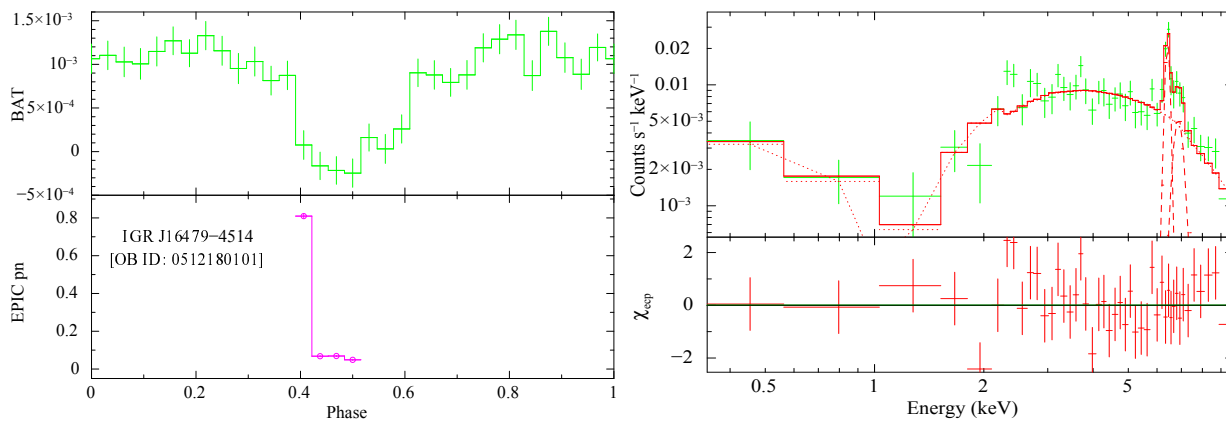


Fig. 3.10 Same as Figure 3.7 for IGR J16479-4514 (OB ID: 0512180101)

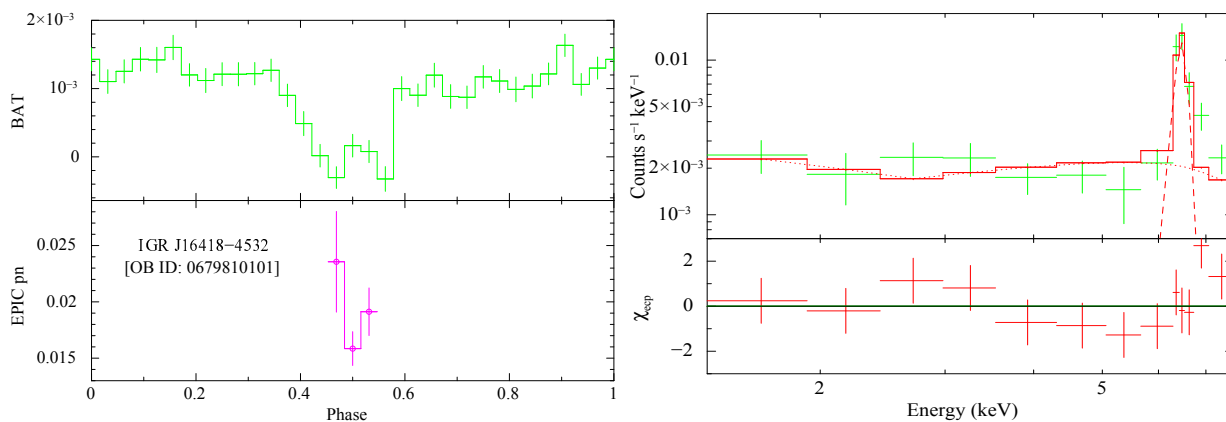


Fig. 3.11 Same as Figure 3.7 for IGR J16418-4532 (OB ID: 0679810101)

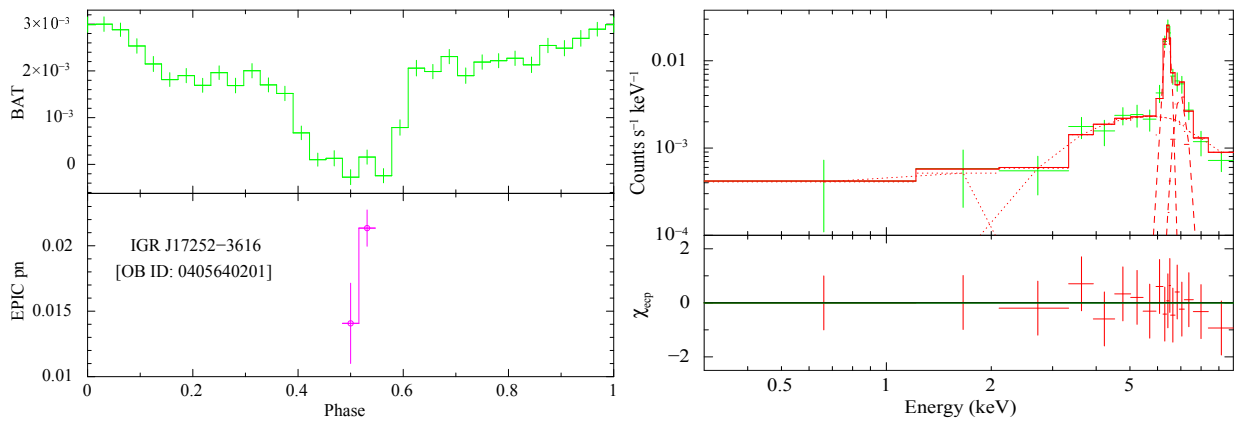


Fig. 3.12 Same as Figure 3.7 for IGR J17252-3616 (OB ID: 0405640201)

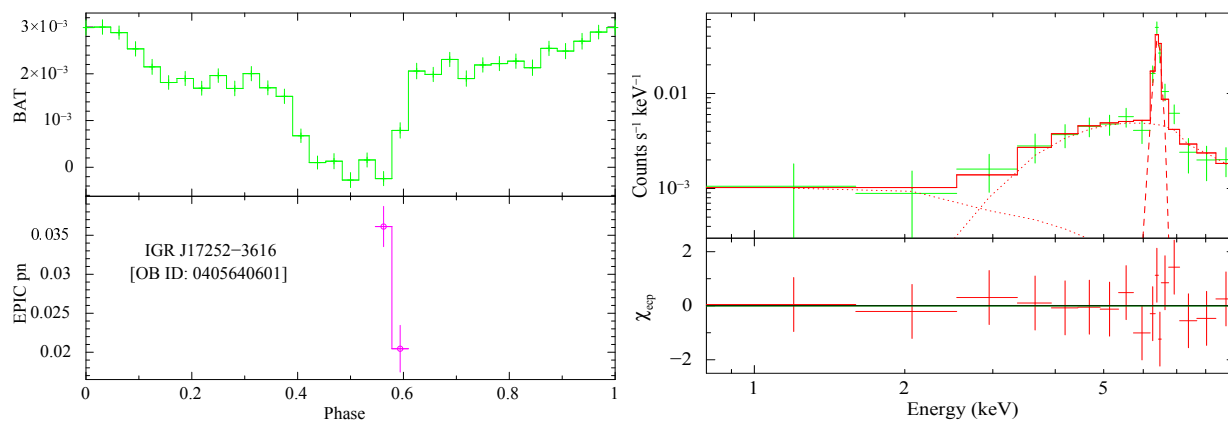


Fig. 3.13 Same as Figure 3.7 for IGR J17252–3616 (OB ID: 0405640601)

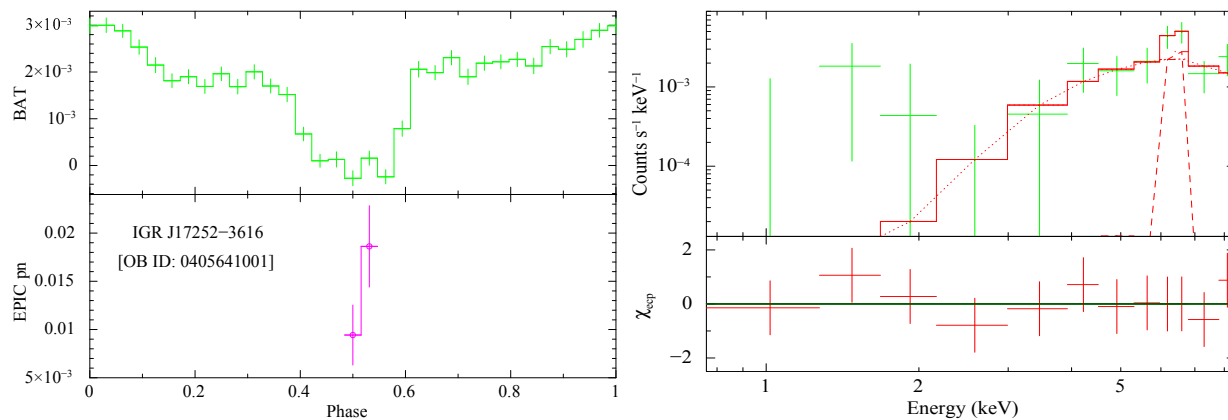


Fig. 3.14 Same as Figure 3.7 for IGR J17252–3616 (OB ID: 0405641001)

Table 3.1 List of basic parameters of the eclipsing HMXBs analyzed in this work, where P_{orb} : Orbital Period, M_C : Mass of the companion, R_C : Radius of the companion star, S_C : Spectral type of the companion, e : Eccentricity of the HMXB orbit, a : Length of the semi major axis of the system, \dot{M}_w : Mass loss of the companion star, d : Distance from Earth. (M_\odot , R_\odot : Mass and radius of Sun respectively)

Source	Discovery	P_{orb} (days)	M_C (M_\odot)	R_C (R_\odot)	S_C	e	a ($a_s \sin i$) (light-sec)	\dot{M}_w ($10^{-7} M_\odot \text{ yr}^{-1}$)	d (kpc)
Cen X-3	Rocket borne detector ^{a1} (1967)	2.09 ^{a2}	(20.5±0.7) ^{a3}	12.1±0.5 ^{a4}	O6.5 II-III ^{a4}	≤0.0016 ^{a5}	39.6612±0.0009 ^{a6}	5.3 ^{y1}	5.7±1.5 ^{a7}
LMC X-4	UHURU (1972) ^{b1}	1.41 ^{b2}	14.5 ^{+1.1a4} _{-1.0}	7.8 ^{+0.3a4} _{-0.4}	O8 III ^{a4}	0.0006±0.0002 ^{b3}	26.343±0.016 ^{b3}	2.4 ^{y1}	49.97±0.19±1.11 ^{b4}
SMC X-1	UHURU (1971) ^{c1}	3.89 ^{c2}	(16.6 ± 0.4) ^{c3}	18 ^{c4}	B0 I ^{c5}	<0.0007 ^{c4}	53.4876 lt-sec ^{c6}	15 ^{y1}	60.6±1.0±2.8 ^{c7}
4U 1700–377	UHURU(1970) ^{d1}	3.412 ^{d1}	(52 ± 2) ^{d2}	21.9 ^{+1.3d2} _{-0.5}	O7f ^{d3}	<0.008 ^{d4}	48-82 ^{d1}	>21 ^{y1}	1.8 ^{d5}
4U 1538–522	UHURU(1974) ^{e1}	3.75 ^{e2}	(19.9±3.4) ^{e3}	17.2±1.0 ^{e3}	B0Iab ^{e4}	0.174±0.015 ^{e5}	53.1±1.5 ^{e5}	8.3 ^{y1}	6.4±1.0 ^{e5}
IGR J18027–2016	INTEGRAL ^{f1a} & BeppoSAX (2003) ^{f1b}	4.56 ^{f2}	18.8–29.3 ^{f2}	(15.0–23.4) ^{f2}	B1-Ib ^{f3}	6.3 ^{f1b}	68±1 ^{f2}	6.3 ^{y1}	-
IGR J16479-4514	INTEGRAL (2003) ^{g1}	3.32 ^{g2}	30 ^{g3}	23.8 ^{g3}	O9.5 Iab ^{g4}	-	(44.85-48.90) ^{z1}	(10-70) ^{y2}	2.8 ^{+4.9g4} _{-1.7}
IGR J16418-4532	INTEGRAL (2004) ^{h1}	3.75 ^{h2}	31.54 ^{h3}	21.41 ^{h3}	BN 0.5 Ia ^{h4}	-	(48.65-53.03) ^{z2}	(2.3-3.8) ^{y3}	13 ^{h5}
IGR J17252–3616	EXOSAT (1984) ⁱ¹	9.7403±0.0004 ⁱ²	15 ⁱ³	21–37 ⁱ²	B0 I–B5 I ⁱ²	<0.19 ⁱ²	101±3 ⁱ²	9.0 ^{y1}	5.3-8.7 ⁱ²

^{a1}(Chodil et al., 1967), ^{a2}(Schreier et al., 1972b), ^{a3}(Ash et al., 1999), ^{a4}(van der Meer et al., 2007), ^{a5}(Bildsten et al., 1997), ^{a6}(Raichur and Paul, 2010), ^{a7}(Thompson and Rothschild, 2009),

^{b1}(Giacconi et al., 1972), ^{b2}(Li et al., 1978); (White, 1978), ^{b3}(Levine et al., 2000), ^{b4}(Pietrzyński et al., 2013),

^{c1}(Leong et al., 1971), ^{c2}(Schreier et al., 1972a), ^{c3}(Val Baker et al., 2005), ^{c4}(Primini et al., 1977), ^{c5}(Reynolds et al., 1993), ^{c6}(Levine et al., 1993), ^{c7}(Hilditch et al., 2005)

^{d1}(Jones et al., 1973), ^{d2}(Clark et al., 2002), ^{d3}(Penny et al., 1973), ^{d4}(Islam and Paul, 2016), ^{d5}(Ankay et al., 2001)

^{e1}(Giacconi et al., 1974), ^{e2}(Becker et al., 1977), ^{e3}(Reynolds et al., 1992), ^{e4}(Parkes et al., 1978), (Falanga et al., 2015), ^{e5}(Mukherjee et al., 2006),

^{f1a}(Revnivtsev et al., 2004a), ^{f1b}(Augello et al., 2003a), ^{f2}(Hill et al., 2005a), (Jain et al., 2009b), ^{f3}(Torrejón et al., 2010a),

^{g1}(Molkov et al., 2003), ^{g2}(Jain et al., 2009a), ^{g3}(Vacca et al., 1996), ^{g4}(Nespoli et al., 2008),

^{h1}(Tomsick et al., 2004), ^{h2}(Corbet et al., 2006), ^{h3}(Martins et al., 2005), ^{h4}(Coleiro et al., 2013),

ⁱ¹(Warwick et al., 1988), ⁱ²(Thompson et al., 2007), ⁱ³(Takeuchi et al., 1990)

^{y1}(Falanga et al. 2015), ^{y2}(Sidoli et al., 2012), ^{y3}(Drave et al., 2013)

^{z1}, ^{z2} Derived from total mass of the binary and the orbital period taken from Coley et al. (2015)

Table 3.2 The *XMM-Newton* EPIC pn log of observations of the HMXBs

Source	Observation ID	Datamode	Submode
LMC X-4	0142800101	IMAGING	PrimeSmallWindow
LMC X-4	0203500201	TIMING	FastTiming
SMC X-1	0011450101	IMAGING	PrimeFullWindow
4U 1700-377	0600950101	IMAGING	PrimeFullWindow
4U 1700-377	0083280401	TIMING	FastBurst
4U 1538-522	0152780201	IMAGING	PrimeFullWindow
IGR J18027-2016	0745060401	IMAGING	PrimeFullWindow
IGR J16479-4514	0512180101	IMAGING	PrimeSmallWindow
IGR J16418-4532	0679810101	IMAGING	PrimeLargeWindow
IGR J17252-3616	0405640201	IMAGING	PrimeLargeWindow
IGR J17252-3616	0405640601	IMAGING	PrimeFullWindow
IGR J17252-3616	0405641001	IMAGING	PrimeLargeWindow

Table 3.3 Line of sight hydrogen column density (N_{H}), photon index (Γ) and blackbody temperature (T_{BB}), χ^2/DOF and total flux in the energy range of (0.3-10.0) keV of 9 eclipsing HMXB systems during eclipse (E) and out-of-eclipse (OOE) phases

Source	Observation ID	State	N_{H} (10^{22} cm^{-2})	Photon Index (Γ)	T_{BB} (keV)	$\chi^2(\text{DOF})$	Total Flux (10^{-11} ergs $\text{cm}^{-2} \text{sec}^{-1}$)
Cen X-3	0111010101	E	$1.50^{+0.10}_{-0.11}$	$0.71^{+0.02}_{-0.06}$	$0.14^{+0.01}_{-0.82}$	197.73(127)	4.47
Cen X-3	0111010101	OOE	$2.07^{+0.18}_{-0.16}$	$0.51^{+0.05}_{-0.02}$	$0.08^{+0.01}_{-0.01}$	207.39(137)	43.74
LMC X-4	0142800101	E	0.1 (frozen)	$0.11^{+0.48}_{-0.32}$	$0.20^{+0.03}_{-0.03}$	38.09(35)	0.11
LMC X-4	0142800101	OOE	0.1 (frozen)	$0.59^{+0.02}_{-0.03}$	$0.05^{+0.01}_{-0.01}$	200.19(157)	30.58
LMC X-4	0203500201	E	0.1 (frozen)	$0.11^{+0.19}_{-0.20}$	$0.17^{+0.01}_{-0.01}$	103.83(94)	0.18
LMC X-4	0203500201	OOE	$0.05^{+0.04}_{-0.04}$	$0.87^{+0.04}_{-0.05}$	-	151.71(144)	15.53
SMC X-1	0011450101	E	$0.03^{+0.02}_{-0.02}$	$-0.56^{+0.23}_{-0.25}$	$0.23^{+0.02}_{-0.01}$	181.73(147)	0.52
SMC X-1	0011450101	OOE	$0.06^{+0.03}_{-0.03}$	$0.20^{+0.17}_{-0.17}$	$0.21^{+0.02}_{-0.02}$	198.21(156)	39.84
4U 1700-377	0600950101	E	$1.01^{+0.32}_{-0.43}$	$-1.34^{+0.14}_{-0.14}$	$0.08^{+0.04}_{-0.06}$	195.06(133)	3.19
4U 1700-377	0083280401	E	$1.56^{+1.37}_{-0.88}$	$-0.07^{+0.27}_{-0.24}$	-	98.22(91)	5.36
4U 1700-377	0083280401	OOE	$38.87^{+37.04}_{-9.27}$	$0.74^{+2.47}_{-0.51}$	$2.39^{+14.25}_{-14.25}$	52.29(55)	44.54
4U 1538-522	0152780201	E	$0.36^{+0.08}_{-0.05}$	$0.22^{+0.06}_{-0.06}$	-	178.19(130)	0.46
4U 1538-522	0152780201	OOE	$17.17^{+1.17}_{-1.12}$	$0.71^{+0.08}_{-0.08}$	$1.53^{+0.88}_{-0.42}$	125.90(126)	13.93
IGR J18027-2016	0745060401	E	$0.34^{+0.52}_{-0.34}$	$-0.24^{+0.24}_{-0.23}$	-	55.54(44)	0.08
IGR J18027-2016	0745060401	OOE	$5.90^{+0.40}_{-0.37}$	$0.71^{+0.08}_{-0.08}$	-	110.04(110)	3.47
IGR J16479-4514	0512180101	E	$4.69^{+4.77}_{-4.49}$	$1.28^{+2.63}_{-2.20}$	$0.07^{+0.39}_{-0.09}$	44.67(35)	0.08
IGR J16418-4532	0679810101	E	0.1(frozen)	$-0.28^{+0.41}_{-0.38}$	-	15.19(8)	0.03
IGR J17252-3616	0405640201	E	$9.34^{+137.59}_{-6.46}$	$0.24^{+0.83}_{-0.75}$	$0.19^{+4.92}_{-0.10}$	6.23(7)	0.04
IGR J17252-3616	0405640601	E	$18.17^{+24.96}_{-12.15}$	$0.81^{+4.92}_{-1.17}$	$1.07^{+0.01}_{-0.001}$	7.66(8)	0.05
IGR J17252-3616	0405641001	E	$13.48^{+43.32}_{-13.48}$	$-0.52^{+4.35}_{-2.47}$	-	3.50(6)	0.03

Table 3.4 Fe K_{α} , Fe XXV and Fe XXVI emission line energy, flux and equivalent width for 9 HMXBs during eclipse (E) and out-of-eclipse (OOE) phases. Line fluxes are given in units of 10^{-4} photons $\text{cm}^{-2} \text{sec}^{-1}$.

Source	Observation ID	State	Fe K_{α} energy (keV)	Fe K_{α} line flux	Fe XXV energy (keV)	Fe XXV line flux	Fe XXVI energy (keV)	Fe XXVI line flux	Fe K_{α} line eqv. width (eV)	Fe XXV line eqv. width (eV)	Fe XXVI line eqv. width (eV)
Cen X-3	0111010101	E	$6.41^{+0.05}_{-0.03}$	$0.88^{+0.08}_{-0.09}$	$6.66^{+0.01}_{-0.01}$	$2.12^{+0.09}_{-0.1}$	$6.94^{+0.01}_{-0.01}$	$1.65^{+0.09}_{-0.09}$	$103.51^{+9.41}_{-10.59}$	$246.32^{+10.46}_{-11.62}$	$209.22^{+11.41}_{-11.41}$
Cen X-3	0111010101	OOE	$6.41^{+0.01}_{-0.01}$	$15.01^{+0.93}_{-0.66}$	$6.68^{+0.01}_{-0.01}$	$11.64^{+0.45}_{-0.58}$	$6.98^{+0.01}_{-0.01}$	$9.58^{+0.49}_{-0.50}$	$188.85^{+11.70}_{-8.3}$	$130.95^{+5.06}_{-6.52}$	$139.00^{+7.1}_{-7.25}$
LMC X-4	0142800101	E	$6.36^{+0.47}_{-0.11}$	$0.08^{+0.07}_{-0.03}$	-	-	-	-	$663.38^{+580.46}_{-248.77}$	-	-
LMC X-4	0142800101	OOE	-	-	$6.56^{+0.03}_{-0.03}$	$3.54^{+0.23}_{-0.24}$	-	-	-	$143.66^{+9.33}_{-9.74}$	-
LMC X-4	0203500201	OOE	$6.38^{+0.04}_{-0.04}$	$1.55^{+0.03}_{-0.03}$	-	-	$6.99^{+0.05}_{-0.05}$	$2.37^{+0.05}_{-0.40}$	$116.15^{+2.25}_{-2.25}$	-	$193.82^{+4.09}_{-32.71}$
SMC X-1	0011450101	E	$6.38^{+0.06}_{-0.06}$	$0.07^{+0.01}_{-0.01}$	-	-	-	-	$125.90^{+17.99}_{-17.99}$	-	-
SMC X-1	0011450101	OOE	-	-	-	-	-	-	-	-	-
4U 1700-377	0600950101	E	$6.39^{+0.002}_{-0.002}$	$4.89^{+0.06}_{-0.06}$	$6.68^{+0.05}_{-0.04}$	$0.26^{+0.05}_{-0.04}$	-	-	$1060.93^{+13.02}_{-13.02}$	$22.37^{+4.30}_{-3.44}$	-
4U 1700-377	0083280401	E	$6.19^{+0.02}_{-0.02}$	$8.79^{+0.69}_{-0.68}$	-	-	-	-	$1429.45^{+112.21}_{-110.58}$	-	-
4U 1700-377	0083280401	OOE	$6.21^{+0.04}_{-0.03}$	$26.29^{+6.54}_{-6.28}$	-	-	-	-	$160.29^{+39.87}_{-38.29}$	-	-
4U 1538-522	0152780201	E	$6.38^{+0.01}_{-0.01}$	$0.57^{+0.03}_{-0.03}$	$6.69^{+0.02}_{-0.02}$	$0.17^{+0.02}_{-0.02}$	$6.95^{+0.02}_{-0.02}$	$0.13^{+0.01}_{-0.01}$	$792.39^{+41.70}_{-41.70}$	$145.10^{+17.07}_{-17.07}$	$180.59^{+13.89}_{-13.89}$
4U 1538-522	0152780201	OOE	$6.42^{+0.07}_{-0.07}$	$2.46^{+0.64}_{-0.57}$	-	-	-	-	$79.10^{+20.58}_{-18.33}$	-	-
IGR J18027-2016	0745060401	E	$6.51^{+0.04}_{-0.04}$	$0.14^{+0.01}_{-0.01}$	-	-	-	-	$1608.31^{+114.88}_{-114.88}$	-	-
IGR J18027-2016	0745060401	OOE	-	-	-	-	-	-	-	-	-
IGR J16479-4514	0512180101	E	$6.41^{+0.02}_{-0.02}$	$0.09^{+0.01}_{-0.01}$	-	-	$6.88^{+0.23}_{-0.12}$	$0.05^{+0.26}_{-0.18}$	$803.46^{+89.27}_{-89.27}$	-	$575.55^{+345.33}_{-230.22}$
IGR J16418-4532	0679810101	E	$6.46^{+0.10}_{-0.04}$	$0.07^{+0.01}_{-0.01}$	-	-	-	-	$1902.82^{+271.83}_{-271.83}$	-	-
IGRJ17252-3616	0405640201	E	$6.40^{+0.03}_{-0.03}$	$0.13^{+0.02}_{-0.03}$	-	-	-	-	$2694.58^{+414.55}_{-621.83}$	-	-
IGRJ17252-3616	0405640601	E	$6.41^{+0.02}_{-0.02}$	$0.18^{+0.04}_{-0.03}$	-	-	-	-	$1830.67^{+406.81}_{-305.11}$	-	-
IGRJ17252-3616	04056401001	E	$6.40^{+0.33}_{-0.27}$	$0.04^{+0.03}_{-0.02}$	-	-	-	-	$920.84^{+690.63}_{-460.42}$	-	-

Table 3.5 Emission line energy, flux and equivalent width other than Fe emission lines in 9 HMXBs during eclipse (E) and out-of-eclipse (OOE) phases. Line fluxes are given in units of 10^{-4} photons $\text{cm}^{-2} \text{sec}^{-1}$.

Line energy (keV)	Source	Observation ID	State	Emission line flux	Emission line eqv. width (eV)
$0.98^{+0.01}_{-0.02}$	Cen X-3	0111010101	E	$10.5^{+5.5}_{-3.6}$	$95.79^{+50.17}_{-32.84}$
$1.43^{+0.02}_{-0.02}$	Cen X-3	0111010101	E	$0.83^{+0.27}_{-0.25}$	$37.24^{+12.11}_{-11.22}$
$1.98^{+0.01}_{-0.02}$	Cen X-3	0111010101	E	$1.24^{+0.25}_{-0.20}$	$101.52^{+20.47}_{-16.37}$
$2.62^{+0.01}_{-0.02}$	Cen X-3	0111010101	E	$0.91^{+0.15}_{-0.11}$	$93.55^{+15.42}_{-11.31}$
$3.34^{+0.04}_{-0.04}$	Cen X-3	0111010101	E	$0.29^{+0.08}_{-0.08}$	$35.37^{+9.76}_{-9.76}$
$1.34^{+0.04}_{-0.06}$	Cen X-3	0111010101	OOE	$65.47^{+24.06}_{-18.12}$	$344.53^{+126.61}_{-95.35}$
$1.79^{+0.03}_{-0.03}$	Cen X-3	0111010101	OOE	$12.23^{+3.27}_{-2.65}$	$113.89^{+30.45}_{-24.68}$
$2.02^{+0.01}_{-0.01}$	Cen X-3	0111010101	OOE	$5.51^{+0.89}_{-1.1}$	$53.47^{+8.64}_{-10.67}$
$2.64^{+0.02}_{-0.02}$	Cen X-3	0111010101	OOE	$2.48^{+0.39}_{-0.40}$	$29.43^{+4.63}_{-4.75}$
$6.19^{+0.15}_{-0.19}$	Cen X-3	0111010101	OOE	$10.41^{+2.39}_{-2.80}$	$133.19^{+30.58}_{-35.82}$
$0.80^{+0.02}_{-0.06}$	LMC X-4	0203500101	OOE	$86.50^{+25.32}_{-13.60}$	$311.36^{+91.14}_{-48.95}$
$0.98^{+0.03}_{-0.04}$	LMC X-4	0203500201	OOE	$5.79^{+2.28}_{-1.62}$	$35.56^{+14.00}_{-9.95}$
$0.81^{+0.10}_{-0.13}$	4U 1700-377	0600950101	E	$8.11^{+32.5}_{-3.95}$	$89.67^{+359.34}_{-43.67}$
$1.28^{+0.05}_{-0.05}$	4U 1700-377	0600950101	E	$2.05^{+0.07}_{-0.40}$	$1207.72^{+41.24}_{-235.65}$
$1.75^{+0.01}_{-0.01}$	4U 1700-377	0600950101	E	$0.87^{+0.14}_{-0.11}$	$897.57^{+144.44}_{-113.48}$
$1.97^{+0.03}_{-0.03}$	4U 1700-377	0600950101	E	$0.16^{+0.03}_{-0.03}$	139^{+26}_{-26}
$2.34^{+0.01}_{-0.01}$	4U 1700-377	0600950101	E	$0.52^{+0.06}_{-0.05}$	$392.35^{+45.27}_{-37.72}$
$2.57^{+0.05}_{-0.06}$	4U 1700-377	0600950101	E	$0.08^{+0.02}_{-0.02}$	$54.12^{+13.53}_{-13.53}$
$2.99^{+0.01}_{-0.01}$	4U 1700-377	0600950101	E	$0.21^{+0.02}_{-0.02}$	$114.54^{+10.91}_{-10.91}$
$3.70^{+0.01}_{-0.01}$	4U 1700-377	0600950101	E	$0.25^{+0.03}_{-0.03}$	$102.35^{+12.28}_{-12.28}$
$4.12^{+0.05}_{-0.05}$	4U 1700-377	0600950101	E	$0.08^{+0.02}_{-0.02}$	$28.80^{+7.2}_{-7.2}$
$7.05^{+0.02}_{-0.01}$	4U 1700-377	0600950101	E	$0.88^{+0.10}_{-0.13}$	$218.62^{+24.84}_{-32.30}$
$7.49^{+0.02}_{-0.02}$	4U 1700-377	0600950101	E	$0.29^{+0.06}_{-0.05}$	$70.82^{+14.65}_{-12.21}$
$1.26^{+0.05}_{-0.07}$	4U 1538-522	0152780201	E	$0.22^{+0.07}_{-0.04}$	$321.28^{+102.22}_{-58.41}$
$1.85^{+0.03}_{-0.03}$	4U 1538-522	0152780201	E	$0.15^{+0.02}_{-0.02}$	$249.50^{+33.27}_{-33.27}$
$2.40^{+0.04}_{-0.03}$	4U 1538-522	0152780201	E	$0.07^{+0.01}_{-0.01}$	$116.25^{+16.61}_{-16.61}$
$6.02^{+0.05}_{-0.05}$	4U 1538-522	0152780201	E	$0.04^{+0.01}_{-0.01}$	$54.26^{+13.56}_{-13.56}$
$7.01^{+0.14}_{-0.40}$	IGRJ17252-3616	0405640201	E	$0.05^{+0.04}_{-0.01}$	$1227.41^{+981.93}_{-245.48}$

Chapter 4

X-ray reprocessing: Through the eclipse spectra of low mass X-ray binaries with *XMM-NEWTON*

4.1 Introduction

"Astronomy is older than physics. In fact, it got physics started by showing the beautiful simplicity of the motion of the stars and planets, the understanding of which was the beginning of physics. But the most remarkable discovery in all of astronomy is that the stars are made of atoms of the same kind as those on the earth." - Richard P. Feynman

Low mass X-ray binary (LMXB) systems host a late type (spectral type A or later i.e K, L, M types) companion star of mass $M \leq 1M_{\odot}$ (or a white dwarf in few cases) as donor star and either black hole or neutron star as compact object. The nuclear time scale i.e the time scale of primary fuel burning is longer in low mass stars, so most of the LMXBs are old

The work presented in this chapter is to be submitted to MNRAS

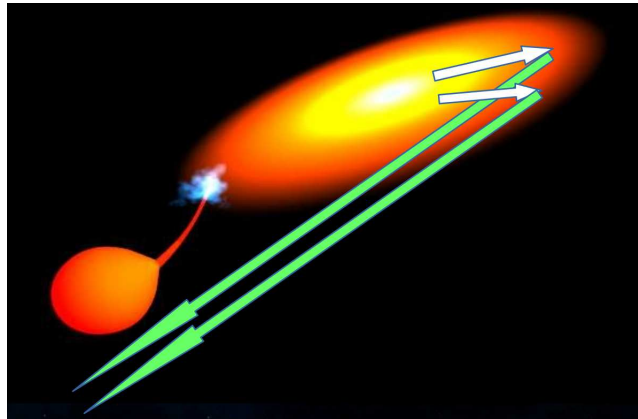


Fig. 4.1 Schematic of X-ray reprocessing in a LMXB system during eclipse. The primary X-ray photons emitted by the compact object are blocked by the companion and some part of the inner accretion disc. Only the reprocessed X-ray emissions scattered from the outer accretion disc reach the observer. The white arrows represent direct X-rays from the compact object, while the green arrows represent the reprocessed X-rays. Image courtesy: Part of the image has been taken from <http://users.uoa.gr/>

systems. Hence matter from the companion is transferred to the compact object via Roche Lobe overflow and the compact object of the LMXB systems is surrounded by accretion disc. In some LMXB systems the compact object accretes matter from slow, dense wind ($< 10^{-10} \text{ M Yr}^{-1}$) of its red giant companion. In LMXB pulsars the accretion disc is truncated at the Alfvén radius and most intense X-rays are generated in the hot accretion column above the poles. In lower magnetic field neutron stars, the disc is extended to the surface of the neutron star and X-rays are generated mostly from inner accretion disc. Some part of these primary X-rays come out of the system directly and a significant fraction of the primary X-rays interacts with the surrounding medium before leaving the system. The study of the secondary X-rays gives useful information about the X-ray reprocessing (as discussed in Chapter 1 and Chapter 3) characteristics of these systems. The X-rays received at the detector on-board space observatories are the combination of these primary and secondary X-rays. During eclipse the compact object is blocked by the companion and the received X-rays are only the reprocessed ones, which makes the X-ray reprocessing studies more clear. Figure 4.1 represents a cartoon picture of X-ray reprocessing in a LMXB system during eclipse.

In this work we have analyzed four LMXB systems (AX J1745.6–2901, EXO 0748–676, XTE 1710–281, MXB 1659–298) during eclipse and out-of-eclipse phases with *XMM-Newton* EPIC pn. Here we try to infer the characteristics of the accretion disc of these systems, which is the main reprocessing agent in the low mass X-ray binaries. Eclipse spectrum of some of the sources have been studied before (MXB 1659-298: Sidoli et al. 2001) but here we report results from first comprehensive study of all available LMXB eclipse and out-of-eclipse spectrum with *XMM-NEWTON* EPIC pn in a systematic manner.

4.2 Observation and data analysis

We referred to Liu et al. (2007) for eclipsing LMXBs and then looked for the available EPIC pn observations in HEASARC online service. We found eclipse observations of 4 LMXBs with a total of 17 observations, which were carried out in the imaging mode. The details of the mode of operation are given in Table 4.1. We used the XMM-Newton Science Analysis Software (SAS) version 14.0.0 to reduce the data. We extracted the event files with the SAS tool EVSELECT. We checked for flaring particle background and did not find it in any of the observations. We extracted the events in the energy range of 0.3-12 keV. We first extracted the lightcurve for the whole duration of observation, then identified the eclipse and out-of-eclipse durations and then extracted the eclipse and out-of-eclipse events using the task EVSELECT. From these events we extracted source along with background images for each observation. From images of each observation we extracted circular source regions and background region of same size of the source region from a region which is free from any other X-ray sources. The radius of the source and hence background region was chosen seeing the image quality, it varied in the range of (18-30)". We checked for pileup with the SAS task EPATPLOT. We did not notice any pile up effect for the energy range we have chosen for the analysis.

4.2.1 EVENT SELECTION FROM THE LIGHTCURVES

We extracted the source and background lightcurves from the source and background region files respectively, from the single and double events (with $PATTERN \leq 4$) for the full exposure time for each observation with the SAS task EVSELECT. We obtained background corrected source lightcurve with the SAS task LCCORR. We extracted two set of events: 1) eclipse events 2) out-of-eclipse persistent events from the event files of each observation. In each observation we noticed the start and end time of all the eclipse phases covered in the observation, then using the SAS task GTIBUILD we generated the good time intervals of all the eclipse phases. Then using the SAS task EVSELECT we extracted the eclipse events for each observation. In a similar manner we extracted out-of-eclipse persistent events for each observation by noticing the start and end time of all the persistent phases. Figure 4.2-4.5 show the eclipse and out-of-eclipse events in the 4 lightcurves of the LMXBs; one lightcurve is shown for each of the sources.

4.2.2 SPECTRAL ANALYSIS

We extracted the eclipse and out-of-eclipse spectra of the 4 LMXBs from the eclipse and out-of-eclipse events respectively, which are shown in Figure 4.2-4.5. For both the eclipse and out-of-eclipse phases, we extracted the spectra from the single and double events (with $PATTERN \leq 4$) excluding the events which are at the edge of a CCD and at the edge to a bad pixel (with $FLAG=0$). We generated response and ancillary files using the SAS task RMFGEN and ARFGEN respectively. We used the SAS task EVSELECT to extract the spectra from the eclipse and out-of-eclipse events using corresponding response and ancillary files. We rebinned the spectra with the SAS routine SPECGROUP to have at least 20 counts per bin to be able to use χ^2 statistics.

Observations of AX J1745.6–2901 cover 2 to 4 eclipses, where as that of EXO 0748–676 and MXB 1659–298 cover 4-8 eclipses and 1-2 eclipses respectively. The observation of XTE J1710–281 covers only one eclipse. For each observation we extracted a single eclipse

spectrum, combining the events from all the eclipses present in that observation. Similarly from each observation we extracted a single out-of-eclipse spectrum.

The eclipse and the out-of-eclipse spectra are shown in the top left and top right panels of Figure 4.6-4.23. The bottom panels show both the spectra together.

ECLIPSE AND OUT-OF-ECLIPSE SPECTRA OF THE LMXBs

For spectral fitting we have used XSPEC v12.8.2. The spectra were primarily fitted with powerlaw (model powerlaw) modified by photoelectric absorption (model phabs). A few of the sources showed excess low energy emission and a blackbody component (model bbodyrad or diskbb) was added to the model for these sources. Excess narrow emission and / or absorption profiles were seen in some spectra at specific energies. The excess at specific energies were fitted with gaussian functions. Additive model gaussian for emission lines and multiplicative model gabs for absorption lines have been used. For some of the observations in the out-of-eclipse phase an additional component for partial covering absorption by partially ionized material (model zxcipcf) was required to fit the spectra. The best fit parameters for the eclipse and the out-of-eclipse spectra for the 4 eclipsing LMXBs and details of the individual sources are discussed below. Figure 4.6-4.23 show the eclipse and out-of-eclipse spectra of all the observations analyzed in this work. The top left and top right panel of these figures respectively show the eclipse and out-of-eclipse spectra with the model components, while the bottom panel show the eclipse and out-of-eclipse spectra together.

AX J1745.6–2901:

We have analyzed 7 EPIC pn observations of AX J1745.6–2901 carried out over a period of ~ 8 and half years. Each observation covers minimum 2 eclipses to maximum 4 eclipses. The eclipse spectra of the 7 observations were best fitted with a powerlaw modified by photoelectric absorption (phabs \times powerlaw). Three of the out-of-eclipse spectra (OB IDs: 0723410301, 0723410401, 0723410501) also gave good fit with model phabs \times powerlaw.

Other four observations required Fe XXV and Fe XXVI absorption lines for a good fit. Amongst these four observations, two (OB IDs: 0402430401, 0762250301) needed one and two emission lines respectively (Table 4.3).

Powerlaw photon index (Γ) is higher during eclipse phases in all the observations except one (OB ID: 0723410501), in this observation the powerlaw photon index is same in both the phases. The line of sight equivalent hydrogen column density (N_H) is above 10^{23} cm^{-2} during each observation in both the phases. The out-of-eclipse to eclipse flux ratio in the energy range of (3-10) keV is in the range of $\sim(5-10)$. The strength (depth) for the Fe XXVI absorption line is higher than Fe XXV absorption line during out-of-eclipse phases except for OB ID 0724210201 where the strength of XXVI absorption line is little lower (Table 4.3) than that of Fe XXV absorption line.

In AX J1745.6–2901, above ~ 3 keV the difference between the intensity in the eclipse and the out-of-eclipse spectra increases. This difference is maximum ~ 5 keV. Ponti et al. (2018) have obtained the spectra for the full duration of the three observations (OB ID: 0402430301, 0402430401, 0724210201) which we have also analyzed in this work. Γ and N_H for the eclipse and out-of-eclipse phases obtained from our analysis are similar to the values they have obtained. The details of the spectral parameters for both the eclipse and out-of-eclipse spectra of AX J1745.6–2901 are given in Table 4.2 and 4.3.

Figure 4.6-4.12 show the eclipse and out-of-eclipse spectra of the 7 observation of AX J1745.6–2901.

EXO 0748–676:

We have analyzed 7 EPIC pn observations of EXO 0748–676 carried out over a period of ~ 2 months. Each observation covers minimum 4 to maximum 8 eclipses. The eclipse spectrum of the 7 observations were initially fitted with a powerlaw modified by photoelectric absorption. A soft excess has been observed and fitted with a blackbody component (model bbodyrad). After that, residuals at specific energies have been observed and those have been fitted with gaussian functions (model gaussian). Minimum 2 to maximum 5 emis-

sion lines have been observed in the eclipse spectra, among which 0.5 keV, 0.6 keV and 0.9 keV emission lines are common. Out-of-eclipse spectra required an additional partial covering absorption by partially ionized material (model `zxipcf`) model for a good fit. Soft excess has been fitted with multi-temperature blackbody component (model `diskbb`) for the out-of-eclipse spectra. ~ 0.6 keV emission line is common to all the out-of-eclipse spectra. 1/2 absorption lines were required for a good fit of the out-of-eclipse spectra except for the observation ID: 0160760601. The details of the models and the spectral parameters for the eclipse and out-of-eclipse spectra of EXO 0748–676 are given in Table 4.4-4.7.

N_H and Γ during eclipse phase have been found in the range of $(0.0003-0.06) \times 10^{22}$ cm^{-2} and $\sim(0.7-1.1)$ respectively. Temperature of the soft X-ray emitting region (T_{BB}) and the corresponding normalization (Norm_{BB}) was observed to have values in the range of $\sim(0.1-0.3)$ keV and $\sim(1-1268)$ in unit of $(\text{km}/10\text{kpc})^2$. The (0.3-10) keV flux values are quite similar in all the observations (0.5-0.6, in unit of 10^{-11} $\text{ergs cm}^{-2} \text{sec}^{-1}$).

N_H in the out-of-eclipse phase increases by $\sim(1-3)$ orders of magnitude from its value in the eclipse phase. The line of sight equivalent hydrogen column density (N_H) for the partially covering ionized absorber has been found in the range of $\sim(3-7) \times 10^{22}$ cm^{-2} . These ionized absorbers have been found to cover (60-80)% (as CvF , the covering factor $=\sim 0.6-0.8$) of the source emission.

T_{in} in the out-of-eclipse phase has been found to be lesser than that during eclipse phase in all of the 7 observations except for OB ID: 0160760801, Norm_{BB} is much higher in the out-of-eclipse phase ($\sim 2065-27933$) than its value in the eclipse phase ($\sim 1-1268$). The flux ratio in the energy range of (0.3-10) keV have been found to be between $\sim(33-44)$.

Figure 4.13-4.19 show the eclipse and out-of-eclipse spectra of 7 observations of EXO 0748–676. Figure 4.20 shows the composite eclipse and out-of-eclipse spectra respectively for these 7 observations. The top panel of Figure 4.20 shows that the eclipse spectra of the 7 observations almost overlap, while the composite out-of-eclipse spectra in the bottom panel shows an overlap only beyond ~ 4 keV.

MXB 1659–298:

We have analyzed two observations of MXB 1659–298 (OB IDs: 0008620601, 0008620701) carried over a period of ~ 1 year. Eclipse spectrum of both the observations were fitted well with model $\text{phabs} \times \text{powerlaw}$. The details of the spectral parameters are given in Table 4.8.

The values of Γ , N_H , 0.5-10 keV flux are nearly same for both the observations in the eclipse phase. The out-of-eclipse spectra of the first observation was best fitted with model $\text{gabs} \times \text{phabs}$ ($\text{pow} + \text{bbodyrad}$), where absorption line is that of Fe XXVI. The best fit for the out-of-eclipse spectra of the second observation has been obtained with model $\text{gabs} \times \text{phabs}$ ($\text{pow} + \text{bbodyrad} + \text{ga} + \text{ga}$), where the absorption lines are Fe XXV and Fe XXVI. Details of the spectral parameters for these fits are given in Tables 4.8 and 4.9.

Γ for the out-of-eclipse spectrum in the second observation is little less than that found in the first one, N_H is almost same in the two out-of-eclipse spectra. The blackbody temperature is higher in the second observation ($T_{\text{BB}} = 1.17$ keV) compared to its value found in the first observation ($T_{\text{BB}} = 1.09$ keV), while blackbody normalization is less in the second observation ($N_{\text{BB}} \sim 10$) than that in the first observation ($N_{\text{BB}} \sim 13$). The 0.5-10 keV flux in both the out-of-eclipse spectra are quite similar. 0.5-10 keV out-of-eclipse to eclipse flux ratio is ~ 22 and ~ 24 in the two observations respectively.

Figure 4.21-4.22 show the eclipse and out-of-eclipse spectra of the 2 observation of MXB 1659–298.

XTE J1710–281:

We have analyzed one observation of XTE J1710–281. The eclipse spectrum has very limited statistics leading to only a few bins in the binned spectrum. The out-of-eclipse spectrum was fitted with the model $\text{phabs} \times \text{powerlaw}$. The N_H is similar to that obtained in the two observations of MXB 1659–298. Only for the estimation of the flux ratio between the out-of-eclipse and eclipse phases we fitted the eclipse spectrum with model $\text{phabs} \times \text{powerlaw}$,

Table 4.1 The EPIC pn observation log of four LMXB systems

Source	Observation ID	Date of observation	Datamode	Submode	Spectral state
AX J1745.6–2901	0402430301	2007-04-01	IMAGING	PrimeFullWindow	Soft ^a
AX J1745.6–2901	0402430401	2007-04-03	IMAGING	PrimeFullWindow	Soft ^a
AX J1745.6–2901	0723410301	2014-02-28	IMAGING	PrimeFullWindow	Hard ^b
AX J1745.6–2901	0723410401	2014-03-10	IMAGING	PrimeFullWindow	Hard ^b
AX J1745.6–2901	0723410501	2014-04-02	IMAGING	PrimeFullWindow	Hard ^b
AX J1745.6–2901	0724210201	2013-08-30	IMAGING	PrimeFullWindow	Soft ^a
AX J1745.6–2901	0762250301	2015-09-27	IMAGING	PrimeFullWindow	
EXO 0748–676	0160760101	2003-09-19	IMAGING	PrimeSmallWindow	Faint-hard ^c
EXO 0748–676	0160760201	2003-09-21	IMAGING	PrimeSmallWindow	Faint-hard ^c
EXO 0748–676	0160760301	2003-09-23	IMAGING	PrimeSmallWindow	Faint-hard ^c
EXO 0748–676	0160760401	2003-09-25	IMAGING	PrimeSmallWindow	Faint-hard ^c
EXO 0748–676	0160760601	2003-10-21	IMAGING	PrimeSmallWindow	Faint-hard ^c
EXO 0748–676	0160760801	2003-10-25	IMAGING	PrimeSmallWindow	Faint-hard ^c
EXO 0748–676	0160761301	2003-11-12	IMAGING	PrimeSmallWindow	Faint-hard ^c
MXB 1659–298	0008620601	2000-03-22	IMAGING	PrimeSmallWindow	
MXB 1659–298	0008620701	2001-02-20	IMAGING	PrimeSmallWindow	
XTE J1710–281	0206990401	2004-02-22	IMAGING	PrimeFullWindow	

^aPonti et al. (2015), ^bPonti et al. (2018), ^cRaman and Paul (2017)

this flux ratio has been found to be ~ 66 . The details of the spectral parameters are given in Table 4.8.

Figure 4.23 shows the eclipse and out-of-eclipse spectra of XTE J1710–281.

Table 4.2 The model and best fit parameters of AX J1745.6–2901, where E: Eclipse, OOE: Out-of-eclipse, pow: powerlaw, N_H : Line of sight hydrogen column density, Γ : Powerlaw photon index, DOF: Degrees of freedom. Flux ratio gives the ratio of (3-10 keV) flux during out-of-eclipse phase with that in eclipse phase

Observation ID	Phase	Model	N_H (10^{22} cm^{-2})	Γ	χ^2/DOF	Flux in (3-10 keV) (10^{-11} ergs cm^{-2} sec^{-1})	Flux ratio (OOE/E)
0402430301	E	(phabs×pow)	$18.32^{+1.78}_{-1.72}$	$3.51^{+0.22}_{-0.21}$	88.13 (75)	2.04	6.58
	OOE	(phabs×gabs×gabs×pow)	$18.93^{+0.20}_{-0.20}$	$2.31^{+0.02}_{-0.02}$	145.60 (103)	13.43	
0402430401	E	(phabs×pow)	$19.70^{+1.92}_{-1.86}$	$3.81^{+0.25}_{-0.24}$	68.01 (69)	1.80	8.12
	OOE	phabs×gabs× gabs (ga + pow)	$21.67^{+0.20}_{-0.21}$	$2.47^{+0.02}_{-0.02}$	173.42 (100)	14.62	
0724210201	E	(phabs×pow)	$18.73^{+1.94}_{-1.88}$	$3.04^{+0.23}_{-0.22}$	85.75 (69)	2.36	6.42
	OOE	(phabs×gabs×gabs×pow)	$22.19^{+0.24}_{-0.24}$	$2.26^{+0.02}_{-0.02}$	170.96 (103)	15.16	
0723410301	E	(phabs×pow)	$12.29^{+13.66}_{-10.93}$	$2.46^{+1.96}_{-1.69}$	4.84 (7)	0.21	10.14
	OOE	(phabs×pow)	$19.72^{+0.86}_{-0.85}$	$1.78^{+0.08}_{-0.08}$	103.11 (101)	2.13	
0723410401	E	(phabs×pow)	$10.34^{+27.87}_{-10.10}$	$1.77^{+3.79}_{-2.03}$	3.42 (3)	0.15	8.93
	OOE	(phabs×pow)	$17.13^{+0.84}_{-0.83}$	$1.63^{+0.08}_{-0.08}$	90.92 (102)	1.34	
0723410501	E	(phabs×pow)	$15.19^{+16.22}_{-13.18}$	$1.87^{+2.03}_{-1.61}$	10.55 (9)	0.27	5.30
	OOE	(phabs×pow)	$19.37^{+1.02}_{-1.00}$	$1.87^{+0.11}_{-0.11}$	74.36 (99)	1.43	
0762250301	E	(phabs×pow)	$18.66^{+4.29}_{-3.98}$	$3.36^{+0.62}_{-0.57}$	36.78 (45)	2.17	9.07
	OOE	phabs×gabs×gabs (ga + ga + pow)	$21.46^{+0.47}_{-0.31}$	$2.10^{+0.03}_{-0.04}$	165.51 (98)	19.69	

Table 4.3 The parameters for emission and absorption lines as found in 4 observations in the OOE phase of AX J1745.6–2901. E_{em} : Emission line energy (keV), w_{em} : Emission line width (keV), F_{em} : Emission line flux (10^{-4} photons cm^{-2} sec^{-1}), EqW : Equivalent width of emission line (keV), E_{ab} : Absorption line energy (keV), w_{ab} : Absorption line width (keV), S_{ab} : Absorption line strength. Line energies and widths are given with 90% confidence limit. Emission line flux, Equivalent width of emission line and absorption line strength are given at 1σ confidence limit.

OB ID	E_{em}	w_{em}	F_{em}	EqW	E_{ab}	w_{ab}	S_{ab}
0402430301	-	-	-	-	$6.68^{+0.09}_{-0.05}$	0.09^{+**}_{-**}	$0.03^{+0.01}_{-0.01}$
	-	-	-	-	$6.95^{+0.03}_{-0.04}$	0.02^{+**}_{-**}	$0.05^{+14.60}_{-0.01}$
0402430401	$7.40^{+0.04}_{-0.05}$	0.12^{+}_{-}	$1.1^{+0.17}_{-0.16}$	$36.82^{+5.69}_{-5.35}$	$6.66^{+0.02}_{-0.02}$	0.01^{+**}_{-**}	$0.04^{+0.04}_{-0.01}$
	-	-	-	-	$6.95^{+0.02}_{-0.01}$	$0.01^{+0.05}_{-0.01}$	0.15^{+**}_{-**}
0724210201	-	-	-	-	$6.71^{+0.26}_{-0.13}$	$0.0036^{+0.46}_{-0.41}$	0.42^{+**}_{-**}
	-	-	-	-	$6.95^{+0.03}_{-0.14}$	$0.0049^{+0.05}_{-0.003}$	0.37^{+**}_{-**}
0762250301	$6.32^{+0.05}_{-0.04}$	0.1(frozen)	$1.47^{+0.21}_{-0.20}$	$26.75^{+3.82}_{-3.64}$	$6.71^{+0.05}_{-0.25}$	0.002^{+**}_{-**}	0.03^{+**}_{-**}
	$7.47^{+0.13}_{-0.20}$	$0.27^{+0.42}_{-0.26}$	$4.49^{+7.96}_{-4.79}$	$117.36^{+208.06}_{-125.20}$	$6.97^{+0.05}_{-0.01}$	0.004^{+**}_{-**}	5.75^{+**}_{-**}

The uncertainty for some of the parameters could not be constrained, these are indicated by **.

Table 4.4 The best fit models for 7 EPIC pn observations of EXO 0748–676 in eclipse (E) and out-of-eclipse (OOE) phase

E	(0160760101 and 0160760201)	$\text{phabs} \times (\text{pow} + \text{ga} + \text{ga} + \text{ga} + \text{ga} + \text{ga} + \text{diskbb})$
	(0160760301 and 0160760401)	$\text{phabs} \times (\text{pow} + \text{ga} + \text{ga} + \text{diskbb})$
	(0160760601 and 0160761301)	$\text{phabs} \times (\text{pow} + \text{ga} + \text{ga} + \text{ga} + \text{diskbb})$
	0160760801	$\text{phabs} \times (\text{pow} + \text{ga} + \text{ga} + \text{ga} + \text{ga} + \text{diskbb})$
OOE	(0160760101, 0160760201, 0160760301, 0160760401, 0160761301)	$\text{gabs} \times \text{phabs} \times (\text{zxipcf} \times \text{pow} + \text{ga} + \text{diskbb})$
	(0160760601 and 0160760801)	$\text{phabs} \times (\text{zxipcf} \times \text{pow} + \text{ga} + \text{diskbb})$

Table 4.5 The best fit model continuum parameters for 7 EPIC pn observations of EXO 0748–676, where E: Eclipse, OOE: Out-of-eclipse, N_H : Line of sight hydrogen column density, Γ : Powerlaw photon index, T_{BB} : Blackbody temperature with model bbodyrad, T_{in} : Blackbody temperature with model diskbb, $Norm_{BB}$: Normalization of model bbodyrad or diskbb, DOF: Degrees of freedom. Flux ratio gives the ratio of (0.3–10 keV) flux during out-of-eclipse phase with that in eclipse phase. Errors are given with 90% confidence limit.

OB ID	Phase	N_H (10^{22} cm^{-2})	Γ	T_{BB} or T_{in} (keV)	$Norm_{BB}$ $(\frac{\text{keV}}{10\text{kpc}})^2$	χ^2 (DOF)	Total Flux in (0.3–10) keV (10^{-11} ergs $\text{cm}^{-2} \text{sec}^{-1}$)	Flux ratio
0160760101	E	$0.06^{+0.07}_{-0.03}$	$0.99^{+0.12}_{-0.11}$	$0.21^{+0.03}_{-0.08}$	$32.24^{+43.30}_{-10.31}$	55.09 (60)	0.56	38.21
	OOE	$0.11^{+0.01}_{-0.01}$	$1.35^{+0.01}_{-0.01}$	$0.11^{+0.01}_{-0.01}$	$27933.00^{+19149.4}_{-9899.57}$	186.64 (160)	21.40	
0160760201	E	$0.02^{+0.03}_{-0.02}$	$1.12^{+0.17}_{-0.17}$	$0.19^{+0.03}_{-0.03}$	$54.90^{+62.55}_{-17.24}$	56.42 (49)	0.53	39.5
	OOE	$0.10^{+0.02}_{-0.02}$	$1.31^{+0.03}_{-0.03}$	$0.13^{+0.01}_{-0.003}$	$10402.40^{+6812.45}_{-9547.45}$	236.33 (163)	20.97	
0160760301	E	$0.001^{+0.08}_0$	$0.72^{+0.26}_{-0.29}$	$0.30^{+0.07}_{-0.06}$	$9.60^{+14.37}_{-5.06}$	83.15 (79)	0.6	39.3
	OOE	$0.09^{+0.01}_{-0.01}$	$1.33^{+0.01}_{-0.01}$	$0.15^{+0.01}_{-0.01}$	$6676.27^{+4949.14}_{-3607.84}$	144.11 (164)	23.58	
0160760401	E	$0.002^{+0.16}_{-0.0}$	$0.72^{+0.23}_{-0.26}$	$0.19^{+0.03}_{-0.04}$	$44.76^{+33.08}_{-33.98}$	40.44 (28)	0.45	42.69
	OOE	$0.04^{+0.01}_{-0.01}$	$1.36^{+0.01}_{-0.01}$	$0.14^{+0.01}_{-0.01}$	$2064.51^{+1581.05}_{-1124.90}$	181.39 (165)	19.21	
0160760601	E	$0.01^{+0.07}_0$	$0.81^{+0.18}_{-0.31}$	$0.17^{+0.03}_{-0.02}$	$113.02^{+97.60}_{-39.24}$	27.81 (31)	0.49	44.24
	OOE	$0.08^{+0.02}_{-0.01}$	$1.32^{+0.02}_{-0.02}$	$0.15^{+0.03}_{-0.02}$	$4389.60^{+4009.33}_{-2675.78}$	242.21 (167)	21.68	
0160760801	E	$0.0003^{+0.15}_{-0.04}$	$1.13^{+0.26}_{-0.17}$	$0.08^{+0.07}_{-0.01}$	1268.31^{+**}_{-**}	26.78 (35)	0.56	33.41
	OOE	$0.11^{+0.02}_{-0.01}$	$1.27^{+0.01}_{-0.01}$	$0.12^{+0.01}_{-0.01}$	$15583.70^{+11716.1}_{-8819.28}$	199.81 (164)	18.71	
0160761301	E	$0.01^{+0.12}_{-0.01}$	$1.09^{+0.17}_{-0.26}$	$0.31^{+0.16}_{-0.31}$	$1.23^{+4.06}_{-1.22}$	52.87 (61)	0.56	35.09
	OOE	$0.09^{+0.01}_{-0.01}$	$1.28^{+0.01}_{-0.03}$	$0.13^{+0.01}_{-0.01}$	$9315.01^{+5518.89}_{-5447.54}$	190.64 (161)	19.65	

The parameter for which uncertainty could not be determined, is indicated by **.

Table 4.6 zxcipcf parameters for 7 EPIC pn observations of EXO 0748–676 during out-of-eclipse (OOE) phase, where N_h : Line of sight hydrogen column density associated with model zxcipcf, $\log(\xi)$: ionization parameter, CvF: covering fraction. Errors are given with 90% confidence limit.

OB ID	Phase	N_h (10^{22} cm^{-2})	$\log(\xi)$	CvF
0160760101	OOE	$5.06^{+0.45}_{-0.16}$	$1.98^{+0.03}_{-0.04}$	$0.70^{+0.03}_{-0.04}$
0160760201	OOE	$5.15^{+0.78}_{-0.69}$	$1.94^{+0.24}_{-0.21}$	$0.67^{+0.03}_{-0.04}$
0160760301	OOE	$3.71^{+0.43}_{-0.49}$	$2.07^{+0.04}_{-0.05}$	$0.65^{+0.06}_{-0.05}$
0160760401	OOE	$6.82^{+0.43}_{-0.41}$	$1.94^{+0.02}_{-0.02}$	$0.66^{+0.02}_{-0.02}$
0160760601	OOE	$4.51^{+0.52}_{-0.51}$	$1.98^{+0.03}_{-0.03}$	$0.77^{+0.07}_{-0.06}$
0160760801	OOE	$6.73^{+0.53}_{-0.25}$	$1.96^{+0.02}_{-0.03}$	$0.74^{+0.03}_{-0.03}$
0160761301	OOE	$6.30^{+0.59}_{-0.46}$	$1.94^{+0.03}_{-0.07}$	$0.66^{+0.04}_{-0.04}$

Table 4.7 The emission and absorption line parameters for 7 EPIC pn observations of EXO 0748–676, E: Eclipse, OOE: Out-of-eclipse, E_{em} : Emission line energy (keV), w_{em} : Emission line width (keV), F_{em} : Emission line flux (10^{-4} photons cm^{-2} sec^{-1}), EqW : Equivalent width of emission line, E_{ab} : Absorption line energy (keV), w_{ab} : Absorption line width (keV), S_{ab} : Absorption line strength. Line energies and widths are given with 90% confidence limit. Emission line flux, Equivalent width of emission line, absorption line strength are given at 1σ confidence limit.

OB ID	Phase	E_{em}	w_{em}	F_{em}	EqW	E_{ab}	w_{ab}	S_{ab}	
0160760101	E	$0.51^{+0.03}_{-0.04}$	$0.11^{+0.02}_{-0.04}$	$10.41^{+4.18}_{-4.18}$	$713.84^{+286.63}_{-286.63}$	-	-	-	
		$0.89^{+0.02}_{-0.02}$	$0.03^{+0.04}_{-0.03}$	$0.95^{+0.70}_{-0.25}$	$134.42^{+99.05}_{-35.37}$	-	-	-	
		$1.40^{+0.42}_{-0.42}$	$(1.09 \times 10^{-4})^{+0.17}_{-0.0}$	$0.19^{+0.06}_{-0.07}$	$67.09^{+21.19}_{-24.72}$	-	-	-	
		$1.81^{+0.05}_{-0.04}$	$(6.78 \times 10^{-4})^{+0.000028}_{-0.82}$	$0.11^{+0.05}_{-0.05}$	$59.00^{+26.82}_{-26.82}$	-	-	-	
		$3.87^{+0.05}_{-0.25}$	$(1.19 \times 10^{-4})^{+19.90}_{-0.00018}$	$0.14^{+0.05}_{-0.05}$	$185.98^{+66.42}_{-66.42}$	-	-	-	
		OOE	$0.60^{+0.01}_{-0.01}$	$0.06^{+0.01}_{-0.01}$	$45.76^{+4.32}_{-4.86}$	$63.04^{+5.95}_{-6.69}$	$1.34^{+0.21}_{-0.31}$	$0.08^{+0.31}_{-0.16}$	$0.01^{+0.00}_{-0.01}$
		-	-	-	-	$6.71^{+0.03}_{-0.04}$	$0.002^{+0.000}_{-0.001}$	3.23^{+***}_{-***}	
	0160760201	E	$0.54^{+0.02}_{-0.03}$	$0.05^{+0.04}_{-0.04}$	$3.04^{+0.10}_{-0.11}$	$176.43^{+5.80}_{-6.38}$	-	-	-
			$0.89^{+0.01}_{-0.02}$	$0.03^{+0.03}_{-0.03}$	$0.81^{+0.32}_{-0.20}$	$100.89^{+39.86}_{-24.91}$	-	-	-
			$1.39^{+0.50}_{-0.03}$	$(8.05 \times 10^{-4})^{+1.15}_{-0.00081}$	$0.18^{+0.07}_{-0.06}$	$59.61^{+23.18}_{-19.87}$	-	-	-
$1.80^{+0.52}_{-0.83}$			$(6.55 \times 10^{-4})^{+0.79}_{-0.00001}$	$0.13^{+0.05}_{-0.05}$	$70.88^{+27.26}_{-27.26}$	-	-	-	
$6.44^{+0.07}_{-0.08}$			$(2.80 \times 10^{-4})^{+0.00028}_{-0.82}$	$0.13^{+0.05}_{-0.05}$	$331.27^{+127.41}_{-127.41}$	-	-	-	
OOE			$0.59^{+0.01}_{-0.02}$	$0.07^{+0.02}_{-0.01}$	$46.39^{+6.15}_{-5.13}$	$66.67^{+8.84}_{-7.37}$	$2.06^{+0.03}_{-0.02}$	$(7.07 \times 10^{-5})^{+***}_{-***}$	17.71^{+***}_{-***}
0160760301		E	$0.52^{+0.02}_{-0.09}$	$0.13^{+0.05}_{-0.04}$	$6.61^{+4.90}_{-2.36}$	$750.12^{+556.06}_{-267.82}$	-	-	-
			$0.88^{+0.03}_{-0.06}$	$0.04^{+0.07}_{-0.04}$	$6.32^{+0.41}_{-0.21}$	$94.06^{+6.10}_{-3.12}$	-	-	-
		OOE	$0.59^{+0.03}_{-0.05}$	$0.07^{+0.07}_{-0.04}$	$37.86^{+4.83}_{-5.99}$	$43.66^{+5.57}_{-6.91}$	$2.03^{+0.04}_{-0.04}$	$(2.65 \times 10^{-4})^{+***}_{-***}$	0.65^{+***}_{-***}
		0160760401	E	$0.49^{+0.09}_{-0.17}$	$0.11^{+0.08}_{-0.10}$	$3.19^{+2.99}_{-2.38}$	$270.95^{+253.96}_{-202.15}$	-	-
$0.89^{+0.04}_{-0.02}$	$(1.55 \times 10^{-4})^{+16.94}_{-0.000155}$			$0.40^{+0.18}_{-0.14}$	$78.72^{+35.42}_{-27.55}$	-	-	-	
OOE	$0.57^{+0.01}_{-0.01}$		$0.02^{+0.02}_{-0.02}$	$5.95^{+1.01}_{-1.01}$	$13.56^{+2.30}_{-2.30}$	$2.14^{+0.02}_{-0.02}$	$0.07^{+0.02}_{-0.02}$	$0.02^{+0.003}_{-0.002}$	
0160760601	E		$0.56^{+0.05}_{-0.02}$	$(1.28 \times 10^{-5})^{+0.0000128}_{-0.82}$	$0.99^{+0.73}_{-0.40}$	$57.12^{+42.12}_{-23.08}$	-	-	-
		$1.27^{+0.05}_{-0.04}$	$0.07^{+0.06}_{-0.02}$	$0.08^{+0.19}_{-0.17}$	$29.19^{+69.33}_{-62.03}$	-	-	-	
		$1.90^{+0.11}_{-0.05}$	$0.13^{+0.10}_{-0.04}$	$0.35^{+0.09}_{-0.09}$	$298.08^{+76.65}_{-76.65}$	-	-	-	
	OOE	$0.56^{+0.03}_{-0.04}$	$0.07^{+0.02}_{-0.02}$	$41.97^{+12.13}_{-6.02}$	$53.19^{+15.37}_{-7.63}$	-	-	-	
0160760801	E	$0.59^{+0.03}_{-0.05}$	$0.07^{+0.08}_{-0.02}$	$2.71^{+32.19}_{-3.11}$	278.91^{+***}_{-***}	-	-	-	
		$0.88^{+0.03}_{-0.06}$	$0.08^{+0.04}_{-0.03}$	$1.30^{+4.79}_{-0.42}$	308.09^{+***}_{-***}	-	-	-	
		$1.28^{+0.05}_{-0.06}$	$0.06^{+0.05}_{-0.06}$	$0.34^{+0.12}_{-0.12}$	$130.67^{+46.12}_{-46.12}$	-	-	-	
		$6.27^{+0.27}_{-0.19}$	$0.19^{+0.23}_{-0.19}$	$0.31^{+0.10}_{-0.11}$	$711.45^{+229.5}_{-252.45}$	-	-	-	
		OOE	$0.59^{+0.01}_{-0.02}$	$0.07^{+0.01}_{-0.01}$	$39.55^{+4.33}_{-3.78}$	$86.04^{+9.42}_{-8.22}$	$6.79^{+0.08}_{-0.08}$	$0.12^{+0.06}_{-0.09}$	$0.02^{+0.00}_{-0.00}$
		0160761301	E	$0.52^{+0.02}_{-0.02}$	$0.09^{+0.07}_{-0.000029}$	$5.49^{+2.69}_{-1.12}$	$670.49^{+328.53}_{-136.78}$	-	-
	$0.88^{+0.02}_{-0.02}$			$0.07^{+0.04}_{-0.04}$	$1.13^{+0.48}_{-0.23}$	$235.71^{+100.12}_{-47.98}$	-	-	-
	$1.31^{+0.24}_{-0.03}$	$3.76 \times 10^{-5}^{+0.09}_{-0.000012}$		$0.18^{+0.07}_{-0.07}$	$60.58^{+23.56}_{-23.56}$	-	-	-	
OOE	$0.59^{+0.01}_{-0.01}$	$0.06^{+0.01}_{-0.01}$	$28.36^{+3.46}_{-3.01}$	$55.31^{+6.75}_{-5.87}$	$2.80^{+0.39}_{-0.22}$	0.18^{+***}_{-***}	$0.007^{+0.005}_{-0.005}$		
	-	-	-	-	$6.95^{+0.08}_{-0.19}$	$9.57 \times 10^{-3}^{+***}_{-***}$	$0.01^{+0.005}_{-0.005}$		

The uncertainty could not be constrained for some of the parameters, these are indicated by

**.

Table 4.8 The best fit parameters of MXB 1659–298 and XTE J1710–281, where E: Eclipse, OOE: Out-of-eclipse, N_{H} : Line of sight hydrogen column density, Γ : Powerlaw photon index, T_{BB} : Blackbody temperature with model bbodyrad, Norm_{BB} : normalization of model bbodyrad, DOF: Degrees of freedom. Flux ratio gives the ratio of (0.5–10 keV) flux during out-of-eclipse phase with that in eclipse phase. Errors are given with 90% confidence limit.

Source (OB ID)	Phase	Model	N_{H} (10^{22} cm^{-2})	Γ	T_{BB} (keV)	Norm_{BB} ($\frac{\text{keV}}{10\text{kpc}}$) ²	χ^2/DOF	Flux (0.5–10 keV) (10^{-11} ergs $\text{cm}^{-2} \text{s}^{-1}$)	Flux ratio
MXB 1659–298 (0008620601)	E	phabs×pow	$0.26^{+0.08}_{-0.07}$	$1.51^{+0.21}_{-0.20}$	-	-	21.66 (25)	3.97	22.44
	OOE	gabs×phabs× (pow + bbodyrad)	$0.28^{+0.01}_{-0.01}$	$1.74^{+0.03}_{-0.03}$	$1.09^{+0.05}_{-0.04}$	$12.76^{+1.78}_{-1.87}$	186.94 (162)	89.11	
MXB 1659–298 (0008620701)	E	phabs×pow	$0.27^{+0.02}_{-0.02}$	$1.57^{+0.05}_{-0.05}$	-	-	104.27 (103)	3.9	24.11
	OOE	gabs×phabs× (pow + bbodyrad + ga + ga)	$0.28^{+0.01}_{-0.03}$	$1.64^{+0.02}_{-0.02}$	$1.17^{+0.03}_{-0.03}$	$10.09^{+1.07}_{-0.85}$	300.36 (156)	94.03	
XTE J1710–281 (0206990401)	E	-	-	-	-	-	-	0.07	66.29
	OOE	phabs×pow	$0.28^{+0.01}_{-0.01}$	$1.92^{+0.02}_{-0.02}$	-	-	197.31 (151)	4.64	

Table 4.9 The emission and absorption line parameters for 1 EPIC pn observation of MXB 1659–298 during out-of-eclipse phase. Line energies and widths are given with 90% confidence limit and Emission line flux, Equivalent width of emission line, absorption line strength are given at 1σ confidence limit.

OB ID	Emission line Energy (keV) (keV)	Emission line width (w_{em}) ($\text{cm}^{-2} \text{sec}^{-1}$)	Emission line flux (10^{-4} photons)	EqW (eV)	Absorption line Energy (keV) (keV)	Absorption line width (w_{ab})	Absorption line strength
0008620601	-	-	-	-	$6.93^{+0.07}_{-0.15}$	0.01^{+***}_{-***}	$0.08^{+0.01}_{-0.01}$
0008620701	$0.52^{+0.47}_{-0.51}$	$0.3^{+0.30}_{-0.26}$	243.10^{+***}_{-***}	56.23^{+}_{-}	$6.72^{+0.02}_{-0.02}$	$0.01^{+0.78}_{-0.00}$	$0.03^{+190.41}_{-176.73}$
	$2.24^{+0.02}_{-0.02}$	$0.03^{+0.04}_{-0.03}$	$4.93^{+0.95}_{-1.12}$	$10.87^{+2.09}_{-2.47}$	$6.99^{+0.02}_{-0.02}$	$0.01^{+0.002}_{-0.001}$	$0.06^{+1.39}_{-0.96}$

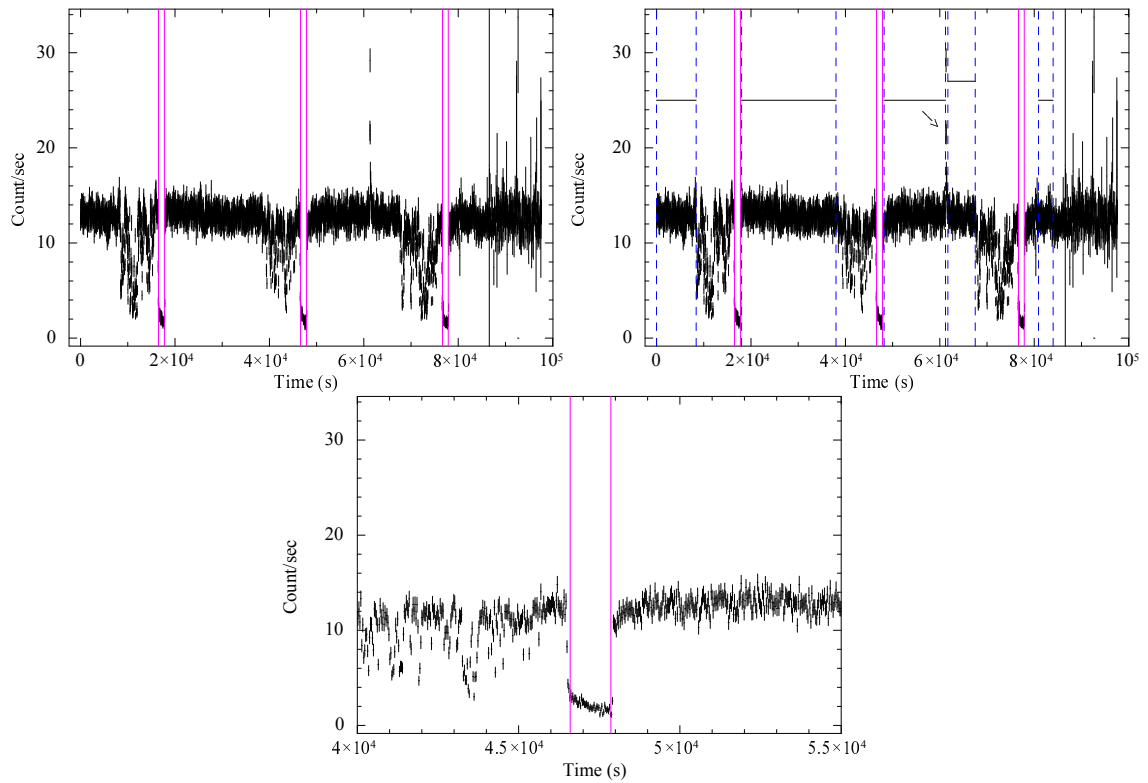


Fig. 4.2 **Top panels:** Left figure: The portions in the EPIC-pn lightcurve of AXJ 1745.6–2901 (OB ID: 0402430401) within the pink solid lines indicate the eclipse events. We extracted the eclipse spectrum of this observation from these events. Right figure: We extracted the out-of-eclipse spectrum from the events within the blue dashed lines, excluding the flare indicated by an arrow near 6×10^4 s. **Bottom panel:** Zoomed view of an eclipse event in the same lightcurve

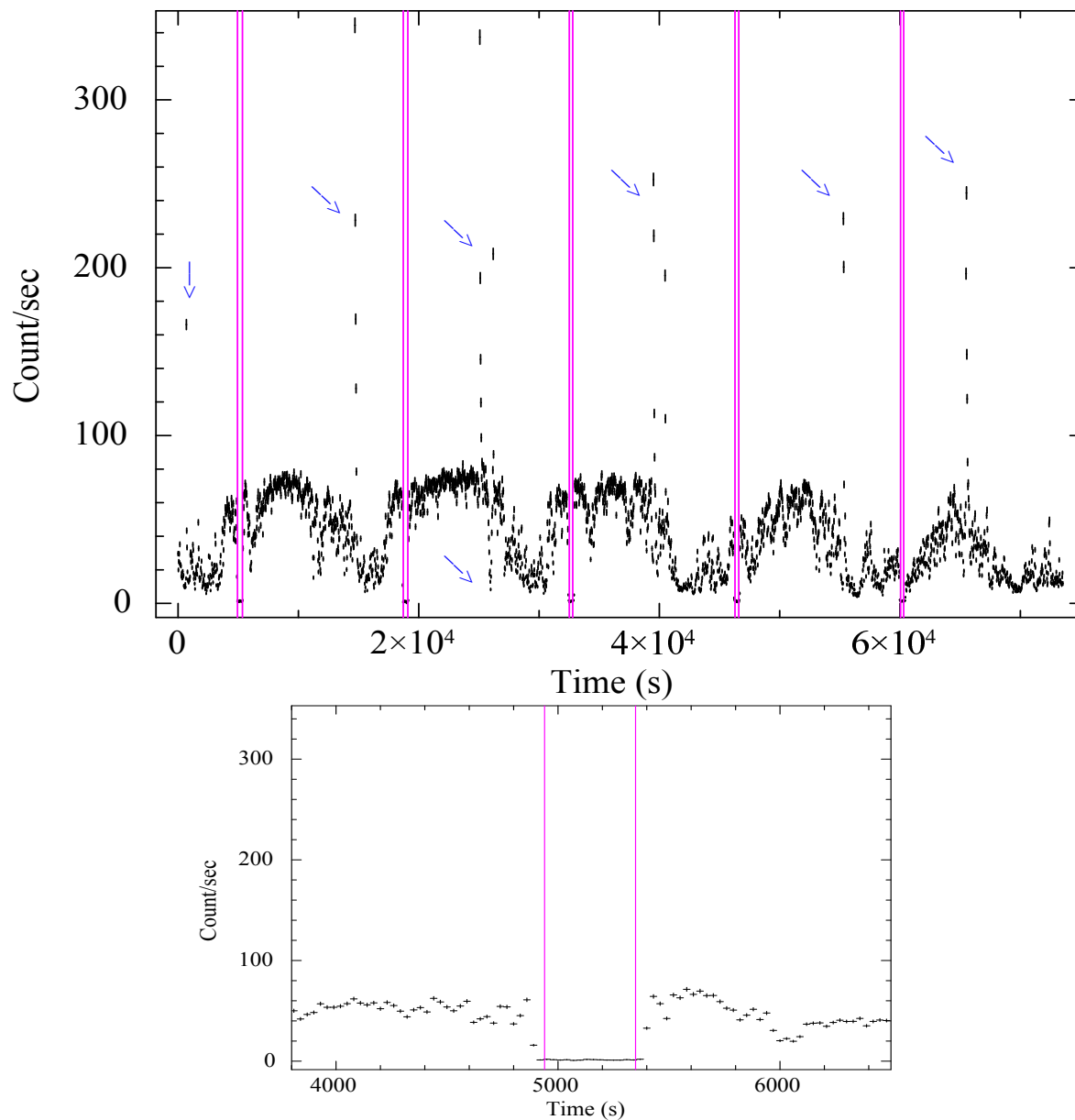


Fig. 4.3 **Top panel:** The events in the EPIC-pn lightcurve of EXO 0748–676 (OB ID: 0160760401), within the pink solid lines indicate the eclipse events. We extracted the eclipse spectrum of this observation from these events. We extracted the out-of-eclipse spectrum from the events outside eclipses but excluding the flares. The flares are indicated by the arrows. **Bottom panel:** Zoomed view of an eclipse event in the above lightcurve.

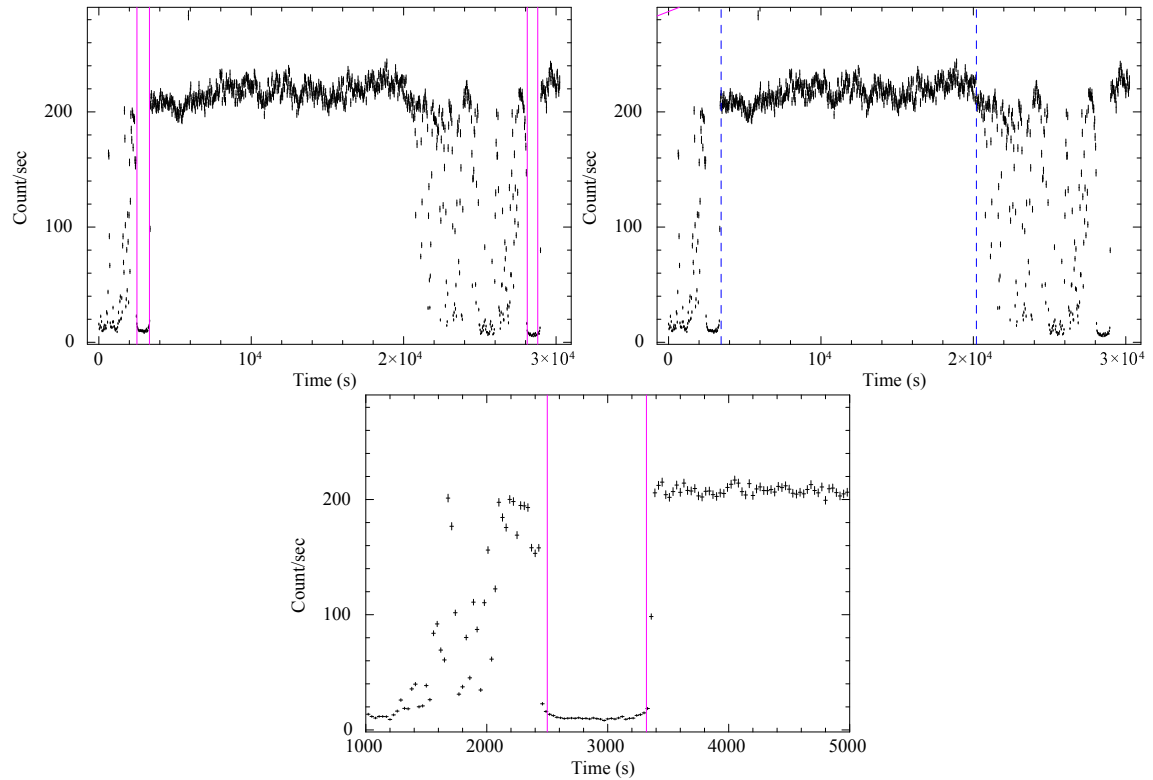


Fig. 4.4 **Top panel:** Left panel: The portions in the EPIC-pn lightcurve of MXB 1659–298 (OB ID: 0008620701) within the pink solid lines indicate the eclipse events. We extracted the eclipse spectrum of this observation from these events. Right panel: We extracted the out-of-eclipse spectrum from the event within the blue dashed lines. **Bottom panel:** Zoomed view of an eclipse event in the above lightcurve

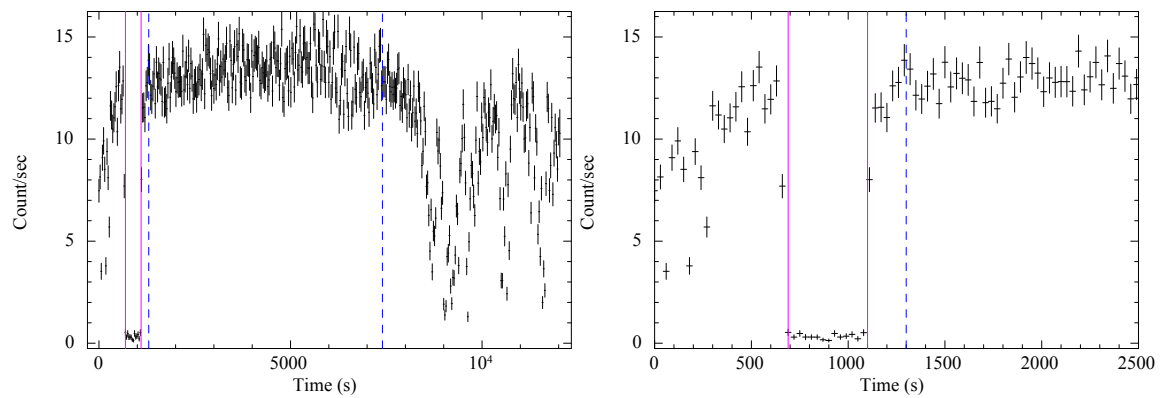


Fig. 4.5 **Left panel:** The event in the EPIC-pn lightcurve of XTE J1710–281 (OB ID: 0206990401), within the pink solid lines indicates the eclipse event. We extracted the eclipse spectrum of this observation from this event. We extracted the out-of-eclipse spectrum from the event shown by two blue dashed lines. **Right panel:** Zoomed view of an eclipse event within two pink solid lines, in the same lightcurve.

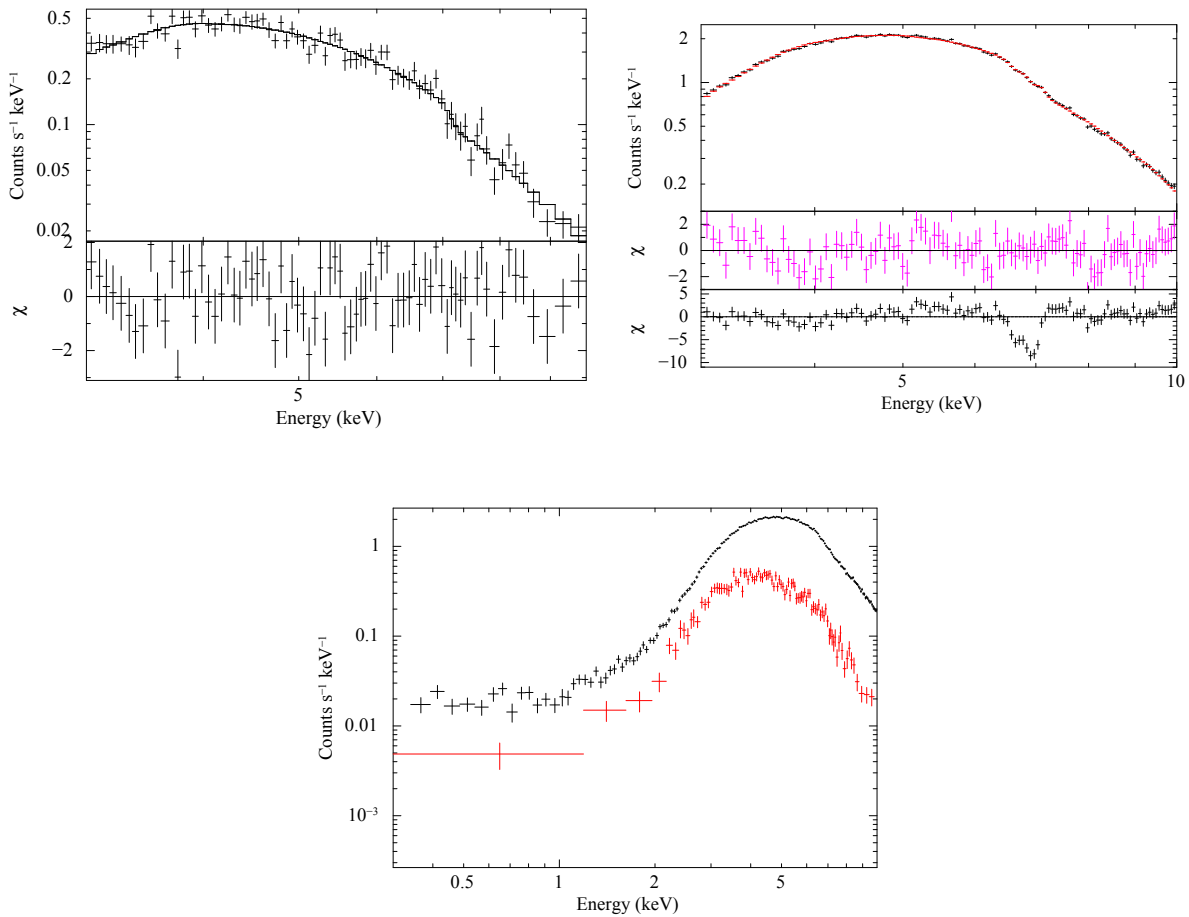


Fig. 4.6 Eclipse (top left) and OOE (top right) spectra of AX J1745.6–2901 (OB ID: 0402430301). The second panel of the top right figure is the contribution of χ towards each bin for the best fit, while the 3rd panel is the same (χ) but excluding the two absorption lines mentioned in Table 4.3. Both the spectra are shown together in the bottom figure.

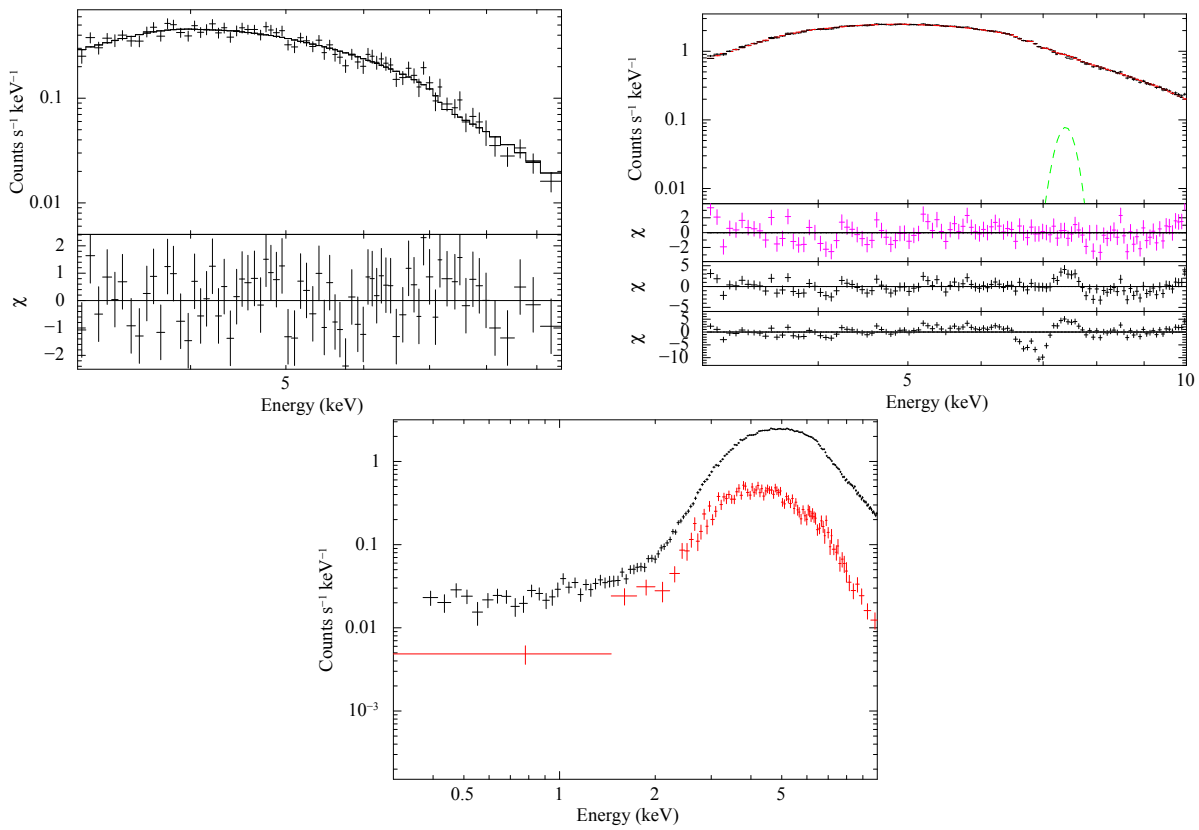


Fig. 4.7 Same as in Figure 4.6, for OB ID: 0402430401. The extra 4th panel in the top right figure shows contribution of χ towards each bin without the two absorption lines and one emission line mentioned in Table 4.3.

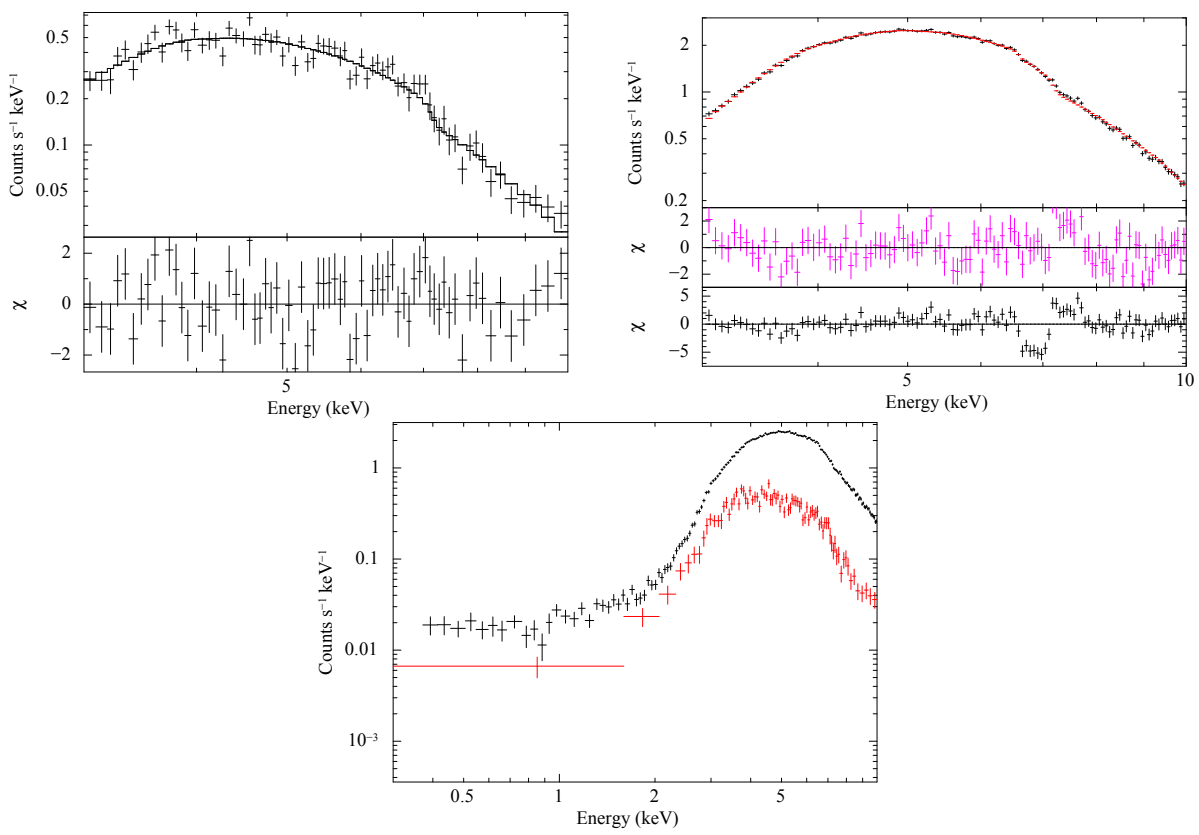


Fig. 4.8 Same as in Figure 4.6, for OB ID: 0724210201

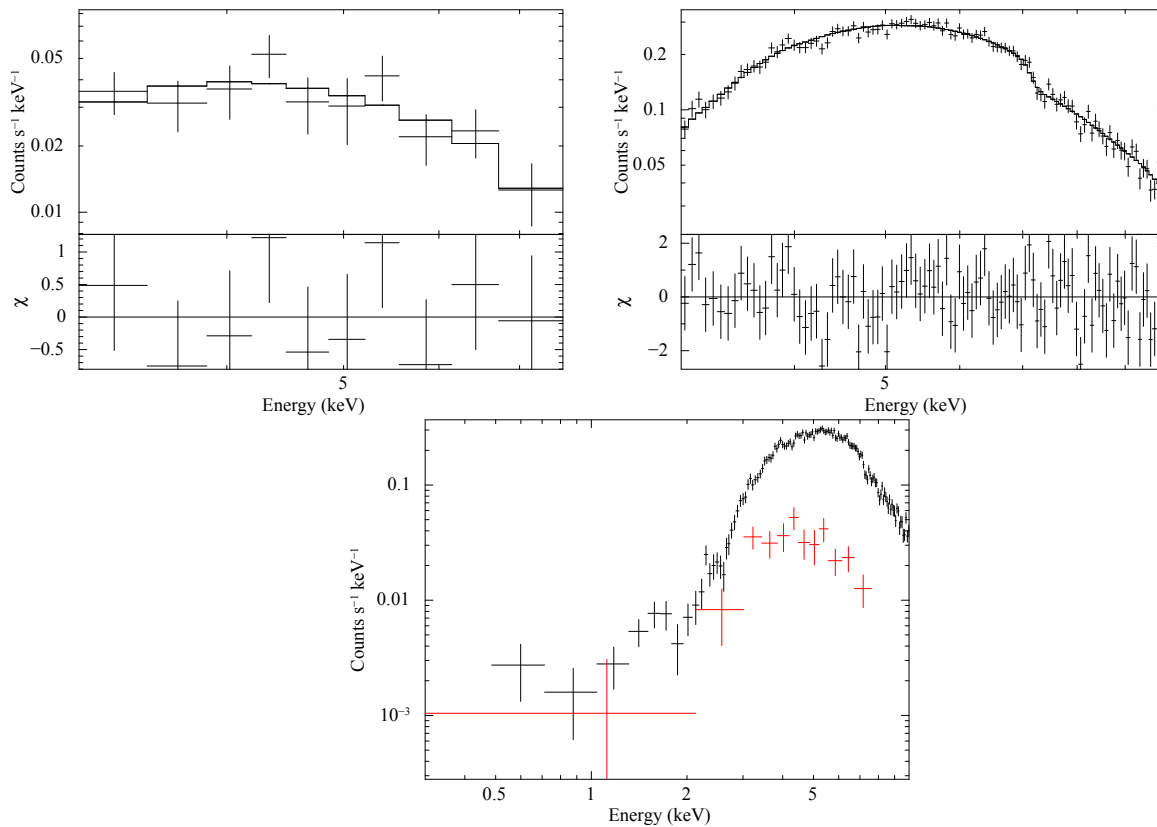


Fig. 4.9 Eclipse (top left) and OOE (top right) spectra of AX J1745.6-2901 (OB ID: 0723410301), The second panel in the top right figure is the contribution of χ towards each bin for the best fit, bottom figure shows both the spectra together.

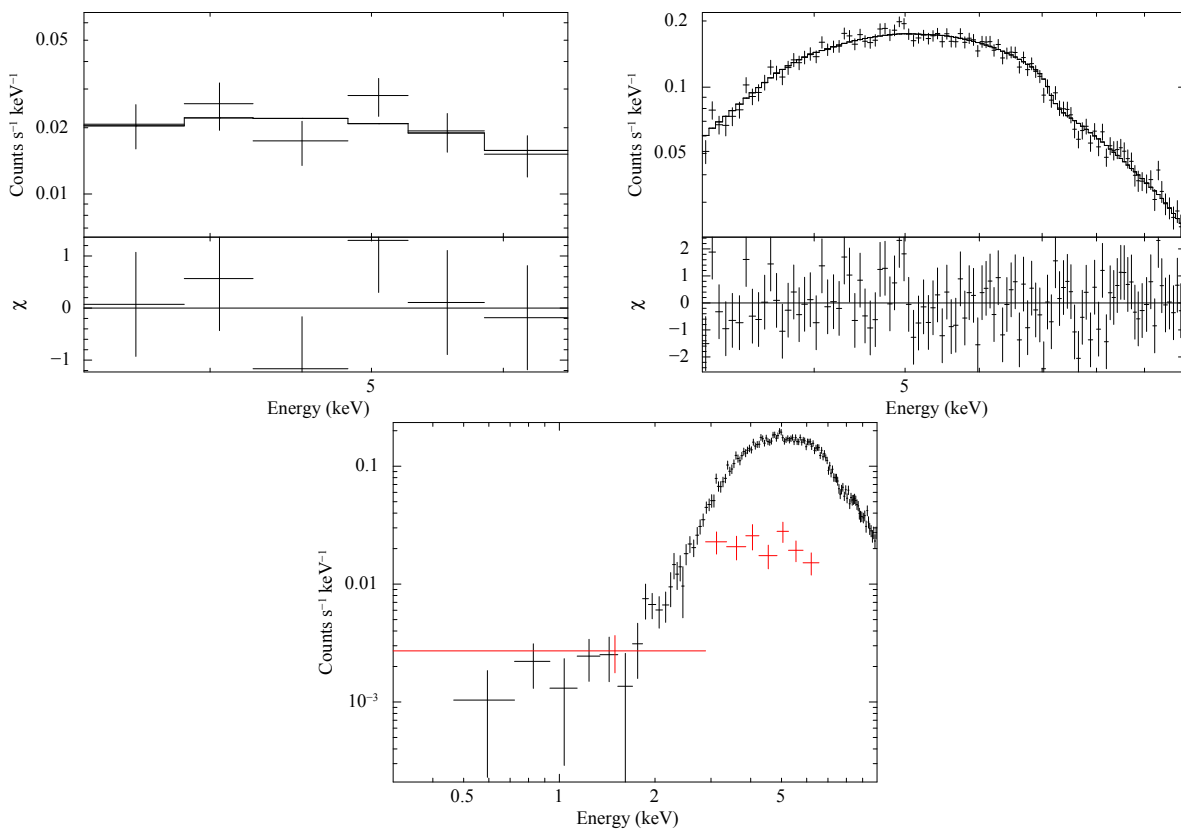


Fig. 4.10 Same as in Figure 4.9, for OB ID: 0723410401

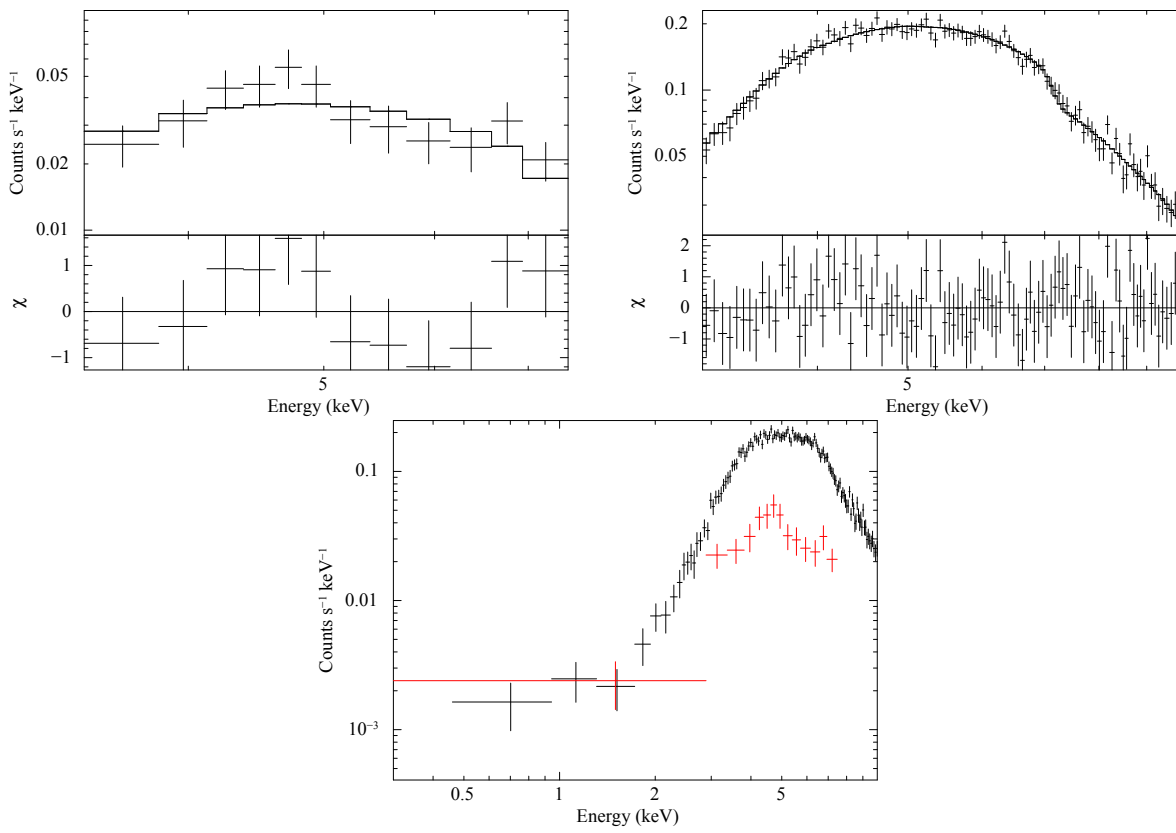


Fig. 4.11 Same as in Figure 4.9, for OB ID: 0723410501

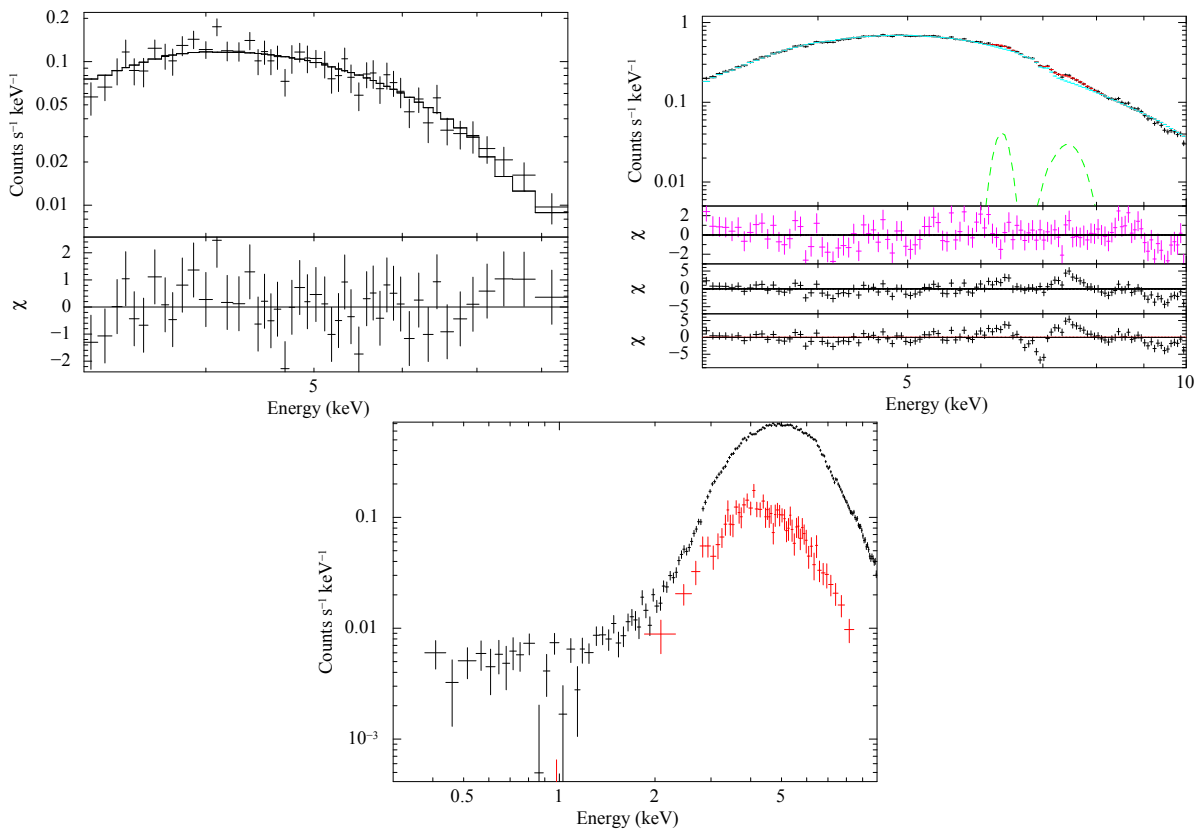


Fig. 4.12 Same as in Figure 4.7, for OB ID: 0762250301. Here the 4th panel in the top right figure is the contribution of χ towards each bin without the two absorption lines and two emission lines mentioned in Table 4.3.

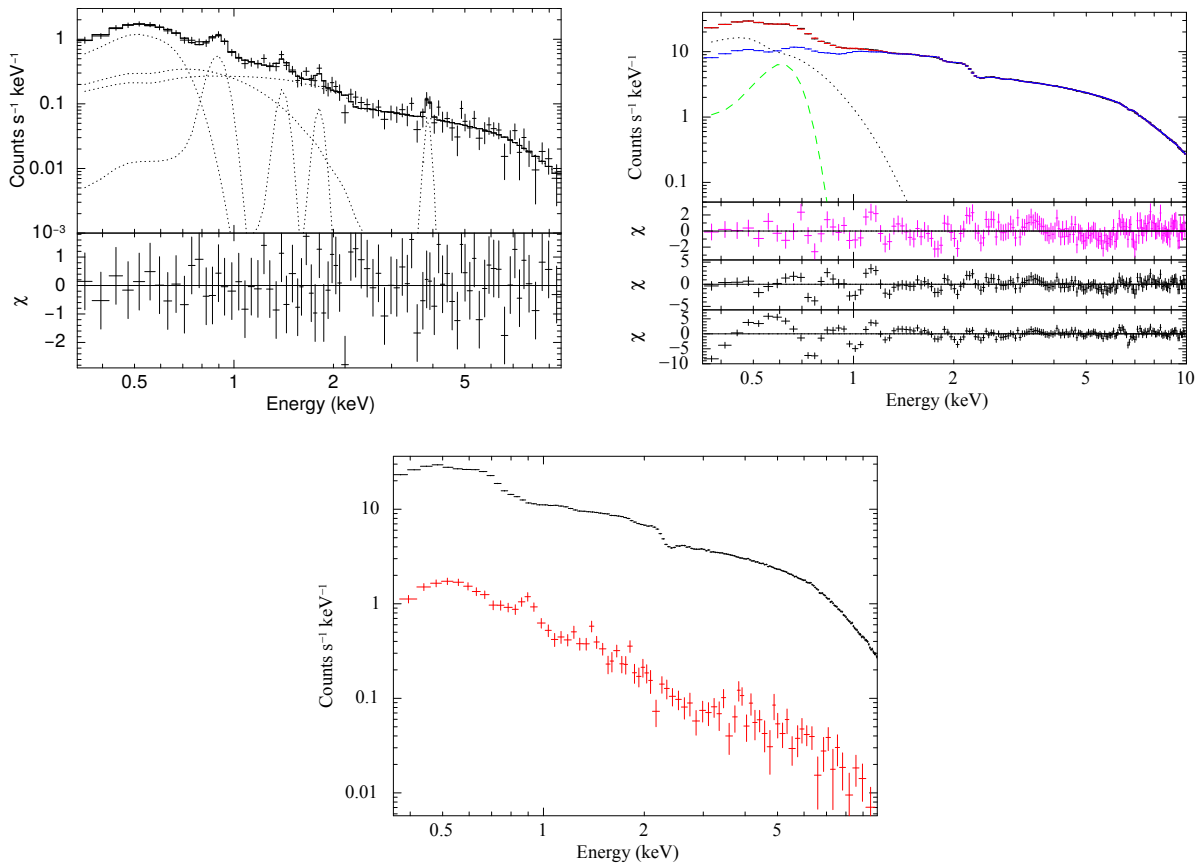


Fig. 4.13 Eclipse (top left) and OOE (top right) spectra of EXO 0748–676 (OB ID: 0160760101). The second panel of the top right figure is the contribution of χ towards each bin for the best fit, the 3rd panel is the same (χ) but excluding the absorption line, while 4th panel shows the χ excluding both the absorption and emission line, mentioned in Table 4.7. Both the spectra are shown together in the bottom panel.

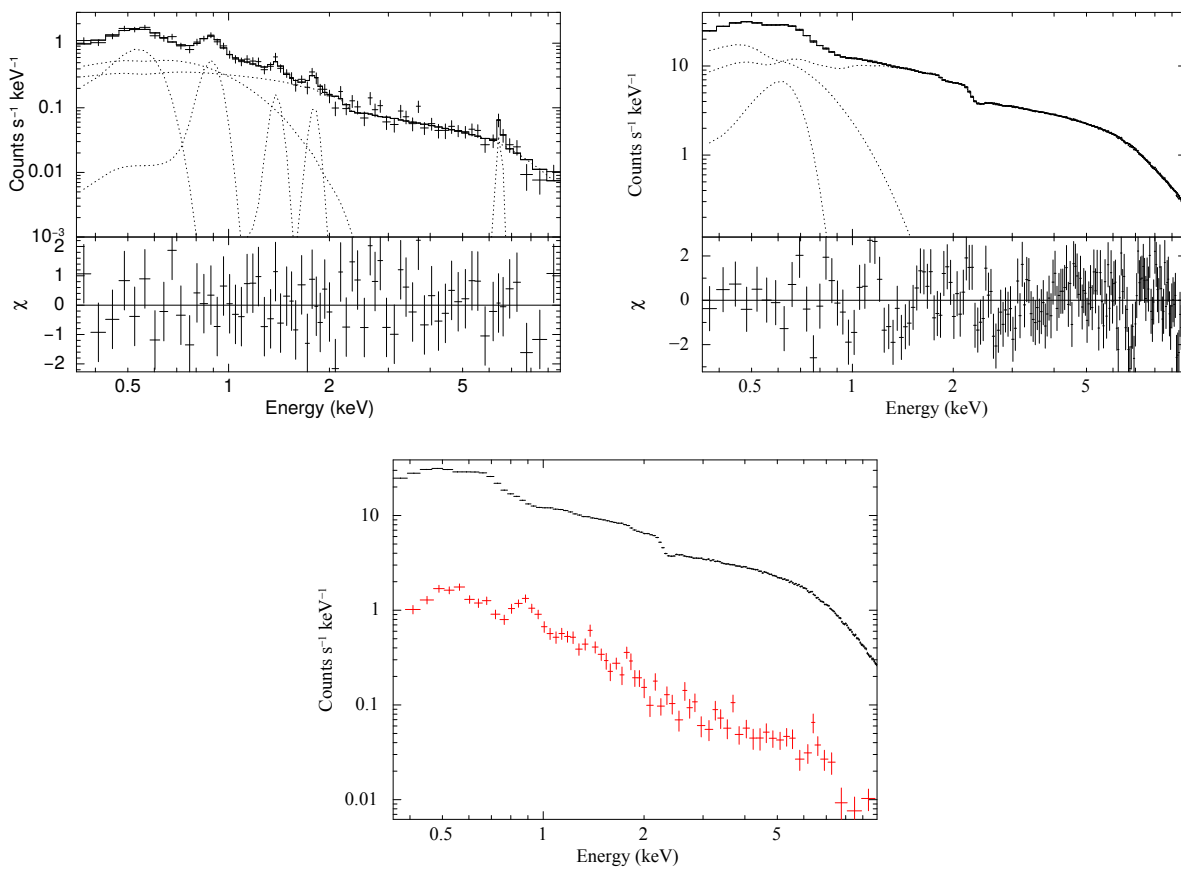


Fig. 4.14 Eclipse (top left) and OOE (top right) spectra of EXO 0748–676 (OB ID: 0160760201). Both the spectra are shown together in the bottom panel.

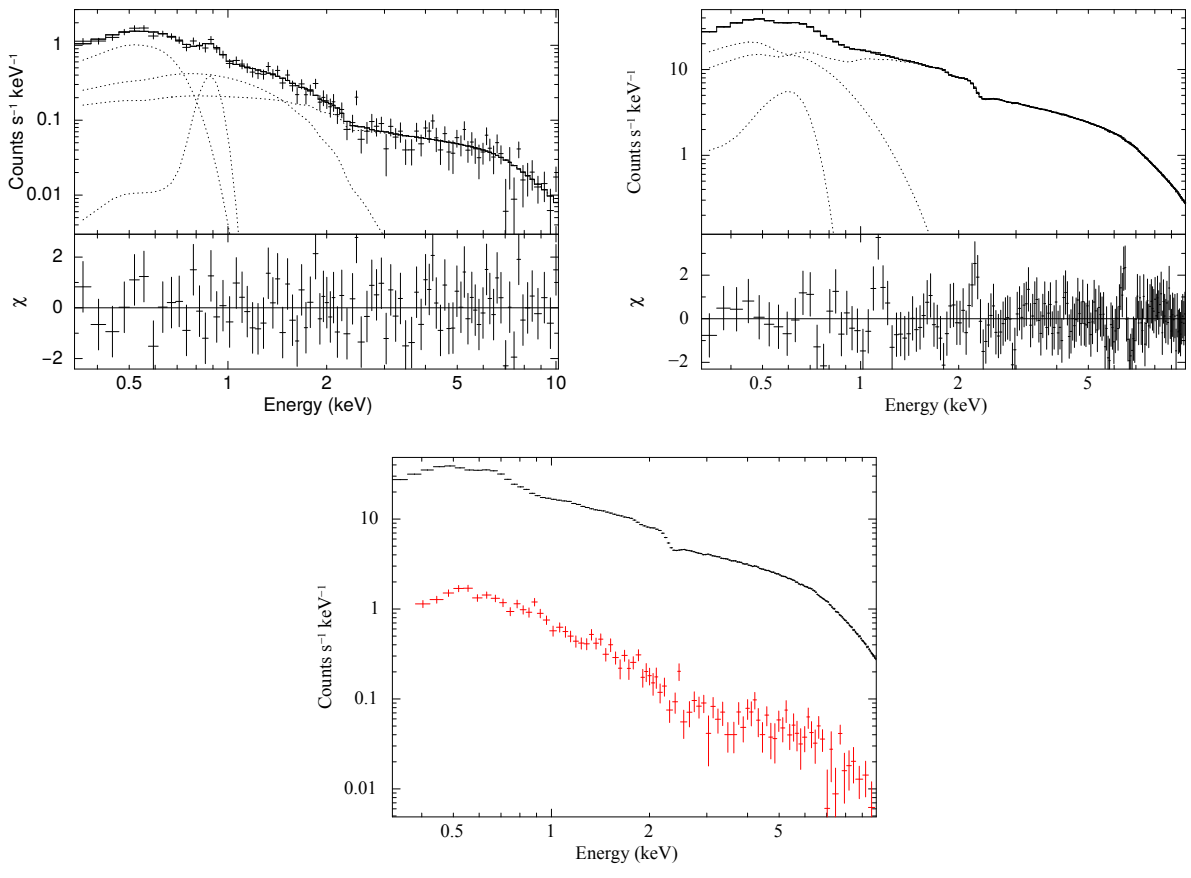


Fig. 4.15 Same as in Figure 4.14, for OB ID: 0160760301

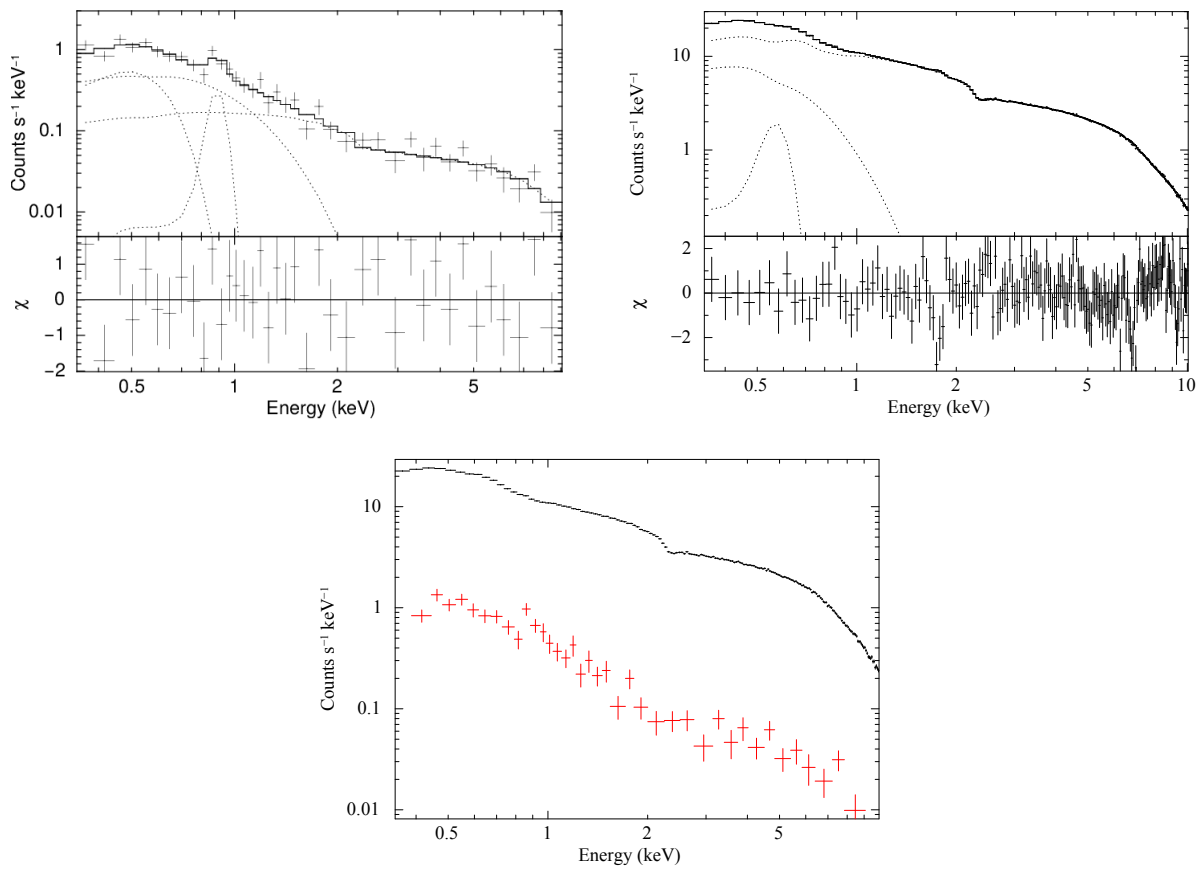


Fig. 4.16 Same as in Figure 4.14, for OB ID: 0160760401

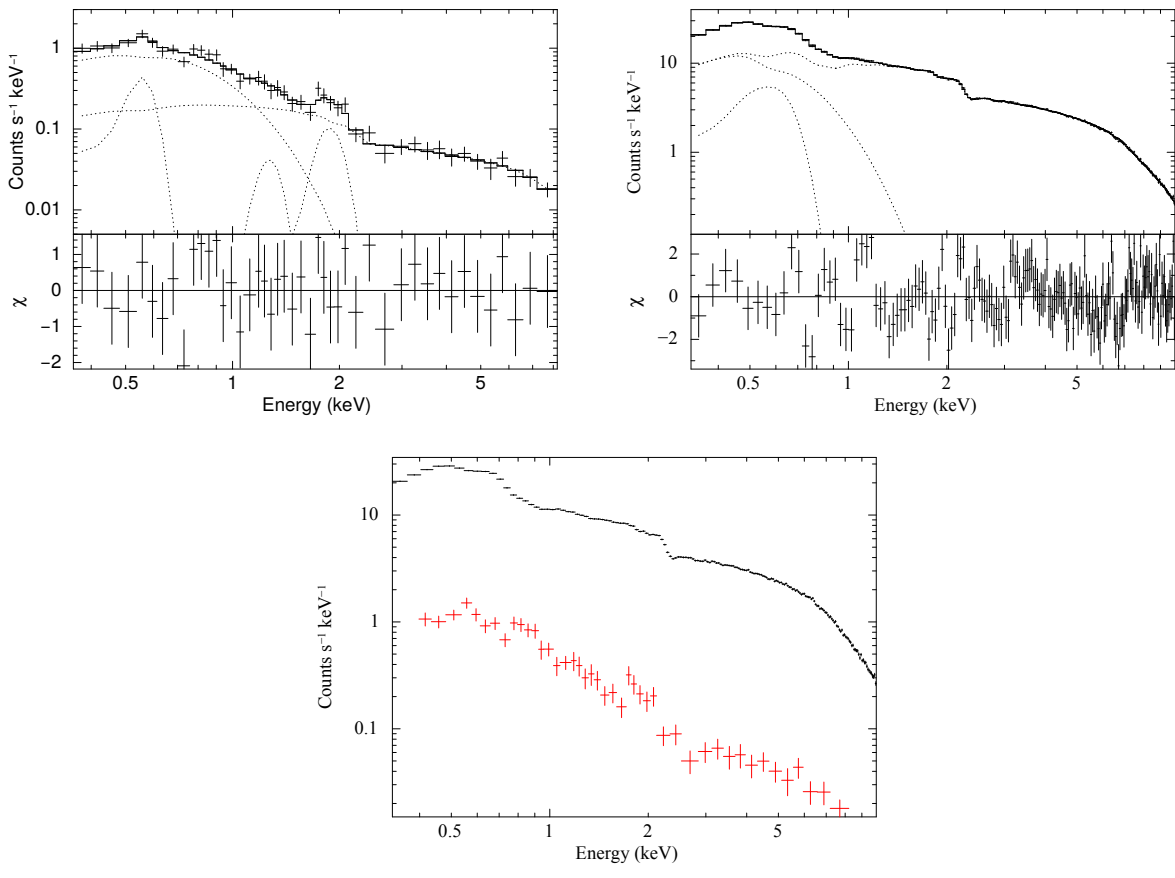


Fig. 4.17 Same as in Figure 4.14, for OB ID: 0160760601

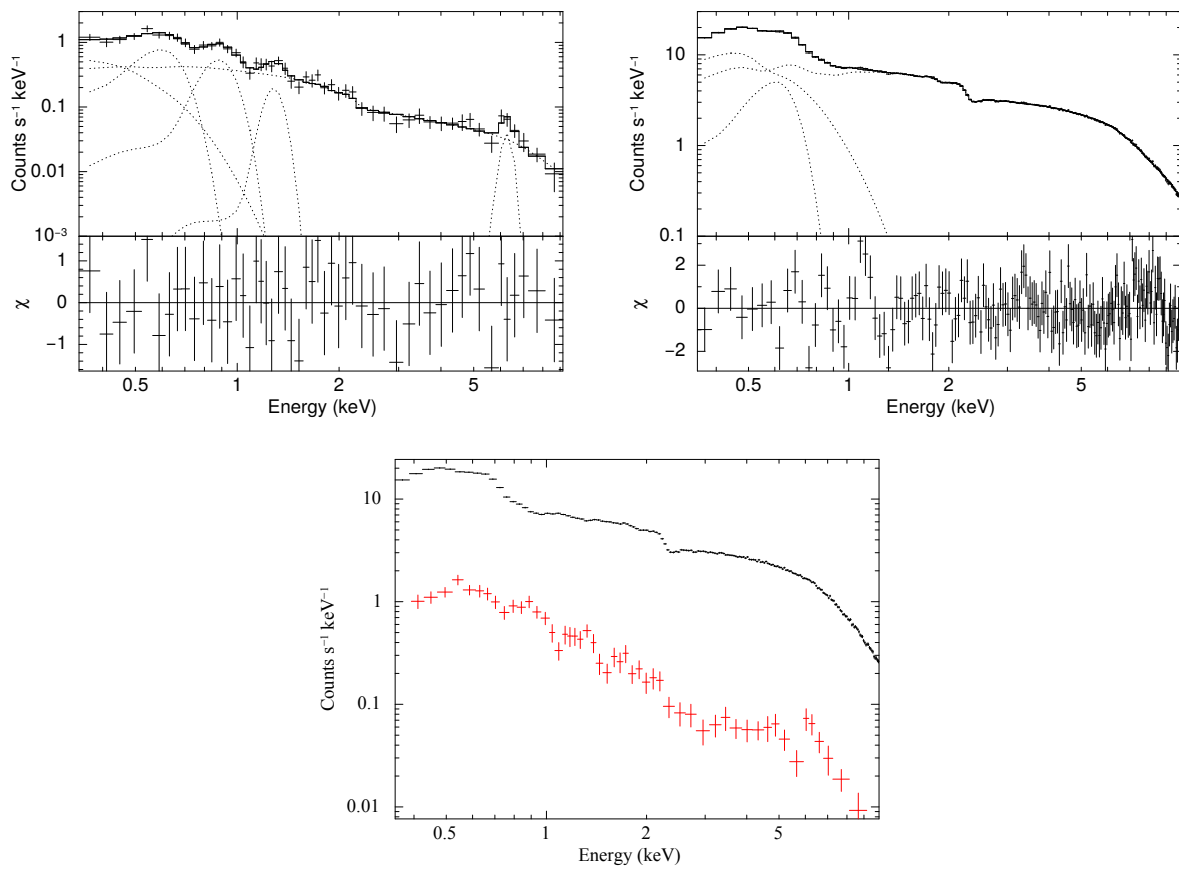


Fig. 4.18 Same as in Figure 4.14, for OB ID: 0160760801

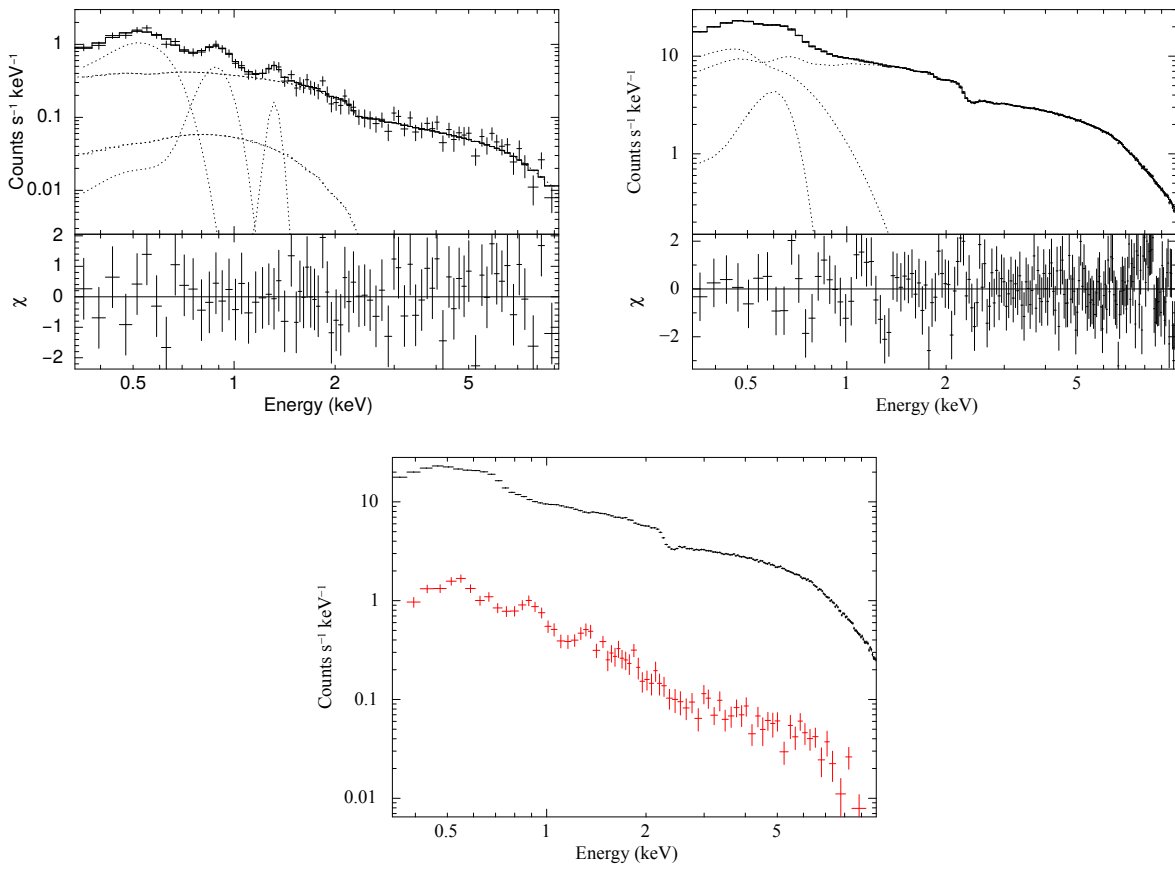


Fig. 4.19 Same as in Figure 4.14, for OB ID: 0160761301

4.3 Discussion

During eclipses in LMXB systems the direct emission is completely blocked by the companion and the detected X-rays are the reprocessed X-rays from the surrounding medium. In LMXBs the main reprocessing agent is the accretion disc and any structures if present in the disc. In some cases slow and dense wind from the red giant companion (Masetti et al. 2007, Nespoli et al. 2010) acts as reprocessing agent. During eclipses the continuum is expected to be strongly suppressed. Emission lines which are often produced in the surrounding medium are expected to be suppressed by a lesser extent. The eclipse spectrum is therefore expected to show larger equivalent width and better detectability of the emission and / absorption lines compared to the out-of-eclipse spectrum. However depending upon the extent of the accretion disc; its orientation with respect to the line of sight; structures in the disc; distribution of the material around the compact object and its density, this effect can be different in different sources.

To understand the X-ray reprocessing properties of LMXB systems we have analyzed 17 observations of 4 LMXB sources. We compared their eclipse and out-of-eclipse spectra and also compared eclipse spectra of these sources. We have found some similarities and significant differences in the reprocessing properties of the LMXB systems we have analyzed. These LMXBs have orbital period in the range of 3.28 hour to 8.35 hour, so far known mass of the companion is in the range the range of $\sim 0.5M_{\odot}$ to $0.9M_{\odot}$ (EXO 0748–676, AXJ 1745.6–2901, MXB 1659–298).

A summary of the comparison of various aspects of the X-ray reprocessing in these LMXBs is as follows: flux ratio of the eclipse to out-of-eclipse spectra shows a wide range, from ~ 5 (in AX J1745.6–2901, OB ID: 0723410501) to ~ 66 (in XTE J1710–281, OB ID: 0206990401), which differs by a factor of ~ 13 . In case of HMXBs we have seen much wider variation (~ 8 -278) in the out-of-eclipse to eclipse flux ratio. In 7 observations of AX J1745.6–2901 and EXO 0748–676 the eclipse to out-of-eclipse flux ratio have been found to have narrow range, (~ 5 -10) and (~ 33 -44) respectively. Two observations of MXB 1659–298 also show similar eclipse to out-of-eclipse flux ratio (22-24). These are smaller factor compared to wind accreting supergiant HMXBs (as seen in Chapter 3), where we have seen

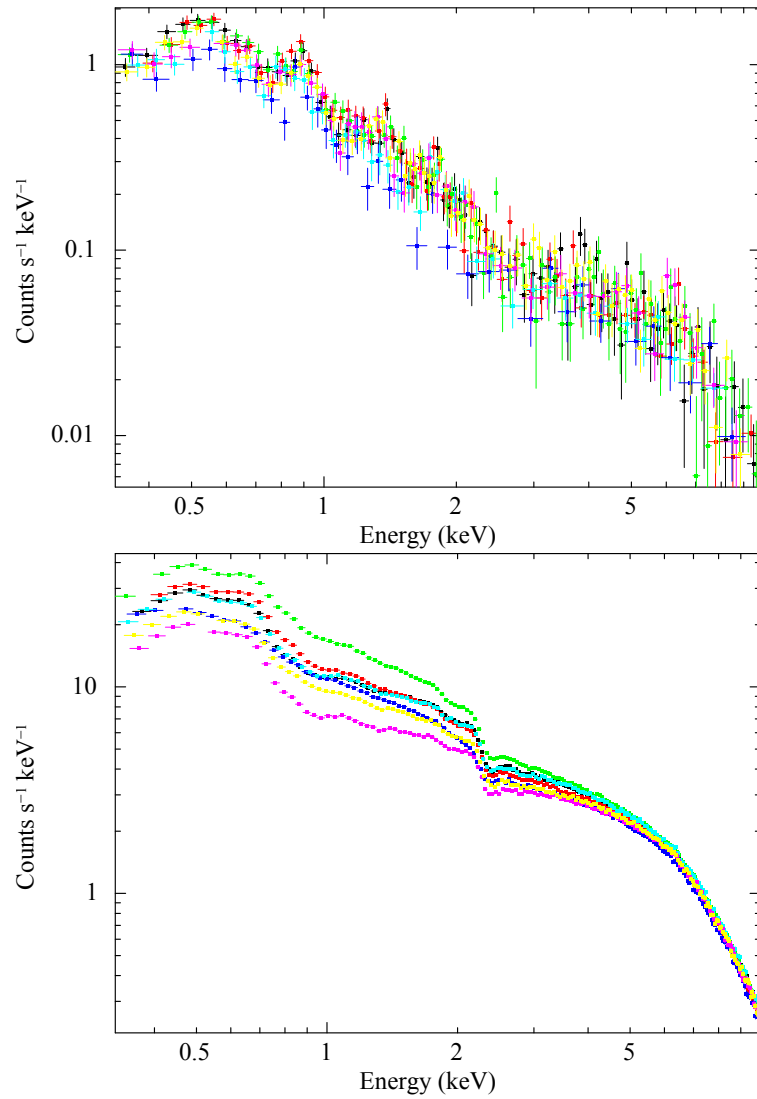


Fig. 4.20 Composite eclipse spectra (top) and OOE spectra (bottom) of EXO 0748–676 for the 7 EPIC-pn observations

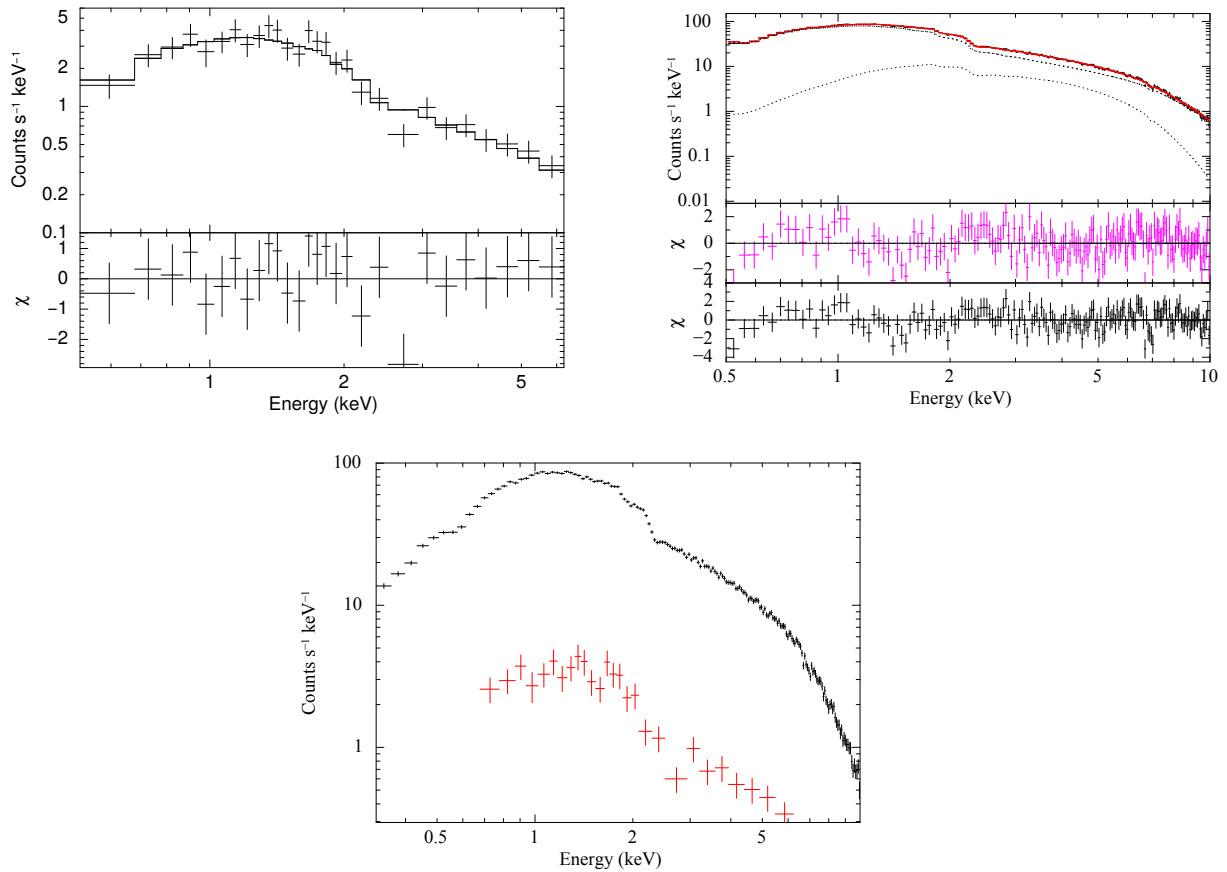


Fig. 4.21 eclipse(top left) and OOE(top right) spectra of MXB 1659–298 (OB ID: 0008620601). The second panel of the top right figure is the contribution of χ towards each bin for the best fit, while the 3rd panel is the same (χ) but excluding the absorption line mentioned in Table 4.9. Both the spectra are shown together in the bottom figure.

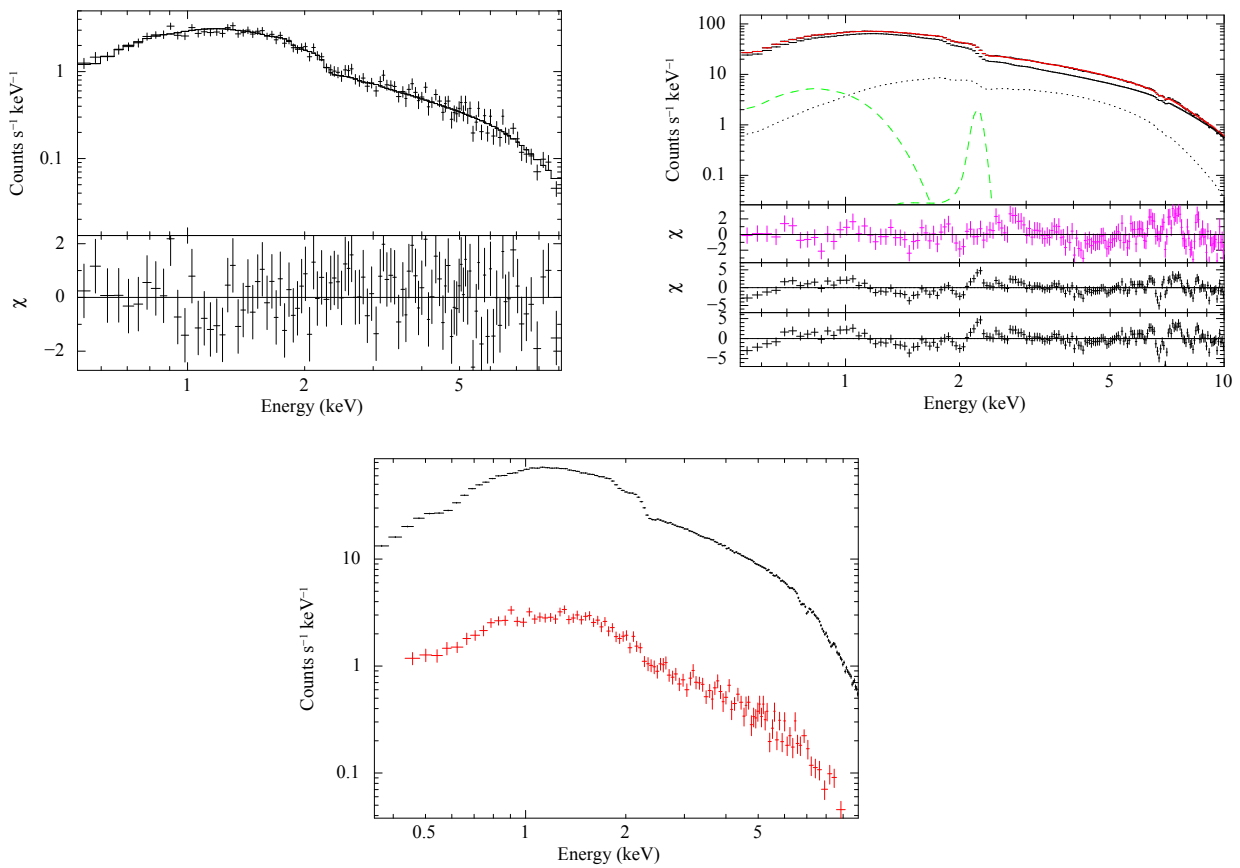


Fig. 4.22 Same as in Figure 4.21, for OB ID: 0008620701. Here the extra 4th panel shows the contribution of χ without the absorption line and two emission lines mentioned in Table 4.9.

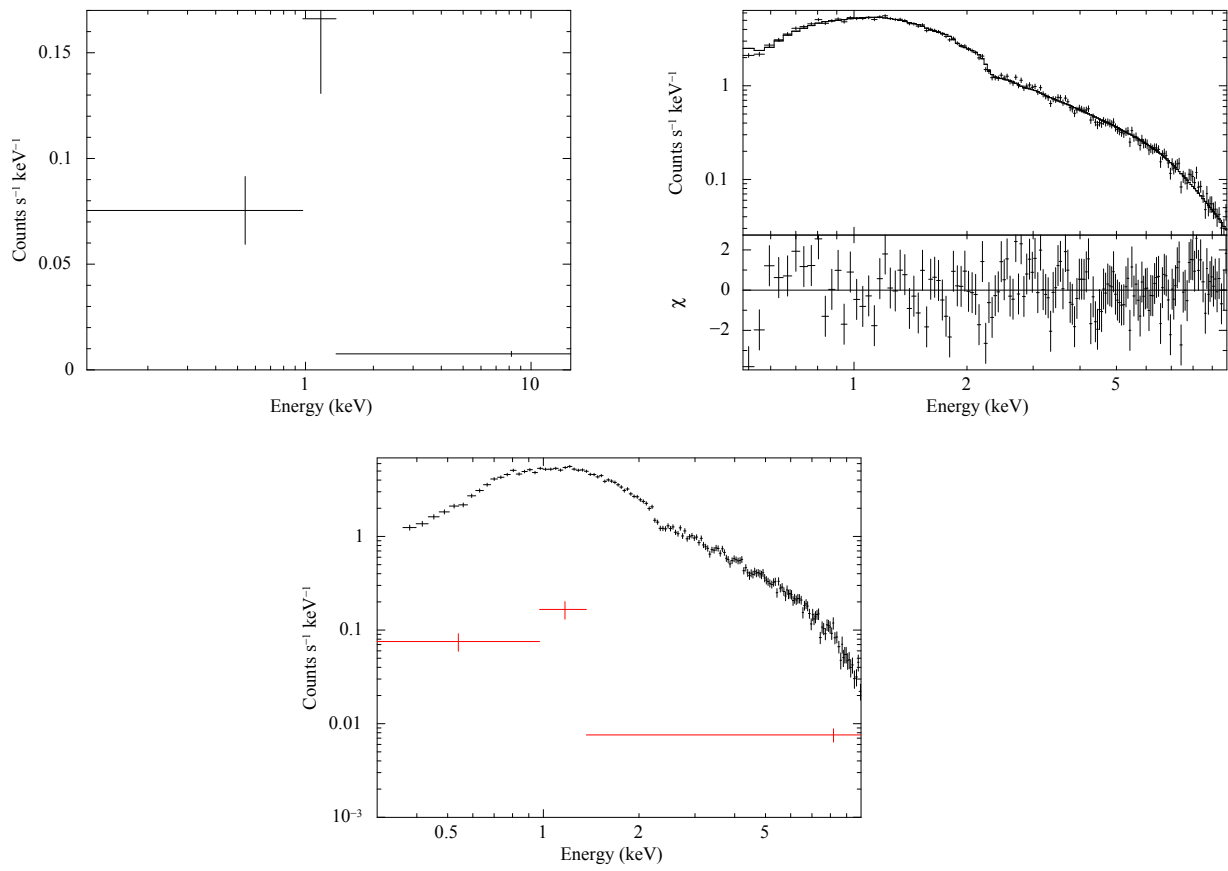


Fig. 4.23 eclipse(top left) and OOE(top right) spectra of XTE J1710–281 (OB ID: 0206990401). Both the spectra are shown together in the bottom panel.

large variation even in the same source within a period of less than a year. These indicate less variable environment surrounding disc-fed systems.

In AX J1745.6–2901, above ~ 3 keV the difference between the intensities in the eclipse and the out-of-eclipse spectra increases. This indicates that the outer accretion disc is not eclipsed during eclipse of the compact object by the companion, as the outer accretion disc emits and reprocesses to softer X-rays. This signifies that the radius of the accretion disc in the system is larger than the radius of the companion. Amongst 7 observations, Fe XXVI and Fe XXV absorption lines have been found in 4 out-of-eclipse (OB IDs: 0402430301, 0402430401, 0724210201, 0762250301) spectra. (Table 4.3). In two of the above mentioned out-of-eclipse spectrum (OB ID: 0402430401, 0762250301) one (7.40 keV) and two emission lines (6.3, 7.47 keV) have been found respectively. The $6.3^{+0.05}_{-0.04}$ keV emission line in the above observation is possibly for the Fe K_{α} emission line. But the origin of $7.40^{+0.04}_{-0.05}$ keV and $7.47^{+0.13}_{-0.20}$ keV emission line is not clear, but addition of these lines significantly reduces the χ^2 values of the spectral fits.

In EXO 0748–676, continuum of the eclipse spectra drops nearly by same factor throughout (0.3–10) keV energy range from that of the out-of-eclipse spectra in all the 7 observations. All 7 out-of-eclipse spectra required partial covering absorption by partially ionized material. The partially ionized materials cover 60–80% of the source emission. This model was not required to fit the eclipse spectra, which indicates that these ionized materials are close to the source and fully blocked during eclipse. The blackbody norm is much higher for the out-of-eclipse spectra than the eclipse spectra, as during eclipse a small portion of the accretion disc radiating as blackbody is visible. When the source comes out of eclipse then much larger region (source and accretion disc) is visible. 2 to 5 emission lines have been found in the 7 eclipse spectra. Two emission lines of energy ~ 0.5 or 0.6 keV and ~ 0.9 keV are common in all the eclipse spectra. ~ 0.6 keV emission line has been found in all the out-of-eclipse spectra. The equivalent width of the emission line which is common in both the eclipse and out-of-eclipse spectra (~ 0.5 or 0.6 keV) is higher during eclipse phases. These indicate presence of Oxygen (O K_{α} line energy: 0.52 keV) and / or Manganese (Mn L_{α} line energy: 0.64 keV) in this LMXB environment. In some of the eclipse spectra (OB

IDs: 0160760101, 0160760201, 0160760601, 0160760801, 0160761301) we have found ~ 1.3 - 1.4 keV emission line. One out-of-eclipse spectrum shows ~ 1.3 keV absorption line. In one eclipse spectrum (OB ID: 0160760201) we have found low ionized/neutral Iron (Fe) K_{α} emission line of energy 6.44 keV (though the detection significance is lower than 3σ) Two out-of-eclipse spectra (OB IDs: 0160760101, 0160760801) show the presence of Fe XXV absorption line and Fe XXVI absorption line has been found in one out-of-eclipse spectrum (OB ID: 0160761301). This indicates presence of Iron in the system. Another observation (OB ID: 0160760801) with the detection of 6.27 keV emission line with high equivalent width (~ 731 eV) also indicates some possibilities of the presence of iron in the system. In some of the out-of-eclipse spectra we have found absorption line near 2 keV (OB IDs: 0160760201, 0160760301, 0160760401). EPIC energy response has pronounced edge near 2 keV, so these absorption lines may not be actual. The composite eclipse spectra for the 7 observations almost overlap (top panel of Figure 4.20), this indicates nearly consistent accretion mechanism during two months of observation period. This also indicates nearly same kind of distribution of matter in the outer accretion disc and in the surrounding region, as during eclipse inner accretion disc is blocked by the companion. Composite out-of-eclipse spectra of the 7 observations show an overlap above ~ 4 keV (bottom panel of Figure 4.20), this indicates some warps kind of structures in the inner accretion disc. These warps possibly vary in structure and density in a manner, that they cause variation in the reprocessing of lower energy X-ray photons, whereas higher energy X-rays are almost unaffected by these warps.

Two observations of MXB 1659–298 show nearly same fluxes in the energy range of (0.5-10)keV in the eclipse phases. Flux ratio of the out-of-eclipse to eclipse phases also quite similar, which signifies X-reprocessing properties do not vary much over a period of ~ 1 year. Detection of Fe XXVI absorption line in the first out-of-eclipse spectrum and that of Fe XXV and Fe XXVI absorption lines in the second observation of the source indicates presence of highly ionized Fe atoms in the system. ~ 5 keV emission line possibly indicates presence of oxygen in the system. The emission line near 2 keV might be due to sharp fall of energy response of EPIC instrument.

Very poor statistics of the eclipse spectrum of XTE J1710–281 could be due to very short duration of the eclipse (single eclipse is covered in this observation) or could be due to non-detection of the reprocessed X-ray photons during eclipse. The second situation is feasible if the accretion disc is very small or the plane of the accretion disc is nearly edge on with respect to our line of sight, hence completely blocked during eclipse.

4.4 Conclusion

- The eclipse spectra for some of the sources are being reported for the first time.
- Most contrasting outcome with respect to the HMXBs is the lack of strong 6.4 keV line in the eclipse spectrum of LMXBs.
- The emission lines in EXO 0748–676 are new discoveries. Accretion mechanism remains nearly same over two months in this source. Some variable warp structure is thought to be present in the inner accretion disc within this period.
- In spite of having much weaker wind environment, the flux ratio of out-of-eclipse to eclipse in LMXBs is in a range comparable to the HMXBs.
- Comparable out-of-eclipse to eclipse flux ratio in AXJ 1745.6–2901 irrespective of intensity state is an important finding.

Chapter 5

Variability study of the High Mass X-ray Binary IGR J18027–2016 with *Swift*–XRT

5.1 Introduction

"As in the experimental sciences, truth cannot be distinguished from error as long as firm principles have not been established through the rigorous observation of facts."

- Louis Pasteur

High Mass X-ray binary (HMXB) systems contain a companion star with mass $\geq 10 M_{\odot}$ (either a main sequence star or a supergiant) and a compact object (either a neutron star or a black hole). Accretion onto the compact object occur via capture of stellar wind or Roche lobe overflow. HMXB systems are divided into two classes: (1) Be X-ray binary (Be HMXB) and (2) Supergiant X-ray binary (sgHMXB) some of which show the Supergiant Fast X-ray Transient (SFXT) Phenomena. Be HMXB and SFXTs are mostly

The work presented in this chapter has been published in MNRAS (Aftab et al. 463: 2032-2038, 2016).
MNRAS: Monthly Notices of the Royal Astronomical Society

transients in nature. In Be HMXBs, the accretion onto the compact object occurs via out-flowing equatorial disk of the companion when and the compact object passing through it (Reig, 2011). Supergiant Fast X-ray Transients (SFXTs) are a sub class of HMXBs discovered with *INTEGRAL*, having recurrent; bright; short flares (Sguera et al., 2005b), reaching $L_X \sim 10^{36} - 10^{37} \text{ erg sec}^{-1}$ (Sidoli et al., 2007), while their quiescent X-ray luminosity is $\sim 10^{32} \text{ ergs sec}^{-1}$ (Bozzo et al., 2010b). Persistent sgHMXBs are found in high luminosity states (X-ray luminosity $L_X = 10^{35} - 10^{36} \text{ ergs sec}^{-1}$) most of the time. Several short off states have been observed in some of these systems: Vela X–1 – Manousakis and Walter (2015); Odaka et al. (2013); GX 301–2 – Göğüş et al. (2011); 4U1907+09 – Doroshenko et al. (2012), 4U 1700–37 – Grebenev et al. (1999), OAO 1657–415 – Pradhan et al. (2014). On the other hand some sgHMXBs like SMC X-1 and LMC X-4 do not show off states, but they have strong short timescale flares (Moon et al., 2003; Moon and Eikenberry, 2001). *INTEGRAL* observation of sgHMXBs show a wide range and type of intensity variation (Walter et al., 2015).

The HMXB IGR J18027–2016 was discovered with *INTEGRAL* – IBIS/ISGRI during the survey of the Galactic Center region in September 2003 (Revnivtsev et al., 2004b). The pulsar is found to have a spin period of $\sim 139 \text{ s}$ (Augello et al., 2003b) and orbital period of 4.57 days (Hill et al., 2005b; Jain et al., 2009c) around a supergiant companion with spectral type B1-Ib (Torrejón et al., 2010b).

Hill et al. (2005b) characterized the combined *XMM-Newton* and *INTEGRAL* X-ray spectrum of the pulsar by a broken power law, modified by a photoelectric absorption along the line of sight hydrogen column density $N_H \sim 10^{23} \text{ cm}^{-2}$. A soft excess is also detected in the spectra of this source (Hill et al., 2005b; Walter et al., 2006). During *INTEGRAL* observations in 2003 and 2004, the source flux in the 18–60 keV energy band was found to be nearly constant (Lutovinov et al., 2005), which is in contrast with other HMXBs in which intensity variation by a factor ~ 10 are often observed. However, nondetection of the source by previous X-ray missions indicates some sort of transient behaviour (Hill et al., 2005b).

In this work, we have analyzed all *Swift*–XRT observations of IGR J18027–2016 to investigate its long term pulsation and spectral characteristics. We searched for pulsations

in all the observations and folded the light-curves with the estimated pulse period to study its pulse profiles. Orbital intensity analysis show some low X-ray intensity episodes of the source, similar to that seen in Vela X-1, GX 301-2, 4U 1907+09 (Manousakis and Walter, 2015; Göğüş et al., 2011; Doroshenko et al., 2012), OAO 1657-415 (Barnstedt et al., 2008) etc. We have further investigated the nature of the system by studying its spectral characteristics at different orbital phases. Our results can put some useful insight into systems having sudden off states in X-ray intensity.

5.2 Data and Analysis

Swift observatory was launched in November 2004 (Gehrels et al., 2004), consisting of 3 sets of instruments: 1) Burst Alert Telescope (BAT), operating in the energy range of 15–150 keV (Barthelmy et al., 2005) 2) X-ray Telescope (XRT), operating in the range of 0.2–10 keV (Burrows et al., 2007) 3) Ultraviolet and Optical Telescope (UVOT), having UV and optical coverage of 170–600 nm (Roming et al 2005). XRT and UVOT are two narrow field instruments, coaligned and pointed to the center of FOV of BAT.

BAT is a coded aperture instrument with CdZnTe detector, having a field of view $100^\circ \times 60^\circ$ and a detection sensitivity of 5.3 mCrab (Krimm et al., 2013b). XRT is a focusing telescope which employs an X-ray CCD detector with a Wolter 1 mirror set of 3.5 m focal length, with 23.6×23.6 arcmin FOV. The imaging array consists of 600×600 image pixels, each with $40 \mu\text{m} \times 40 \mu\text{m}$ size and 2.5 arcsec/pixel resolution. It operates on 3 read-out modes namely Imaging (IM), Windowed Timing (WT) and Photon Counting (PC) mode with few sub modes. In Imaging mode (IM), image of the object is obtained by CCD read-out. Photons are allowed to pile up and photon recognition is not done in this mode. Windowed timing mode (WT) produces 1.7 ms resolution timing with 1D position information and full energy resolution for flux less than 600 mCrab. Photon counting mode (PC) contributes to full imaging and spectroscopic resolution with time resolution of 2.6 sec.

We have analyzed 33 separate *Swift*-XRT observations of IGR J18027-2016 from MJD 54141 to 56171. We have also used ~ 10.5 years of *Swift*-BAT lightcurve to make an ac-

curate estimation of the orbital period of this system.⁴ Minimum exposure time amongst 33 *Swift*–XRT observations ~ 300 sec and maximum exposure ~ 10 kilosec. We used Photon Counting (PC) mode data, because 32 observations out of 33 had only this datamode. We filtered level1 data with the task XRTPIPELINE and obtained cleaned event files for all observations. For the barycenter correction of the time column of the event files we used the FTOOL BARYCORR. We extracted the source photons from a region with $60''$ radius centering the source and the background photons from a similar region in the FOV that is free of any other X-ray sources. We used these source and background region files to extract corresponding lightcurves and spectra using XSELECT v2.4C.

We have generated exposure maps with the task XRTEXPOMAP to correct for the loss of flux due to some hot CCD pixels. We then used this exposure map to create ancillary file with the routine XRTMKARF which was then used for the spectral fitting in XSPEC. We obtained the response file from the latest *Swift* calibration dataset CALDB v1.3.0. For 5 observations, the source could not be distinctly identified from the background, even with the task XRTCENTROID. For these observations, we extracted the lightcurves and spectra with region files centered at the R.A.(18h 02m 41.94s) and Dec.($-20^\circ 17' 17.3''$) of the source (Torrejón et al., 2010b). Observation at MJD 54141 was longer in duration (~ 10 ks) and observations at MJD 56085 and 56096 showed significant difference in the count rate at the beginning and at the end of the observation. So we divided lightcurves and spectra of these three observations into two parts to investigate them separately. Therefore, we have total 36 separate lightcurves and spectra to carry out timing and spectral analysis.

5.2.1 Pulsation Analysis

We searched for pulsations with the FTOOL EFSEARCH for all the observations in which the source is clearly visible in the image and the total number of source photons were more than 600. EFSEARCH results of all these lightcurves gave a maximum χ^2 of greater than 100 for 32 phasebins per period indicating a clear detection of the X-ray pulses. Table 1 shows the exposure time, total number of photons in $60''$ source region, average count rate,

⁴ <http://swift.gsfc.nasa.gov/results/transients/weak/IGRJ18027-2016>

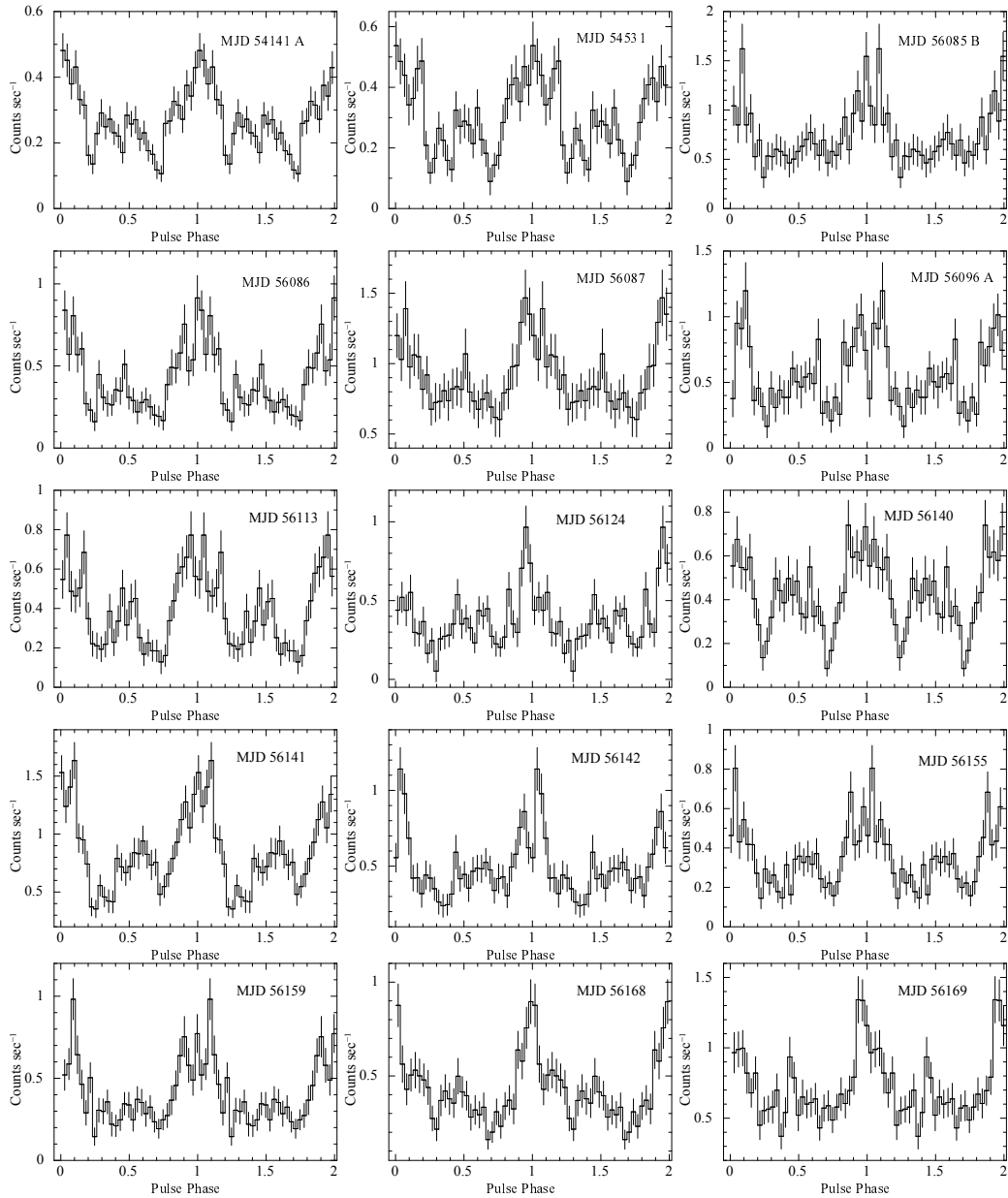


Fig. 5.1 Pulse profiles of 15 observations with clear detection of pulsation, folded with their estimated pulse periods and with 32 phasebins/period. Main peaks of all the profiles have been aligned at phase 1.0. The MJD of each observations are labelled inside each panel.

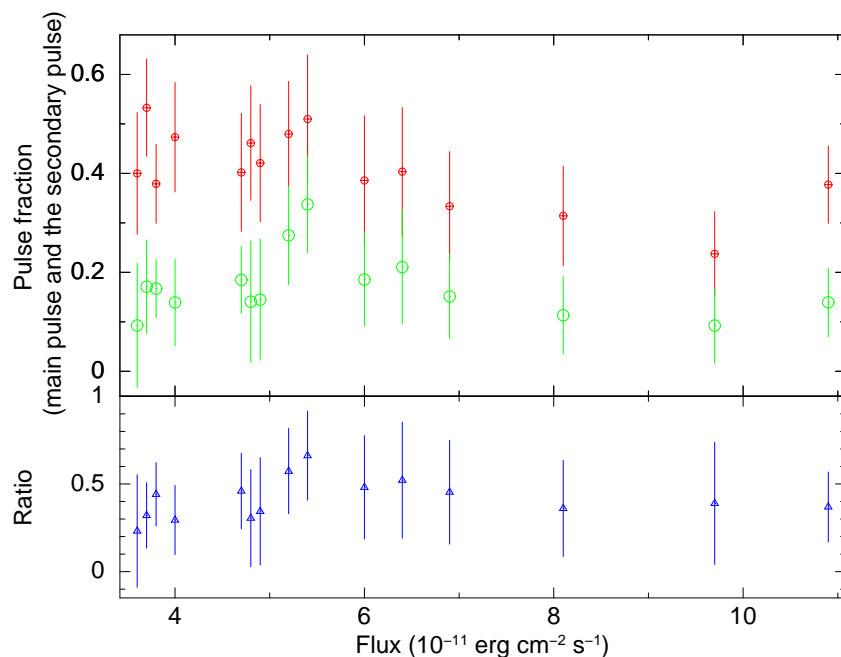


Fig. 5.2 Top panel: Pulse fraction of the main or primary (red) and secondary pulse (green) plotted as function of flux. Bottom panel: Ratio of the pulse fraction of the primary to the secondary pulse fraction plotted as function of flux.

pulse period and orbital phase of all observations, along with the observations which were divided into two parts mentioned in Section 2, arranged in the ascending order of the total number of source photons.

Light curve of each observations with pulsation detected were folded with corresponding pulse periods. Folded pulse profile of the 15 observations with pulsation detected are shown in Figure 5.1. The pulse profiles have been aligned such that the phase of the main peak of each profile lies at 1.0. As seen in Figure 5.1, most of the pulse profiles show a double peaked structure, with a possible indication of variation in relative intensity of the peaks. Only for the purpose of comparing the strengths of the two peaks, we fitted each of these pulse profiles with two gaussian, one for the primary pulse and the other for the secondary along with an unpulsed component. We define pulse fraction of the two peaks as the fractional area of the two gaussians. We obtained pulse fraction for both the peaks and plotted them in the top panel of Figure 5.2 along with their ratio i.e. the relative pulse fraction of the secondary to the primary in the bottom panel as function of flux. We see that

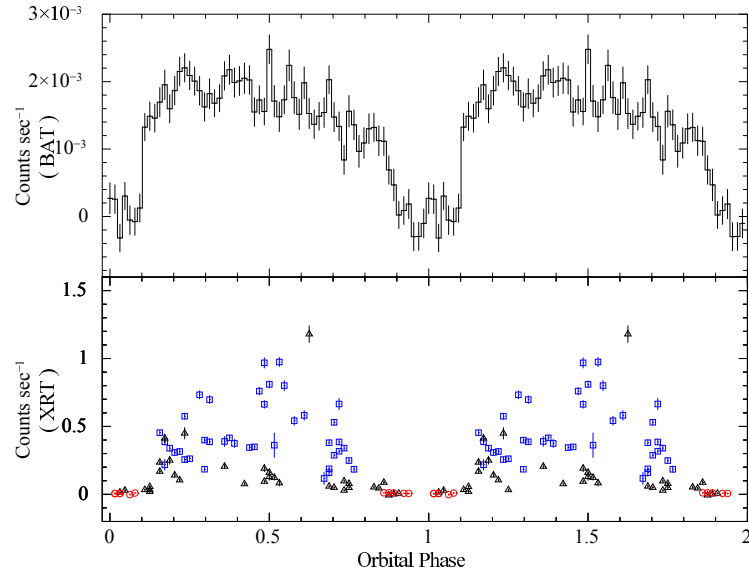


Fig. 5.3 **Top panel:** Orbital intensity profile of IGR J18027–2016 obtained by folding *Swift*–BAT light-curve with orbital period of 394843 sec. **Bottom panel:** *Swift*–XRT lightcurves modulo same orbital period in three colours: pulsation detected where number of source photons is greater than 600 – blue, number of source photons is less than 600 – black; faint – red.

while the overall pulse fraction has a weak negative correlation with the flux, the relative pulse fraction of the two peaks is nearly constant.

5.2.2 Orbital period analysis

We have searched for orbital period in the *Swift*–BAT light curve with the FTOOLS task EFSEARCH and found it to be 394843 sec (4.57 days; similar to P_{orb} determined by Hill et al. 2005b; Jain et al. 2009c). We then folded the *Swift*–BAT lightcurve with this orbital period, and in the folded profile (shown in the top panel of Figure 5.3), we can see an eclipse for duration of nearly $\frac{1}{4}$ th of the orbital period. In the bottom panel of Figure 5.3, we have plotted the orbital phase-wise X-ray count-rates obtained from all *Swift*–XRT lightcurves in three colours: pulsation detected where source photon is greater then 600 – blue; source photon less than 600 – black; faint, i.e. where source could not be seen clearly – red. To investigate any intensity variations other than the long time averaged orbital intensity

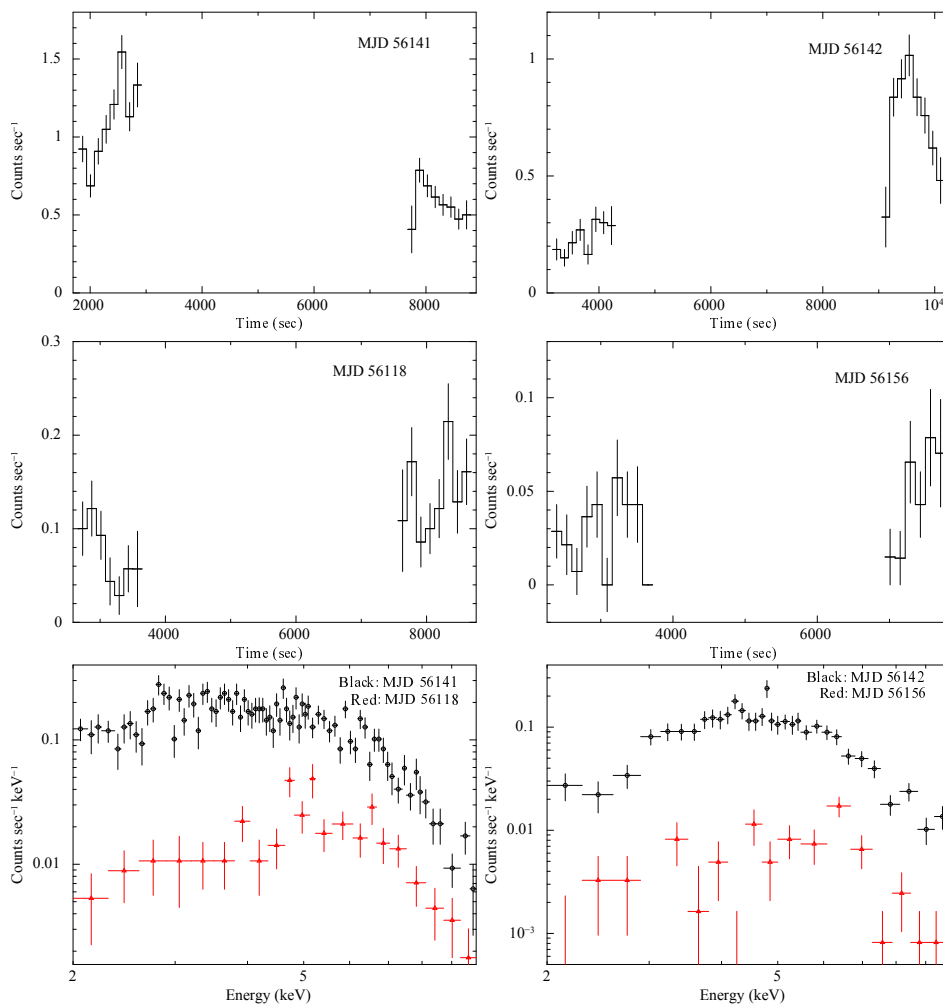


Fig. 5.4 **Left panel:** The top and middle panel show the light-curves of two observations centered at orbital phase 0.48–0.52. In the top panel, the light-curve of an observation (MJD 56141) shows a high count-rate whereas the middle panel shows another observation (MJD 56118) in the same orbital phase range, having a low count-rate. The lower panel is the plot of spectra of these two observations which bring out the fact that in the same orbital phase range, the X-ray intensities vary by a factor of ~ 10 . **Right panel:** Same is shown for another set of observations (MJD 56142 and MJD 56156) centered at orbital phase range 0.69–0.75, but showing a large change in X-ray intensities.

modulation, multiple observations with *Swift*–XRT during the same orbital phase range are not averaged here, unlike the orbital profile shown in Figure 3 in Bozzo et al. (2015).

In Figure 5.3, the bottom panel shows the variability in count-rate of the source in the orbital intensity profile with the pointed *Swift*–XRT observations, whereas the *Swift*–BAT orbital intensity profile is averaged over many orbital cycles, indicating a sub-orbital variability similar to that seen in IGR J16393-4643 (Islam et al., 2015) and OAO 1657–415 (Pradhan et al. 2014; Barnstedt et al. 2008). Around orbital phase 0.5, there are multiple *Swift*–XRT observations showing significant difference in the count rates. We have shown spectra and lightcurve for two parts of observations carried out in same orbital phase ranges (0.48-0.52, 0.69-0.75) in Figure 5.4. The light curve is binned with 140 seconds (close to the spin period of the pulsar) to avoid seeing any effect of the pulse profile related variation in the light curve. In the top panel in Figure 5.4 there are about 140 photons per bin and the variability in the light curves is clearly larger than the photon noise (represented by the 1σ error bars in each bin). The number of counts per bin in the two light curves shown in the middle panel is smaller and have correspondingly larger uncertainties. No intensity variation can be ascertained in the light curves shown in the middle panels. Spectra of these two observations are shown in the lower panel of Figure 5.4 which bring out the fact that in the same orbital phase range, the X-ray intensities vary by a factor of ~ 10 .

5.2.3 Spectral Analysis

We fitted X-ray spectrum for 21 observations, having moderate statistics, using XSPEC v12.8.2 in the energy range of 2.0–9.0 keV. Because of limited statistics, we could not carry out spectral analysis for the rest of the observations. The spectra were modeled with a power law modified by a photoelectric absorption by column density of absorbing matter along our line of sight. We have found the equivalent column density of hydrogen (N_H) in the range of 10^{22} – 10^{23} cm^{-2} . A few of the spectra showed some residuals at 6.4 keV and we have used a gaussian line to model the 6.4 keV Fe K_α emission line by keeping the line energy fixed at 6.4 keV and width to 0.01 keV with the aim of detecting or putting upper limits on the detection of the line. With addition of the iron line component, four spectra

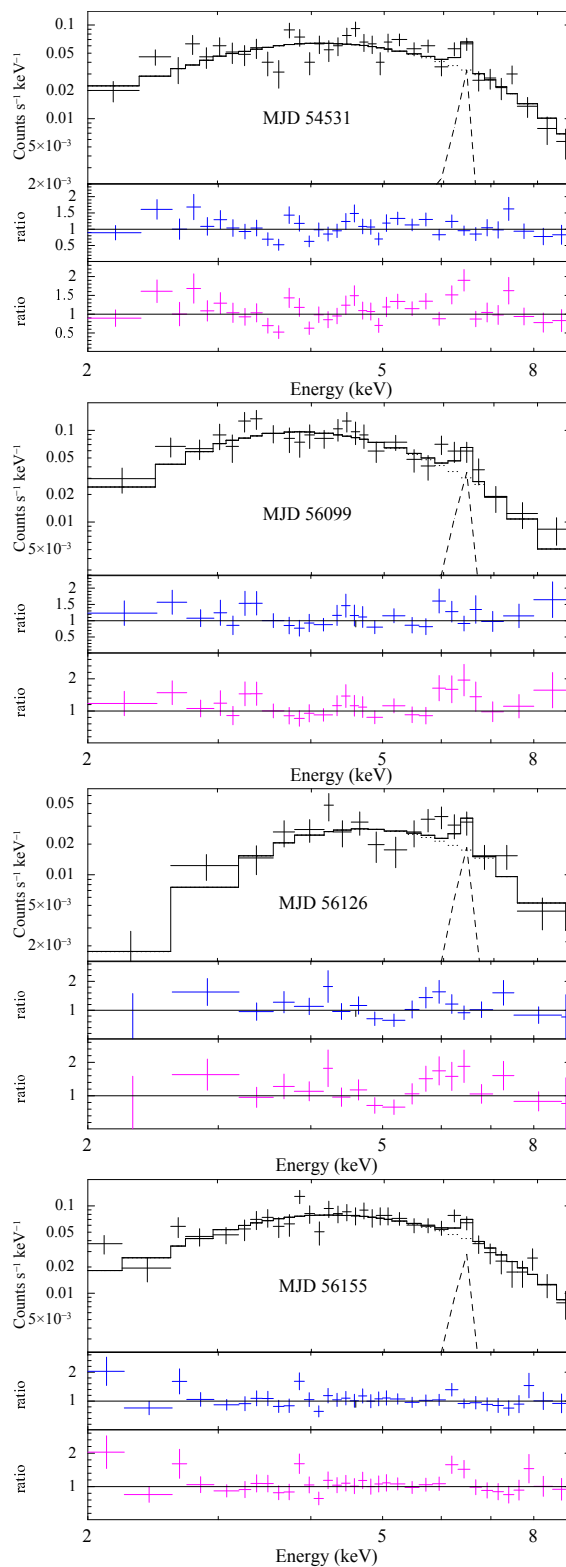


Fig. 5.5 Four observations at MJD 54531, 56099, 56126, 56155 in *Swift*-XRT of IGR J18027–2016 which show Fe K_{α} emission line in the spectra. 2nd and 3rd panel respectively show ratio of the data and best fit models with and without the iron emission line.

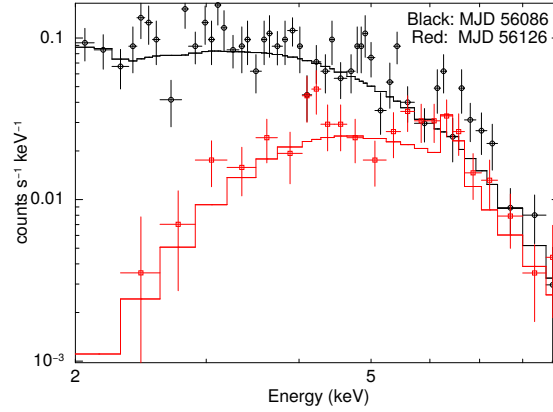


Fig. 5.6 Spectra at MJD 56086 AND 56126 are plotted together to show the variation in low energy absorption

showed improvement in χ^2 in the range of 5-12 for 38 degrees of freedom, indicating false detection probability in the range of 0.006 to 0.03 in each case. These four spectra are shown in Figure 5.5 along with the best fitted models. Ratio of the data to model are also shown with and without the iron line component. We have plotted two spectra in Figure 5.6 obtained at MJD 56086 and 56126 to show the variation in the absorption at low energies. The spectra clearly indicate large difference in column density.

We tabulated values of different spectral parameters and their errors with 90% confidence limit in Table 2, except for the errors on Fe line flux and equivalent width which are given at 1σ confidence limit. We have also fitted the spectra from the remaining observations with a power law, only for the purpose of estimating the total flux. Flux during the out-of-eclipse orbital phase are found to be in the range of $(0.4-14) \times 10^{-11}$ ergs cm^{-2} sec^{-1} . We have plotted the spectral parameters N_H , Γ , Fe line flux, equivalent width and total flux (2.0–9.0 keV) from the system in Figure 5.7.

5.3 Discussion

In this work, we have analyzed all available *Swift*–XRT observations of the HMXB source IGR J18027–2016, to study its pulsations and variability characteristics. Pulsations have been detected in all the observations having a total number of source photons greater than

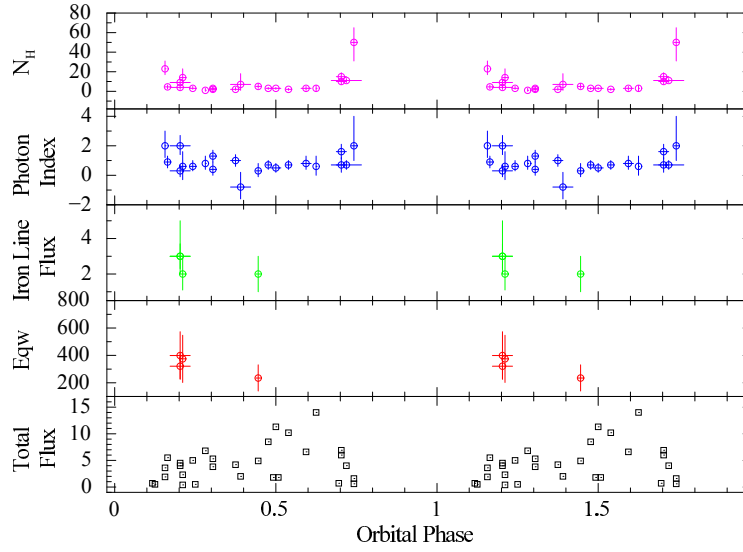


Fig. 5.7 Variation of column density of hydrogen (N_H in units of 10^{22}cm^{-2}), photon index (Γ), line flux of Fe K_α (in units of photons $\text{cm}^{-2}\text{sec}^{-1}$), equivalent width of Fe K_α line (Eqw in units of eV), total flux (F in the units of $10^{-11}\text{ergs.cm}^{-2}\text{sec}^{-1}$).

600 (Table 1) and the light-curves of these observations were folded with the pulse periods to create pulse profiles (Figure 5.1). Some of the pulse profiles are found to have double peaked structure. We therefore carried out an analysis of the pulse profile and determined the pulse fractions of the two peaks. We have plotted these pulse fractions and their ratio (primary pulse fraction to the secondary) in Figure 5.2 as function of flux and find no evidence for significant variation in the pulse profiles over a factor ~ 3 variation in flux.

The pulse profiles of accreting X-ray pulsars show strong energy dependence (Nagase, 1989), usually having simpler pulse profile at higher energies ($>10\text{keV}$) and complex profile at low energy, often resulting due to phase locked absorption. However in a given energy band, most persistent HMXB pulsars *i.e.* sources with supergiant companion have pulse profiles that are stable over long periods of time (Vela X–1 – Kreykenbohm et al. 1999, Maitra and Paul 2013). The transient pulsars, on the other hand, show very strong time/luminosity dependence of the pulse profile, which can be attributed to the changes in the structure of the X-ray emission region (accretion column) during the transient phase (Devasia et al., 2011). The limited pulse profile changes in IGR J18027–2016 is consistent with other persistent HMXBs.

The long term averaged orbital intensity profile of this source created with *Swift*–BAT light-curves is smoothly varying, having an eclipse lasting for about 1/4 th of the orbit (top panel of Figure 5.3). The *Swift*–XRT and *INTEGRAL* light-curves, when averaged also give smoothly varying orbital intensity profiles (Bozzo et al., 2015; Hill et al., 2005b). However, the *Swift*–XRT light-curves, when plotted individually for all the observations as a function of orbital phase, shows a significant count-rate variation outside the eclipse (bottom panel of Fig 5.3). Within the same observation carried out around orbital phase 0.3-0.5 (MJD: 56085), the X-ray count-rates are found to vary by a factor of 36. A maximum count-rate variation (a factor of 48) is shown by two non-eclipse observations at MJD 56085 and MJD 56087. These short term variation could also be due to hydrodynamical instabilities. Manousakis and Walter (2015) has produced the hard X-ray variation observed with *INTEGRAL*-ISGRI and RXTE-PCA with hydrodynamical instabilities predicted by simple model without considering intrinsic clumping or propeller effect. In some cases like in OAO 1657–415, the variations in X-ray intensity may also arise due to the accretion onto the compact object by inhomogeneous clumpy winds (Oskinova et al., 2013; Pradhan et al., 2014; Barnstedt et al., 2008).

In the present work, we detect several low X-ray intensity episodes (For *e.g* in orbital phases 0.5 and 0.7) in the supergiant HMXB IGR J18027–2016, indicating these episodes to be either off-states like episode similar to Vela X–1 (Doroshenko et al., 2011) or presence of clumpy wind like OAO 1657–415 (Pradhan et al., 2014; Barnstedt et al., 2008). From these XRT observations, we cannot distinguish from either of these two scenarios.

X-ray spectra were extracted for 21 *Swift*–XRT observations, having moderate statistics to fit with a simple power-law model, modified for photo-electric absorption (parameter values given in Table 2). The value of absorption column density N_H is as high as $5 \times 10^{23} \text{ cm}^{-2}$, which is similar to the values obtained by Hill et al. (2005b); Walter et al. (2006), and indicate a dense circumstellar environment around the neutron star. From Figure 5.7, we see an increase in N_H just before and after the eclipse, similar to that seen in 4U 1538–52 (Rodes-Roca et al., 2015). The equivalent width of Fe line estimated by Hill et al. (2005b) and Walter et al. (2006) from the *XMM-Newton* observation of this source was less than 40

eV. Though the statistical significance is not high, in 4 *Swift*–XRT observations, we found a presence of Fe K α emission line, having equivalent width in the range of 250–400 eV (Table 2). Such high equivalent width of Fe line are found in some HMXBs like GX 301–2 (Islam and Paul, 2014b), IGR J16479–4514 (Walter et al., 2006), GX 1+4 (Kotani et al., 1999), Cen X–3 (Naik et al., 2011). Due to poor statistics below 2 keV, we can not search for evidence of soft excess in any *Swift*–XRT observations.

IGR J18027–2016 presents an interesting case of a supergiant source showing evidence of low X-ray intensity states, similar to well known sources like Vela X-1. Detailed X-ray timing and spectroscopic observations of IGR J18027–2016 at various orbital phases with other X-ray missions would be useful to understand the nature of these low intensity states.

Table 5.1 Log of observations with exposure time, total number of source photons, average count-rate, pulse period and orbital phase. A and B refers to the observations which were split as mentioned in Section 2.

Observation MJD	Observation ID	Exposure time (sec)	Total no of photons in source region	Average count-rate (counts/sec)	Pulse Period (sec)	Orbital Phase
56143	00035720023	929	6	0.01	-	0.02 - 0.03
56098	00035720011	874	8	0.01	-	0.06 - 0.08
56085 A	00035720005 A	442	16	0.04	-	0.13
56171	00035720034	2025	22	0.01	-	0.92 - 0.94
56144	00035720024	2093	26	0.01	-	0.02 - 0.03
56125	00035720017	2035	29	0.01	-	0.86 - 0.89
56089	00035720009	989	42	0.04	-	0.25
56157	00035720027	1913	50	0.03	-	0.03 - 0.05
56156	00035720026	2035	81	0.04	-	0.73 - 0.75
56167	00035720030	1975	99	0.05	-	0.11 - 0.13
56170	00035720033	1988	126	0.06	-	0.69 - 0.70
55751	00035720004	692	127	0.18	-	0.16
54141 B	00035720001 B	3798	142	0.03	-	0.83 - 0.91
56128	00035720019	1231	180	0.15	-	0.48 - 0.53
56088	00035720008	2020	204	0.10	-	0.73 - 0.75
56118	00035720015	1878	218	0.12	-	0.48 - 0.5
56126	00035720018	1898	252	0.13	-	0.20 - 0.22
56100	00035720013	2170	282	0.13	-	0.36 - 0.42
56158	00035720028	1523	376	0.25	-	0.16
56096 B	00035720010 B	327	415	1.18	-	0.63
56099	00035720012	1121	417	0.39	-	0.17 - 0.23
56096 A	00035720010 A	1059	620	0.56	140.12±0.01	0.58 - 0.61
56085 B	00035720005 B	852	699	0.73	141.31±0.01	0.28
56113	00035720014	1920	719	0.41	139.69±0.01	0.30 - 0.31
56155	00035720025	2143	772	0.36	140.01±0.01	0.44 - 0.45
56124	00035720016	1855	780	0.42	143.35±0.01	0.69 - 0.72
56086	00035720006	1873	796	0.43	139.75±0.01	0.30 - 0.31
56159	00035720029	1968	822	0.42	140.01±0.01	0.36 - 0.39
56140	00035720020	1955	876	0.45	139.66±0.01	0.16 - 0.17
56168	00035720031	2038	900	0.44	140.14±0.01	0.23 - 0.25
54531	00035720002	2914	909	0.31	139.66±0.01	0.17 - 0.23
56142	00035720022	1960	1035	0.53	139.48±0.01	0.69 - 0.72
56087	00035720007	1446	1329	0.92	143.25±0.01	0.53 - 0.55
56169	00035720032	1865	1370	0.74	140.20±0.01	0.47 - 0.48
54141 A	00035720001 A	5789	1617	0.27	139.95±0.01	0.67 - 0.77
56141	00035720021	1970	1729	0.88	139.87±0.01	0.48 - 0.52

Table 5.2 Spectral parameters for *Swift*–XRT observations along with quoted errors which are given for 90% confidence limits, except for Fe line flux and equivalent width which are quoted of 1σ confidence limit. For rest of the observations, only total flux is calculated and tabulated. χ^2 and Degrees of freedom of the fit are also included, where the first one corresponds to that obtained with Fe K_{α} line frozen with energy 6.4 keV and width 0.01 keV and the second values are without the Fe line. First 15 observations are those for which we have detected pulsation and the source photon number is greater than 600 and for rest of the observations source photon number is below 600.

MJD	N_H (10^{22}cm^{-2})	Photon Index (Γ)	Fe line Flux (10^{-4}photons $\text{cm}^{-2}\text{sec}^{-1}$)	χ^2	Degrees of freedom (DOF)	Fe line Eqv. Width (eV)	Total Flux (10^{-11}ergs $\text{cm}^{-2}\text{sec}^{-1}$)
54141A	11_{-2}^{+2}	$0.7_{-0.3}^{+0.3}$	-	46.58	39	-	4.0
54531	4_{-2}^{+2}	$0.3_{-0.4}^{+0.4}$	$3_{-0.7}^{+0.7}$	53.61	38	321_{-94}^{+94}	4.0
				65.40	39		
56085B	1_{-1}^{+2}	$0.8_{-0.4}^{+0.5}$	-	46.41	39	-	6.8
56086	2_{-1}^{+2}	$1.3_{-0.4}^{+0.4}$	-	69.59	39	-	3.8
56087	2_{-1}^{+1}	$0.7_{-0.3}^{+0.3}$	-	32.80	39	-	10.2
56096A	3_{-2}^{+2}	$0.8_{-0.4}^{+0.5}$	-	42.07	39	-	6.6
56113	3_{-2}^{+2}	$0.4_{-0.4}^{+0.5}$	-	37.32	39	-	5.3
56124	10_{-3}^{+4}	$0.7_{-0.5}^{+0.5}$	-	49.68	39	-	6.0
56140	4.5_{-2}^{+2}	$0.9_{-0.4}^{+0.4}$	-	48.29	39	-	5.5
56141	3_{-1}^{+1}	$0.5_{-0.3}^{+0.3}$	-	50.26	39	-	11.3
56142	15_{-3}^{+4}	$1.6_{-0.5}^{+0.5}$	-	47.05	39	-	6.9
56155	5_{-2}^{+3}	$0.3_{-0.4}^{+0.5}$	2_{-1}^{+1}	34.93	38	235_{-95}^{+96}	4.9
				41.02	39		
56159	2_{-1}^{+2}	$1.0_{-0.4}^{+0.4}$	-	33.88	39	-	4.2
56168	3_{-1}^{+2}	$0.6_{-0.3}^{+0.4}$	-	69.17	39	-	5.0
56169	3_{-1}^{+1}	$0.7_{-0.3}^{+0.3}$	-	54.10	39	-	8.5
54141B	-	-	-	-	-	-	0.4
55751	-	-	-	-	-	-	1.9
56088	50_{-19}^{+15}	2_{-1}^{+2}	-	33.34	39	-	1.6
56096B	3_{-3}^{+3}	$0.6_{-0.6}^{+0.7}$	-	34.57	39	-	14.0
56099	9_{-3}^{+3}	$2_{-0.6}^{+0.7}$	3_{-1}^{+2}	41.19	38	399_{-172}^{+174}	4.5
				46.54	39		
56100	7_{-6}^{+11}	$-0.8_{-0.8}^{+1.0}$	-	38.95	39	-	2.0
56118	-	-	-	-	-	-	1.8
56126	14_{-6}^{+9}	$0.6_{-0.9}^{+1.0}$	$2_{-0.9}^{+0.9}$	30.40	38	375_{-173}^{+172}	2.3
				35.07	39		
56128	-	-	-	-	-	-	1.8
56085A	-	-	-	-	-	-	0.5
56089	-	-	-	-	-	-	0.5
56156	-	-	-	-	-	-	0.6
56158	23_{-6}^{+8}	$2_{-0.8}^{+1}$	-	40.93	39	-	3.6
56167	-	-	-	-	-	-	0.7
56170	-	-	-	-	-	-	0.7

Chapter 6

Exploring the timing and spectral behaviour of IGR J00370+6122 with *Suzaku* and *XMM-Newton*

"We all have our time machines. Some take us back, they're called memories. Some take us forward, they're called dreams."

- Jeremy Irons

6.1 Introduction

The high mass X-ray binary IGR J00370+6122 was discovered with *INTEGRAL* observation of the Cassiopeia region in 2003 (den Hartog et al., 2006). The optical companion BD +60°73 was classified as giant B0.5 II-III star and the optical observations did not find an evidence of circumstellar disk in the system (Reig et al., 2005). This makes the source very interesting since it is neither a BeHMXB system nor a supergiant HMXB (sgHMXB), the two major classes of HMXBs. Optical photometry of the system estimates the source distance to be 3 kpc (Reig et al., 2005). Optical spectroscopy of the companion star estimates its radius and mass to be $(16.5 \pm 2.3) R_{\odot}$ and $(10 \pm 5) M_{\odot}$ respectively (González-Galán et al., 2014). Data from All Sky Monitor (ASM) on board *Rossi X-ray Timing Explorer (RXTE)*

showed recurrent outbursts with a periodicity of ~ 15.66 days, which was interpreted to be the orbital period of the system (den Hartog et al., 2006). Using *RXTE* Proportional Counter Array (PCA) data, in't Zand et al. (2007) found a modulation in the X-ray flux with 346 sec during a bright X-ray flare, which they interpreted as the spin period of the putative neutron star. However, this evidence of the periodicity was not very conclusive due to both low significance of the pulsation search results and pulsation being detected only in 4000 sec of the flaring data.

Accretion powered pulsars in Be-HMXBs show smaller pulse period though they have smaller average accretion rate compared to the sgHMXBs which have larger average accretion rate. The orbital and spin period of the source is plotted in the Corbet diagram given in Figure 6.1. It lies at the boundary of supergiant HMXBs and Be-HMXBs. It is intriguing to study some accretion powered pulsars in systems that are intermediate between the Be-HMXBs and sgHMXBs like IGR J00370+6122.

In this work we report our studies from a *Suzaku* and a *XMM-Newton* observation to explore the nature of the compact object in IGR J00370+6122. Here we make a comparison of the results from our analysis with previous results obtained with *RXTE* and *INTEGRAL* and *BeppoSAX*.

6.2 Observation and data analysis

Details about the *Suzaku*, *XXMM Newton* and *Swift* mission are given in Chapter 2.

We have analyzed ~ 21 ks of *Suzaku* XIS data (OB ID: 402064010, observed during 22-23 June 2007) and ~ 23 ks of *XMM-Newton* EPIC pn data (OB ID: 0501450101, observed during 9-10 February 2008) for the system IGR J00370+6122. We have also obtained orbital period of 15.66 days from 14 years of BAT lightcurve (Krimm et al., 2013a) with the help of HEASARC FTOOL EFSEARCH. With this period we have obtained orbital profile of the source from BAT lightcurve, which is shown in the top panel of Figure 6.3.

IGR J00370+6122 was observed with *Suzaku* XIS 0, XIS 1 and XIS 3 in 'Window 1/4' mode with a time resolution of 2 s. From the level 1 XIS data we have obtained cleaned

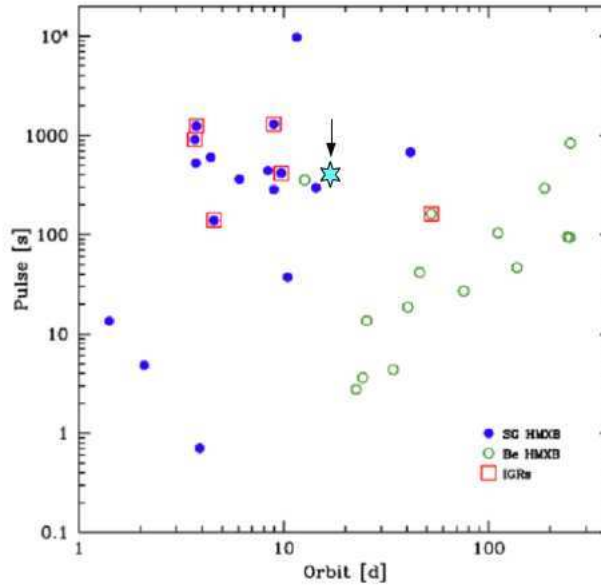


Fig. 6.1 Corbet diagram of HMXBs showing the distribution of pulse period and spin period of known HMXBs. The cyan star is the position of IGR J00370+6122, with orbital period of 15.6 days and tentative spin period of 346 secs. It lies at the boundary of supergiant HMXBs and Be-HMXBs and is an interesting source because its optical companion is neither a supergiant nor a Be star. Image credit: Corbet 1986

event files using some screening criteria given in *Suzaku* ABC guide. From XIS data we have extracted circular source region of 139 arcsec radius around the source centroid and extracted background region of same size from a region free of any other X-ray source.

IGR J00370+6122 was observed with *XMM-Newton* EPIC pn in PrimeSmallWindow mode with a time resolution of 5.7 ms. We used the *XMM-Newton* Science Analysis Software (SAS) version 14.0.0 to reduce the EPIC pn data. From the EPIC pn raw data of the source we have obtained event file with the SAS tool EVSELECT. We have extracted circular source and background region of 15 arcsec radius from EPIC pn data in the similar manner as obtained from *Suzaku* XIS events.

We checked for pile up in both the *Suzaku* XIS and *XMM-Newton* EPIC pn data and did not find any.

6.2.1 Timing analysis

XMM-Newton

We obtained *XMM-Newton* EPIC pn source and background lightcurves from source and background region file respectively using SAS tool EVSELECT. Using HEASARC FTOOL LCMATH we obtained background subtracted source lightcurves from the source and background lightcurves. The EPIC pn lightcurve with 100 s bin size is shown in the bottom figure of Figure 6.2. The lightcurve shows a large variability, by a factor of more than 10. Folded orbital profiles of the source with *Swift*-BAT and *XMM-Newton* EPIC pn indicates that the source was observed with *XMM-Newton* in high state (Figure 6.3). We have searched for pulsation in the EPIC pn lightcurve around the pulse period of the source (346 s) reported by in't Zand et al. (2007). We did not find any pulsation in the EPIC pn lightcurve of IGR J00370+6122 in the whole range of the lightcurve. χ^2 versus search periods plot for EPIC pn lightcurve is given in Figure 6.4 (top panel), in which the period search was carried out in the range of (0-1000) s. Due to large variability in the light curve at 100-1000 seconds time scale, the EFSEARCH result shows many peaks, but none of the peaks are statistically significant.

Suzaku

We obtained *Suzaku* XIS source and background lightcurves from corresponding source and background region files respectively using HEASARC FTOOL XSELECT. We obtained background corrected source lightcurves from the source and background lightcurves using HEASARC FTOOL LCMATH. The lightcurves with 100 s bin size are shown in the bottom panel (XIS 0, XIS 1, XIS 3 lightcurves in top, middle and bottom panel respectively) of Figure 6.2. The lightcurves show a variability by a factor more than 10. Folded orbital profiles of the source with *Swift*-BAT and *Suzaku* XIS instruments with a period of 15.66 days (den Hartog et al., 2006) indicate that the source was observed with *Suzaku* in low state (Figure 6.3). We have searched for pulsation in the source with HEASARC FTOOL EFSEARCH for all the values of time in the time span of the XIS lightcurves, with a trial

Table 6.1 The best fit model (phabs×(pow + bbodyrad)) parameters of IGR J00370+6122 with *XMM-Newton* EPIC pn instrument. N_H , Γ , N_{PL} , T_{BB} , N_{BB} denote line of sight equivalent hydrogen column density, Powerlaw photon index and Powerlaw Normalization, black-body temperature, Normalization of model bbodyrad respectively.

N_H	Γ	N_{PL} (10^{-4} photons $\text{keV}^{-1} \text{cm}^{-2} \text{s}^{-1}$)	T_{BB} keV	N_{BB} ($\text{km}/10\text{kpc}$) ²	$\chi^2(\text{DOF})$	Flux (0.3-10 keV) (10^{-11} ergs $\text{cm}^{-2} \text{s}^{-1}$)
$0.59^{+0.03}_{-0.03}$	$0.87^{+0.07}_{-0.07}$	$29.23^{+3.95}_{-3.89}$	$1.27^{+0.04}_{-0.04}$	$1.20^{+0.16}_{-0.14}$	204.14 (171)	7.64

Table 6.2 The simultaneous best fit model parameters of IGR J00370+6122 with three *Suzaku* XIS instruments. N_H , Γ , N_{PL} denote line of sight equivalent hydrogen column density, Powerlaw photon index and Powerlaw Normalization respectively.

N_H	Γ	N_{PL} (10^{-4} photons $\text{keV}^{-1} \text{cm}^{-2} \text{s}^{-1}$)	$\chi^2(\text{DOF})$	Flux (0.3-10 keV) (10^{-11} ergs $\text{cm}^{-2} \text{s}^{-1}$)
$1.22^{+0.1}_{-0.1}$	$2.13^{+0.09}_{-0.08}$	$9.24^{+1.28}_{-1.10}$	588.11 (501)	0.20

period of previously reported pulse period of 346 s (in't Zand et al., 2007). We did not find any pulsation in the XIS lightcurves, the plot of χ^2 versus search periods for XIS 0, XIS 1, XIS 3 are given in Figure 6.4, where the period search was carried out in the range of (0-1000) s as was done for the *XMM-Newton* EPIC-pn lightcurve.

6.3 Spectral analysis

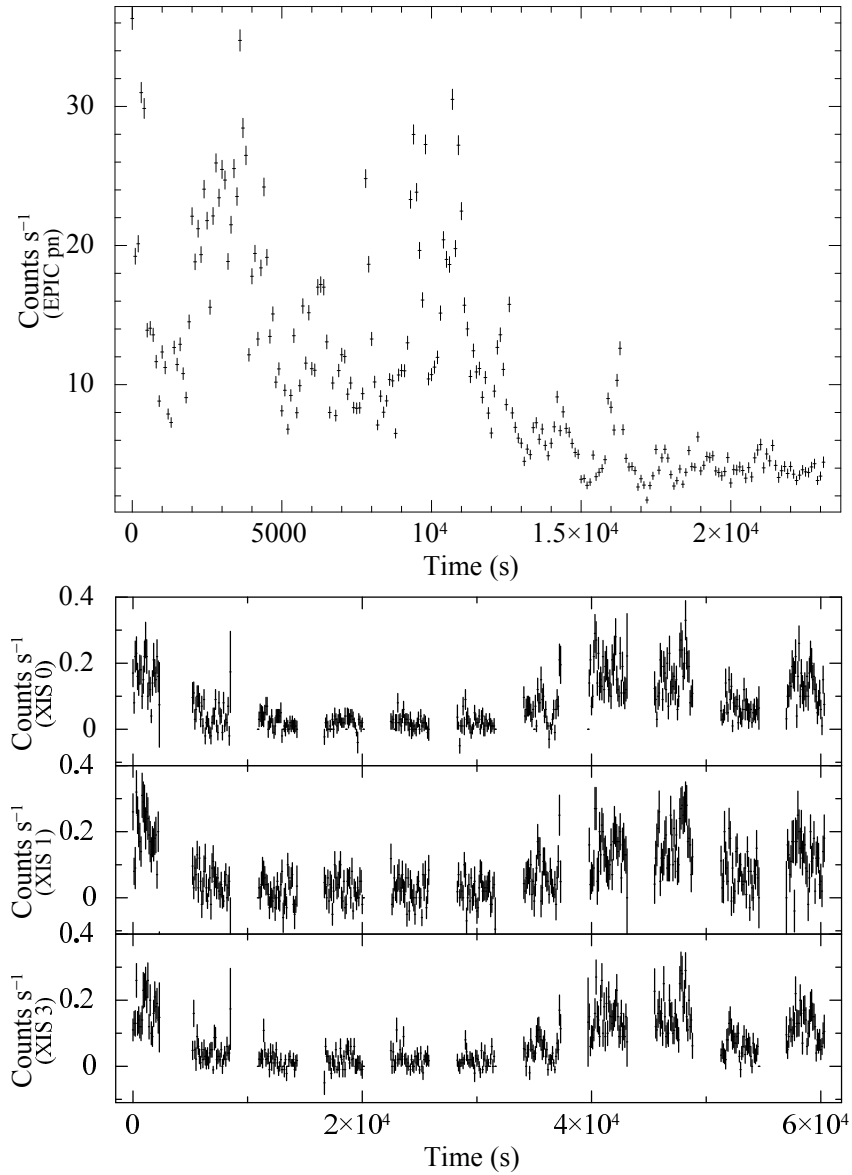


Fig. 6.2 **Top Figure:** 0.3-10 keV *XMM-Newton* EPIC pn lightcurve. **Bottom Figure:** 0.2-12 keV *Suzaku* XIS (XIS 0, XIS 1, XIS 3 in panel 1, 2, 3 respectively) lightcurves. Bin size of all the lightcurves is 100 s.

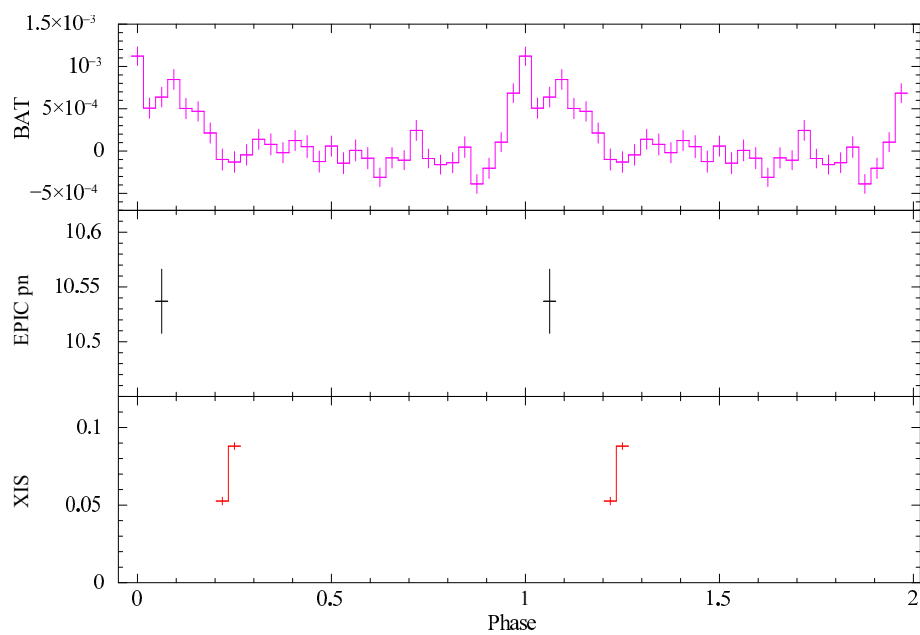


Fig. 6.3 **Top panel:** orbital intensity profile of IGR J00370+6122 obtained by folding *Swift*-BAT light curve with orbital period of 1353024 s (15.66 days). **Middle panel:** *XMM-Newton* EPIC pn lightcurve modulo same orbital period. **Bottom panel:** *Suzaku* XIS 0 light curve modulo same orbital period.

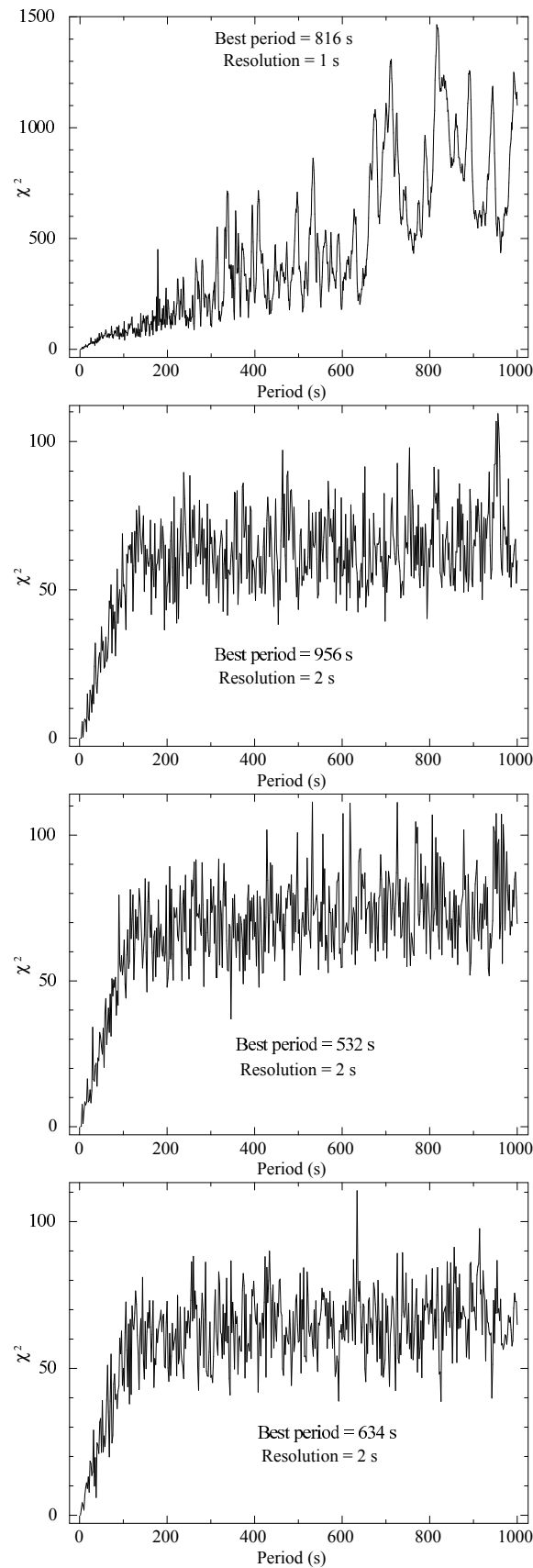


Fig. 6.4 Variation of χ^2 with trial spin periods around reported 346 s in't Zand et al. (2007) periodicity of IGR J00370+6122 using *XMM-Newton* EPIC pn (top figure) and *Suzaku* XIS (XIS 0, XIS 1, XIS 3 in the 2nd, 3rd and bottom figure respectively) lightcurves.

XMM-Newton

Using the region files we extracted EPIC pn source and background spectra with SAS task EVSELECT from the single and double events (with PATTERN \leq 4). We excluded the events which are at the edge of a CCD and at the edge to a bad pixel (with FLAG=0). We generated response and ancillary files using the SAS task RMFGEN and ARFGEN respectively. We rebinned the spectra with the SAS routine SPECGROUP to have at least 20 counts per bin to be able to use χ^2 statistics.

We obtained best fit for the EPIC pn spectra with model powerlaw and blackbody radiation modified by photoelectric absorption (phabs \times (pow + bbodyrad)). The spectral parameters for the best fit are given in Table 6.1. The blackbody temperature has been found to have value of 1.27 keV. Total flux in the energy range of 0.3-10 keV has been found to be 7.64×10^{-11} ergs cm $^{-2}$ s $^{-1}$. We did not detect 6.4 keV Fe K $_{\alpha}$ emission line, which is very common in HMXBs. Fixing the energy and width of Fe K $_{\alpha}$ emission line with 6.4 keV and 0.01 keV respectively we find an upper limit of flux and equivalent width of 1.83×10^{-5} photons cm $^{-2}$ sec $^{-1}$ and 14.31 keV respectively. The EPIC pn spectra fitted with model phabs \times (pow + bbodyrad) is shown in the top figure of Figure 6.5. The bottom panel of this figure gives contribution of χ^2 towards each bin.

Suzaku

We extracted XIS spectra and their responses (combined response and ancillary files) from the region files with the HEASARC FTOOL XSELECT. With this task we obtained spectra rebinned in 2048 channels. We fitted the spectra with HEASARC package XSPEC version: 12.8.2. We removed the channels from the spectral fitting which correspond to artificial structures in the XIS spectra around the Si edge and Au edge, near the energy range of 1.75-2.23 keV.

We simultaneously fitted the 3 XIS spectra. We have obtained good fit with a spectral model consisting of a powerlaw modified by photoelectric absorption (model components phabs \times pow in XSPEC). The spectral parameters for the best fit are given in Table 6.2. We obtained higher value of powerlaw photon index (Γ) for XIS spectra compared to its value

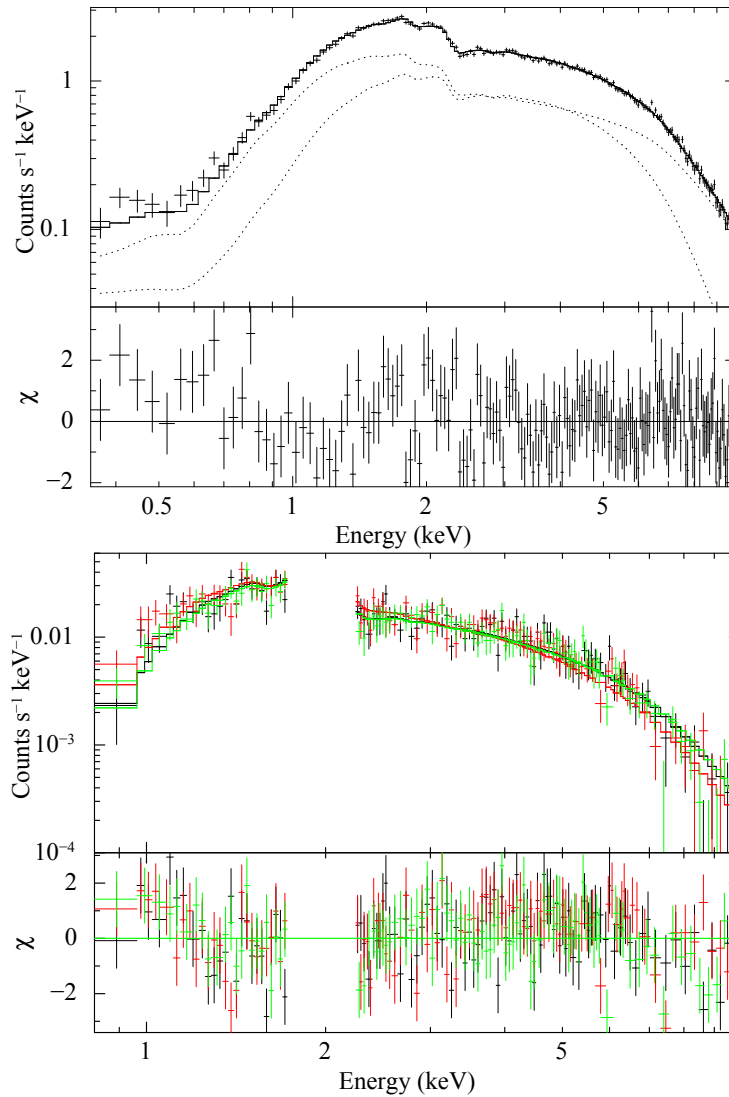


Fig. 6.5 **Top figure:** *XMM-Newton* EPIC pn spectrum of the source fitted with power-law and blackbody radiation (bbodyrad) modified by photoelectric absorption. **Bottom figure:** *Suzaku* XIS (XIS 0:black, XIS 1:red, XIS 3:green) spectra of IGR J00370+6122 fitted with powerlaw modified by photoelectric absorption. Top panels show normalized $\text{Counts s}^{-1} \text{keV}^{-1}$ and bottom panels of both the figures show the difference between data and best fit model scaled by the error (square of this term is the contribution to χ^2) for each bin.

found in EPIC pn spectrum. 0.3-10 keV flux has been found to be 2.0×10^{-11} ergs $\text{cm}^{-2} \text{s}^{-1}$ which is smaller by a factor of ~ 30 than the flux found with EPIC pn in the same energy range. Total flux in the energy range of 0.3-10 keV has been found to be 0.20×10^{-11} ergs $\text{cm}^{-2} \text{s}^{-1}$. 3 XIS spectra are shown in top figure of Figure 6.5. The bottom panel of this figure gives contribution of each bin towards χ^2 .

6.4 Discussion

An overwhelming fraction of the HMXBs host a slowly spinning, highly magnetized ($B \sim 10^{12}$ Gauss) neutron star as the compact object. These HMXBs are predominantly wind-fed systems, where a small fraction of the stellar wind of the companion star is captured by the neutron star, making it an accretion powered X-ray pulsar. However, to conclusively identify the compact object as a neutron star, it is essential to detect pulsations, period of which is the spin. Detection of pulsation also allows measurement of the orbital parameters which is very useful to understand the accretion process and to measure accretion torque, especially if the orbit is eccentric and if there is significant orbital dependence of mass accretion rate, for example in GX 301–2 (Islam & Paul 2014).

INTEGRAL has led to discoveries of many highly obscured HMXBs and HMXBs showing fast X-ray transient behavior (SFXTs), which were not detected previously by other missions. The spin period has been conclusively detected in some of these HMXBs whereas for majority of the sources, the spin period of the compact object is still uncertain. The biggest reason for this uncertainty is that, these highly obscured HMXBs have a hard spectra and being in the galactic plane they have large absorption column density and are fainter in soft X-rays compared to other bright HMXBs.

In this work, we have analyzed a *Suzaku* XIS and a *XMM-Newton* EPIC pn observation of IGR J00370+6122, to explore the nature of the compact object in the system. Pulse period of ~ 346 s has been reported earlier with pointed *RXTE*-PCA observation during a bright X-ray flare (in't Zand et al., 2007). Other than this observation, pulsation has not

been detected in the source. In our timing studies we have not detected any pulsation in the source with any of the XIS or EPIC pn data.

We have obtained *Suzaku* XIS and *XMM-Newton* EPIC pn spectra. Total flux in the energy range of (0.3-10) keV during the *Suzaku* observation has been found to be 0.2×10^{-11} ergs cm⁻² s⁻¹ which is lower by a factor more than 30 compared to its value found during the *XMM-Newton* observation. A blackbody component of temperature ~ 1 keV with emitter size of ~ 1 km is detected in the *XMM-Newton* spectrum which is absent in the *Suzaku* spectra.

A blackbody component of ~ 1 keV temperature and size of about 1 km or less is known in some other HMXBs. For example in X-ray binary system SW J2000.6+3120, blackbody component of 1.2 keV and 1.5 keV was detected in two *Suzaku* observations (Pradhan et al., 2013). In transient pulsar 3A 0535+262, blackbody component (temperature 1.33 keV, emitter size 0.08 km) was detected only in one observation out of three *BeppoSAX* observations (Mukherjee and Paul, 2005). The difference between the flux during the *XMM-Newton* and the *Suzaku* observation can perhaps be due to i) orbital intensity variation, which can be due to different visibility of the neutron star at different orbital phases ii) periodically variable mass accretion rate, which is possible if the binary has significant eccentricity or if it accretes at least partially from an outflowing disk of the companion (not yet detected). The blackbody component perhaps originates at the polar cap region which is visible during *XMM-Newton* observation, but at low intensity state (*Suzaku* observation) this component is absent.

den Hartog et al. (2006) too have reported variability in this source. They have obtained total flux of $\sim 1, \sim 3, \sim 11$ in units of 10^{-11} ergs cm⁻² s⁻¹ in the energy range of (5-20) keV with *RXTE*-PCA, *INTEGRAL*-IBIS-ISGRI and *BeppoSAX*-Wide-Field Camera respectively. In two ToO (Time of Opportunity) observations with *RXTE* in 2004 May and June, den Hartog et al. (2006) have found the source in low states with fluxes 1.4 mCrab and 1.1 mCrab respectively. In 4 archival *BeppoSAX* data near expected peak phase they have found flux in the range of (3-15) mCrab. With *RXTE*-PCA spectrum in't Zand et al. (2007) have obtained higher value of the total flux ($\sim 2 \times 10^{-10}$ ergs cm⁻² s⁻¹) in the energy range of (3-

20) keV. They have obtained one order of magnitude higher value of the equivalent hydrogen column density ($N_H \sim 9 \times 10^{22} \text{ cm}^{-2}$) compared to the line of sight N_H along Galactic center. They suggest that the compact object is embedded in the dense wind of its companion. We have obtained low value of powerlaw photon index (~ 0.9) with *XMM-Newton* but moderate value (~ 2) with *Suzaku*. den Hartog et al. (2006) have obtained powerlaw photon index of ~ 2.9 , ~ 1.9 , ~ 2.6 with *RXTE-PCA*, *INTEGRAL-IBIS-ISGRI* and *BeppoSAX-Wide-Field Camera* respectively. We have found N_H (Table 6.2 and 6.1) to have values nearly equal (from *Suzaku* XIS spectra) to that along Galactic center and even lesser than that (from *XMM-Newton* EPIC pn spectrum). This indicates the compact object is traversing through variable wind structures of its companion. sgHMXB and SFXT systems show variable wind morphology. But the estimated mass of the companion ($10 \pm 5 M_\odot$) by González-Galán et al. (2014) rules out the possibility of the companion to be a supergiant.

Both the *Suzaku* XIS and *XMM-Newton* EPIC pn spectra show some similarities with the spectra of a pulsar in an X-ray binary system. Supergiant HMXB 4U 1700–377 too show a pulsar like spectra, but till now no pulsation has been found in the system. Cyclotron Resonant Scattering Feature (CRSF) which gives an estimation of magnetic field of the compact object if it is a neutron star, is found above ~ 20 keV. So detection or non-detection of Cyclotron line can put useful insights into the nature of the system. To confirm the nature of the compact object in IGR J00370+6122 we need broad-band X-ray observation with missions like *NuSTAR* and *ASTROSAT*. The large area of LAXPC at harder energies compared to any other X-ray mission flown so far, provides us a unique opportunity to determine the spin period of many highly obscured HMXBs. We have obtained *ASTROSAT-SXT* and LAXPC data of the source and we are hopeful that analysis of these data will soon reveal the nature of the compact object and accretion process in the system.

Chapter 7

Summary and future prospects

"I can live with doubt and uncertainty. I think it's much more interesting to live not knowing than to have answers which might be wrong."

- Richard P. Feynman

In this thesis we have studied X-ray reprocessing properties in 9 HMXB and 4 LMXB systems through eclipses with *XMM Newton* EPIC pn (Chapter 3 and 4). We carried out first comprehensive study of X-ray reprocessing with eclipse spectra in HMXB and LMXB systems. We have also studied spectral and timing properties of two HMXBs IGR J18027–2016 (Chapter 5) and IGR J00370+6122 (Chapter 6) in details to understand accretion mechanisms in these systems with *Swift* and *Suzaku*, *XMM Newton* respectively.

Companion's wind in HMXBs is the main reprocessing agent of primary X-rays. We have found a wide diversity in the X-ray reprocessing properties in these systems. Even in the same HMXB (LMC X–4) the reprocessing varies by a large factor at different epochs. We have found signatures of various other elements in HMXB systems. Complex of Fe emission lines are more significant in eclipse phases in most of the HMXB systems compared to out-of-eclipse phases, as equivalent width of these emission lines during eclipses have been found to be higher. Equivalent width of Fe emission lines in SFXTs too have been found to be large during eclipses similar to that in SgHMXBs.

However few exceptions have been seen. For example in Cen X-3, the low ionized Fe K_{α} emission line has low equivalent width during eclipse. This possibly indicates low ionized Fe atoms to be closer to the source compared to highly ionized Fe atoms, this can happen if the Fe atoms nearer to the source are in very dense accretion disc and / or accretion stream. Second observation of LMC X-4 also indicates the same possibility. In the second observation of LMC X-4, detection of low ionized Fe k_{α} emission line was marginal but it was moderate in the out-of-eclipse phase. This opens up future avenues to look into the systems in greater details with orbital phase resolved spectral studies in both the eclipse and out-of-eclipse phases, to understand the physical origin of this different behaviour as compared to other HMXB systems. The Fe k_{α} emission line has been found to be very weak in SMC X-1. SMC X-1 has been observed to switch between two stable superorbital period of ~ 40 days and ~ 65 days respectively (Trowbridge et al. 2007, Hu et al. 2011). It would be interesting to carry out spectral study of this system in different superorbital phases to get more insight into the physical scenario of accretion in the system. In few systems (4U 1538-522, IGR J17252-3616) we have found different origin for the hard and soft X-rays, physical reason behind this is not very clear. Further spectral studies during eclipse and out-of-eclipse phases of these sources with *XMM Newton*, *Chandra*, *NuSTAR* can put valuable insights into the physical condition of accretion and its connection with the distribution of matter in the systems.

Accretion disc in LMXBs is the main X-ray reprocessing agent. We have found less dynamic X-ray reprocessing properties in LMXB systems (Chapter 4) than HMXBs. In spite of having much weaker wind environment, the flux ratio of out-of-eclipse to eclipse in LMXBs is in a range comparable to the HMXBs. Most contrasting outcome with respect to the HMXBs is the lack of strong 6.4 keV emission line in the eclipse spectrum of LMXBs. Environment of LMXB systems showed presence of different materials like HMXBs, but their equivalent widths have been found to be much lower as compared to their values found in HMXB systems. Comparable out-of-eclipse to eclipse flux ratio in AXJ 1745.6-2901 irrespective of intensity state is an important finding. 7 observations of EXO 0748-676 and

2 observations of MXB 1659–298 showed nearly steady source emission. We have found variable structures on the accretion disc of EXO 0748–676 over a period of ~ 2 months. Emission lines in EXO 0748–676 are new discoveries. Eclipse spectrum of XTE J1710–281 gives an indication of very small accretion disc of the system.

We have studied HMXB IGR J18027–2016 with 5.5 years of *Swift*–XRT data (Chapter 5). We have found variability including off-states like features with 33 *Swift*–XRT observations, while long term average orbital profile with *Swift*–BAT shows smooth variation in the the out-of-eclipse phases. Since its discovery the source did not show any low intensity states other than these *Swift*–XRT observations. The underlying physical cause is not yet clear. Variability in SgHMXBs can be caused due to its i) high magnetic field with the onset of centrifugal barrier or magnetic inhibition (Bozzo et al. 2008) ii) accretion from clumpy wind (Barnstedt et al. 2008; Oskinova, Feldmeier & Kretschmar 2013; Pradhan et al. 2014) iii) hydrodynamical instabilities (Manousakis & Walter 2015) etc. This provides opportunities for further work of verifying these possibilities by estimating magnetic field from the Cyclotron Resonant Scattering Feature (CRSF) with *ASTROSAT* and *NuSTAR*, if found. We have detected pulsation in only 15 observations. Though some of the observations have very poor statistics, but in some of the observations even with longer exposure time we have not seen any pulsation. Good timing resolution of *ASTROSAT*-LAXPC can put useful insight into the accretion mechanisms in the system. Some of the *Swift*–XRT spectra showed presence of low ionized Fe atoms in the system. Orbital phase resolved spectroscopy with *XMM Newton* and *Chandra* can reveal the distribution of Fe atoms and their ionization state in the system.

We have studied IGR J00370+6122 in high and low states with *Suzaku* and *XMM Newton* respectively. We have not detected any pulsation of the source in our timing studies with these missions. We could not study the system in hard X-rays because of some anomalies in *Suzaku* Hard X-ray detector (HXD) data. We have obtained the *ASTROSAT* data for the source. We are hopeful that LAXPC with its higher effective area compared to *RXTE*-PCA,

Suzaku-XIS and *XMM Newton*-EPIC-pn will provide us opportunities to probe the nature of the compact object of the system in this source. LAXPC with CZTI onboard *ASTROSAT* will give an opportunity to search for CRSF feature in the broadband spectra. If found then the nature of the compact object would be established as neutron star.

References

- M. A. Abramowicz and W. Kluźniak. A precise determination of black hole spin in GRO J1655-40. *A&A*, 374:L19–L20, August 2001. doi: 10.1051/0004-6361:20010791.
- M. A. Abramowicz, W. Kluzniak, Z. Stuchlík, and G. Török. Twin peak QPOs frequencies in microquasars and Sgr A*. The resonance and other orbital models. In S. Hledík and Z. Stuchlík, editors, *RAGtime 4/5: Workshops on black holes and neutron stars*, pages 1–23, December 2004.
- N. Aftab and B. Paul. X-ray reprocessing: through eclipse spectra of low mass X-ray binaries (in preparation).
- N. Aftab and B. Paul. X-ray reprocessing: through eclipse spectra of high mass X-ray binaries (submitted). *MNRAS*, 2018.
- N. Aftab, N. Islam, and B. Paul. Variability study of the high-mass X-ray binary IGR J18027-2016 with Swift-XRT. *MNRAS*, 463:2032–2038, December 2016. doi: 10.1093/mnras/stw2037.
- M. A. Alpar and J. Shaham. Is GX5 - 1 a millisecond pulsar? *Nature*, 316:239–241, July 1985. doi: 10.1038/316239a0.
- A. Ankaa, L. Kaper, J. H. J. de Bruijne, J. Dewi, R. Hoogerwerf, and G. J. Savonije. The origin of the runaway high-mass X-ray binary HD 153919/4U1700-37. *A&A*, 370:170–175, April 2001. doi: 10.1051/0004-6361:20010192.
- T. D. C. Ash, A. P. Reynolds, P. Roche, A. J. Norton, M. D. Still, and L. Morales-Rueda. The mass of the neutron star in Centaurus X-3. *MNRAS*, 307:357–364, August 1999. doi: 10.1046/j.1365-8711.1999.02605.x.
- G. Augello, R. Iaria, N. R. Robba, T. Di Salvo, L. Burderi, G. Lavagetto, and L. Stella. BeppoSAX Serendipitous Discovery of the X-Ray Pulsar SAX J1802.7-2017. *ApJ*, 596:L63–L66, October 2003a. doi: 10.1086/379092.
- G. Augello, R. Iaria, N. R. Robba, T. Di Salvo, L. Burderi, G. Lavagetto, and L. Stella. BeppoSAX Serendipitous Discovery of the X-Ray Pulsar SAX J1802.7-2017. *ApJ*, 596:L63–L66, October 2003b. doi: 10.1086/379092.
- A. Bahramian, J. C. Gladstone, C. O. Heinke, R. Wijnands, R. Kaur, and D. Altamirano. Revealing a new symbiotic X-ray binary with Gemini Near-infrared Integral Field Spectrograph. *MNRAS*, 441:640–645, June 2014. doi: 10.1093/mnras/stu611.

- R. Barnard, U. Kolb, and J. P. Osborne. Tracing a Z-track in the M 31 X-ray binary RX J0042.6+4115. *A&A*, 411:553–557, December 2003. doi: 10.1051/0004-6361:20031513.
- J. Barnstedt, R. Staubert, A. Santangelo, C. Ferrigno, D. Horns, D. Klochkov, P. Kretschmar, I. Kreykenbohm, A. Segreto, and J. Wilms. INTEGRAL observations of the variability of OAO 1657-415. *A&A*, 486:293–302, July 2008. doi: 10.1051/0004-6361:20078707.
- S. D. Barthelmy, L. M. Barbier, J. R. Cummings, E. E. Fenimore, N. Gehrels, D. Hullinger, H. A. Krimm, C. B. Markwardt, D. M. Palmer, A. Parsons, G. Sato, M. Suzuki, T. Takahashi, M. Tashiro, and J. Tueller. The Burst Alert Telescope (BAT) on the SWIFT Midex Mission. *Space Sci. Rev.*, 120:143–164, October 2005. doi: 10.1007/s11214-005-5096-3.
- M. M. Basko and R. A. Sunyaev. The limiting luminosity of accreting neutron stars with magnetic fields. *MNRAS*, 175:395–417, May 1976. doi: 10.1093/mnras/175.2.395.
- P. A. Becker. Dynamical Structure of Radiation-dominated Pulsar Accretion Shocks. *ApJ*, 498:790–801, May 1998. doi: 10.1086/305568.
- R. H. Becker, J. H. Swank, E. A. Boldt, S. S. Holt, P. J. Serlemitsos, S. H. Pravdo, and J. R. Saba. A1540-53, an eclipsing X-ray binary pulsator. *ApJ*, 216:L11–L14, August 1977. doi: 10.1086/182498.
- M. C. Begelman, C. F. McKee, and G. A. Shields. Compton heated winds and coronae above accretion disks. I Dynamics. *ApJ*, 271:70–88, August 1983. doi: 10.1086/161178.
- R. D. Belian, J. P. Conner, and W. D. Evans. The discovery of X-ray bursts from a region in the constellation Norma. *ApJ*, 206:L135–L138, June 1976. doi: 10.1086/182151.
- A. Beri and B. Paul. Post-flare formation of the accretion stream and a dip in pulse profiles of LMC X-4. *New A*, 56:94–101, October 2017a. doi: 10.1016/j.newast.2017.05.001.
- A. Beri and B. Paul. Post-flare formation of the accretion stream and a dip in pulse profiles of LMC X-4. *New A*, 56:94–101, October 2017b. doi: 10.1016/j.newast.2017.05.001.
- L. Bildsten, D. Chakrabarty, J. Chiu, M. H. Finger, D. T. Koh, R. W. Nelson, T. A. Prince, B. C. Rubin, D. M. Scott, M. Stollberg, B. A. Vaughan, C. A. Wilson, and R. B. Wilson. Observations of Accreting Pulsars. *ApJS*, 113:367–408, December 1997. doi: 10.1086/313060.
- A. J. Bird, A. Bazzano, L. Bassani, F. Capitanio, M. Fiocchi, A. B. Hill, A. Malizia, V. A. McBride, S. Scaringi, V. Sguera, J. B. Stephen, P. Ubertini, A. J. Dean, F. Lebrun, R. Terrier, M. Renaud, F. Mattana, D. Götz, J. Rodriguez, G. Belanger, R. Walter, and C. Winkler. The Fourth IBIS/ISGRI Soft Gamma-ray Survey Catalog. *ApJS*, 186:1–9, January 2010. doi: 10.1088/0067-0049/186/1/1.
- G. R. Blumenthal and R. J. Gould. Bremsstrahlung, Synchrotron Radiation, and Compton Scattering of High-Energy Electrons Traversing Dilute Gases. *Reviews of Modern Physics*, 42:237–271, 1970. doi: 10.1103/RevModPhys.42.237.
- H. Bondi. On spherically symmetrical accretion. *MNRAS*, 112:195, 1952. doi: 10.1093/mnras/112.2.195.

- H. Bondi and F. Hoyle. On the mechanism of accretion by stars. *MNRAS*, 104:273, 1944. doi: 10.1093/mnras/104.5.273.
- E. Bozzo, M. Falanga, and L. Stella. Are There Magnetars in High-Mass X-Ray Binaries? The Case of Supergiant Fast X-Ray Transients. *ApJ*, 683:1031-1044, August 2008. doi: 10.1086/589990.
- E. Bozzo, L. Stella, C. Ferrigno, A. Giunta, M. Falanga, S. Campana, G. Israel, and J. C. Leyder. The supergiant fast X-ray transients XTE J1739-302 and IGR J08408-4503 in quiescence with XMM-Newton. *A&A*, 519:A6, September 2010a. doi: 10.1051/0004-6361/201014095.
- E. Bozzo, L. Stella, C. Ferrigno, A. Giunta, M. Falanga, S. Campana, G. Israel, and J. C. Leyder. The supergiant fast X-ray transients XTE J1739-302 and IGR J08408-4503 in quiescence with XMM-Newton. *A&A*, 519:A6, September 2010b. doi: 10.1051/0004-6361/201014095.
- E. Bozzo, A. Giunta, G. Cusumano, C. Ferrigno, R. Walter, S. Campana, M. Falanga, G. Israel, and L. Stella. XMM-Newton observations of IGR J18410-0535: the ingestion of a clump by a supergiant fast X-ray transient. *A&A*, 531:A130, July 2011. doi: 10.1051/0004-6361/201116726.
- E. Bozzo, P. Romano, L. Ducci, F. Bernardini, and M. Falanga. Supergiant fast X-ray transients as an under-luminous class of supergiant X-ray binaries. *Advances in Space Research*, 55:1255–1263, February 2015. doi: 10.1016/j.asr.2014.11.012.
- D. J. Burnard, J. Arons, and S. M. Lea. Accretion onto magnetized neutron stars - X-ray pulsars with intermediate rotation rates. *ApJ*, 266:175–187, March 1983. doi: 10.1086/160768.
- D. N. Burrows, J. A. Kennea, A. F. Abbey, A. Beardmore, S. Campana, M. Capalbi, G. Chincarini, G. Cusumano, P. A. Evans, J. E. Hill, P. Giommi, M. Goad, O. Godet, A. Moretti, D. C. Morris, J. P. Osborne, C. Pagani, K. L. Page, M. Perri, J. Racusin, P. Romano, R. L. C. Starling, G. Tagliaferri, F. Tamburelli, L. G. Tyler, and R. Willingale. The swift x-ray telescope: status and performance. In *Society of Photo-Optical Instrumentation Engineers (SPIE) Conference Series*, volume 6686 of *Society of Photo-Optical Instrumentation Engineers (SPIE) Conference Series*, page 7, September 2007. doi: 10.1117/12.735130.
- A. Busboom, H. Elders-Boll, and H. D. Schotten. Uniformly Redundant Arrays. *Experimental Astronomy*, 8:97–123, 1998.
- J. Casares, I. Negueruela, M. Ribó, I. Ribas, J. M. Paredes, A. Herrero, and S. Simón-Díaz. A Be-type star with a black-hole companion. *Nature*, 505:378–381, January 2014. doi: 10.1038/nature12916.
- S. Chandrasekhar. The Maximum Mass of Ideal White Dwarfs. *ApJ*, 74:81, July 1931. doi: 10.1086/143324.
- C. Chevalier and S. A. Ilovaisky. The binary nature of the LMC X-4 optical candidate. *A&A*, 59:L9–L12, July 1977.

- G. Chodil, H. Mark, R. Rodrigues, F. Seward, C. D. Swift, W. A. Hiltner, G. Wallerstein, and E. J. Mannery. Spectral and Location Measurements of Several Cosmic X-Ray Sources Including a Variable Source in Centaurus. *Physical Review Letters*, 19:681–683, September 1967. doi: 10.1103/PhysRevLett.19.681.
- M. J. Church and M. Bałucińska-Church. Measurements of accretion disc corona size in LMXB: consequences for Comptonization and LMXB models. *MNRAS*, 348:955–963, March 2004. doi: 10.1111/j.1365-2966.2004.07162.x.
- M. J. Church, G. S. Halai, and M. Bałucińska-Church. An explanation of the Z-track sources. *A&A*, 460:233–244, December 2006. doi: 10.1051/0004-6361:20065035.
- M. J. Church, A. Gibiec, and M. Bałucińska-Church. The nature of the island and banana states in atoll sources and a unified model for low-mass X-ray binaries. *MNRAS*, 438:2784–2797, March 2014. doi: 10.1093/mnras/stt2364.
- J. S. Clark, S. P. Goodwin, P. A. Crowther, L. Kaper, M. Fairbairn, N. Langer, and C. Brocksopp. Physical parameters of the high-mass X-ray binary <ASTROBJ>4U1700-37</ASTROBJ>. *A&A*, 392:909–920, September 2002. doi: 10.1051/0004-6361:20021184.
- M. Coe, R. H. D. Corbet, K. E. McGowan, and V. A. McBride. The Population of High-Mass X-Ray Binaries in the Small Magellanic Cloud. In J. Martí, P. L. Luque-Escamilla, and J. A. Combi, editors, *High Energy Phenomena in Massive Stars*, volume 422 of *Astronomical Society of the Pacific Conference Series*, page 224, May 2010.
- A. Coleiro, S. Chaty, J. A. Zurita Heras, F. Rahoui, and J. A. Tomsick. Infrared identification of high-mass X-ray binaries discovered by INTEGRAL. *A&A*, 560:A108, December 2013. doi: 10.1051/0004-6361/201322382.
- J. B. Coley, R. H. D. Corbet, and H. A. Krimm. Probing the Masses and Radii of Donor Stars in Eclipsing X-Ray Binaries with the Swift Burst Alert Telescope. *ApJ*, 808:140, August 2015. doi: 10.1088/0004-637X/808/2/140.
- R. Corbet, L. Barbier, S. Barthelmy, J. Cummings, E. Fenimore, N. Gehrels, D. Hullinger, H. Krimm, C. Markwardt, D. Palmer, A. Parsons, T. Sakamoto, G. Sato, J. Tueller, and R. Remillard. Swift/BAT and RXTE/ASM Discovery of the Orbital Period of IGR J16418-4532. *The Astronomer's Telegram*, 779, March 2006.
- R. H. D. Corbet. The three types of high-mass X-ray pulsator. *MNRAS*, 220:1047–1056, June 1986. doi: 10.1093/mnras/220.4.1047.
- R. H. D. Corbet and H. A. Krimm. Superorbital Periodic Modulation in Wind-accretion High-mass X-Ray Binaries from Swift Burst Alert Telescope Observations. *ApJ*, 778:45, November 2013. doi: 10.1088/0004-637X/778/1/45.
- R. H. D. Corbet, J. L. Sokoloski, K. Mukai, C. B. Markwardt, and J. Tueller. A Comparison of the Variability of the Symbiotic X-Ray Binaries GX 1+4, 4U 1954+31, and 4U 1700+24 from Swift BAT and RXTE ASM Observations. *ApJ*, 675:1424-1435, March 2008. doi: 10.1086/526337.

- K. Davidson and J. P. Ostriker. Neutron-Star Accretion in a Stellar Wind: Model for a Pulsed X-Ray Source. *ApJ*, 179:585–598, January 1973. doi: 10.1086/151897.
- R. E. Davies and J. E. Pringle. Spindown of neutron stars in close binary systems. II. *MNRAS*, 196:209–224, July 1981. doi: 10.1093/mnras/196.2.209.
- P. R. den Hartog, W. Hermsen, L. Kuiper, J. Vink, J. J. M. in't Zand, and W. Collmar. INTEGRAL survey of the Cassiopeia region in hard X rays. *A&A*, 451:587–602, May 2006. doi: 10.1051/0004-6361:20054711.
- J. Devasia, M. James, B. Paul, and K. Indulekha. Timing and spectral studies of the transient X-ray pulsar GX 304-1 during an outburst. *MNRAS*, 417:348–358, October 2011. doi: 10.1111/j.1365-2966.2011.19269.x.
- V. Doroshenko, A. Santangelo, and V. Suleimanov. Witnessing the magnetospheric boundary at work in Vela X-1. *A&A*, 529:A52, May 2011. doi: 10.1051/0004-6361/201116482.
- V. Doroshenko, A. Santangelo, L. Ducci, and D. Klochkov. Supergiant, fast, but not so transient 4U 1907+09. *A&A*, 548:A19, December 2012. doi: 10.1051/0004-6361/201220085.
- J. P. Doty, W. H. G. Lewin, and J. A. Hoffman. SAS 3 observations of GX 1 + 4. *ApJ*, 243:257–262, January 1981. doi: 10.1086/158592.
- J. B. Dove, J. Wilms, and M. C. Begelman. Self-Consistent Thermal Accretion Disk Corona Models for Compact Objects. I: Properties of the Corona and the Spectrum of Escaping Radiation. *ApJ*, 487:747, October 1997. doi: 10.1086/304632.
- S. P. Drave, A. J. Bird, L. Sidoli, V. Sguera, V. A. McBride, A. B. Hill, A. Bazzano, and M. E. Goossens. INTEGRAL and XMM-Newton observations of IGR J16418-4532: evidence of accretion regime transitions in a supergiant fast X-ray transient. *MNRAS*, 433:528–542, July 2013. doi: 10.1093/mnras/stt754.
- L. Ducci, L. Sidoli, S. Mereghetti, A. Paizis, and P. Romano. The structure of blue supergiant winds and the accretion in supergiant high-mass X-ray binaries. *MNRAS*, 398:2152–2165, October 2009. doi: 10.1111/j.1365-2966.2009.15265.x.
- K. Ebisawa, C. S. R. Day, T. R. Kallman, F. Nagase, T. Kotani, K. Kawashima, S. Kitamoto, and J. W. Woo. X-Ray Spectroscopy of Centaurus X-3 with ASCA over an Eclipse. *PASJ*, 48:425–440, June 1996. doi: 10.1093/pasj/48.3.425.
- V. Estrada-Carpenter, R. I. Hynes, C. Britt, C. Johnson, P. Jonker, T. J. Maccarone, M. Torres, D. Steeghs, S. Greiss, G. Nelemans, and Galactic Bulge Survey Collaboration. Examining XMM Observations in the Galactic Bulge Survey Region. In *American Astronomical Society Meeting Abstracts #223*, volume 223 of *American Astronomical Society Meeting Abstracts*, page 155.33, January 2014.
- M. Falanga, E. Bozzo, A. Lutovinov, J. M. Bonnet-Bidaud, Y. Fetisova, and J. Puls. Ephemeris, orbital decay, and masses of ten eclipsing high-mass X-ray binaries. *A&A*, 577:A130, May 2015. doi: 10.1051/0004-6361/201425191.

- A. Feldmeier. Time-dependent structure and energy transfer in hot star winds. *A&A*, 299: 523, July 1995.
- M. H. Finger, D. T. Koh, R. W. Nelson, T. A. Prince, B. A. Vaughan, and R. B. Wilson. Discovery of hard X-ray pulsations from the transient source GRO J1744 - 28. *Nature*, 381:291–293, May 1996. doi: 10.1038/381291a0.
- J. Frank, A. King, and D. J. Raine. *Accretion Power in Astrophysics: Third Edition*. January 2002.
- N. Gehrels, G. Chincarini, P. Giommi, K. O. Mason, J. A. Nousek, A. A. Wells, N. E. White, S. D. Barthelmy, D. N. Burrows, L. R. Cominsky, K. C. Hurley, F. E. Marshall, P. Mészáros, P. W. A. Roming, L. Angelini, L. M. Barbier, T. Belloni, S. Campana, P. A. Caraveo, M. M. Chester, O. Citterio, T. L. Cline, M. S. Cropper, J. R. Cummings, A. J. Dean, E. D. Feigelson, E. E. Fenimore, D. A. Frail, A. S. Fruchter, G. P. Garmire, K. Gendreau, G. Ghisellini, J. Greiner, J. E. Hill, S. D. Hunsberger, H. A. Krimm, S. R. Kulkarni, P. Kumar, F. Lebrun, N. M. Lloyd-Ronning, C. B. Markwardt, B. J. Mattson, R. F. Mushotzky, J. P. Norris, J. Osborne, B. Paczynski, D. M. Palmer, H.-S. Park, A. M. Parsons, J. Paul, M. J. Rees, C. S. Reynolds, J. E. Rhoads, T. P. Sasseen, B. E. Schaefer, A. T. Short, A. P. Smale, I. A. Smith, L. Stella, G. Tagliaferri, T. Takahashi, M. Tashiro, L. K. Townsley, J. Tueller, M. J. L. Turner, M. Vietri, W. Voges, M. J. Ward, R. Willingale, F. M. Zerbi, and W. W. Zhang. The Swift Gamma-Ray Burst Mission. *ApJ*, 611:1005–1020, August 2004. doi: 10.1086/422091.
- P. Ghosh and F. K. Lamb. Accretion by rotating magnetic neutron stars. III - Accretion torques and period changes in pulsating X-ray sources. *ApJ*, 234:296–316, November 1979. doi: 10.1086/157498.
- P. Ghosh, R. F. Elsner, M. C. Weisskopf, and P. G. Sutherland. The asymmetric 4.8 hour X-ray modulation of Cygnus X-3 - Model light curves and inferred orbital parameters. *ApJ*, 251:230–245, December 1981. doi: 10.1086/159458.
- R. Giacconi, H. Gursky, E. Kellogg, E. Schreier, and H. Tananbaum. Discovery of Periodic X-Ray Pulsations in Centaurus X-3 from UHURU. *ApJ*, 167:L67, July 1971. doi: 10.1086/180762.
- R. Giacconi, S. Murray, H. Gursky, E. Kellogg, E. Schreier, and H. Tananbaum. The Uhuru catalog of X-ray sources. *ApJ*, 178:281–308, December 1972. doi: 10.1086/151790.
- R. Giacconi, S. Murray, H. Gursky, E. Kellogg, E. Schreier, T. Matilsky, D. Koch, and H. Tananbaum. The Third UHURU Catalog of X-Ray Sources. *ApJS*, 27:37, February 1974. doi: 10.1086/190288.
- A. González-Galán, I. Negueruela, N. Castro, S. Simón-Díaz, J. Lorenzo, and F. Vardell. Astrophysical parameters and orbital solution of the peculiar X-ray transient IGR J00370+6122. *A&A*, 566:A131, June 2014. doi: 10.1051/0004-6361/201423554.
- E. Göğüş, I. Kreykenbohm, and T. M. Belloni. Discovery of a peculiar dip from GX 301-2. *A&A*, 525:L6, January 2011. doi: 10.1051/0004-6361/201015905.

- S. A. Grebenev, O. V. Lyashenko, M. N. Pavlinsky, and R. A. Sunyaev. X-Ray Variability of 4U1700-37 According to Art-Pigranat. *Astrophysical Letters and Communications*, 38: 89, 1999.
- J. G. Greenhill, D. Galloway, and M. C. Storey. Luminosity Dependent Changes of Pulse Profiles in the X-ray Binary GX 1+4. *PASA*, 15:254–258, July 1998. doi: 10.1071/AS98254.
- H.-J. Grimm, M. Gilfanov, and R. Sunyaev. X-ray binaries in the Milky Way and other galaxies. *Chinese Journal of Astronomy and Astrophysics Supplement*, 3:257–269, December 2003. doi: 10.1088/1009-9271/3/S1/257.
- J. Grindlay, H. Gursky, H. Schnopper, D. R. Parsignault, J. Heise, A. C. Brinkman, and J. Schrijver. Discovery of intense X-ray bursts from the globular cluster NGC 6624. *ApJ*, 205:L127–L130, May 1976. doi: 10.1086/182105.
- A. K. Harding and J. K. Daugherty. Cyclotron resonant scattering and absorption. *ApJ*, 374: 687–699, June 1991. doi: 10.1086/170153.
- G. Hasinger and M. van der Klis. Two patterns of correlated X-ray timing and spectral behaviour in low-mass X-ray binaries. *A&A*, 225:79–96, November 1989.
- R. W. Hilditch, I. D. Howarth, and T. J. Harries. Forty eclipsing binaries in the Small Magellanic Cloud: fundamental parameters and Cloud distance. *MNRAS*, 357:304–324, February 2005. doi: 10.1111/j.1365-2966.2005.08653.x.
- A. B. Hill, R. Walter, C. Knigge, A. Bazzano, G. Bélanger, A. J. Bird, A. J. Dean, J. L. Galache, A. Malizia, M. Renaud, J. Stephen, and P. Ubertini. The 1-50 keV spectral and timing analysis of IGR J18027-2016: an eclipsing, high mass X-ray binary. *A&A*, 439: 255–263, August 2005a. doi: 10.1051/0004-6361:20052937.
- A. B. Hill, R. Walter, C. Knigge, A. Bazzano, G. Bélanger, A. J. Bird, A. J. Dean, J. L. Galache, A. Malizia, M. Renaud, J. Stephen, and P. Ubertini. The 1-50 keV spectral and timing analysis of IGR J18027-2016: an eclipsing, high mass X-ray binary. *A&A*, 439: 255–263, August 2005b. doi: 10.1051/0004-6361:20052937.
- K. H. Hinkle, F. C. Fekel, R. R. Joyce, P. R. Wood, V. V. Smith, and T. Lebzelter. Infrared Spectroscopy of Symbiotic Stars. IV. V2116 Ophiuchi/GX 1+4, The Neutron Star Symbiotic. *ApJ*, 641:479–487, April 2006. doi: 10.1086/500350.
- J. Homan, M. van der Klis, R. Wijnands, T. Belloni, R. Fender, M. Klein-Wolt, P. Casella, M. Méndez, E. Gallo, W. H. G. Lewin, and N. Gehrels. Rossi X-Ray Timing Explorer Observations of the First Transient Z Source XTE J1701-462: Shedding New Light on Mass Accretion in Luminous Neutron Star X-Ray Binaries. *ApJ*, 656:420–430, February 2007. doi: 10.1086/510447.
- C.-P. Hu, Y. Chou, M.-C. Wu, T.-C. Yang, and Y.-H. Su. Time-frequency Analysis of the Superorbital Modulation of the X-Ray Binary SMC X-1 Using the Hilbert-Huang Transform. *ApJ*, 740:67, October 2011. doi: 10.1088/0004-637X/740/2/67.

- R. I. Hynes, M. A. P. Torres, C. O. Heinke, T. J. Maccarone, V. J. Mikles, C. T. Britt, C. Knigge, S. Greiss, P. G. Jonker, D. Steeghs, G. Nelemans, R. M. Bandyopadhyay, and C. B. Johnson. CXOGBS J173620.2-293338: A Candidate Symbiotic X-Ray Binary Associated with a Bulge Carbon Star. *ApJ*, 780:11, January 2014. doi: 10.1088/0004-637X/780/1/11.
- J. J. M. in 't Zand, T. Bagnoli, C. D'Angelo, A. Patruno, D. K. Galloway, M. B. M. van der Klis, A. L. Watts, and H. L. Marshall. Chandra spectroscopy of Rapid Burster type-I X-ray bursts. *ArXiv e-prints*, March 2017.
- J. J. M. in't Zand. *A coded-mask imager as monitor of Galactic X-ray sources*. PhD thesis, Space Research Organization Netherlands, Sorbonnelaan 2, 3584 CA Utrecht, The Netherlands, 1992.
- J. J. M. in't Zand, L. Kuiper, P. R. den Hartog, W. Hermsen, and R. H. D. Corbet. A probable accretion-powered X-ray pulsar in IGR J00370+6122. *A&A*, 469:1063–1068, July 2007. doi: 10.1051/0004-6361:20077189.
- N. Islam and B. Paul. Orbital phase resolved spectroscopy of GX 301-2 with MAXI. *MNRAS*, 441:2539–2545, July 2014a. doi: 10.1093/mnras/stu756.
- N. Islam and B. Paul. Orbital phase resolved spectroscopy of GX 301-2 with MAXI. *MNRAS*, 441:2539–2545, July 2014b. doi: 10.1093/mnras/stu756.
- N. Islam and B. Paul. Orbital evolution and search for eccentricity and apsidal motion in the eclipsing HMXB 4U 1700-37. *MNRAS*, 461:816–824, September 2016. doi: 10.1093/mnras/stw1299.
- N. Islam, C. Maitra, P. Pradhan, and B. Paul. A Suzaku view of IGR J16393-4643. *MNRAS*, 446:4148–4154, February 2015. doi: 10.1093/mnras/stu2395.
- F. J. Jablonski, M. G. Pereira, J. Braga, and C. D. Gneiding. Discovery of Optical Pulsations in V2116 Ophiuchi equivalent to GX 1+4. *ApJ*, 482:L171–L174, June 1997. doi: 10.1086/310699.
- J. D. Jackson. *Classical electrodynamics*. 1975.
- C. Jain, B. Paul, and A. Dutta. Discovery of a short orbital period in the Supergiant Fast X-ray Transient IGR J16479-4514. *MNRAS*, 397:L11–L15, July 2009a. doi: 10.1111/j.1745-3933.2009.00668.x.
- C. Jain, B. Paul, and A. Dutta. Orbital X-ray modulation study of three supergiant HMXBs. *Research in Astronomy and Astrophysics*, 9:1303–1316, December 2009b. doi: 10.1088/1674-4527/9/12/002.
- C. Jain, B. Paul, and A. Dutta. Orbital X-ray modulation study of three supergiant HMXBs. *Research in Astronomy and Astrophysics*, 9:1303–1316, December 2009c. doi: 10.1088/1674-4527/9/12/002.
- P. A. Jenke, M. H. Finger, C. A. Wilson-Hodge, and A. Camero-Arranz. Orbital Decay and Evidence of Disk Formation in the X-Ray Binary Pulsar OAO 1657-415. *ApJ*, 759:124, November 2012. doi: 10.1088/0004-637X/759/2/124.

- C. Jones, W. Forman, H. Tananbaum, E. Schreier, H. Gursky, E. Kellogg, and R. Giacconi. Evidence for the Binary Nature of 2u 1700-37. *ApJ*, 181:L43, April 1973. doi: 10.1086/181181.
- S. Kato. Resonant Excitation of Disk Oscillations by Warps: A Model of kHz QPOs. *PASJ*, 56:905–922, October 2004. doi: 10.1093/pasj/56.5.905.
- S. Kato. A Resonance Model of Quasi-Periodic Oscillations of Low-Mass X-Ray Binaries. *PASJ*, 57:L17–L20, June 2005. doi: 10.1093/pasj/57.3.L17.
- J. I. Katz. Thirty-five-day Periodicity in Her X-1. *Nature Physical Science*, 246:87–89, December 1973. doi: 10.1038/physci246087a0.
- G. F. Knoll. *Radiation detection and measurement*. 2000.
- U. Kolb. *Extreme Environment Astrophysics*. May 2010.
- T. Kotani, T. Dotani, F. Nagase, J. G. Greenhill, S. H. Pravdo, and L. Angelini. ASCA and Ginga Observations of GX 1+4. *ApJ*, 510:369–378, January 1999. doi: 10.1086/306552.
- K. Koyama, H. Tsunemi, T. Dotani, M. W. Bautz, K. Hayashida, T. G. Tsuru, H. Matsumoto, Y. Ogawara, G. R. Ricker, J. Doty, S. E. Kissel, R. Foster, H. Nakajima, H. Yamaguchi, H. Mori, M. Sakano, K. Hamaguchi, M. Nishiuchi, E. Miyata, K. Torii, M. Namiki, S. Katsuda, D. Matsuura, T. Miyauchi, N. Anabuki, N. Tawa, M. Ozaki, H. Murakami, Y. Maeda, Y. Ichikawa, G. Y. Prigozhin, E. A. Boughan, B. Lamarr, E. D. Miller, B. E. Burke, J. A. Gregory, A. Pillsbury, A. Bamba, J. S. Hiraga, A. Senda, H. Katayama, S. Kitamoto, M. Tsujimoto, T. Kohmura, Y. Tsuboi, and H. Awaki. X-Ray Imaging Spectrometer (XIS) on Board Suzaku. *PASJ*, 59:23–33, January 2007. doi: 10.1093/pasj/59.sp1.S23.
- P. Kretschmar. *Hochenergie-röntgenspektren der akkretierenden Röntgenpulsare Vela X-1 und A 0535+26*. PhD thesis, Eberhard-Karls-Universität Tübingen, 1996.
- I. Kreykenbohm, P. Kretschmar, J. Wilms, R. Staubert, E. Kendziorra, D. E. Gruber, W. A. Heindl, and R. E. Rothschild. VELA X-1 as seen by RXTE. *A&A*, 341:141–150, January 1999.
- H. A. Krimm, S. T. Holland, R. H. D. Corbet, A. B. Pearlman, P. Romano, J. A. Kennea, J. S. Bloom, S. D. Barthelmy, W. H. Baumgartner, J. R. Cummings, N. Gehrels, A. Y. Lien, C. B. Markwardt, D. M. Palmer, T. Sakamoto, M. Stamatikos, and T. N. Ukwatta. The Swift/BAT Hard X-Ray Transient Monitor. *ApJS*, 209:14, November 2013a. doi: 10.1088/0067-0049/209/1/14.
- H. A. Krimm, S. T. Holland, R. H. D. Corbet, A. B. Pearlman, P. Romano, J. A. Kennea, J. S. Bloom, S. D. Barthelmy, W. H. Baumgartner, J. R. Cummings, N. Gehrels, A. Y. Lien, C. B. Markwardt, D. M. Palmer, T. Sakamoto, M. Stamatikos, and T. N. Ukwatta. The Swift/BAT Hard X-Ray Transient Monitor. *ApJS*, 209:14, November 2013b. doi: 10.1088/0067-0049/209/1/14.
- R.-P. Kudritzki and J. Puls. Winds from Hot Stars. *ARA&A*, 38:613–666, 2000. doi: 10.1146/annurev.astro.38.1.613.

- J. Lense and H. Thirring. Über den Einfluß der Eigenrotation der Zentralkörper auf die Bewegung der Planeten und Monde nach der Einsteinschen Gravitationstheorie. *Physikalische Zeitschrift*, 19, 1918.
- C. Leong, E. Kellogg, H. Gursky, H. Tananbaum, and R. Giacconi. X-Ray Emission from the Magellanic Clouds Observed by UHURU. *ApJ*, 170:L67, December 1971. doi: 10.1086/180842.
- M. Lesser. A Summary of Charge-Coupled Devices for Astronomy. *PASP*, 127:1097, November 2015. doi: 10.1086/684054.
- A. Levine, S. Rappaport, J. E. Deeter, P. E. Boynton, and F. Nagase. Discovery of orbital decay in SMC X-1. *ApJ*, 410:328–341, June 1993. doi: 10.1086/172750.
- A. M. Levine, S. A. Rappaport, and G. Zojcheski. Orbital Decay in LMC X-4. *ApJ*, 541:194–202, September 2000. doi: 10.1086/309398.
- W. H. G. Lewin, J. van Paradijs, and R. E. Taam. X-Ray Bursts. *Space Sci. Rev.*, 62:223–389, September 1993. doi: 10.1007/BF00196124.
- F. Li, S. Rappaport, and A. Epstein. Observation of X-ray eclipses from LMC X-4. *Nature*, 271:37, January 1978. doi: 10.1038/271037a0.
- Q. Z. Liu, J. van Paradijs, and E. P. J. van den Heuvel. A catalogue of high-mass X-ray binaries. *A&AS*, 147:25–49, November 2000. doi: 10.1051/aas:2000288.
- Q. Z. Liu, J. van Paradijs, and E. P. J. van den Heuvel. Catalogue of high-mass X-ray binaries in the Galaxy (4th edition). *A&A*, 455:1165–1168, September 2006. doi: 10.1051/0004-6361:20064987.
- Q. Z. Liu, J. van Paradijs, and E. P. J. van den Heuvel. A catalogue of low-mass X-ray binaries in the Galaxy, LMC, and SMC (Fourth edition). *A&A*, 469:807–810, July 2007. doi: 10.1051/0004-6361:20077303.
- D. H. Lumb, N. Schartel, and F. A. Jansen. XMM-Newton (X-Ray Multi-Mirror Mission) Observatory. *ArXiv e-prints*, February 2012.
- A. Lutovinov, M. Revnivtsev, S. Molokov, and R. Sunyaev. INTEGRAL observations of five sources in the Galactic Center region. *A&A*, 430:997–1003, February 2005. doi: 10.1051/0004-6361:20041677.
- C. Maitra and B. Paul. Pulse-phase-resolved Spectroscopy of Vela X-1 with Suzaku. *ApJ*, 763:79, February 2013. doi: 10.1088/0004-637X/763/2/79.
- P. R. Maloney and M. C. Begelman. The Origin of Warped, Precessing Accretions Disks in X-Ray Binaries. *ApJ*, 491:L43–L46, December 1997. doi: 10.1086/311058.
- A. Manousakis and R. Walter. Origin of the X-ray off-states in Vela X-1. *A&A*, 575:A58, March 2015. doi: 10.1051/0004-6361/201321414.
- F. Martins, D. Schaerer, and D. J. Hillier. A new calibration of stellar parameters of Galactic O stars. *A&A*, 436:1049–1065, June 2005. doi: 10.1051/0004-6361:20042386.

- N. Masetti, M. Orlandini, E. Palazzi, L. Amati, and F. Frontera. M-type giants as optical counterparts of X-ray sources 4U 1700+24 and 4U 1954+319. *A&A*, 453:295–299, July 2006. doi: 10.1051/0004-6361:20065025.
- N. Masetti, R. Landi, M. L. Pretorius, V. Sguera, A. J. Bird, M. Perri, P. A. Charles, J. A. Kennea, A. Malizia, and P. Ubertini. IGR J16194-2810: a new symbiotic X-ray binary. *A&A*, 470:331–337, July 2007. doi: 10.1051/0004-6361:20077509.
- A. B. Mason, J. S. Clark, A. J. Norton, I. Negueruela, and P. Roche. Spectral classification of the mass donors in the high-mass X-ray binaries EXO 1722-363 and OAO 1657-415. *A&A*, 505:281–286, October 2009. doi: 10.1051/0004-6361/200912480.
- K. O. Mason, G. Branduardi, and P. Sanford. The X-ray behavior of 3U 1700-37. *ApJ*, 203:L29–L33, January 1976. doi: 10.1086/182012.
- K. O. Mason, A. Breeveld, R. Much, M. Carter, F. A. Cordova, M. S. Cropper, J. Fordham, H. Huckle, C. Ho, H. Kawakami, J. Kennea, T. Kennedy, J. Mittaz, D. Pandel, W. C. Priedhorsky, T. Sasseen, R. Shirey, P. Smith, and J.-M. Vreux. The XMM-Newton optical/UV monitor telescope. *A&A*, 365:L36–L44, January 2001. doi: 10.1051/0004-6361:20000044.
- M. Matsuoka, K. Kawasaki, S. Ueno, H. Tomida, M. Kohama, M. Suzuki, Y. Adachi, M. Ishikawa, T. Mihara, M. Sugizaki, N. Isobe, Y. Nakagawa, H. Tsunemi, E. Miyata, N. Kawai, J. Kataoka, M. Morii, A. Yoshida, H. Negoro, M. Nakajima, Y. Ueda, H. Chujo, K. Yamaoka, O. Yamazaki, S. Nakahira, T. You, R. Ishiwata, S. Miyoshi, S. Eguchi, K. Hiroi, H. Katayama, and K. Ebisawa. The MAXI Mission on the ISS: Science and Instruments for Monitoring All-Sky X-Ray Images. *PASJ*, 61:999–1010, October 2009. doi: 10.1093/pasj/61.5.999.
- S. Molkov, N. Mowlavi, A. Goldwurm, A. Strong, N. Lund, J. Paul, and T. Oosterbroek. Igr J16479-4514. *The Astronomer's Telegram*, 176, August 2003.
- D.-S. Moon and S. S. Eikenberry. Large X-Ray Flares from LMC X-4: Discovery of Millihertz Quasi-periodic Oscillations and Quasi-periodic Oscillation-Modulated Pulsations. *ApJ*, 549:L225–L228, March 2001. doi: 10.1086/319160.
- D.-S. Moon, S. S. Eikenberry, and I. M. Wasserman. SMC X-1 as an Intermediate-Stage Flaring X-Ray Pulsar. *ApJ*, 582:L91–L94, January 2003. doi: 10.1086/367782.
- S. E. Motta, A. Rouco-Escorial, E. Kuulkers, T. Muñoz-Darias, and A. Sanna. Links between quasi-periodic oscillations and accretion states in neutron star low-mass X-ray binaries. *MNRAS*, 468:2311–2324, June 2017. doi: 10.1093/mnras/stx570.
- U. Mukherjee and B. Paul. X-ray properties of the transient pulsar 3A 0535+262 in quiescence. *A&A*, 431:667–672, February 2005. doi: 10.1051/0004-6361:20041665.
- U. Mukherjee, H. Raichur, B. Paul, S. Naik, and N. Bhatt. Orbital Evolution and Orbital Phase Resolved Spectroscopy of the HMXB Pulsar 4U 1538-52 with RXTE-PCA and BeppoSAX. *Journal of Astrophysics and Astronomy*, 27:411–423, December 2006. doi: 10.1007/BF02709367.

- B. N. Mück. *Low-mass X-ray binary studies with XMM–Newton*. PhD thesis, Eberhard-Karls-Universität Tübingen, 2014.
- F. Nagase. Accretion-powered X-ray pulsars. *PASJ*, 41:1–79, 1989.
- S. Naik and B. Paul. Timing and Spectral Studies of LMC X-4 in High and Low States with BeppoSAX: Detection of Pulsations in the Soft Spectral Component. *ApJ*, 600:351–357, January 2004. doi: 10.1086/379803.
- S. Naik and B. Paul. Investigation of variability of iron emission lines in Centaurus X-3. *Bulletin of the Astronomical Society of India*, 40:503, December 2012.
- S. Naik, B. Paul, and Z. Ali. X-Ray Spectroscopy of the High-mass X-Ray Binary Pulsar Centaurus X-3 over Its Binary Orbit. *ApJ*, 737:79, August 2011. doi: 10.1088/0004-637X/737/2/79.
- E. Nespoli, J. Fabregat, and R. E. Mennickent. Unveiling the nature of six HMXBs through IR spectroscopy. *A&A*, 486:911–917, August 2008. doi: 10.1051/0004-6361:200809645.
- E. Nespoli, J. Fabregat, and R. E. Mennickent. K-band spectroscopy of IGR J16358-4726 and IGR J16393-4643: two new symbiotic X-ray binaries. *A&A*, 516:A94, June 2010. doi: 10.1051/0004-6361/200913410.
- H. Odaka, D. Khangulyan, Y. T. Tanaka, S. Watanabe, T. Takahashi, and K. Makishima. Short-term Variability of X-Rays from Accreting Neutron Star Vela X-1. I. Suzaku Observations. *ApJ*, 767:70, April 2013. doi: 10.1088/0004-637X/767/1/70.
- G. I. Ogilvie and G. Dubus. Precessing warped accretion discs in X-ray binaries. *MNRAS*, 320:485–503, February 2001. doi: 10.1046/j.1365-8711.2001.04011.x.
- L. M. Oskinova, A. Feldmeier, and W.-R. Hamann. High-resolution X-ray spectroscopy of bright O-type stars. *MNRAS*, 372:313–326, October 2006. doi: 10.1111/j.1365-2966.2006.10858.x.
- L. M. Oskinova, W.-R. Hamann, and A. Feldmeier. Neglecting the porosity of hot-star winds can lead to underestimating mass-loss rates. *A&A*, 476:1331–1340, December 2007. doi: 10.1051/0004-6361:20066377.
- L. M. Oskinova, A. Feldmeier, and P. Kretschmar. Clumped stellar winds in supergiant high-mass X-ray binaries. In C. M. Zhang, T. Belloni, M. Méndez, and S. N. Zhang, editors, *IAU Symposium*, volume 290 of *IAU Symposium*, pages 287–288, February 2013. doi: 10.1017/S1743921312020042.
- G. E. Parkes, P. G. Murdin, and K. O. Mason. The optical counterpart of the binary X-ray pulsar 4U1538-52. *MNRAS*, 184:73P–77P, September 1978. doi: 10.1093/mnras/184.1.73P.
- B. Paul and S. Naik. Transient High Mass X-ray Binaries. *Bulletin of the Astronomical Society of India*, 39:429–449, September 2011a.

- B. Paul and S. Naik. Transient High Mass X-ray Binaries. *Bulletin of the Astronomical Society of India*, 39:429–449, September 2011b.
- A. J. Penny, R. P. Olowin, J. E. Penfold, and P. R. Warren. Photometry of HD 153919 = 2U 1700-37. *MNRAS*, 163:7P–12P, 1973. doi: 10.1093/mnras/163.1.7P.
- G. Pietrzyński, D. Graczyk, W. Gieren, I. B. Thompson, B. Pilecki, A. Udalski, I. Soszyński, S. Kozłowski, P. Konorski, K. Suchomska, G. Bono, P. G. P. Moroni, S. Villanova, N. Nardetto, F. Bresolin, R. P. Kudritzki, J. Storm, A. Gallenne, R. Smolec, D. Minniti, M. Kubiak, M. K. Szymański, R. Poleski, Ł. Wyrzykowski, K. Ulaczyk, P. Pietrukowicz, M. Górski, and P. Karczmarek. An eclipsing-binary distance to the Large Magellanic Cloud accurate to two per cent. *Nature*, 495:76–79, March 2013. doi: 10.1038/nature11878.
- G. Ponti, S. Bianchi, T. Muñoz-Darias, B. De Marco, T. Dwelly, R. P. Fender, K. Nandra, N. Rea, K. Mori, D. Haggard, C. O. Heinke, N. Degenaar, T. Aramaki, M. Clavel, A. Goldwurm, C. J. Hailey, G. L. Israel, M. R. Morris, A. Rushton, and R. Terrier. On the Fe K absorption - accretion state connection in the Galactic Centre neutron star X-ray binary AX J1745.6-2901. *MNRAS*, 446:1536–1550, January 2015. doi: 10.1093/mnras/stu1853.
- G. Ponti, S. Bianchi, T. Muñoz-Darias, K. Mori, K. De, A. Rau, B. De Marco, C. Hailey, J. Tomsick, K. K. Madsen, M. Clavel, F. Rahoui, D. V. Lal, S. Roy, and D. Stern. NuSTAR + XMM-Newton monitoring of the neutron star transient AX J1745.6-2901. *MNRAS*, 473:2304–2323, January 2018. doi: 10.1093/mnras/stx2425.
- P. Pradhan, C. Maitra, B. Paul, and B. C. Paul. Revisiting SW J2000.6+3210: a persistent Be X-ray pulsar? *MNRAS*, 436:945–952, December 2013. doi: 10.1093/mnras/stt1504.
- P. Pradhan, C. Maitra, B. Paul, N. Islam, and B. C. Paul. Variations in the pulsation and spectral characteristics of OAO 1657-415. *MNRAS*, 442:2691–2700, August 2014. doi: 10.1093/mnras/stu1034.
- W. C. Priedhorsky, J. Terrell, and S. S. Holt. Evidence for an about 300 day period in Cygnus X-1. *ApJ*, 270:233–238, July 1983. doi: 10.1086/161114.
- F. Primini, S. Rappaport, and P. C. Joss. Pulse profile and refined orbital elements for SMC X-1. *ApJ*, 217:543–548, October 1977. doi: 10.1086/155603.
- H. Raichur and B. Paul. Effect of pulse profile variations on measurement of eccentricity in orbits of Cen X-3 and SMC X-1. *MNRAS*, 401:1532–1539, January 2010. doi: 10.1111/j.1365-2966.2009.15778.x.
- A. F. Rajoelimanana, P. A. Charles, and A. Udalski. Very long-term optical variability of high-mass X-ray binaries in the Small Magellanic Cloud. *MNRAS*, 413:1600–1622, May 2011. doi: 10.1111/j.1365-2966.2011.18243.x.
- G. Raman and B. Paul. X-ray and optical orbital modulation of EXO 0748-676 : A co-variability study using XMM-Newton. *New A*, 54:122–139, July 2017. doi: 10.1016/j.newast.2017.02.001.
- P. Reig. Be/X-ray binaries. *Ap&SS*, 332:1–29, March 2011. doi: 10.1007/s10509-010-0575-8.

- P. Reig, I. Negueruela, G. Papamastorakis, A. Manousakis, and T. Kougentakis. Identification of the optical counterparts of high-mass X-ray binaries through optical photometry and spectroscopy. *A&A*, 440:637–646, September 2005. doi: 10.1051/0004-6361:20052684.
- M. G. Revnivtsev, R. A. Sunyaev, D. A. Varshalovich, V. V. Zheleznyakov, A. M. Cherepashchuk, A. A. Lutovinov, E. M. Churazov, S. A. Grebenev, and M. R. Gilfanov. A Hard X-ray Survey of the Galactic-Center Region with the IBIS Telescope of the INTEGRAL Observatory: A Catalog of Sources. *Astronomy Letters*, 30:382–389, June 2004a. doi: 10.1134/1.1764884.
- M. G. Revnivtsev, R. A. Sunyaev, D. A. Varshalovich, V. V. Zheleznyakov, A. M. Cherepashchuk, A. A. Lutovinov, E. M. Churazov, S. A. Grebenev, and M. R. Gilfanov. A Hard X-ray Survey of the Galactic-Center Region with the IBIS Telescope of the INTEGRAL Observatory: A Catalog of Sources. *Astronomy Letters*, 30:382–389, June 2004b. doi: 10.1134/1.1764884.
- A. P. Reynolds, S. A. Bell, and R. W. Hilditch. Optical spectroscopy of the massive X-ray binary QV Nor (4U 1538 - 52). *MNRAS*, 256:631–640, June 1992. doi: 10.1093/mnras/256.3.631.
- A. P. Reynolds, R. W. Hilditch, S. A. Bell, and G. Hill. Optical spectroscopy of the massive X-ray binary SMC X-1/Sk 160. *MNRAS*, 261:337–345, March 1993. doi: 10.1093/mnras/261.2.337.
- J. J. Rodes-Roca, T. Mihara, S. Nakahira, J. M. Torrejón, Á. Giménez-García, and G. Bernabéu. Orbital phase-resolved spectroscopy of 4U 1538-52 with MAXI. *A&A*, 580:A140, August 2015. doi: 10.1051/0004-6361/201425323.
- P. Romano, L. Sidoli, V. Mangano, S. Mereghetti, and G. Cusumano. Swift/XRT observes the fifth outburst of the periodic supergiant fast X-ray transient IGR J11215-5952. *A&A*, 469:L5–L8, July 2007. doi: 10.1051/0004-6361:20077383.
- G. E. Romero, M. M. Kaufman Bernadó, and I. F. Mirabel. Recurrent microblazar activity in Cygnus X-1? *A&A*, 393:L61–L64, October 2002. doi: 10.1051/0004-6361:20021205.
- G. B. Rybicki and A. P. Lightman. *Radiative processes in astrophysics*. 1979.
- G. J. Savonije. Roche-lobe overflow in X-ray binaries. *A&A*, 62:317–338, January 1978.
- E. Schreier, R. Levinson, H. Gursky, E. Kellogg, H. Tananbaum, and R. Giacconi. Evidence for the Binary Nature of Centaurus X-3 from UHURU X-Ray Observations. *ApJ*, 172:L79, March 1972a. doi: 10.1086/180896.
- E. Schreier, R. Levinson, H. Gursky, E. Kellogg, H. Tananbaum, and R. Giacconi. Evidence for the Binary Nature of Centaurus X-3 from UHURU X-Ray Observations. *ApJ*, 172:L79, March 1972b. doi: 10.1086/180896.
- J. F. Sepinsky, B. Willems, V. Kalogera, and F. A. Rasio. Interacting Binaries with Eccentric Orbits: Secular Orbital Evolution Due to Conservative Mass Transfer. *ApJ*, 667:1170–1184, October 2007. doi: 10.1086/520911.

- V. Sguera, E. J. Barlow, A. J. Bird, D. J. Clark, A. J. Dean, A. B. Hill, L. Moran, S. E. Shaw, D. R. Willis, A. Bazzano, P. Ubertini, and A. Malizia. INTEGRAL observations of recurrent fast X-ray transient sources. *A&A*, 444:221–231, December 2005a. doi: 10.1051/0004-6361:20053103.
- V. Sguera, E. J. Barlow, A. J. Bird, D. J. Clark, A. J. Dean, A. B. Hill, L. Moran, S. E. Shaw, D. R. Willis, A. Bazzano, P. Ubertini, and A. Malizia. INTEGRAL observations of recurrent fast X-ray transient sources. *A&A*, 444:221–231, December 2005b. doi: 10.1051/0004-6361:20053103.
- N. Shakura and K. Postnov. Wind Accretion - Observations Vs Theory. *ArXiv e-prints*, February 2017.
- N. Shakura, K. Postnov, A. Kochetkova, and L. Hjalmarsdotter. Theory of quasi-spherical accretion in X-ray pulsars. *MNRAS*, 420:216–236, February 2012. doi: 10.1111/j.1365-2966.2011.20026.x.
- N. I. Shakura and R. A. Sunyaev. Black holes in binary systems. Observational appearance. *A&A*, 24:337–355, 1973.
- L. Sidoli, T. Oosterbroek, A. N. Parmar, D. Lumb, and C. Erd. An XMM-Newton study of the X-ray binary MXB 1659-298 and the discovery of narrow X-ray absorption lines. *A&A*, 379:540–550, November 2001. doi: 10.1051/0004-6361:20011322.
- L. Sidoli, P. Romano, S. Mereghetti, A. Paizis, S. Vercellone, V. Mangano, and D. Götz. An alternative hypothesis for the outburst mechanism in supergiant fast X-ray transients: the case of IGR J11215-5952. *A&A*, 476:1307–1315, December 2007. doi: 10.1051/0004-6361:20078137.
- L. Sidoli, P. Esposito, and L. Ducci. The longest observation of a low-intensity state from a supergiant fast X-ray transient: Suzaku observes IGRJ08408-4503. *MNRAS*, 409:611–618, December 2010. doi: 10.1111/j.1365-2966.2010.17320.x.
- L. Sidoli, P. Esposito, V. Sguera, A. Bodaghee, J. A. Tomsick, K. Pottschmidt, J. Rodriguez, P. Romano, and J. Wilms. The Supergiant Fast X-ray Transient with the shortest orbital period: Suzaku observes one orbit in IGR J16479-4514. In *Proceedings of “An INTEGRAL view of the high-energy sky (the first 10 years)” - 9th INTEGRAL Workshop and celebration of the 10th anniversary of the launch (INTEGRAL 2012). 15-19 October 2012. Bibliotheque Nationale de France, Paris, France. Published online at http://pos.sissa.it/cgi-bin/reader/conf.cgi?confid=176, id.34, page 34, 2012.*
- B. A. Smith. Astronomical imaging applications for CCDs. In S. Iwasa and W. J. White, editors, *Charge-Coupled Device Technology and Applications*, 1976.
- D. M. Smith, W. A. Heindl, and J. H. Swank. Orbital and Superorbital Periods of 1E 1740.7-2942 and GRS 1758-258. *ApJ*, 578:L129–L132, October 2002. doi: 10.1086/344701.
- R. Sood, S. Farrell, P. O’Neill, and S. Dieters. Super-orbital periods in X-ray binaries. *Advances in Space Research*, 40:1528–1531, 2007. doi: 10.1016/j.asr.2007.02.057.

- L. Stella and R. Rosner. Magnetic field instabilities in accretion disks. *ApJ*, 277:312–321, February 1984. doi: 10.1086/161697.
- L. Stella, M. Vietri, and S. M. Morsink. Correlations in the Quasi-periodic Oscillation Frequencies of Low-Mass X-Ray Binaries and the Relativistic Precession Model. *ApJ*, 524:L63–L66, October 1999. doi: 10.1086/312291.
- T. Strohmayer and L. Keek. IGR J17062-6143 Is an Accreting Millisecond X-Ray Pulsar. *ApJ*, 836:L23, February 2017. doi: 10.3847/2041-8213/aa5e51.
- L. Strüder, U. Briel, K. Dennerl, R. Hartmann, E. Kendziorra, N. Meidinger, E. Pfeffermann, C. Reppin, B. Aschenbach, W. Bornemann, H. Bräuninger, W. Burkert, M. Elender, M. Freyberg, F. Haberl, G. Hartner, F. Heuschmann, H. Hippmann, E. Kastelic, S. Kemmer, G. Kettenring, W. Kink, N. Krause, S. Müller, A. Oppitz, W. Pietsch, M. Popp, P. Predehl, A. Read, K. H. Stephan, D. Stötter, J. Trümper, P. Holl, J. Kemmer, H. Soltau, R. Stötter, U. Weber, U. Weichert, C. von Zanthier, D. Carathanassis, G. Lutz, R. H. Richter, P. Solc, H. Böttcher, M. Kuster, R. Staubert, A. Abbey, A. Holland, M. Turner, M. Balasini, G. F. Bignami, N. La Palombara, G. Villa, W. Buttler, F. Gianini, R. Lainé, D. Lumb, and P. Dhez. The European Photon Imaging Camera on XMM-Newton: The pn-CCD camera. *A&A*, 365:L18–L26, January 2001. doi: 10.1051/0004-6361:20000066.
- Y. Takeuchi, K. Koyama, and R. S. Warwick. Further GINGA observations of the new X-ray pulsar X1722-36. *PASJ*, 42:287–293, April 1990.
- T. W. J. Thompson and R. E. Rothschild. The X-Ray Halo of Cen X-3. *ApJ*, 691:1744–1753, February 2009. doi: 10.1088/0004-637X/691/2/1744.
- T. W. J. Thompson, J. A. Tomsick, J. J. M. in 't Zand, R. E. Rothschild, and R. Walter. The Orbit of the Eclipsing X-Ray Pulsar EXO 1722-363. *ApJ*, 661:447–457, May 2007. doi: 10.1086/513458.
- L. Titarchuk and V. Osherovich. The Global Normal Disk Oscillations and the Persistent Low-Frequency Quasi-periodic Oscillations in X-Ray Binaries. *ApJ*, 542:L111–L114, October 2000. doi: 10.1086/312935.
- J. A. Tomsick, R. Lingenfelter, S. Corbel, A. Goldwurm, and P. Kaaret. Two New INTEGRAL Sources: IGR J15479-4529 and IGR J16418-4532. *The Astronomer's Telegram*, 224, January 2004.
- O. D. Toropina, M. M. Romanova, and R. V. E. Lovelace. Spinning-down of moving magnetars in the propeller regime. *MNRAS*, 371:569–576, September 2006. doi: 10.1111/j.1365-2966.2006.10667.x.
- J. M. Torrejón, I. Negueruela, D. M. Smith, and T. E. Harrison. Near-infrared survey of high mass X-ray binary candidates. *A&A*, 510:A61, February 2010a. doi: 10.1051/0004-6361/200912619.
- J. M. Torrejón, I. Negueruela, D. M. Smith, and T. E. Harrison. Near-infrared survey of high mass X-ray binary candidates. *A&A*, 510:A61, February 2010b. doi: 10.1051/0004-6361/200912619.

- S. Trowbridge, M. A. Nowak, and J. Wilms. Tracking the Orbital and Superorbital Periods of SMC X-1. *ApJ*, 670:624–634, November 2007. doi: 10.1086/522075.
- H. Tsunemi, S. Kitamoto, M. Manabe, S. Miyamoto, K. Yamashita, and M. Nakagawa. All Sky Monitor on board the GINGA satellite and its performance. *PASJ*, 41:391–403, 1989.
- M. J. L. Turner, A. Abbey, M. Arnaud, M. Balasini, M. Barbera, E. Belsole, P. J. Bennie, J. P. Bernard, G. F. Bignami, M. Boer, U. Briel, I. Butler, C. Cara, C. Chabaud, R. Cole, A. Collura, M. Conte, A. Cros, M. Denby, P. Dhez, G. Di Coco, J. Dowson, P. Ferrando, S. Ghizzardi, F. Gianotti, C. V. Goodall, L. Gretton, R. G. Griffiths, O. Hainaut, J. F. Hochedez, A. D. Holland, E. Jourdain, E. Kendziorra, A. Lagostina, R. Laine, N. La Palombara, M. Lortholary, D. Lumb, P. Marty, S. Molendi, C. Pigot, E. Poindron, K. A. Pounds, J. N. Reeves, C. Reppin, R. Rothenflug, P. Salvétat, J. L. Sauvageot, D. Schmitt, S. Sembay, A. D. T. Short, J. Spragg, J. Stephen, L. Strüder, A. Tiengo, M. Trifoglio, J. Trümper, S. Vercellone, L. Vigroux, G. Villa, M. J. Ward, S. Whitehead, and E. Zonca. The European Photon Imaging Camera on XMM-Newton: The MOS cameras : The MOS cameras. *A&A*, 365:L27–L35, January 2001. doi: 10.1051/0004-6361:20000087.
- W. D. Vacca, C. D. Garmany, and J. M. Shull. The Lyman-Continuum Fluxes and Stellar Parameters of O and Early B-Type Stars. *ApJ*, 460:914, April 1996. doi: 10.1086/177020.
- A. K. F. Val Baker, A. J. Norton, and H. Quaintrell. The mass of the neutron star in SMC X-1. *A&A*, 441:685–688, October 2005. doi: 10.1051/0004-6361:20053074.
- M. van der Klis. Quasi-periodic oscillations and noise in low-mass X-ray binaries. *ARA&A*, 27:517–553, 1989. doi: 10.1146/annurev.aa.27.090189.002505.
- A. van der Meer, L. Kaper, T. di Salvo, M. Méndez, M. van der Klis, P. Barr, and N. R. Trams. XMM-Newton X-ray spectroscopy of the high-mass X-ray binary 4U 1700-37 at low flux. *A&A*, 432:999–1012, March 2005. doi: 10.1051/0004-6361:20041288.
- A. van der Meer, L. Kaper, M. H. van Kerkwijk, M. H. M. Heemskerk, and E. P. J. van den Heuvel. Determination of the mass of the neutron star in <ASTROBJ>SMC X-1</ASTROBJ>, <ASTROBJ>LMC X-4</ASTROBJ>, and <ASTROBJ>Cen X-3</ASTROBJ> with VLT/UVES. *A&A*, 473:523–538, October 2007. doi: 10.1051/0004-6361:20066025.
- R. Walter and J. Zurita Heras. Probing clumpy stellar winds with a neutron star. *A&A*, 476:335–340, December 2007. doi: 10.1051/0004-6361:20078353.
- R. Walter, J. Zurita Heras, L. Bassani, A. Bazzano, A. Bodaghee, A. Dean, P. Dubath, A. N. Parmar, M. Renaud, and P. Ubertini. XMM-Newton and INTEGRAL observations of new absorbed supergiant high-mass X-ray binaries. *A&A*, 453:133–143, July 2006. doi: 10.1051/0004-6361:20053719.
- R. Walter, A. A. Lutovinov, E. Bozzo, and S. S. Tsygankov. High-Mass X-ray Binaries in the Milky Way: A closer look with INTEGRAL. *ArXiv e-prints*, May 2015.
- J. J. Wang and H.-K. Chang. Links Between Z Sources and Atoll Sources. In C. M. Zhang, T. Belloni, M. Méndez, and S. N. Zhang, editors, *Feeding Compact Objects: Accretion on All Scales*, volume 290 of *IAU Symposium*, pages 331–332, February 2013. doi: 10.1017/S1743921312020261.

- Z. Wang and D. Chakrabarty. The Orbital Period of the Ultracompact Low-Mass X-Ray Binary 4U 1543-624. *ApJ*, 616:L139–L142, December 2004. doi: 10.1086/426787.
- R. S. Warwick, M. G. Watson, and R. Willingale. EXOSAT observations of the X-ray pulsar 4U1145-619. *Space Sci. Rev.*, 40:429–432, April 1985. doi: 10.1007/BF00179852.
- R. S. Warwick, A. J. Norton, M. J. L. Turner, M. G. Watson, and R. Willingale. A survey of the galactic plane with EXOSAT. *MNRAS*, 232:551–564, June 1988. doi: 10.1093/mnras/232.3.551.
- L. Wen, A. M. Levine, R. H. D. Corbet, and H. V. Bradt. A Systematic Search for Periodicities in RXTE ASM Data. *ApJS*, 163:372–392, April 2006. doi: 10.1086/500648.
- N. E. White. Discovery of eclipsing nature of LMC X-4. *Nature*, 271:38–40, January 1978. doi: 10.1038/271038a0.
- N. E. White and S. S. Holt. Accretion disk coronae. *ApJ*, 257:318–337, June 1982. doi: 10.1086/159991.